Path length dependence of jet quenching measured with ALICE at the LHC

Redmer Alexander Bertens

A catalogue record is available from Utrecht University Library

ISBN: 978–90–393–6651–6

Typeset using LaTeX

Path length dependence of jet quenching measured with ALICE at the LHC

Padlengte afhankelijkheid van jet onderdrukking
gemeten met ALICE bij de LHC

(met een samenvatting in het Nederlands)

Proefschrift

ter verkrijging van de graad van doctor aan de Universiteit Utrecht op gezag van de rector magnificus, prof. dr. G. J. van der Zwaan, ingevolge het besluit van het college voor promoties in het openbaar te verdedigen op maandag 31 oktober 2016 des ochtends te 12.45 uur

door

Redmer Alexander Bertens

geboren op 10 januari 1985
te Zeist

Promotor:	Prof. dr. R. J. M. Snellings
Copromotor:	Dr. ir. M. van Leeuwen

– Johann Sebastian Bach, *from BWV 564,2 – Adagio C-dur (1712?)*

Contents

V Miscellany 141

Prolegomena

Jets are used to probe the quark-gluon plasma (QGP) that is created in heavy-ion collisions, by using the fact that medium-induced parton energy loss from elastic and radiative interactions between partons and the QGP lead to a modification of the measured jet spectrum. The dependence of the energy loss on the in-medium path-length provides insight into the energy-loss mechanisms and can be studied by measuring jet production relative to the orientation of the second-order symmetry plane Ψ_2. The azimuthal asymmetry in the jet production is quantified as $v_2^{\text{ch jet}}$, the second-order coefficient of the Fourier expansion of the azimuthal distribution of jets relative to Ψ_n, the orientation of the symmetry axes of the initial nucleon distribution of the collision overlap region.

In this dissertation, measurements of $v_2^{\text{ch jet}}$ of $R = 0.2$ charged jets, reconstructed with the anti-k_{T} jet finder algorithm in Pb–Pb collisions with 0–5% and 30–50% collision centrality are presented. Jets are reconstructed at mid-rapidity ($|\eta_{\text{jet}}| < 0.7$) using charged constituent tracks with momenta $0.15 < p_{\mathrm{T}} < 100$ GeV/c, and are required to contain a charged hadron with $p_{\mathrm{T}} \geq 3$ GeV/c. The underlying event energy is subtracted jet-by-jet using a description which takes into account dominant hydrodynamic flow harmonics v_2 and v_3. The coefficient $v_2^{\text{ch jet}}$ is obtained from p_{T}-differential jet yields measured with respect to the experimentally accessible event plane $\Psi_{\text{EP, }2}$, which is reconstructed at forward rapidities ($2.8 < \eta < 5.1$ and $-3.7 < \eta < -1.7$).

The reported $v_2^{\text{ch jet}}$ has been corrected back to the azimuthal anisotropy with respect to the underlying symmetry plane Ψ_2 by applying an event plane resolution correction. The jet p_{T} spectra are corrected for fluctuations in the background transverse momentum density and detector effects through an unfolding procedure which is applied for different azimuthal orientations independently. The detector corrections correct back to particle level jets consisting of only primary charged particles from the collision.

Significant non-zero $v_2^{\text{ch jet}}$ is observed in peripheral collisions for $20 < p_{\mathrm{T}}^{\text{jet}} < 90$ GeV/c. The observed $v_2^{\text{ch jet}}$ in central collisions is of similar magnitude, but the uncertainties are larger and therefore the results are not significantly different from zero. The azimuthal dependence of the jet production is similar to suppression observed in measurements of v_2 of single charged particles at high p_{T} and v_2^{jet} of jets comprising both charged and neutral fragments. Good agreement between the data and predictions from JEWEL, an energy-loss model simulating parton shower evolution in the presence of a dense QCD medium, is found in peripheral collisions.

Part I

Introduction and theory

1 A brief introduction

1.1 The Standard Model

The Standard Model[a] is a relativistic quantum field theory which describes the interactions between *elementary particles* (particles which have no known substructure) by the exchange of force carriers called *gauge bosons*. Interactions in the Standard Model are classified into two fundamental sectors: strong and electroweak. Electroweak interactions are mediated by the charged W^+ and W^- bosons, and the neutral Z^0 and γ bosons. At low energies ($<$ 100 GeV/c), the symmetry of the electroweak SU(2)$\times$U(1) group is spontaneously broken by the Higgs mechanism and the weak and electromagnetic force manifest themselves as two distinct phenomena: the weak force, affecting all fermions (spin 1/2 particles), and the electromagnetic force, working on all charged particles via γ exchanges (although it should be noted that the electromagnetic interaction between quarks is very small compared to the strong interaction). The recent discovery of the Higgs boson [3, 4], predicted as early as 1964 but due to its large mass experimentally out of reach until the LHC era, has been of key importance, as without a mechanism for spontaneous electroweak symmetry breaking, fermions, as well as the $W^\pm$ and Z^0 bosons that govern the weak interaction, remain massless in the Standard Model. Both the weak and electromagnetic interaction are well-understood and can be described by Quantum Electrodynamics (QED) and Electroweak Theory (EWT).

1.2 Quantum Chromodynamics

The third interaction described by the Standard Model is that of massive, color-charged *quarks* via the exchange of massless bosons called *gluons*. This *strong force* is described by quantum chromodynamics (QCD), a non-abelian quantum field gauge theory, based on local symmetry of the SU(3) group. The strong interaction is mediated by the exchange of *color*, the QCD analogue of electrical charge, with ‘charges’ red, green and blue (opposed by anti-red, anti-green and anti-blue). Each quark carries a single color charge. Gluons however, carry not one, but two charges (color and anti-color). The key difference between the electroweak and strong interaction is that as a result of this, gluons can self-interact [5], giving rise to QCD phenomena of *color confinement* and *asymptotic freedom.*

The contribution of self interactions between gluons in QCD dynamics is evident from the

[a] A full description of the Standard Model is beyond the scope of this work; extensive texts, which have served as the basis for this chapter, can e.g. be found in [1, 2].

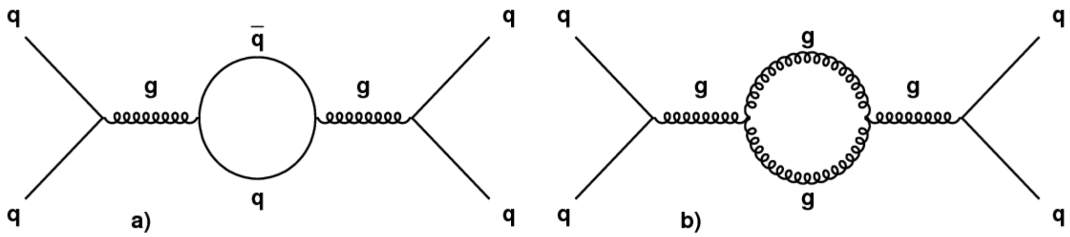

Figure 1.1: Left: a virtual $q\overline{q}$ pair screens color charges, analogous to QED screening via the creation of a virtual e^+, e^- pair. Right: three point gluon interactions allow for the creation of virtual $g\overline{g}$ pairs, which augment (anti-screen) color charges at large distances. From [6].

gauge invariant QCD Lagrangian,

$$\mathscr{L}_{\mathrm{QCD}} = \overline{q}(i\gamma^{\mu}d_{\mu} - m)q - g(\overline{q}\gamma^{\mu}\lambda_a q)A^a_{\mu} - \frac{1}{4}G^a_{\mu\nu}G^{\mu\nu}_a. \tag{1.1}$$

in which q denote quark fields, A^a_{μ} represent the vector gluon fields, γ^{μ} are the Dirac matrices and m corresponds to mass. In order to achieve gauge invariance, the field strength tensor is constructed as

$$G^a_{\mu\nu} = \partial_{\mu}A^a_{\nu} - \partial_{\nu}A^a_{\mu} - gf_{abc}A^b_{\mu}A^c_{\nu} \tag{1.2}$$

with f_{abc} the structure constant. Expressing Eq. 1.2 and Eq. 1.1 in 'symbolic' form, the quark (q), gluon (g) dynamics are clearly recognizable,

$$\mathscr{L}_{\mathrm{QCD}} = \underbrace{\text{“}\overline{q}q\text{”}}_{\text{q propagation}} + \underbrace{\text{“}A^2\text{”}}_{\text{g proparation}} + \underbrace{g\text{“}\overline{q}qA\text{”}}_{\text{qg interaction}} + \underbrace{g\text{“}A^3\text{”}}_{\text{ggg interaction}} + \underbrace{g^2\text{“}A^4\text{”}}_{\text{gggg interaction}} . \tag{1.3}$$

The first three terms of Eq. 1.3 describe free propagation of quarks and gluons in vacuum, and quark-gluon interactions. The remaining two terms signal the presence of three- and four-point gluon self interactions.

Gluon self interactions are unique to QCD and cause *anti-screening effects*. In both QCD and QED, loop diagrams as in the left panel of Fig. 1.1 are allowed, which effectively decrease the coupling strength at increasing distances as the pair of virtual particles in the loop briefly polarizes the vacuum (an effect called *screening*). In QCD, diagrams as on the right panel of Fig. 1.1 are also allowed since gluons, in contrast to electroweak bosons, can self interact. As gluons are charged, these loops *anti-screen* (and thus augment) the color fields. As a result of anti-screening, the QCD coupling strength, governed by the coupling constant α_s, rises increasingly for interactions with low momentum transfer as a result of strong anti-screening, whereas at high energies it asymptotically decreases to zero. The value of α_s as function of energy transfer is shown in Fig. 1.2.

The effect of anti-screening on particle dynamics in QCD can most easily be illustrated by looking at the effective QCD potential V at separation distance x between a $q\overline{q}$ pair, which is parametrized as the sum of a Yukawa potential (a screened Coulomb term) and the potential of a string with tension κ,

$$V(x) \propto -\frac{\alpha_s}{x} + \kappa x. \tag{1.4}$$

The potential increases monotonically as function of x, until at some point the $q\overline{q}$ pair is separated so far that it becomes energetically favorable to create a new $q\overline{q}$ pair from vacuum rather

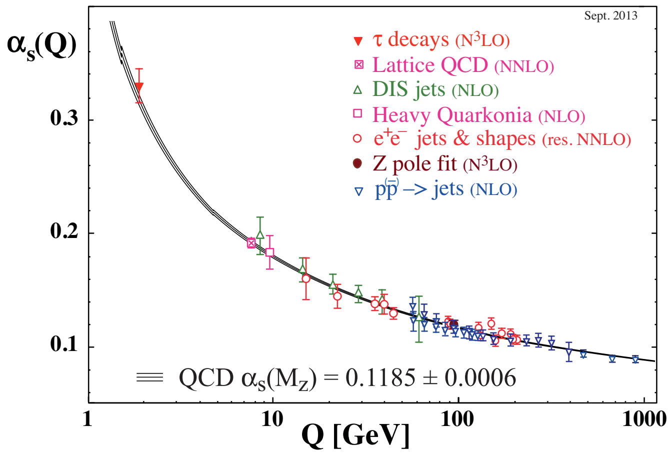

Figure 1.2: Evolution of coupling constant α_s as function of momentum transfer Q, experimental data (points) and predictions from QCD (bands). From [8].

than to extend the string, which leads to the QCD phenomenon of *color confinement*: quarks are confined to colorless bound states called *hadrons*. A colorless state is created by either combining two quarks with equal color and anti color into a *meson*, or by combining three quarks of configuration red, green blue (or their anti-colors) into a *baryon*[b]. Conversely, at very short distances or high energy transfers, color screening effects become negligible and α_s decreases asymptotically, a property of QCD called *asymptotic freedom*. The potential V vanishes and quarks and gluons can exist as free particles.

The behavior of the coupling constant α_s defines the unique properties that govern QCD dynamics (confinement and asymptotic freedom), but at the same time precludes direct theoretical predictions for many QCD processes as *perturbation theory* cannot be applied. Perturbation theory relies on finding an approximate solution A, by reducing the problem to a perturbation of a well-known and exactly solvable problem with solution A_0. A can then be expressed as deviations from the exactly known solution in terms of an asymptotic series

$$A = A_0 + \epsilon A_1 + \epsilon^2 A_2 + ... + \epsilon^n A_n. \tag{1.5}$$

The precision of the solution depends on at which point series Eq. 1.5 is truncated, where A_0 is generally called 'leading order (LO)', A_1 'next to leading order (NLO)', etc. When parameter $\epsilon \ll 1$ it is sufficient to solve only the first few terms of the right-hand side of Eq. 1.5 to find A with reasonable precision. Systems in quantum field theory are generally expressed as a perturbation series where parameter ϵ is proportional to the coupling constant α. For QED, with a coupling constant of $\frac{1}{137}$, perturbation theory is applicable. The coupling constant α_s for QCD however rises asymptotically at low Q (see Fig. 1.2), meaning that only at large Q perturbative solutions can be found. At energy regimes in which perturbative calculations fail to describe QCD dynamics, effective theories have to be applied, which use phenomenological approaches, or discretized non-perturbative modeling (*lattice QCD calculations* [9]), the precision of which is limited by computing power.

[b] Recent results [7] from the LHCb collaboration report the discovery of a pentaquark - a colorless bound state of five quarks. At the time of writing however it is not clear whether this is a state of a tightly bound meson and baryon or a true pentaquark state.

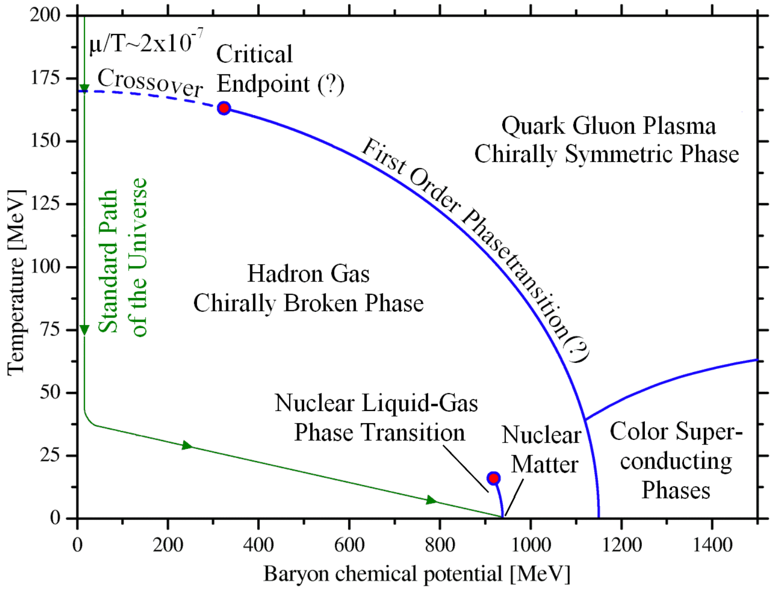

Figure 1.3: Sketch of the QCD phase diagram (from [11]), the green line depicts current knowledge on the evolution of the universe [12]. The LHC is expected to cover the top left corner of the phase diagram, of very high temperature but low density.

1.3 The Quark-Gluon Plasma

As discussed in the previous section, the coupling between quarks and gluons is not constant, meaning that at very high color charge densities, quarks and gluons are no longer confined to bound hadronic states. The phase of matter that is composed of deconfined quarks and gluons, which can move over long distances, is called the *quark-gluon plasma* (QGP). The dynamics of free quarks and gluons is poorly understood from first principles, as the large value of α_s precludes using perturbative calculations. Estimates from lattice QCD calculations currently predict that the phase transition from 'bound' nuclear matter to the QGP phase occurs at temperatures of ≈ 155 MeV or a density of 1 GeV/fm^3 [10] (a schematic view of the QCD phase diagram is given in Fig. 1.3). Temperatures exceeding these critical values are thought to only have existed in nature during the first microseconds after the Big Bang (see the green curve in Fig. 1.3). QGP matter as result of extreme net baryonic density may exist at the core of extremely dense neutron stars.

The QGP can be created and studied in the laboratory by colliding heavy-ions which have been accelerated to relativistic energies in a particle accelerator. The first relativistic heavy-ion collisions (carried out in a fixed target configuration) took place in the Bevalac accelerator at the Lawrence Berkeley National Laboratory in 1974 [13]; however the first indirect evidence for a QGP creation was claimed at the *European Organization for Nuclear Research* (CERN) in 2000 [14], and the *Relativistic Heavy-Ion Collider* (RHIC, New York, USA) in 2005 [15]. The most powerful heavy-ion collider currently in operation is the *Large Hadron Collider* (LHC) located at CERN, Geneva, which has accelerated lead (Pb) nuclei to a center-of-mass energy per nucleon pair of $\sqrt{s_{\mathrm{NN}}} = 2.76$ TeV in 2010 and 2011, and will operate at an energy of $\sqrt{s_{\mathrm{NN}}}$

= 5.02 TeV between 2015 and 2017.

This dissertation will describe in detail the measurement of azimuthal anisotropy of charged particle jets, $v_2^{\text{ch jet}}$, performed using collisions of Pb nuclei accelerated by the LHC and recorded with the ALICE detector in 2010 and 2011. The $v_2^{\text{ch jet}}$ measurement is aimed at understanding the properties of the QGP by penetrating it with a well-understood probe (a highly energetic parton), and observing how this probe is modified by the QGP, thereby deducing the plasma's properties and dynamics.

The text is structured as follows: Chapter 2 gives in an introduction to concepts of in-medium parton energy loss, connects measurements to QGP dynamics and motivates $v_2^{\text{ch jet}}$ as observable. Chapters 3, 4 and 5 explain in detail how the $v_2^{\text{ch jet}}$ measurement is carried out, starting with an overview of the ALICE experiment and data taking (Ch. 3), after which the data analysis is covered (Ch. 4) and concluding with closure tests that are used to validate the analysis (Ch. 5 and Ch. 6). Final results are presented and placed in a broader context in Chapter 7. An outlook for future prospects is finally given in Chapter 8.

Natural units ($c = \hbar = k_{\text{B}} = 1$) are used throughout this dissertation, with the exception of descriptions of detector geometry (which are given in système international units). Unless otherwise indicated, matrices are represented as boldface capitals, whereas boldface non-capitalized letters denote vectors. Scalars and four-vectors are given in italics, the latter with indices in Greek when relevant. Parts of the text have appeared in [16–18].

2 | Parton energy loss

The heavy-ion program at ALICE (see Ch. 3) is aimed at studying strongly interacting matter in ultra-relativistic nuclear collisions where the formation of a quark gluon plasma (QGP) is expected. As explained briefly in the introduction, properties of the QGP can be inferred by quantifying how a highly energetic probe is modified while traversing the QGP. These highly energetic probes are quarks and gluons, collectively called *partons*, emitted in the early stage (prior to QGP formation) of nucleus-nucleus collisions, which lose energy as they traverse the QGP medium. In this chapter, energy loss mechanisms and the dependence on the parton's trajectory through the QGP are explained (§ 2.2). Experimental evidence for parton energy loss is discussed (§ 2.3) and the connection to other measurements of QGP properties (§ 2.4) is examined, and finally, the $v_2^{\mathrm{ch\ jet}}$ measurement, which is directly sensitive to the length of a parton's trajectory through the QGP, is motivated (§ 2.5).

2.1 QGP formation in heavy-ion collisions

A space-time diagram of the evolution of a nucleus-nucleus collision is sketched in Fig. 2.1. The left-hand side of the diagram depicts the evolution of a collision in which no QGP is formed. Particles, e.g. protons, collide at the origin of the axes. After the initial scattering, hadrons are quickly formed. A short hadron gas phase is possible during which the gas composition can change as a result of interactions between particles. Finally, the system becomes so dilute that it freezes out into final state particles that can be observed in a detector.

In the case of the formation of a QGP (the right hand side of the figure), the initial pre-equilibrium phase is rapidly followed by a QGP phase, in which deconfined quarks and gluons can undergo multiple interactions and form a system which is in local thermal equilibrium as the mean free path of in the system is small compared the total system size. In this stage, the plasma dynamics are well described phenomenologically using dissipative relativistic fluid dynamics ([19, 20], see § 2.2.3). The collision system rapidly expands in the vacuum and cools down, until the temperature of the plasma reaches the critical temperature of the QGP phase transition and quarks are bound into color-confined states. The formed hadrons can still interact as long as the mean free path of the gas is short, but eventually the chemical composition of the system is fixed and the final state particles are recorded by the detector.

2.1.1 Tomography: studying the QGP via parton energy loss

As explained in § 1.2, the cross section $\sigma^{ij\to k}$ for the parton scattering $ij \to k$ can be calculated using perturbative QCD (pQCD) calculations if the momentum transfer Q is large enough. To

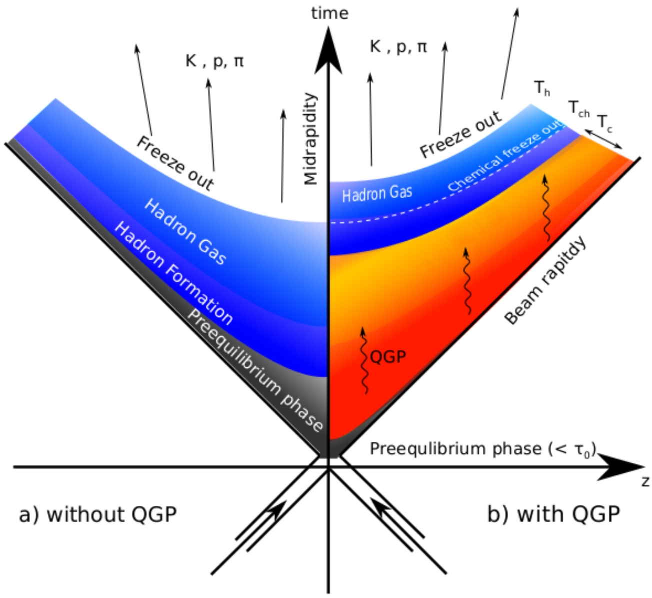

Figure 2.1: Space-time evolution of a nucleus-nucleus collisions without QGP formation (left) compared to the evolution with QGP formation (right).

describe from theory which final state particles (or jet) x will be produced in a collision when hadrons h_1, h_2 scatter, this cross section needs to be convoluted with the probability of finding partons ij inside the colliding hadrons, and with a description of how state x is produced out of k. Under the assumption that scattering and fragmentation are independent long- and short distance processes, the cross-section can be factorized (the *factorization theorem*) and written as [21–23]

$$\sigma_{h_1 h_2 \to x} = \underbrace{f_i^{h_1}(x_1, Q^2) f_j^{h_2}(x_2, Q^2)}_{\text{(n)PDF}} \otimes \underbrace{\sigma^{ij \to k}(x_1 p_1, x_2 p_2, Q^2)}_{\text{pQCD}} \otimes \underbrace{D_{k \to x}(z, Q^2)}_{\text{fragmentation}} \tag{2.1}$$

where $f(x, Q^2)$ are the *parton distribution functions*, which give the likelihood of finding parton i carrying momentum fraction x of the hadron at momentum transfer Q^2, and $D(z, Q^2)$ represent the fragmentation function, which describes how parton k fragments to final state object x, which carries fraction z of the original quark momentum, at energy scale Q^2. The factorization assumption, evaluated using NLO partonic cross sections, has been shown [24–27] to predict measured cross sections well for transverse momenta of $p_T > 5$ GeV/c.

PDFs are obtained from measured cross sections in e.g. Deep Inelastic Scattering (DIS)[a] of leptons off nucleons. At low Q^2, PDFs are constrained by data; at higher Q^2 where low coupling strength allow for pQCD calculations, PDFs are evaluated beyond the experimental range using the DGLAP evolution equations [28–30], so that the experimentally obtained PDFs can be used for a wide range of center-of-mass energies.

After the initial scattering, produced partons undergo fragmentation by radiation of gluons which in turn can split to $q\bar{q}$ pairs, leading to a collimated shower of fragmented particles

[a] At large Q^2, inelastic scattering of a lepton off a proton can be viewed as elastic scattering of the electron off a 'free' quark within the proton.

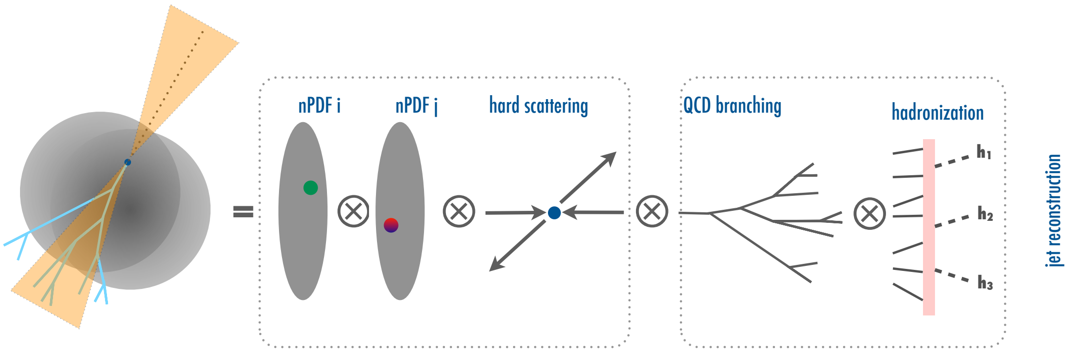

Figure 2.2: Jet production in a heavy-ion collision (from [35]). A hard scattering takes place within the nucleus-nucleus overlap region. A parton shower forms, and its fragments hadronize into a collimated spray of particles: a jet. Jet production is calculable from nPDFs and the hard scattering cross-section. The QCD branching and hadronization are modified with respect to the vacuum case by the presence of the hot and dense QGP.

emitted under shallow angles with respect to the original parton. These radiation patterns can be implemented in Monte Carlo generators by using the Sudakov form factor [31, 32], which describes the survival probability of a parton at a given energy scale. At some point fragmentation enters the non-perturbative regime, and showered partons eventually hadronize (non-perturbatively) into colorless, final state particles. Although hadronization is not fully understood, it can be phenomenologically modeled using e.g. the Lund model [33, 34]. The collimated bunches of colorless hadrons that originate from a hard scattering are called *'jets'*.

Jets are modified by the QGP, and can thus be used to study it; an idea already proposed in the early 1980s [36] and illustrated in Fig. 2.2. Initial hard parton interactions occur instantaneously at the moment of the collision between nuclei, whereas the formation time of the QGP is finite as a system in (local) thermal equilibrium needs to be formed. The jet production itself can therefore be calculated using arguments similar to those given in Eq. 2.1, using nuclear PDFs (nPDFs) which are known experimentally. The parton shower following the hard scattering however is modified by the QGP, as partons lose energy in the QGP medium via (multiple) scattering on medium constituents and additional medium-induced gluon radiation [37]. The resulting energy loss of the jet can be measured and constrains QGP properties.

2.2 Energy loss mechanisms

Partons traversing the QGP medium lose energy via collisional and radiative processes. Both energy loss mechanisms contribute to the total energy loss of the initial hard partons. The relative importance of the two mechanisms and the explicit dependence on the parton's trajectory through the QGP is studied via e.g. the $v_2^{\text{ch jet}}$ measurement.

2.2.1 Collisional energy loss

The dense QGP can, when considering energy loss, be modeled as (light) constituents that serve as scattering centers for the propagating, highly energetic quarks or gluons. Consider a parton - e.g. quark Q - of energy E that transfers energy to a medium constituent via elastic scattering. These scatterings have the form of $Qq \rightarrow Qq$ or $Qg \longrightarrow Qg$, where q, g represent a medium quark or gluon respectively. The energy loss $-\frac{\mathrm{d}E}{\mathrm{d}z}$ that Q suffers per unit length can be described as [36]

$$-\frac{\mathrm{d}E}{\mathrm{d}z} = \sum_{p=q,g} \int d^3k \rho_p(k) \int \mathrm{d}q^2 J\omega \frac{\mathrm{d}\sigma^{Qp\rightarrow Qp}}{\mathrm{d}q^2} \tag{2.2}$$

where p denotes the plasma constituent (quark or gluon), q^2 is the invariant four-momentum transfer, $\omega = E - E'$ is the energy transfer (with E the energy of the incoming Q and E' the energy of the outgoing parton), $\mathrm{d}\sigma/\mathrm{d}q^2$ is the differential cross-section, J represents the flux factor, and $\rho_p(k)$ is the density of plasma constituents of momentum k which, in a thermalized system, is given by Bose-Einstein and Fermi-Dirac statistics,

$$\rho_q(k) = \frac{4N_cN_f}{(2\pi)^3} n_F(k), \qquad \rho_g(k) = \frac{2(N_c^2-1)}{(2\pi)^3} n_B(k) \tag{2.3}$$

where N_f is the number of quark flavors, and n_F, n_B are the Fermi-Dirac and Bose-Einstein distributions which give the probability of finding a parton at given energy state k. Assuming that most momentum transfers q^2 are small, the cross differential cross section is

$$\frac{\mathrm{d}\sigma^{Qp\rightarrow Qp}}{\mathrm{d}q^2} \simeq C_p \frac{2\pi\alpha_s^2}{q^4} \tag{2.4}$$

where color factors C are defined for N_c colors as

$$C_q = \frac{N_c^2-1}{2N_c^2}, \qquad C_g = 1. \tag{2.5}$$

When parton momenta E, E' greatly exceed the plasma constituent momentum k, $J\omega \simeq q^2/2k$ [b]. Using expressions 2.3, 2.4, and 2.5, Eq. 2.2 can be integrated [38] to find a (somewhat qualitative) expression of the differential energy loss (where the logarithm results from integration of q^{-2}

[b]This expression is found when all partons are considered to be massless (i.e. in the limit chosen limit of $E, E' \gg \omega, k$). The flux factor is [36]

$$J = 1 - \cos\theta \tag{2.6}$$

where θ is the laboratory angle between the incident partons. For elastic processes, Bjorken x equals one so that the quark, parton scattering kinematics obey

$$x = \frac{q^2}{2k\cdot\omega} = 1 \tag{2.7}$$

with $k\cdot\omega$ as the scalar product of the four-vectors representing the medium constituent and energy loss of the incoming quark. Rewriting this expression, one finds

$$q^2 = 2k\cdot\omega \simeq 2k\omega - k\omega\cos\theta \simeq 2k\omega(1-\cos\theta) \simeq 2k\omega J. \tag{2.8}$$

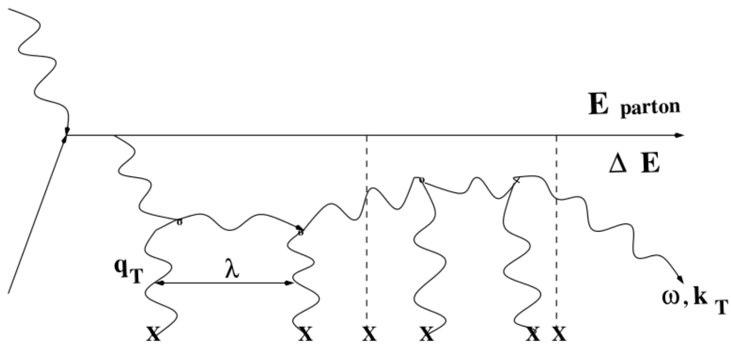

Figure 2.3: In-medium energy loss through gluon radiation. An incoming parton radiates off a gluon, after which the gluon undergoes multiple inelastic scatterings with the medium. The outgoing parton-gluon system no longer forms a color singlet state. From [43].

dq^2),

$$-\frac{\mathrm{d}E}{\mathrm{d}z} = \pi\alpha_s^2 \sum_p C_p \int \frac{d^3k}{k}\rho_p(k) \ln\left(\frac{q^2_{\mathrm{max}}}{q^2_{\mathrm{min}}}\right)$$
$$\simeq \frac{4\pi\alpha_s^2 T^2}{3}\left(1+\frac{N_f}{6}\right)\ln\left(\frac{cE}{\alpha_s T}\right) \tag{2.9}$$

where c is a numerical constant $\mathcal{O}(1)$, $N_c = 3$ and T is the plasma temperature. The choice of minimum and maximum momentum transfer q^2_{min} and q^2_{max} is somewhat ambiguous; in Eq. 2.9, screening mass $\mu = \mathcal{O}(\alpha_s T^2)$ is used as q_{min} and $\sqrt{dTE}$ as q_{max} [39], with d a constant $\mathcal{O}(1)$. A consistent treatment of q_{min} is given by the Braaten-Pisarski method [40]; the expression in the second line of Eq. 2.9 however suffices for the heuristic description in this section.

Because of the T^2 dependence of Eq. 2.9, the collisional energy loss per unit length is proportional to $\sqrt{\epsilon}$, the square root of the energy density of the QGP [38]. The magnitude of the energy loss however is very sensitive to the effective coupling strength α_s of Q to the low momentum constituent.

Contrary to the behavior that will be shown for radiative energy loss, average collisional energy loss per unit distance has no dependence on the size of the QGP, and integrating Eq. 2.9 over z, using finite plasma size $\int_0^L dz = L$ leads to the observation that average energy loss $\langle \Delta E \rangle$ of a parton as a result of elastic scattering in the medium is proportional to in-medium path length L.

Expression 2.9 is derived for quarks; the collisional energy loss for gluons, can be determined following the same argumentation and is $\frac{9}{4}$ times larger [41].

2.2.2 Radiative energy loss

The dominant [42] parton energy-loss mechanism is sketched in Fig. 2.3. An incoming parton radiates a gluon (either before or after the parton enters the medium), which subsequently undergoes multiple inelastic scatterings with the medium.

The average energy loss for a highly energetic parton as a result of gluon radiation can be written as

$$\langle \Delta E \rangle = \int \mathrm{d}\omega \mathrm{d}z \; \omega \frac{\mathrm{d}^2 I}{\mathrm{d}\omega \mathrm{d}z} \tag{2.10}$$

where $\frac{\mathrm{d}I}{\mathrm{d}\omega}$ is the single gluon spectrum, which represents the rate at which a parton radiates gluons of energy ω, and z is a coordinate along the parton's trajectory.

Radiated gluons have a finite formation time τ_f [44–46]

$$\tau_f \simeq \frac{\omega}{k_\perp^2} \tag{2.11}$$

where $k_\perp$ is the gluon momentum perpendicular to the initial parton trajectory. τ_f can be seen as the time that passes until the initial parton and gluon no longer form a coherent object, meaning that the relative phase of the gluon and radiating parton is in the order of unity. During this time, the gluon can undergo further elastic rescatterings and acquire additional momentum (see Fig. 2.3) but further gluon emission off the initial parton is suppressed. For highly energetic gluons, $\omega \gg k_\perp$ and $\tau_f > \lambda$ (with λ the mean free path length of the gluon in the medium) meaning that multiple scattering centers will act as one coherent source for radiation.

As a result of this finite formation time, the single gluon spectrum can be divided into three distinct energy regimes [42, 47],

$$\omega \frac{\mathrm{d}^2 I}{\mathrm{d}\omega \mathrm{d}z} \simeq \begin{cases} \frac{\alpha_s}{\lambda} & \omega < \omega_{\mathrm{BH}} \\ \frac{\alpha_s}{\lambda}\sqrt{\frac{\lambda\mu^2}{\omega}} & \omega_{\mathrm{BH}} < \omega < \omega_{\mathrm{fact}} \\ \frac{\alpha_s}{L} & \omega_{\mathrm{fact}} < \omega < E \end{cases} . \tag{2.12}$$

which depend on ω and differ in how the propagating parton resolves scattering centers within the medium.

At low gluon energies (the Bethe-Heitler energy regime with $\tau < \lambda$ and $\omega < \omega_{\mathrm{BH}}$), all scattering centers in the medium act as single sources of radiation. At intermediate gluon energies ($\omega_{\mathrm{BH}} < \omega < \omega_{\mathrm{fact}}$, the Landau-Pomeranchuk-Migdal (LPM) [48–50] regime) multiple scattering centers act as a coherent scattering source, leading to a suppression of gluon emissions. At very high gluon energies ($\omega > \omega_{\mathrm{fact}}$, the factorization regime) the entire medium acts as one single scattering source.

The total average energy loss $\langle \Delta E \rangle$ can be obtained, in the limit that $E \to \infty$, by integrating Eq. 2.10 over $\mathrm{d}\omega$ and $\mathrm{d}z$, using appropriate boundary conditions [47]

$$\omega_{\mathrm{BH}} \sim \lambda\mu^2 \ll \omega \ll \omega_{\mathrm{fact}} \sim \frac{\mu^2 L^2}{\lambda} \leq E. \tag{2.13}$$

Heuristically, the boundary conditions in Eq. 2.13 can be derived[c] by introducing the *coherence length* l_{coh} as

$$l_{\mathrm{coh}} \simeq \frac{\omega}{\langle k_\perp^2 \rangle_{l_{\mathrm{coh}}}}. \tag{2.14}$$

Assuming that the gluon follows a random walk pattern through the medium, its accumulated transverse momentum can be expressed in terms of the number of scattering centers in the medium N, and the screening radius μ, via the standard equivalence

$$\langle k_\perp^2 \rangle \equiv N\mu^2 \simeq \frac{L}{\lambda}\mu^2. \tag{2.15}$$

[c]For details, see [47, 51].

The coherence length l_{coh} can now be used to introduce the reduction – caused by the finite formation time – of the effective number of scatterings,

$$\langle k_\perp^2 \rangle_{l_{\text{coh}}} \equiv N_{\text{coh}} \mu^2 \simeq \frac{l_{\text{coh}}}{\lambda} \mu^2 \tag{2.16}$$

where N_{coh} $(\leq N)$ is the number of effective scattering centers. With Eqs 2.14 and 2.16, l_{coh} can be expressed as

$$l_{\text{coh}} \simeq \sqrt{\frac{\omega \lambda}{\mu^2}}, \tag{2.17}$$

so that

$$N_{\text{coh}} \simeq \sqrt{\frac{\omega}{\lambda \mu^2}} \equiv \sqrt{\frac{\omega}{E_{\text{LPM}}}}, \tag{2.18}$$

where newly introduced parameter E_{LPM} serves the purpose of explicitly connecting the different regimes of the gluon spectrum (Eq 2.12) to the number of coherent scattering centers (i.e. $N_{\text{coh}} \simeq N, N_{\text{coh}} < N, N_{\text{coh}} \simeq 1$), thereby defining the different regimes of Eq. 2.12.

In the Bethe-Heitler regime, incoherent radiation takes place on $N = L/\lambda$ scattering centers, $l_{\text{coh}} \leq \lambda$ and $\omega \leq E_{\text{LPM}}$. Using the single scattering spectrum,

$$\omega \frac{\mathrm{d}I}{\mathrm{d}\omega} \simeq \alpha_s \tag{2.19}$$

the differential energy spectrum per unit length is

$$\omega \frac{\mathrm{d}^2 I}{\mathrm{d}\omega \mathrm{d}z}\bigg|_{\text{BH}} = \frac{\omega}{L} \frac{\mathrm{d}I}{\mathrm{d}\omega}\bigg|_{L} \simeq \frac{\alpha_s}{\lambda}. \tag{2.20}$$

In the LPM regime, multiple scattering centers act as one coherent source of scattering, so the coherence length is larger than the average mean free path λ, but smaller than total length L (i.e. $\lambda < l_{\text{coh}} < L$). With Eqs 2.17 and 2.19, the differential energy spectrum per unit length can be expressed as

$$\omega \frac{\mathrm{d}^2 I}{\mathrm{d}\omega \mathrm{d}z}\bigg|_{l_{\text{coh}}} = \frac{\omega}{l_{\text{coh}}} \frac{\mathrm{d}I}{\mathrm{d}\omega}\bigg|_{l_{\text{coh}}} \simeq \frac{\alpha_s}{\lambda} \sqrt{\frac{\lambda \mu^2}{\omega}}, \tag{2.21}$$

which means that the suppression of radiation in the LPM regime compared to that of the Bethe-Heitler regime is of magnitude $\sqrt{E_{\text{LPM}}/\omega}$.

Finally, in the factorization regime, only one scattering center is active ($l_{\text{coh}} \geq L$). This regime is entered at $\omega_{\text{fact}} \simeq \frac{\mu^2}{\lambda} L^2$, so that (following Eqs 2.16 and 2.17 with $L \simeq \lambda$), $N_{\text{coh}} \simeq 1$ and

$$\omega \frac{\mathrm{d}^2 I}{\mathrm{d}\omega \mathrm{d}z} \simeq \frac{\alpha_s}{L}. \tag{2.22}$$

To obtain the total average energy loss that a parton suffers along a trajectory of length L, Eq. 2.10 is integrated, using the conditions summarized in Eq. 2.13, to find

$$\langle \Delta E \rangle (L) \sim c_1 \alpha_s E + c_2 \alpha_s \frac{\mu^2 L^2}{\lambda} \tag{2.23}$$

with c_i constants of $\mathcal{O}(1)$. The first term on the right-hand side of the Eq. 2.23 is the contribution of the factorization regime, which is independent of L. The second term shows that total energy loss from induced gluon radiation increases quadratically with in-medium length L and is, in the high energy limit, independent of parton energy E, meaning that relative parton energy loss from radiative processes is expected to decrease with increasing parton momenta (as is visible in e.g. Fig. 2.4).

Calculations in which the interactions of the virtual gluons that are emitted into the medium are described using the AdS/CFT correspondence [52] suggest an even stronger (L^3) dependence of radiative energy loss on the path length [53].

2.2.3 Modeling the medium: initial geometry and hydrodynamics

The previous subsections gave a (heuristic) description of energy loss of hard partons in a QGP medium. A meaningful comparison between observed energy loss and energy loss formalisms however can only be made when the medium itself, in which energy is lost, is modeled (e.g. to extract information on the QGP density along the trajectory of the parton). (Viscous) relativistic hydrodynamics is the most widely used theory to model medium dynamics, and has been suggested already over half a century ago [54]. The hydrodynamic ansatz can be justified when realizing that the mean free path of particles in the collision system is much smaller than the characteristic system size, suggesting a description of the medium as a liquid. As input to hydrodynamics the equation of state

$$P = P(\epsilon, n) \tag{2.24}$$

is defined as pressure P as function of energy density ϵ and baryon density n, which can experimentally be tuned to the number of produced particles at a given collision configuration. The most notable difference between relativistic and non-relativistic hydrodynamics lies in the four-velocity extension of the classic velocity $\mathbf{v}$

$$u^\mu = \left(\frac{1}{\sqrt{1-|\mathbf{v}|^2}}, \frac{\mathbf{v}}{\sqrt{1-|\mathbf{v}|^2}} \right) \tag{2.25}$$

the first component of which is the Lorentz contraction factor. Dynamics of the system itself are fully defined from conservation laws, e.g. energy-momentum conservation and baryon number conservation,

$$\partial_\mu T^{\mu\nu} = 0 \qquad \partial_\mu j_b^\mu = 0 \tag{2.26}$$

where $T^{\mu\nu}$ is the energy-momentum tensor and j_b^μ baryon number current. In the case of ideal hydrodynamics,

$$T^{\mu\nu} = (\epsilon + P)u^\mu u^\nu - g^{\mu\nu} P \qquad j_b^\mu = n_b u^\mu \tag{2.27}$$

where n_b is the net baryon density, ϵ is the energy density, $g^{\mu\nu}$ represents the Minkovski metric and P is the pressure in the local rest frame which moves with four-velocity u^μ in the global frame. In case of viscous hydrodynamics, additional (macroscopic) transport coefficients need to be defined, such as shear viscosity η. Transport coefficients depend directly on the microscopic scattering dynamics within the system and govern the time delay between the appearance of thermodynamic gradients and dissipative currents in response to these gradients (see § 2.4.1). Transport coefficients are taken into account by extending $T^{\mu\nu}$ with an additional shear stress tensor $\pi^{\mu\nu}$,

$$T^{\mu\nu} = (\epsilon + P)u^\mu u^\nu - g^{\mu\nu} P + \pi^{\mu\nu} \tag{2.28}$$

the relative importance of which is governed by shear viscosity η as

$$\pi^{\mu\nu} = 2\eta \langle \nabla^\mu u^\nu \rangle \qquad \nabla^\mu = \Delta^{\mu\nu} \partial_\nu \tag{2.29}$$

Hydrodynamic equations are generally solved in 3+1 or 2+1 dimensions; in the latter case, longitudinal boost invariance is assumed (i.e. neglecting dependence of the evolution in the longitudinal direction, commonly expressed in rapidity η[d]). For a comprehensive overview of relativistic hydrodynamics, see [55, 56].

2.2.3.1 The Glauber Model

Any (expanding) system must have an initial configuration. In nuclear collisions this *initial geometry* (the distribution of nucleon-nucleon scatterings in the overlap region) is not accessible experimentally. A widely used approach for modeling the initial geometry is the Glauber model [57], in which two nuclei are arranged with at impact parameter $\mathbf{b}$[e], which is sampled randomly from a linearly decreasing distribution. The nucleon density is generally parametrized by a Fermi distribution

$$\rho(r) = \rho_0 \left(\frac{1 + \omega (r/R)^2}{1 + \exp \frac{r-R}{a}} \right) \tag{2.30}$$

where ρ_0 is the nucleon density at the center of the nucleus, a represents skin depth, R is the nuclear radius and w quantifies deviations from a spherical shape; the latter three parameters are extracted in low-energy electron scattering. Eq. 2.30 can either be used as a continuous nucleon density (the optical Glauber approach) or at specific spatial coordinates (the Monte Carlo approach)[f]. Soft particle production in the Glauber model is generally taken to be proportional to the number of nucleons that undergo at least one interaction (N_{part}), high p_{T}-processes scale with the number of binary nucleon-nucleon collisions (N_{coll}). Initial energy density is calculated from a linear combination of N_{part} and N_{coll} densities.

A second, frequently used approach in modeling initial conditions is the *Color Glass Condensate* (CGC) [58] ansatz, in which saturated gluon structure functions inside the target and projectile nuclei are parametrized and initial gluon production in the overlap region is calculated using perturbative techniques, implemented e.g. in the Monte Carlo Kharzeev-Levin-Nardi (MC-KLN) model [59].

2.3 Experimental signatures of parton energy loss

The most direct approach of measuring parton energy loss is via the nuclear modification factor R_{AA} [60, 61], of highly energetic single hadrons, defined as

$$R_{\mathrm{AA}} = \frac{\mathrm{d}^2 N_{\mathrm{AA}} / \mathrm{d}p_{\mathrm{T}} \mathrm{d}\eta}{\langle T_{\mathrm{AA}} \rangle \cdot \mathrm{d}^2 \sigma_{\mathrm{pp}} / \mathrm{d}p_{\mathrm{T}} \mathrm{d}\eta} \tag{2.31}$$

where $\mathrm{d}^2 N_{\mathrm{AA}} / \mathrm{d}p_{\mathrm{T}} \mathrm{d}\eta$ represents the differential particle yield in nucleus-nucleus collisions and $\mathrm{d}^2 \sigma_{\mathrm{pp}} / \mathrm{d}p_{\mathrm{T}} \mathrm{d}\eta$ is the differential cross-section in proton-proton collisions. The nuclear overlap function $\langle T_{\mathrm{AA}} \rangle$ is derived from a Glauber model [57, 62, 63] and proportional to the number of

[d] See Eq. 3.1 for a definition of rapidity η.

[e] The impact parameter $\mathbf{b}$ is a vector connecting the center of the two nuclei and not a measurable quantity. To distinguish experimentally between collisions with small or large impact parameters, heavy-ion collisions are classified into centrality classes, which are determined from the number of particles that are produced in a collisions. 0% collision centrality refers to the most central (largest multiplicity) events (at very small $\mathbf{b}$). See § 3.3.2 for a full discussion.

[f] For details, see [57].

binary collisions $\langle N_{\mathrm{coll}}\rangle$. In the absence of the formation of a system in which partons lose energy, a Pb–Pb collision can be seen as an independent superposition of nucleon nucleon collisions. The nuclear overlap function is directly proportional to the number of independent proton proton collisions within the overlap region of the colliding nuclei. At high p_{T} the R_{AA} is expected to be 1 if no QGP is formed; at low momenta, the particle production is dominated by soft processes and the T_{AA} scaling is not expected to hold [64]. The validity of these assumptions has been tested by measuring the R_{AA} of particles which are *not* sensitive to QCD dynamics, such as the (γ, $\mathrm{W}^{\pm}$, Z^0), which is found to be 1 within uncertainties [65, 66].

Figure 2.4 shows the R_{AA} measured in central collisions for several collision energies ($\sqrt{s_{\mathrm{NN}}}$ = 17.3 GeV, 200 GeV, and 2.76 TeV). At RHIC and LHC energies, the R_{AA} is below unity, suggesting strong suppression of highly energetic partons in the medium. The suppression decreases with increasing p_{T}, indicating that the relative strength of the energy loss decreases with increasing p_{T}. Similar measurements in proton-lead collisions [67], where QGP formation is not expected, confirm that the observed suppression is truly an effect of energy loss in the plasma rather than a 'cold' nuclear effect[g].

2.3.1 Extracting transport coefficients

In addition to shear viscosity η (briefly introduced in § 2.2.3), material dynamics can be parametrized by transport coefficients which are more directly related to parton energy loss. In the context of radiative energy loss, the medium dependence of the energy loss is controlled by the jet transport coefficient $\hat{q}$ [46], which quantifies the transverse momentum diffusion[h] in a given material as the average squared momentum transfer $\langle q_{\perp}^2\rangle$ between a parton and the medium per unit length λ, where $_{\perp}$ denotes the momentum component perpendicular to the partons' trajectory,

$$\hat{q} = \frac{\langle q_{\perp}^2\rangle}{\lambda} = \rho \int \mathrm{d}q_{\perp}^2 q_{\perp}^2 \frac{\mathrm{d}\sigma}{\mathrm{d}q_{\perp}^2}. \tag{2.32}$$

As $\hat{q}$ is a function of medium density ρ and parton-medium interaction cross section σ (as given as the right most term of equality 2.32), it is expected to have a dependence on local temperature T and the energy of the parton along which trajectory $\hat{q}$ is evaluated. It can be shown [77] that the average energy loss of the parton (again for the limit $E \to \infty$) has a dependence on the medium size L

$$\Delta E \simeq \alpha_s \hat{q} L^2. \tag{2.33}$$

Model predictions of the R_{AA} of single hadrons from five models, which take different approaches to parton energy loss in a non-uniform, hydrodynamically expanding medium, have been compared [78] to extract a common $\hat{q}$ value as function of temperature T. For details on the modeling of parton energy loss, the reader is referred to [78] and references therein. Briefly summarizing, in the CUJET [79] a scattering potential is modeled which is governed by tuning the strong coupling constant, the Debye screening mass and the density of scattering centers; the HT-BW

[g]It should be noted that at the time of writing, discussion on *collectivity in small systems* is still ongoing, and the dynamics of the system created in p–Pb collisions is not well understood, especially in light of recent measurements on flow and long-range correlations in p–Pb systems. A wealth of publications has recently come available on this subject, e.g. [68–72].

[h]In literature, the coefficient $\hat{e}$, 'longitudinal drag' [74] is often associated with collisional energy loss in the longitudinal direction. In the following discussion however, only $\hat{q}$ will be considered. The relative importance of radiative and elastic energy loss can possibly be disentangled by measuring the quenching of jets originating from heavy quarks, as radiative energy loss is expected to be suppressed for heavy quarks (the so-called 'dead cone' effect' [75, 76]).

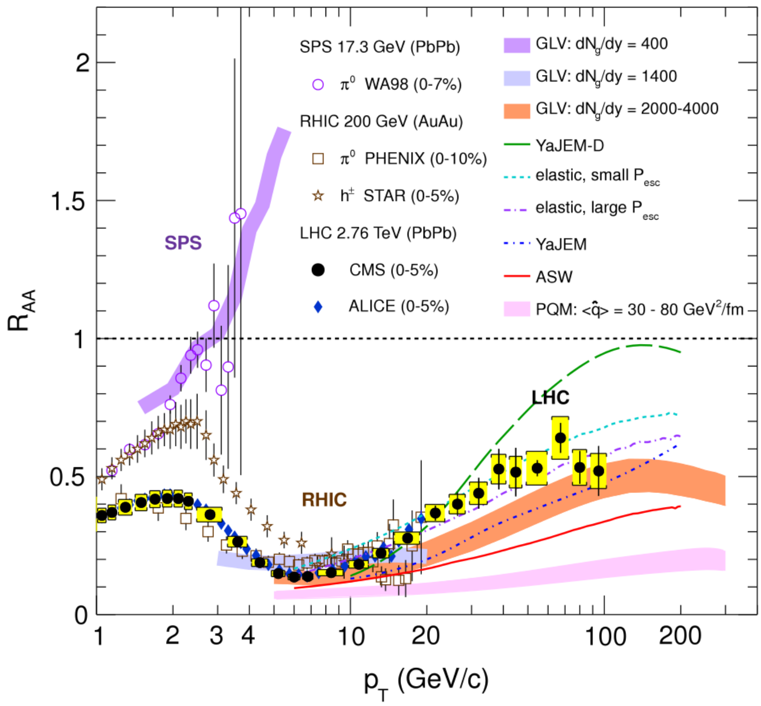

Figure 2.4: R_{AA} of charged particles and neutral pions measured at central collisions for several collision energies ($\sqrt{s_{\mathrm{NN}}}$ = 17.3 GeV, 200 GeV, and 2.76 TeV). At RHIC and LHC energies, the R_{AA} is strongly suppressed for transverse momenta where the N_{coll} scaling is expected to be valid. From [73].

[80] and HT-M [81] approaches use $\hat{q}$ as the only free model parameter; and the MARTINI [82] and McGILL AMY [83], based on hard-thermal-loop resummed thermal field theory, have as only free parameter the strong coupling constant. For medium parametrization, the HT-BW model uses a 3+1 ideal hydrodynamic medium, whereas CUJET, HT-M, and McGILL AMY use 2+1 viscous hydrodynamics, tuned to RHIC and LHC data. The results of the models are summarized in Fig. 2.6 as $\hat{q}$ of a p_{T} = 10 GeV/c quark, originating at the origin of a central collision at a set temperature T. These $\hat{q}$ values are found by making variations in the free parameters of the models, and minimizing the difference between the model predictions and the RHIC and LHC single hadron R_{AA}, as illustrated in Fig. 2.5 for variations in α_s for the CUJET model. In this figure, the two panels on the left show measurements (points) of the R_{AA} at RHIC (far left) and the LHC, and curves corresponding to model predictions at different values of α_s. The right-most panel shows the difference between the model predictions and data in terms of the reduced χ^2 as function of α_s for both RHIC and LHC data. When the spread of the outcomes of the different models is considered as a 'theoretical uncertainty', $\hat{q}$ at an initial time of τ_0 = 0.6 fm/c for the same p_{T} = 10 GeV/c quark is 1.2 ± 0.3 GeV^2/fm at T = 370 MeV and 1.9 ± 0.7 GeV^2/fm at T = 470 MeV (the maximum temperatures considered for RHIC and the LHC in the most central collisions respectively). To illustrate the importance of the medium description for the evaluation of $\hat{q}$, the right hand side of Fig. 2.6 shows $\hat{q}$ along a parton

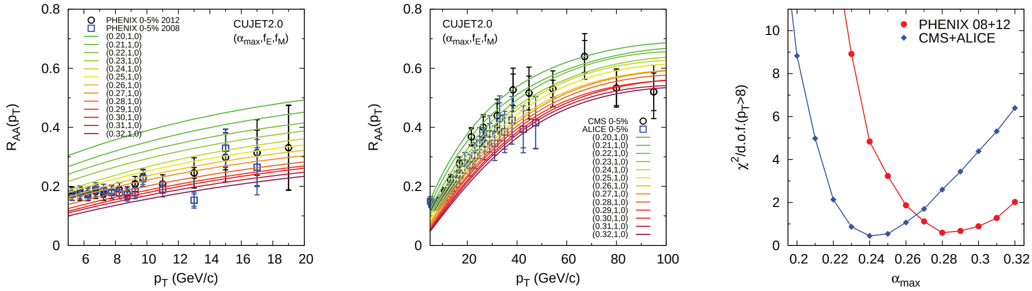

Figure 2.5: Two panels on the left show measurements (points) of the $R_{\rm AA}$ at RHIC (far left) and the LHC, and curves corresponding to model predictions at different values of α_s. The right most panel shows the difference between the model predictions and data in terms of the reduced χ^2 as function of α_s for both RHIC and LHC data. From [78].

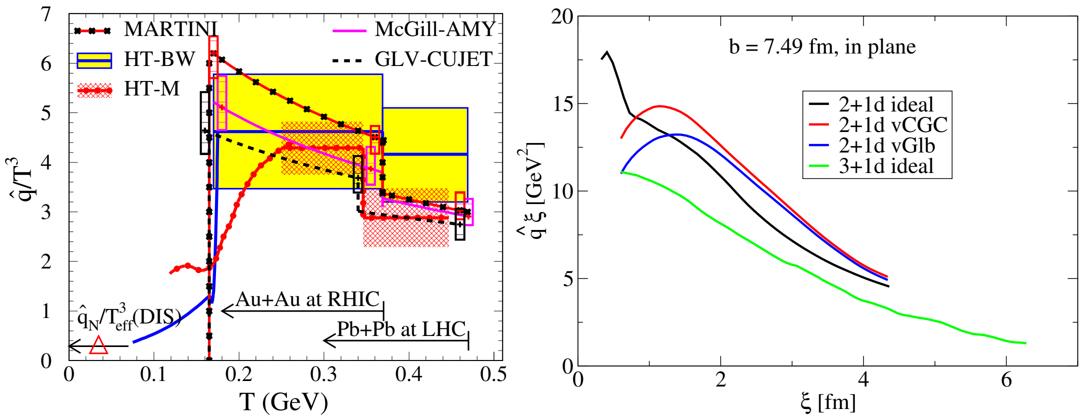

Figure 2.6: Left (from [78]): $\hat{q}/T^3$ as function of T at the origin of a central collision. Right (from [84]) $\hat{q}$ along parton trajectory ξ for different medium parametrizations, using the ASW [85] model for medium induced radiative energy loss in pQCD.

trajectory ξ for different medium models (these trajectories are *not* the trajectories used in [78], but rather come from [84]).

2.4 A broader context

To further understand the properties of the medium that is created in heavy-ion collisions, but also to understand the experimental difficulties that will be described in detail in Chapter 4, a few words have to be dedicated to 'soft' observables. So far, the discussion of medium dynamics has limited itself to (observations sensitive to) the modification of a highly energetic probe by the collision medium. Medium properties can however also be derived by direct study.

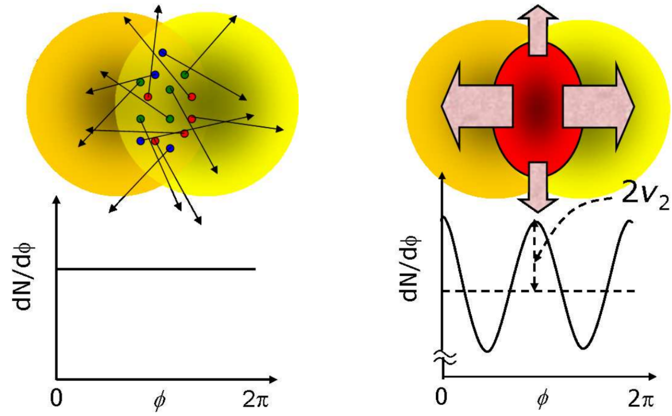

Figure 2.7: The collision overlap region at finite impact parameter has an approximately elliptic shape. In a non-thermalized system (left) particle emission is isotropic. A thermalized system (right) expands anisotropically. This anisotropy can be quantified by amplitudes v_n. Figures from [56].

2.4.1 Flow: quantifying azimuthal anisotropy

At finite impact parameter, Pb–Pb collision systems are anisotropic and have a (roughly) elliptic shape, its eccentricity determined by the impact parameter. Fig. 2.7 sketches the geometry of a semi-central heavy-ion collision. If the collision system does not exhibit collective behavior, particles will be emitted without a preferred direction. If the system thermalizes however, the pressure gradient along the minor axis of the overlap ellipse will be larger than the gradient along the major axis, resulting in a larger net momentum production along the minor axis of the ellipse. The efficiency with which the initial deviations from a spherical overlap region, that cause the pressure gradients in the plasma, are transferred momentum space anisotropy, are governed by the shear viscosity. This anisotropy in momentum space (*anisotropic flow*) manifests itself (at low transverse momenta) as azimuthal modulation of energy density. This modulation is generally quantified using a Fourier expansion [86–88],

$$\frac{\mathrm{d}N}{\mathrm{d}[\varphi - \Psi_n]} \propto 1 + \sum_n 2v_n \cos(n[\varphi - \Psi_n]) \tag{2.34}$$

where φ is the azimuthal angle of a track and Ψ_n represents the orientation of the n-th order symmetry axis of the system in the transverse plane, with p_T-dependent harmonic coefficients [89, 90]

$$v_n(p_\mathrm{T}) = \langle\langle \cos(n[\varphi - \Psi_n])\rangle\rangle. \tag{2.35}$$

where $\langle\langle\ldots\rangle\rangle$ denotes an average over all particles per event, and all collisions in a data sample.

The picture given in 2.7 is rather simplified, as it presents a scenario where matter is distributed smoothly within the colliding nuclei, and the only symmetry plane orientation is defined by the beam axis and impact parameter. In reality however, fluctuations in the distribution of participating nucleons within the nuclei lead to a deviation between the reaction plane and the participant plane Ψ_pp [91], which is defined as the symmetry axis of the distribution of participating nucleons. The left panel of figure 2.8 illustrates this effect: the reaction plane (defined by

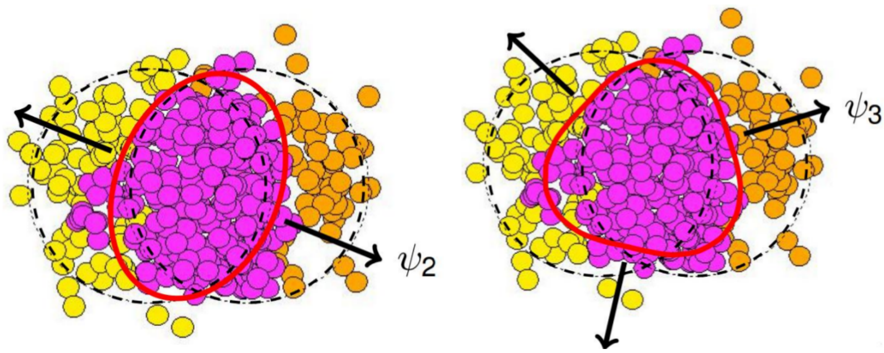

Figure 2.8: Fluctuations lead to a deviation between the reaction plane (horizontal) and the participant plane Ψ_{pp} [91] (left). Fluctuations also generate additional odd harmonic symmetry planes Ψ_n (right).

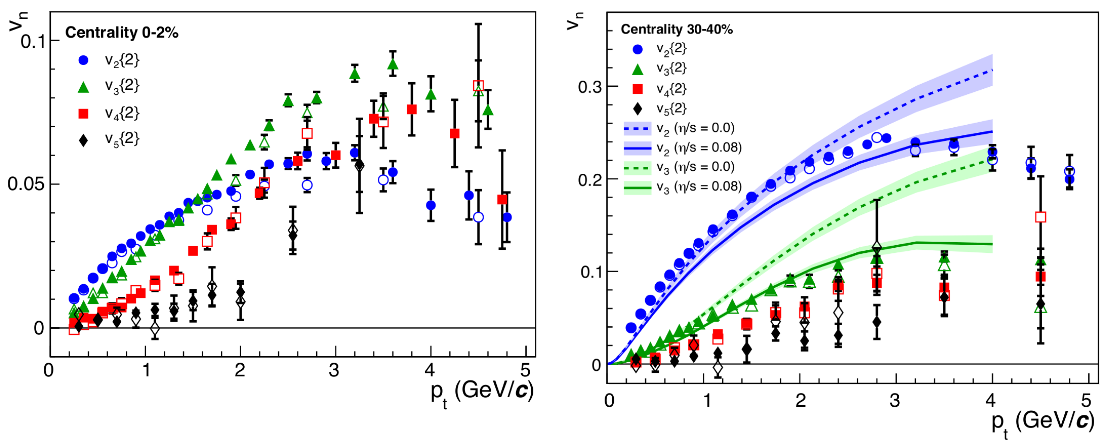

Figure 2.9: Left: v_n harmonics, generated mainly by fluctuations, in 0–2% central collisions. Right: v_n harmonics in 30–40% central collisions, with predictions from ideal and viscous hydrodynamics for v_2 and v_3, using Glauber initial conditions. From [91].

the beam axis and the impact parameter) is a horizontal line; the 2^{nd}-order symmetry plane of the participant distribution Ψ_2 however is tilted. In addition to this, event-by-event fluctuations of the nucleon geometry generate additional odd harmonic symmetry planes Ψ_n, as illustrated in the right panel of Fig. 2.8, which give rise to odd harmonics v_3, v_5, etc [91]. Measurements of v_n harmonics in semi-central collisions are shown Fig. 2.9 (right) together with predictions from viscous hydrodynamics. Higher harmonic v_n coefficients are more sensitive to η/s than v_2 [92]. The same figure shows v_n harmonics in very central collisions, which confirms the importance of fluctuations in the initial nucleon distribution.

2.4.2 v_n and insights from viscous hydrodynamics

Detailed information on the macroscopic plasma parameters, as well as hadronization mechanisms, can be extracted from measurements of v_n harmonics for identified particles, taking

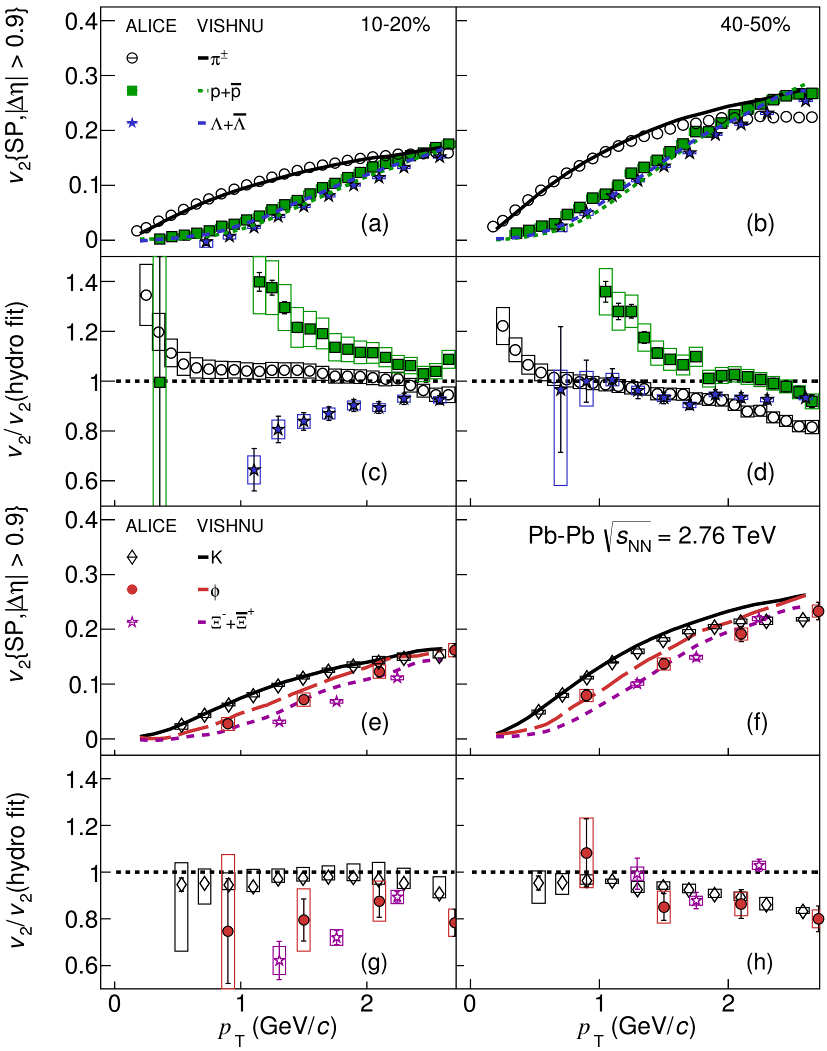

Figure 2.10: Elliptic flow coefficient v_2 for different hadron species ($\pi^\pm, p+\overline{p}, \Lambda+\overline{\Lambda}, K, \phi, \Xi^- + \overline{\Xi}^+$) in various centrality classes [93]. At low momentum, v_2 is described reasonably well by VISHNU [94–96] predictions.

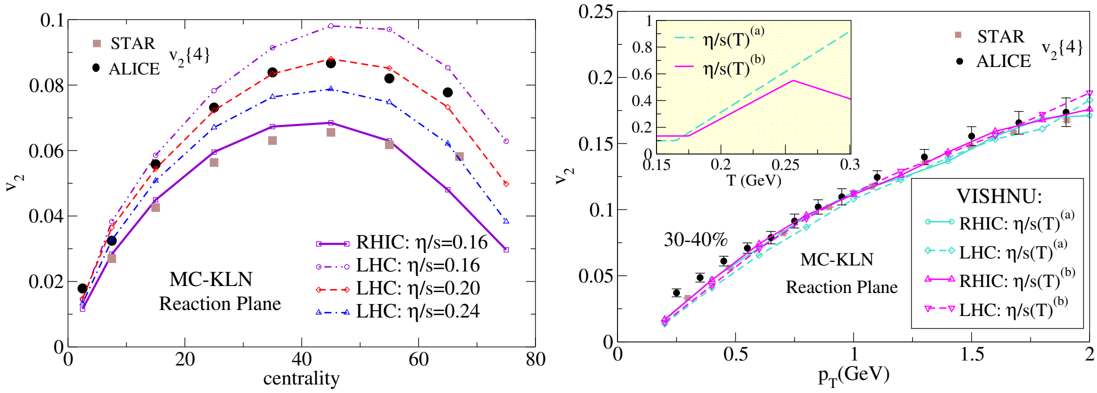

Figure 2.11: Elliptic flow (v_2) measured by ALICE and STAR, p_T-integrated as function of centrality (left) and p_T-differential in 30-40% collision centrality (right) together with predictions from viscous hydrodynamics at different η/s. From [97, 98].

advantage of the mass differences between different particle species, as a common velocity boost from the expanding plasma will affect different masses differently. In Fig. 2.10 the v_2 measurement [93] of identified hadrons ($\pi^{\pm}, p + \overline{p}, \Lambda + \overline{\Lambda}, K, \phi, \Xi^- + \overline{\Xi}^+$) in two centrality classes (10–20% and 30–40%) is shown. The measurement is compared to predictions from VISHNU [94–96] which uses a 2+1d viscous hydrodynamic medium description, which transitions into a hadronic evolution cascade via elastic, semi-elastic and inelastic scatterings, at a 'switching temperature' of 165 MeV. The MC-KLN [59] model is used as initial condition, after which hydrodynamic evolution begins at an initial time of $\tau_0 = 0.9$ fm/c and using a fixed (no temperature dependence) value of $\eta/s = 0.16$. The model predictions describe qualitatively the mass ordering of the p_T-differential v_2 that is observed. For a full discussion of these results, see [93].

To test whether the QGP has the same shear viscosity at RHIC energies as it does at LHC energies - a question similar to the T dependence of $\hat{q}$ as shown in Fig. 2.6 - the left panel of Fig. 2.11 shows predictions for p_T-integrated v_2 as function of collision centrality for different values of η/s. The predictions for the LHC are shown as dashed curves, that for RHIC as a solid line. The figure also shows results from the corresponding v_2 measurements[i] performed by ALICE and STAR. The comparison between model and data suggests an increase of η/s between LHC and RHIC.

The right-hand side of Fig. 2.11, shows measurements and model predictions of p_T-differential v_2 in 30-40% collision centrality. The system evolution is modeled with the VISHNU [94–96] model of viscous hydrodynamics, using two temperature-dependent parameterizations (marked a and b) of η/s. Both forms (a and b) can simultaneously describe the ALICE and STAR data, therefore neither shape can be excluded.

2.4.3 Shear viscosity and parton energy loss

In the collision medium (or more generally, in any medium) interactions between constituents are responsible for generating (shear) viscosity. In principle, these interactions have the same strength as the interactions between a hard parton and the medium. From a microscopic point

[i] p_T-integrated for $0.15 < p_\mathrm{T} < 2.0$ GeV/c at $|\eta| < 1$ for RHIC and $0.2 < p_\mathrm{T} < 5$ GeV/c at $|\eta| < 0.8$ for the LHC.

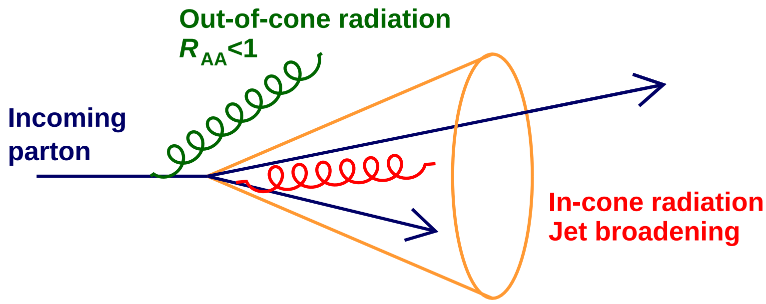

Figure 2.12: Parton energy loss manifests itself as in-cone radiation, leading to a modification of the distribution of energy within the jet (jet broadening) or out-of-cone radiation, quantified by a jet $R_{\mathrm{AA}} < 1$.

of view, shear viscosity is determined by the mean free path λ, typical momentum $\langle p \rangle$, and the density of medium constituents ρ, as [99]

$$\eta \simeq \rho \langle p \rangle \lambda, \tag{2.36}$$

from which, for a weakly coupled plasma, the connection [100]

$$\frac{\eta}{s} \approx 1.25 \left(\frac{T^3}{\hat{q}} \right) \tag{2.37}$$

can be derived, implying that a large value of $\hat{q}$ corresponds to small values of η/s.

Best estimates of $\hat{q}$ and η/s as extracted for RHIC and LHC energies in Figs 2.6 and 2.11 show that the proportionality as suggested in Eq. 2.37 holds reasonable well: η/s is found to be to be slightly larger at the LHC than at RHIC, while the best fit values of $\hat{q}/T^3$ favor a slightly lower value at the LHC as compared to RHIC. [94–96]

2.5 Jets

In the previous sections, parton energy loss mechanisms have been explained and connected to experimental signatures of in-medium parton energy loss (namely the R_{AA} of single hadrons). Jet measurements, in which the kinematic properties of an entire parton shower are measured rather than that of one single hadron, are experimentally more challenging but remove the theoretical uncertainties that arise from the ill-understood physics of hadronization, thus allowing for a more direct comparison to theoretical predictions.

Figure 2.12 shows schematically how parton energy loss is connected to jet observables. An experimentally defined *jet cone*, drawn in orange, defines the jet: the summed four-momenta of all particles reconstructed within this cone should equal the energy of the initial incoming

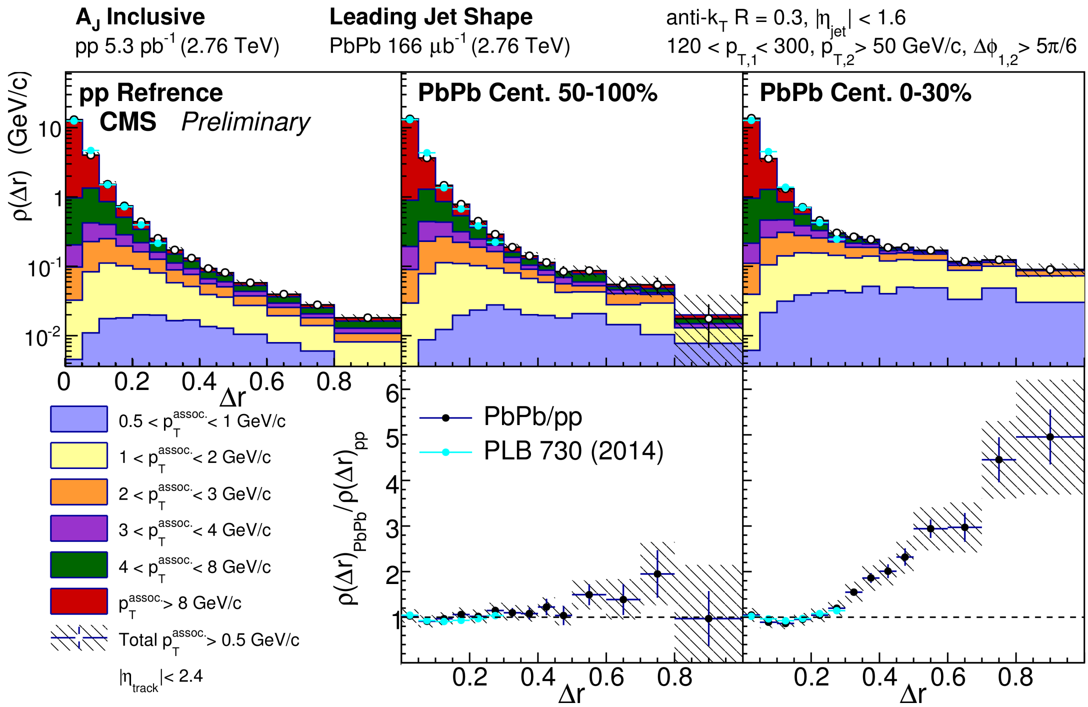

Figure 2.13: Lower panels: ratio $\rho(\Delta r)_{Pb-Pb}/\rho(\Delta r)_{pp}$. An excess of energy at high Δr is visible in Pb–Pb collisions, whereas the distribution of tracks close to the jet axis remains approximately unmodified. Upper panels: pp (left) and Pb–Pb jet composition, split into p_{T}-intervals of constituent tracks. From [101, 102].

parton. The opening angle of the jet is determined by the cone radius R[j]. An incoming parton radiates gluons, prior to and during the partonic showering. If radiation occurs at shallow angles (*in-cone* radiation), the gluon's energy remains within the jet cone, resulting in a change of the p_{T} distribution of constituent tracks *within* the jet cone.

Changes in the composition of the jet as a result of shallow-angle radiation of gluons can e.g. be investigated by looking at the p_{T}-distribution of tracks around the jet axis (both in- and outside of the jet cone) [101, 102], defined as

$$\rho(r) = \frac{1}{\delta r}\frac{1}{N_{\mathrm{jets}}}\frac{\sum_{\mathrm{tracks}\in[r_a,r_b)} p_{\mathrm{T}}}{p_{\mathrm{T}}^{\mathrm{jet}}} \tag{2.38}$$

where the first two fractions serve as normalization factors ($\int \rho(r)\ \mathrm{d}r$ is normalized to 1). $\rho(r)$ is extracted by integrating momentum distributions in η, φ in annuli with radial width $\delta r =$ 0.05, where each ring has an inner radius of $r_a = r - \delta r/2$ and an outer radius of $r_b = r - \delta r/2$. p_{T} represents single track transverse momentum and $p_{\mathrm{T}}^{\mathrm{jet}}$ represents the momentum of the jet.

[j]The exact meaning of jet resolution parameter R depends on the algorithm that is used for jet reconstruction. A formal definition of R is given in § 4.2, for a qualitative appreciation of results at this point this definition suffices. Besides fragments of an incoming parton, tracks emitted from the medium itself will also be included in the jet cone. Chapter 4 will describe in detail how jet energy from the initial hard parton can be separated from the energy of the medium itself.

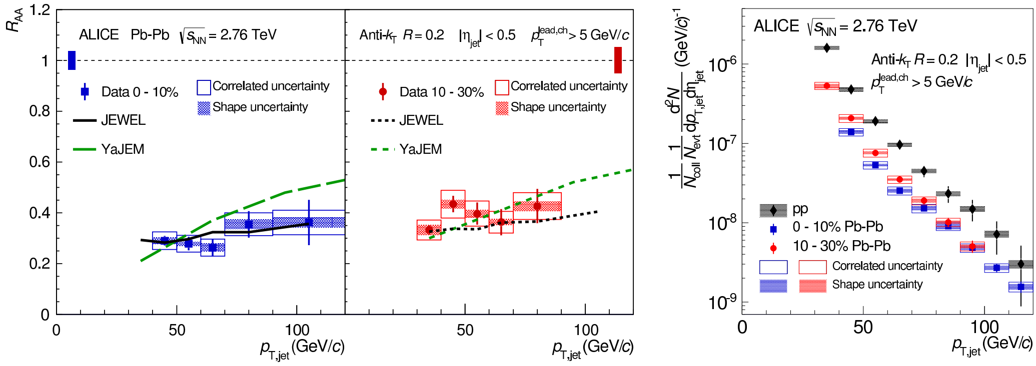

Figure 2.14: Left: R_{AA} of jets in 0–10% and 10–30% collision centrality, derived from scaled jet yields in pp and Pb–Pb collisions (shown right). Jet production is strongly suppressed, indicating out-of-cone radiation. From [120].

Figure 2.13 shows $\rho(r)$ as function of radius Δr, as measured in pp collisions (top left panel) where the stacked, different colors represent a splitting of the jet structure in p_{T} intervals of constituent tracks. The panels on top middle and top right show the same observable measured in Pb–Pb collisions at 50-100% and 0-30% centrality. Figures are made for the most energetic jet in the event, with $120 < p_{\mathrm{T}} < 300$ GeV/c. The figures indicate that jets in the Pb–Pb medium have a composition different than that in pp; a larger number of tracks with low p_{T} are measured. The lower panels show the ratio $\rho(\Delta r)_{Pb-Pb}/\rho(\Delta r)_{pp}$. An excess of energy at high Δr is seen in Pb–Pb collisions, whereas the distribution of tracks close to the jet axis remains approximately unmodified, indicating strong transverse broadening of the parton shower shape as a result of the QCD medium.

If, on the other hand, a gluon is radiated at a sufficiently large angle, its energy will not be reconstructed within the jet cone, and the radiation is considered to be *out-of-cone*, leading to a jet $R_{\mathrm{AA}} < 1$. Out-of-cone jet energy loss is shown in Fig. 2.14, where on the right panel p_{T}-differential cross sections of jets measured in proton-proton collisions (black markers) and Pb–Pb collisions at different collision centralities are given, and on the left-hand panels the jet R_{AA}, as given by Eq. 2.31. In both centrality classes, an $R_{\mathrm{AA}} < 1$ is observed over the full p_{T} range, meaning that jets lose a significant fraction of their energy in the QGP medium, indicating strong out-of-cone radiation. The two lines (black and dashed green) represent model predictions for two different models, JEWEL [103, 104] and YaJEM [105–107], which employ the energy loss mechanisms as given earlier to model jet quenching (more detailed information will be given in Ch. 7). Similar observations have been made [108] using the R_{CP}, defined as

$$R_{\mathrm{CP}} = \frac{\langle T_{\mathrm{AA}}\rangle \cdot \mathrm{d}^2\sigma_{\mathrm{pp}}/\mathrm{d}p_{\mathrm{T}}\mathrm{d}\eta|_{\mathrm{central}}}{\langle T_{\mathrm{AA}}\rangle \cdot \mathrm{d}^2\sigma_{\mathrm{pp}}/\mathrm{d}p_{\mathrm{T}}\mathrm{d}\eta|_{\mathrm{peripheral}}} \tag{2.39}$$

in which the ratio of scaled spectra in central to peripheral collisions is taken rather than the ratio of scaled pp to Pb–Pb collisions. The R_{CP} is found to be < 1, consistent with out-of-cone radiation[k].

[k] A complete overview of observables sensitive to jet energy loss would take up a dissertation of its own, for further reading see e.g. [109–119].

2.5.1 Path-length dependence of energy loss : $v_2^{\text{ch jet}}$

To constrain the underlying physics mechanisms that govern energy loss in the QGP medium, measurements as e.g. shown in Figs 2.14 and 2.13 are used as input to constrain theoretical models. As has been discussed in § 2.2, different energy loss mechanisms are expected to have a different dependence on the length L of the parton trajectory through the QGP. The observable that will be measured in this dissertation, $v_2^{\text{ch jet}}$, is directly sensitive to the dependence of energy loss on the length of the parton trajectory.

Jets from initial hard scatterings are emitted without a preferred direction in the x–y plane, so the differential jet yield in vacuum (without QGP formation) is distributed uniformly in azimuth φ. In non-central Pb–Pb collisions, the initial overlap region of the colliding nuclei in the transverse plane has an approximately elliptic shape (as shown in Fig. 2.7). Jets emitted along the minor axis of the ellipse (defined as the *in-plane* direction) on average traverse less medium - and are therefore expected to lose less energy - than jets that are emitted along the major axis of the ellipse (the *out-of-plane* direction).

The dependence of jet production on the angle relative to the second-harmonic symmetry plane Ψ_2 can be used to probe the path-length dependence of jet energy loss. This dependence is quantified by the parameter $v_2^{\text{ch jet}}$ (as for the v_n harmonic that quantifies anisotropic flow), the coefficient of the second term in a Fourier expansion of the azimuthal distribution of jets relative to symmetry planes Ψ_n,

$$\frac{\mathrm{d}N}{\mathrm{d}[\varphi_{\text{jet}} - \Psi_n]} \propto 1 + \sum_{n=1}^{\infty} 2v_n^{\text{jet}} \cos(n[\varphi_{\text{jet}} - \Psi_n]), \tag{2.40}$$

where φ_{jet} denotes the azimuthal angle of the jet.

In central collisions, the distance that a parton travels through the plasma is approximately equal in the in-plane and out-of-plane directions, therefore a small $v_2^{\text{ch jet}}$ is expected from simple geometric arguments. In semi-central collisions the average in-medium distance is shorter, while the relative difference between the average distances in-plane and out-of-plane is larger, hence a non-zero $v_2^{\text{ch jet}}$ is expected. Fluctuations in the initial distribution of nucleons within the overlap region however can lead to additional contributions to $v_2^{\text{ch jet}}$ and higher harmonic coefficients in the Fourier decomposition (similar to the generation of higher order v_n coefficients as shown in Fig. 2.9).

The observable $v_2^{\text{ch jet}}$ is different from the (jet) R_{AA} or R_{CP} as it directly connects jet energy loss to path length at fixed medium temperatures and densities by probing different path lengths within the same event rather than e.g. comparing energy loss in different centrality classes; thereby it allows for a more precise quantification of the path-length dependence of parton energy loss.

Part II

Experiment and analysis

3 | Experimental setup

The work, presented in this dissertation, is based on data collected by the ALICE experiment at CERN, Geneva. This chapter will briefly outline the process of data taking, starting from accelerating lead ions (§ 3.1), followed by an explanation of ALICE (§ 3.2), focusing on the detector elements that are used in this work, and ending at the data selection (§ 3.3), Monte Carlo modeling (§ 3.4) and computation (§ 3.5).

3.1 CERN accelerator complex

Lead nuclei, which are collided to create the QGP in the laboratory, are accelerated to relativistic velocities in the Large Hadron Collider (LHC, for a detailed description see [121]), located at depths between 50 and 175 m underneath the Swiss-French border near Geneva. The LHC lies within a 27 km annular cave (used previously for the LEP accelerator) and contains two beam pipes to allow for bunches of identically charged particles to be accelerated in opposite directions.

A schematic overview of the CERN accelerator complex is given in Fig. 3.1. Lead ions are initially accelerated in LINAC 3 (a linear accelerator). During this initial acceleration electrons are removed from the nucleus. LINAC 3 injects its ions into the Low Energy Ion Ring (LEIR) which splits each long pulse of ions into dense bunches of 2.2×10^8 ions per bunch; the bunches are subsequently injected into the Proton Synchrotron (PS), where all remaining electrons are stripped, after which the nuclei are accelerated to $\sqrt{s_{\mathrm{NN}}} = 450$ GeV by the Super Proton Synchrotron and injected into the LHC, which finally accelerates the nuclei to an energy of $\sqrt{s_{\mathrm{NN}}} = 2.76$ TeV. Protons start their acceleration in LINAC 2, after which they are accelerated up to 1.4 GeV by the Proton Synchrotron Booster to be injected in the PS and from there follow the same path as lead ions.

Particles can collide at the four points where the beam pipes cross, at each of the four points a detector is situated: two general purpose detectors (ATLAS [122], CMS [123]), and two dedicated detectors (ALICE, running a dedicated heavy-ion program; LHCb [124], running a dedicated b-physics program).

3.2 ALICE

ALICE (A Large Ion Collider Experiment) consists of 18 subsystems (see Fig. 3.2) which can (roughly) be divided into three sections: the forward muon spectrometer (comprising the muon filter and trigger chambers, and the muon tracking chambers), A COsmic Ray DEtec-

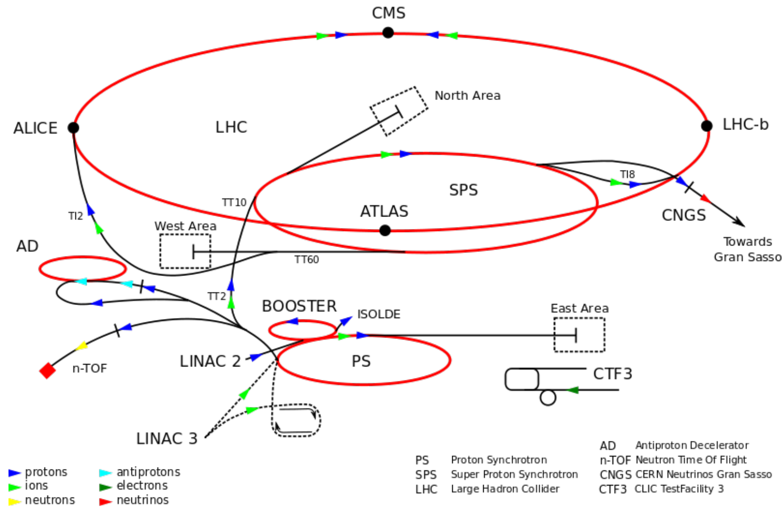

Figure 3.1: The accelerator complex as currently in operation at CERN, Geneva. Lead ions are initially accelerated and stripped of their electrons in LINAC 3, subsequent acceleration and bunching is done by the PS and SPS system. Protons acceleration starts at LINAC 2, after additional acceleration in the BOOSTER ring. The PS and SPS serve as injectors for the LHC. Collisions take place at the four points of the LHC where the beams cross (ATLAS, ALICE, CMS, and LHCb).

tor (ACORDE), and the central barrel detectors which are located within the L3 solenoid. A detailed overview of the design of the ALICE experiment and its performance can be found in [125–128], this section will only focus on the detectors which are directly used to gather the data necessary for this dissertation: the *Inner Tracking System* (ITS, § 3.2.1), *Time Projection Chamber* (TPC, § 3.2.2), *V0 system* (V0, § 3.2.3) and *Electromagnetic Calorimeter* (EMCal, § 3.2.4[a]).

All subsystems use a common coordinate system to indicate the trajectories of particles within the detector. ALICE uses a right-handed Cartesian coordinate system in which the positive x-axis points towards the center of the LHC. The z-axis lies along the beam axis, the muon spectrometer is situated at negative z. Particle kinematics are commonly expressed in terms of *transverse momentum* p_{T} (the magnitude of the projection of momentum vector $\mathbf{p}$ in the $x-y$ plane), *azimuthal angle* φ (opened in the $x-y$ plane) and *pseudorapidity* η, as measure of the polar angle θ (opening in the $y-z$ plane) with respect to the z-axis, defined as

$$\eta = -\ln\left(\tan\frac{\theta}{2}\right) = \ln\left(\frac{|\mathbf{p}| + p_{\mathrm{L}}}{|\mathbf{p}| - p_{\mathrm{L}}}\right)\Big/2. \tag{3.1}$$

For relativistic particles, η approximates rapidity y as total energy $E \approx |\mathbf{p}|$. Charged particles trajectories are curved in the x–y plane as a result of the 0.5 T magnetic field provided by the L3 solenoid; the direction of the field lines (positive or negative z) depends on the polarity of the magnet and can be flipped. The radius of curvature r, is directly proportional to the ratio of p_{T} to the field strength B, where the sign of the curvature is determined by charge q, meaning

[a]No information from the electromagnetic calorimeter was used for the results presented in Ch. 7. Exploratory studies, presented in Ch 8, *do* use information from this system however.

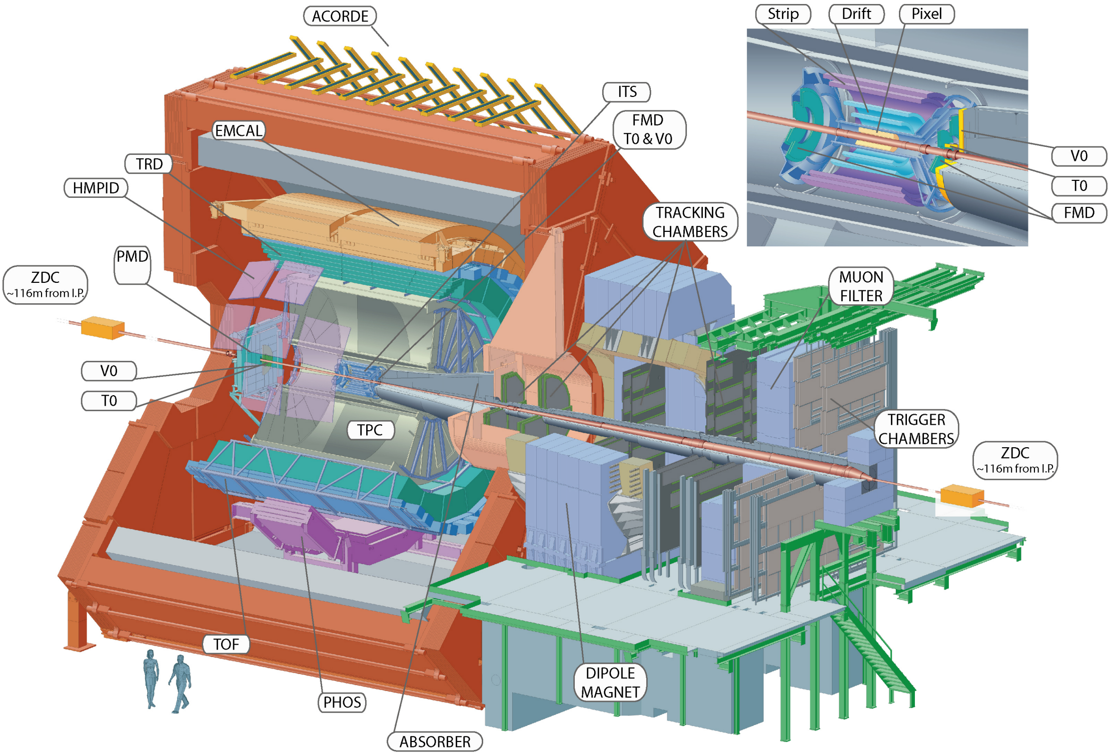

Figure 3.2: Schematic view of the ALICE detector and its most important components. Taken from [129].

that p_{T} can be determined from

$$p_{\mathrm{T}} \propto qrB. \tag{3.2}$$

As the field strength is known to high precision, the p_{T} resolution of tracks depends largely on the precision of the determination of r; the track selection (see § 3.3.3) is therefore aimed at maximizing track length.

3.2.1 ITS

The detector system located most closely to the nominal collision point is the ITS [130] (see Fig. 3.2, details in top-right corner). The ITS consists of three pairs of concentric cylindrical detector layers (with a maximum diameter of 87.2 cm, see the left panel of Fig. 3.3), each pair forming a subsystem employing different technologies, with the innermost layers *Silicon Pixel Detectors* (SPD), the middle layers using *Silicon Drift Detectors* and the outermost layers using *Silicon Strip Detectors*. The different techniques provide appropriate resolution at the six radii where track density differs. The ITS is a semiconductor detector: charged particles traversing the silicon pads free charges in the doped semiconductor material (silicon) which cause small ionization currents.

The ITS is used primarily for locating the primary interaction *vertex* (the point of collision) and for the reconstruction of particle trajectories (*tracking*), as explained briefly in § 3.3.3. It

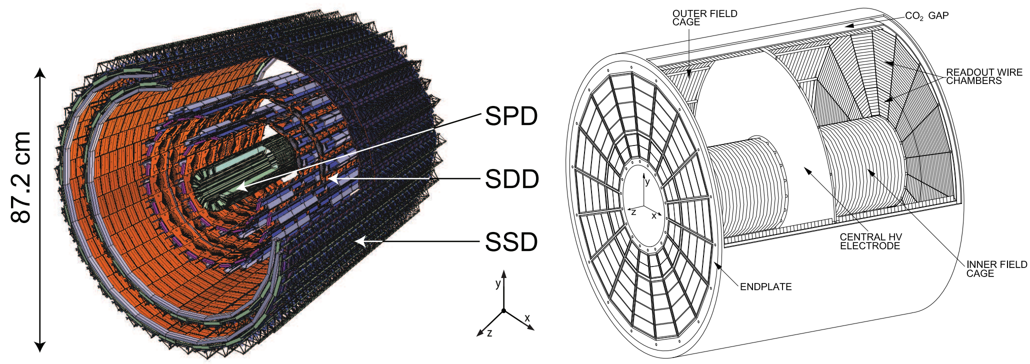

Figure 3.3: Design of the ITS detector (left, from [130]). Design of the TPC detector (right, from [131].

covers $|\eta| < 0.9$ and full azimuth (φ).

3.2.2 TPC

The TPC [131] is a cylindrical detector filled with a mixture of Neon (90%) and CO_2(10%). It is placed symmetrically around the nominal interaction vertex, its inner radius at 84.1 cm (the ITS is placed within the inner radius) and its outer radius at 246.6 cm, extending 2.5 m in both longitudinal directions. The gas volume is divided by a central high voltage (100kV) electrode at $\eta = 0$, which induces an electric field with a gradient of 400 V cm^{-1} parallel to the beam line (see Fig. 3.3, right side). As charged particles traverse the gas volume, gas molecules are ionized and freed electrons drift towards wire chambers that are mounted at the end plates of the gas volume. Near the high-voltage anode wires of readout chambers, electrons are accelerated and locally ionize the gas mixture, leading to an amplification of the signal. The cloud of free electrons is absorbed by the anode wire, while ionized gas molecules recombine with electrons emitted from cathode: the positive ions induce an electric signal, directly proportional to the energy loss of the original particle in the gas mixture, which is recorded in readout pads. The TPC readout is divided into 18 trapezoidal sectors at each cap, which are subdivided into two sections: the *inner readout chambers* (IROC) and *outer readout chambers* (OROC).

Unlike the ITS, which has sensors recording the x, y and z coordinates of ionizations, the TPC only has segmentation in the x–y plane (in which the end plates are mounted). The radial distance r and azimuthal angle φ of tracks are therefore measured directly, the trajectory of tracks along the z-direction is calculated from the drift time of the electrons within the gas volume. The TPC covers a p_T range of 0.1 GeV/$c \leq p_T \leq$ 100 GeV/c (at higher momenta the p_T resolution is too limited for analysis) over a pseudo-rapidity range of $|\eta| \leq 0.9$ for tracks which are fully contained in the gas volume.

3.2.3 V0 system

The V0 system consists of two arrays of scintillators located at opposite sides ($2.8 < \eta < 5.1$ and $-3.7 < \eta < -1.7$) of the interaction point. The position of the V0 detectors with respect to the ITS and TPC is shown in the left panel of Fig. 3.4. The V0 system is divided into an A (-η) and C (+η) side. Both sides consist of four concentric rings, each ring divided into eight segments of

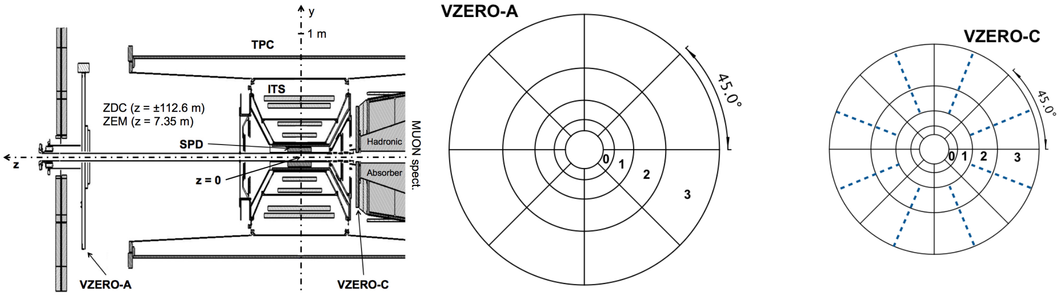

Figure 3.4: The V0 system consists of two arrays of scintillators located at opposite sides of the interaction point (left). It is divided into an A ($-\eta$) and C ($+\eta$) side. Both sides consist of four concentric rings, each ring divided into eight segments of equal azimuthal width (right). Figure from [132].

equal azimuthal width (see Fig. 3.4). The scintillating BC404 plastic of the segments emits light when subjected to ionizing radiation; this light is guided by optical fibers to photo-multiplier tubes from which the V0 signals can be read.

The V0 signal strength is directly proportional to the multiplicity of charged particles incident on the detector. A coincidence of signals of the V0 and ITS is used as an online trigger system, which fires when a given threshold signal is exceeded. Additionally, the V0 system is used to determine event centrality in Pb–Pb collisions, and, making use of its segmentation in azimuth, to determine the event plane orientation (see § 3.3.1 and 4.3).

3.2.4 EMCal

The EMCal [133] is an electromagnetic lead-scintillator sampling calorimeter. It is placed in between the TPC and the inner wall of the L3 magnet and has limited acceptance ($|\eta| < 0.7$, $1.4 < \varphi < \pi$) but high granularity ($\Delta\eta \times \Delta\varphi = 0.014 \times 0.014$). Incoming particles at sufficient energies interact with the lead, which leads to alternating sequences of e^-, e^+ pair creation and Bremsstrahlung for electrons and photons (and (in)elastic scatterings for hadronic processes), forming a particle shower in the detector. The recorded multiplicity that is seen by the scintillator material is proportional to the energy of the original incoming particle. The spatial configuration of the EMCal (comprising alternating layers of 1.44 mm Pb and 1.76 mm polystyrene) is optimized to fully reconstruct electromagnetic showers; hadronic showers are only partially contained.

The EMCal in this work is used only in § 8.2.1 and not to obtain the results presented in Ch. 7. Its information complements TPC and ITS data, as it can detect particles which have no charge (e.g. neutrons and neutral pions). In addition, the EMCal can be used as a trigger detector, recording an event only when a (partial) shower, surpassing a given threshold in energy, is detected, effectively selecting events in which a hard scattering has occurred. This will be further discussed in § 8.2.1.

3.3 Data sample

The data presented in this dissertation were recorded in the Pb–Pb data taking periods in 2010 and 2011 at $\sqrt{s_{\rm NN}} = 2.76$ TeV and consist of a total of 6.8×10^6 events with 0–5% centrality

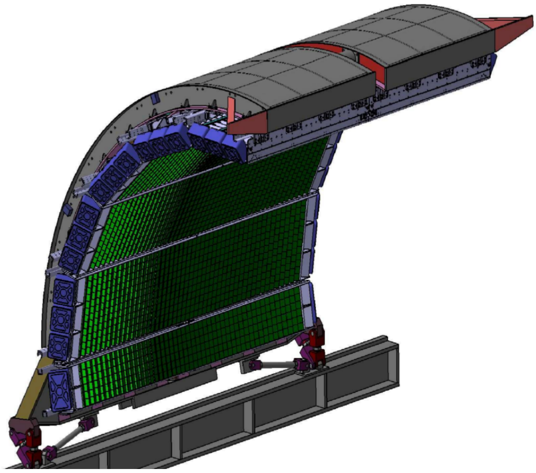

Figure 3.5: The EMCal is an electromagnetic lead-scintillator sampling calorimeter. It lies in between the TPC and the inner wall of the L3 magnet and has limited acceptance ($|\eta| < 0.7$, $1.4 < \varphi < \pi$). Picture from [133].

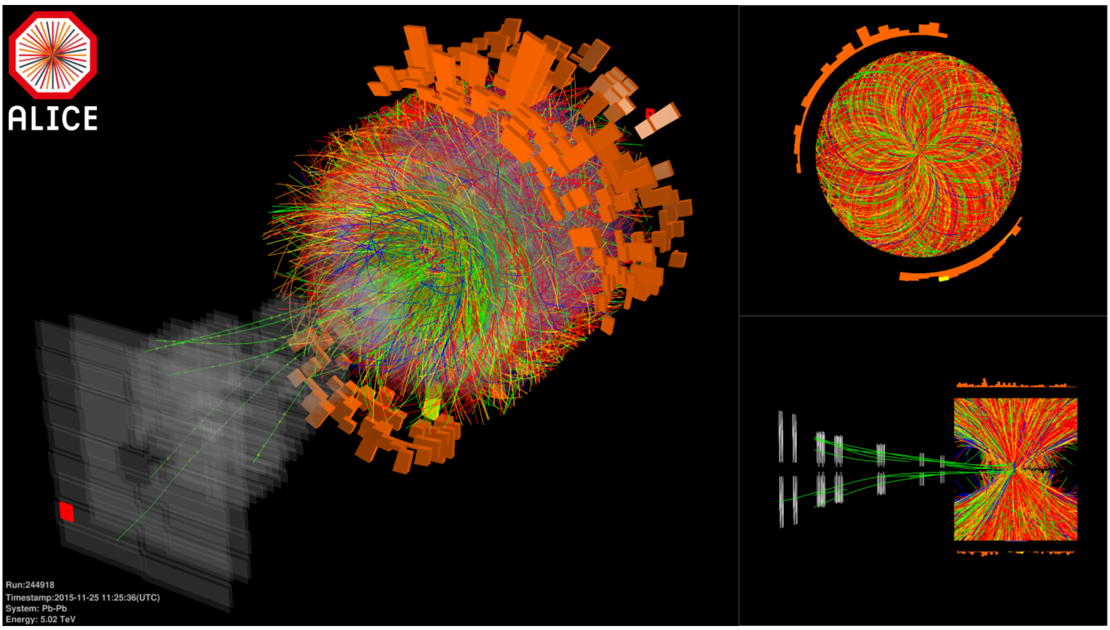

Figure 3.6: Event display, of collision recorded during the 2015 Pb–Pb data-taking period. Colored lines represent charged particle tracks (where different colors correspond to different particle species). The orange rectangles show energy depositions in the EMCal and DCal calorimeters (where the volume of the rectangle is proportional to the amount of energy deposited).

and 8.6×10^6 events with 30–50% centrality, corresponding to integrated luminosities of $\mathcal{L} = 18$ $\mu\mathrm{b}^{-1}$ and $\mathcal{L} = 5.6$ $\mu\mathrm{b}^{-1}$, respectively. All events that are used in the analysis are subjected to event selection criteria and are classified into centrality classes.

3.3.1 Event selection

Collisions occur when highly focused bunches of ions cross at the origin of the detector. The majority of interactions of the ions however are not hadronic nucleus–nucleus interactions, but rather electromagnetic processes or interactions with the accelerator itself. The aim of event selection is to select hadronic interactions (*events*) with high efficiency, rejecting all other processes which lead to (observable) particle production. Event selection is generally divided into two steps: *online* selection, performed instantaneously at the moment of collision, and *offline* selection, performed on a recorded data set.

Online event selection is based on collecting information from multiple detectors and recording an event when a specified set of detectors simultaneously record a signal exceeding a predefined threshold (a *trigger*). The trigger conditions [132] used in the 2010 Pb–Pb data taking are at least two out of the following three signals

- Two pixel chips hit in the outer layer of the SPD;
- A signal in the V0A;
- A signal in the V0C;

with the V0 threshold approximately equal to the mean energy deposited by one minimum ionizing particle. For the high luminosity runs in 2010, a coincidence between SPD, V0A and V0C is required, to suppress signals from electromagnetic processes. These trigger conditions correspond to the *minimum bias* event selection, which comprises the full hadronic cross section[b]. In the 2011 data taking period a coincidence of the SPD requirement and a multiplicity-dependent V0 threshold is used (the effect of which is shown in Fig. 3.8). The trigger is fully efficient in the centrality ranges used in Ch. 4 through Ch. 7. Centrality estimation using the V0 system does not bias the $\Psi_{\mathrm{EP},\ n}$ determination [134] (see Ch. 4).

After triggering, the event sample is still contaminated by events which pass the trigger conditions but are not part of the hadronic cross section. These comprise mainly scatterings of ions with residual gas molecules in the beam pipe, and ions from the beam halo which interact with the accelerator itself. Timing information from the V0 system is used to reject these events. Satellite collisions, which are incidental collisions that can occur when an ion moves from one bunch to another and then collides with ions from the opposite beam, are removed from the event sample by requiring that the collision occurs within $|z| < 10$ cm of the nominal interaction point. This requirement additionally means that the number of accessible clusters for track reconstruction in the TPC, is approximately equal for positive and negative η.

The largest 'physical' background is that of electromagnetic processes, electromagnetic interactions between the nuclei, and neutron emission. These processes lead to very low multiplicity events (which would end up at 90%-100% centrality); details on rejection can be found in [135].

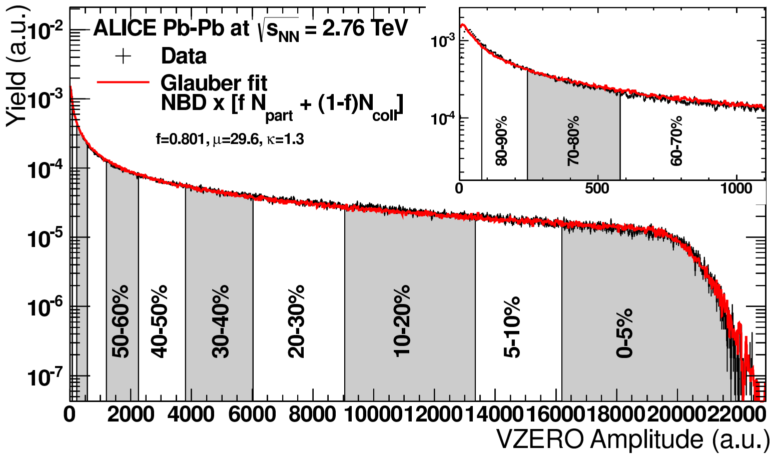

Figure 3.7: V0 amplitude (in arbitrary units (a.u.)), divided in centrality classes according to Eq. 3.3. The red line represents the Glauber fit. Figure from [132].

3.3.2 Centrality determination

Collision centrality, the measure of overlap of the colliding nuclei, is expressed as a percentage of the total nuclear interaction cross section σ. The centrality percentile c of an AA collision with an impact parameter $\mathbf{b}$ is defined by integrating the impact parameter distribution $\mathrm{d}\sigma/\mathrm{d}b'$ as

$$c = \frac{\int_0^{\mathbf{b}} \mathrm{d}\sigma/\mathrm{d}\mathbf{b}'\, \mathrm{d}'\mathbf{b}'}{\int_0^{\infty} \mathrm{d}\sigma/\mathrm{d}\mathbf{b}'\, \mathrm{d}\mathbf{b}'} = \frac{1}{\sigma_{AA}} \int_0^{\mathbf{b}} \frac{\mathrm{d}\sigma}{\mathrm{d}\mathbf{b}'} \mathrm{d}\mathbf{b}'. \tag{3.3}$$

Since the impact parameter is not a measurable quantity, centrality percentile c is experimentally defined by the percentile of the hadronic cross section corresponding to a particle multiplicity above a given threshold ($N_{\mathrm{ch}}^{\mathrm{THR}}$)

$$c' \approx \frac{1}{\sigma_{\mathrm{AA}}} \int_{N_{\mathrm{ch}}^{\mathrm{THR}}}^{\infty} \frac{\mathrm{d}\sigma}{\mathrm{d}N'_{\mathrm{ch}}} \mathrm{d}N'_{\mathrm{ch}}. \tag{3.4}$$

In practice, the cross section is replaced by the number of observed events, corrected for trigger efficiency and determined in a region where the contribution of QED processes to the total cross section is negligible [135]. The absolute scale of the centrality is determined by the *anchor point*, AP, which is chosen as the amplitude recorded by the V0 detector equivalent to 90% of the hadronic cross section. The determination of the AP requires the knowledge of the trigger efficiency and the remaining background contamination in nuclear collision events. The AP is chosen based on multiplicity predictions from a Glauber Monte Carlo fit to the experimental multiplicity distribution (see Fig. 3.7) where emission of particles is parametrized by a convolution of two negative binomial probability distributions around N_{part} and N_{coll} [136–138].

[b]The minimum bias sample includes, as the name implies, all events from hadronic interactions, without imposing a bias on the event selection. A bias is introduced in e.g. § 8.2.1, where the online event selection only selects events in which a jet of a given energy is produced. This leads to a specific subset (a 'biased sample') of events. Biased events samples can be useful when e.g. investigating rare phenomena, but may render the outcome of the measurement difficult to compare to theoretical predictions.

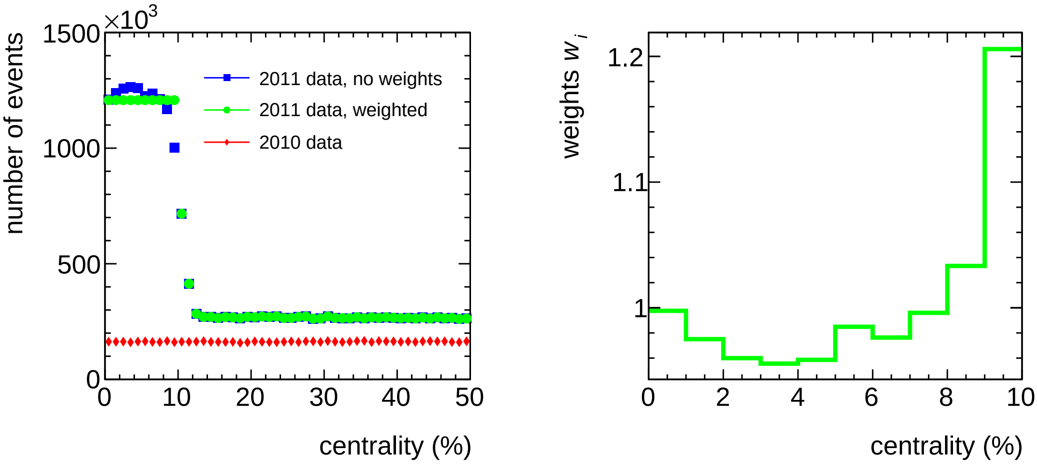

Figure 3.8: Left panel: centrality distribution of accepted events for the LHC11h run. Blue open squares mark the original centrality distribution, the green markers represent the flattened centrality distribution. The centrality distribution in the LHC10h data is given as red diamonds. Right panel: centrality weights as a function of centrality percentile. Centrality weights are only used in the 10 % most central collisions.

The mapping of V0 amplitudes to centrality classes is performed on *minimum bias* events, which sample the full hadronic cross section. If the full hadronic cross section is sampled, the centrality distribution is uniform. In the 2011 data taking however, a centrality trigger is introduced: the trigger efficiency is based on V0 multiplicity to have a larger relative contribution of central events to the total event sample (see the blue data points in the left panel of Fig. 3.8 for the resulting centrality distribution). The finite efficiency of the trigger near the trigger threshold (8–12% centrality) leads to a non-uniform centrality selection. To correct for this non-uniformity and ensure that events from each centrality percentile have an equal contribution to the final measured $v_2^{\text{ch jet}}$, information from events in each centrality percentile i is multiplied by weight

$$w_i = \frac{\langle N \rangle}{N_i} \tag{3.5}$$

where $\langle N \rangle$ is the average number of events in a centrality percentile between 0–10% centrality, and N_i is the observed number of events in centrality percentile interval i[c]. The weighted centrality distribution for events from the 2011 run is shown as green markers in the left panel of Fig. 3.8, applied weights are shown in the right panel of the same figure. The original centrality distribution of the 2011 data is shown as blue open square markers, the 2010 data (red closed diamonds) is flat.

3.3.3 Event and track selection

Particles that traverse the detector leave energy deposits that are read out. Tracking is the process of converting these measurements to particle trajectories (*tracks*) with kinematic properties that can be used in physics analysis.

[c]In principle the centrality percentile is a real-valued number. Weights are constructed in discrete centrality percentile intervals with a width of 1%.

Event reconstruction starts at determining the location of the primary interaction point (or 'primary vertex') from clusters in the two SPD layers of the ITS. After the primary vertex is reconstructed in three dimensions, particle trajectories are constructed using a Kalman filtering algorithm [139]. As initial seeds of track finding, charge depositions at the outer edge of the TPC, where the spatial separation between the trajectories is at a maximum, are used. Tracks are propagated inward until the inner wall of the TPC is reached, after which the track is matched to charge depositions in the outer layer of the SSD, and further propagated into the ITS. In a second fitting pass, this procedure is inverted and a track is fitted starting at the innermost layer of the ITS, and finally propagated to clusters out of the TPC (into e.g. the TRD of TOF detectors). Multiple tracks are allowed to share a fraction of clusters. Trajectories based on a subset of information (e.g. 'tracklets', constructed from only ITS hits, or trajectories containing only information for the TPC) can also be reconstructed and used in analysis. For a full description of event and track reconstruction, see [126–128].

Charged particle tracks in this analysis are reconstructed from information in the ITS and TPC and are selected in a pseudorapidity range $|\eta| < 0.9$ with transverse momenta $0.15 < p_{\rm T} < 100$ GeV/c. Including the ITS in the reconstruction ensures sufficient momentum resolution by maximizing the track length. Since the SPD acceptance is non-uniform in azimuth[d], two classes of tracks are used. The first class requires at least three hits per track in the ITS, with at least one hit per track in the SPD. The second class contains tracks without hits in the SPD, in which case the primary interaction vertex is used as an additional constraint for the momentum determination. For each track, the expected number of TPC space points is calculated based on its trajectory; tracks are accepted if they have at least 80% of these expected TPC space-points, with a minimum of 70 TPC points. Tracks produced from interactions between particles and the detector, as well as tracks originating from weak decays (*secondary tracks*) are rejected by requiring that the minimum distance of the track to the primary vertex (the *distance of closest approach*) is < 2.4 cm in the radial direction and < 3.1 cm in the longitudinal direction. In addition to this requirement, particle trajectories reconstructed by combining ITS and TPC information and trajectories derived from using TPC information only (but constraining the origin of the track to the primary vertex) may not differ more than six standard deviations. After track selection, the contribution of secondary tracks to the track sample is less than 10% for tracks with $p_{\rm T} < 1$ GeV/c and negligible for tracks with higher transverse momentum.

3.4 Monte Carlo simulations

To validate analysis techniques and to correct for instrumental effects, model events are generated. These events are generally called *Monte Carlo* events, as they rely on random sampling of physical distributions (e.g. the impact parameter or position of nucleons within the nucleus). Two Monte Carlo event generators are used, for proton proton collisions (PYTHIA) and nucleus–nucleus collisions (HIJING). The event generators produce *particle-level* information, i.e. events that are generated without propagating the particles through the detector. To simulate the interaction of created particles with the detector material, the *transport code* GEANT3 [140] is used to create *detector-level* events.

[d] During part of the 2011 data taking, the TPC acceptance is also non-uniform. Details on this can be found in App. A.

3.4.1 HIJING

The HIJING [141] event generator (*Heavy-Ion Jet Interaction Generator*) is used to generate nucleus–nucleus collisions. As ansatz HIJING models nucleus–nucleus events as a superposition of (independent) pp collisions, hence it does not generate collective effects such as v_n harmonics (see § 2.4.1). HIJING uses nPDFs to account for effects of nuclear shadowing. Nucleons are placed inside the nuclei according to a Woods-Saxon distribution. Jet production from hard scatterings is modeled using pQCD calculations; jet quenching is introduced from a parametrization of $\mathrm{d}E/\mathrm{d}x$ of partons traversing the medium. Fragmentation and additional particle production from soft processes in the non-perturbative regime is calculated using the Lund FRITIOF model [142, 143]. The Lund string model [33, 34] is used for the hadronization step to final state particles. HIJING events in this work are used to test the efficiency of particle tracking and consequently the efficiency jet finding in high multiplicity environments (see § 4.5).

3.4.2 PYTHIA

PYTHIA [144] is used to generate high energy proton–proton collisions. Scattering probabilities are evaluated using PDFs and pQCD. Subsequent parton showering is evaluated perturbatively and, at lower energies, non-perturbatively using Lund model string fragmentation. Non-perturbative processes in PYTHIA rely on phenomenological descriptions, parameters of which are tuned to experimental data (the set of tunes commonly used at the LHC experiments are the Perugia tunes [145]). To hadronize particles into colorless final states, the Lund model is used. $2 \to 2$ scatterings are forced at specified virtuality intervals which are governed by the parameter $p_{\mathrm{T}}^{\mathrm{hard}}$, which controls the momentum exchange between the two incoming partons. To generate a realistic PYTHIA event sample, scatterings are generated separately in different $p_{\mathrm{T}}^{\mathrm{hard}}$ intervals, and merged into a final sample applying weights

$$w_{p_{\mathrm{T}}^{\mathrm{hard}}} = \frac{\sigma_{p_{\mathrm{T}}^{\mathrm{hard}}}}{N_{\mathrm{trials}}} \tag{3.6}$$

where $\sigma_{p_{\mathrm{T}}^{\mathrm{hard}}}$ denotes the average cross-section within a $p_{\mathrm{T}}^{\mathrm{hard}}$ interval, and N_{trials} is the number of generated events in this interval.

3.4.3 GEANT3

GEANT3 [140] (*GEometry ANd Tracking*) is not an event generator, but a *transport code*: simulation software that describes the passage of elementary particles through matter[e]. GEANT3 is used to simulate how particles, created in e.g. a collision, interact (via e.g. scattering or absorption) with the detector material, thus quantifying in which way the experiment itself (including the magnetic field) distorts the measurement. For GEANT simulations, which can be run inside the AliROOT (§ 3.5) framework, the full detector geometry, including detector conditions (e.g. polarity of the magnetic field) have to be simulated. Tracks that serve as input to GEANT3 are the aforementioned *particle-level*, and are *in this work* primary charged particles (produced by an event generator, e.g. PYTHIA), which comprise all prompt charged particles produced in the collision as well as products of strong and electromagnetic decays, while products of weak decays of strange hadrons are rejected. GEANT3 subsequently 'transports' these particles through the detector material and outputs a set of *detector-level* tracks.

[e] Originally created at CERN, GEANT is now used in a wide variety of fields, ranging from space research to usage in hospitals where radiation treatments in oncology are tuned in simulations.

3.5 The analysis within the AliROOT framework

Data analysis at the ALICE experiment is performed using the AliROOT framework [146–148], a collection of c++ libraries developed for the ALICE experiment as an extension of the ROOT framework [149]. ROOT itself comprises a collection of c++ libraries, developed at CERN and widely used in high energy physics, aimed at data processing, statistical analysis, visualization and data storage. The framework contains a line-by-line c++ interpreter, but can transparently be used in combination with other languages (e.g. Python, R) as well.

The AliROOT framework provides an additional layer to ROOT, which contains common tools for ALICE specific data analysis and simulation (such as interfaces to Monte Carlo event generators, transport codes, jet finding algorithms, track and event selection criteria). Data processing is performed via automated distribution of computational tasks by the ALIce ENvironment (ALIEN [150]) on the world wide computing GRID [151], on which, at the time of writing, ALICE has access to $\approx$ 70k CPU cores.

4 | Data analysis

In Ch. 2, the harmonic coefficient $v_2^{\text{ch jet}}$ was introduced to quantify the path length dependence of parton energy loss in the QGP. The following chapter covers *data analysis*: converting the $\simeq$ 700 terabyte of reconstructed tracks recorded by ALICE between 2010 and 2011 to $v_2^{\text{ch jet}}$. This chapter starts with an overview (§ 4.1), after which the analysis is broken down into four sections, 4.2 through 4.5, each of which covers a distinct analysis step. A treatment of uncertainties and validation of the results of the analysis is given in Chapters 5 and 6.

4.1 Overview

As explained in Ch. 2, $v_2^{\text{ch jet}}$ is the coefficient of the second term in a Fourier expansion of the azimuthal distribution of jets relative to symmetry planes Ψ_n (Eq. 2.40), which can be expressed as

$$\frac{\mathrm{d}N}{\mathrm{d}\left(\Delta\varphi_n\right)} \propto 1 + \sum_{n=1}^{\infty} 2v_n^{\text{jet}} \cos\left[n\left(\Delta\varphi_n\right)\right]. \tag{4.1}$$

with the jet azimuthal angle φ_{jet} relative to symmetry plane angle Ψ_n written as $\Delta\varphi_n = \varphi_{\text{jet}} - \Psi_n$[a]. The definition of coefficient v_2^{jet} is illustrated in Fig. 4.1. On the left panel, two colliding nuclei and the overlap region are shown. The right side of the figure shows a sketch of the resulting distribution of $\Delta\varphi_2$. This distribution is modulated around $\Delta\varphi_2$, as jets emitted along the minor axis of the overlap ellipse traverse less QGP medium than jets emitted along the major axis. This modulation is periodic with a period of π and amplitude $v_2^{\text{ch jet}}$.

As already explain in § 2.4.1, harmonic coefficients v_n^{jet} of the series Eq. 4.1 are given by [89, 90]

$$v_n^{\text{jet}}(p_{\mathrm{T}}) = \langle\langle \cos\left(n\left[\Delta\varphi_n\right]\right)\rangle\rangle \tag{4.2}$$

- where the inner brackets in $\langle\langle ... \rangle\rangle$ denote an average over all tracks, and the outer brackets are an all-event average - and thus calculable from jet p_{T}, jet orientation φ_{jet} and symmetry plane angles Ψ_2. Equation 4.2 is of little practical use, however. Parton showers (jets) and their orientation need to be reconstructed from tracks that are recorded by the detector (so neither p_{T} or φ_{jet} are directly available). Secondly, the symmetry plane angle Ψ_2 can only approximately be determined. A third concern is the fact that, per collision, an abundance of particles which are *not* showered from initial hard scatterings but rather a product of uncorrelated low momentum transfer scatterings, is created. Experimentally, there is no tool to distinguish between 'background' tracks and 'signal' tracks, therefore the reconstructed jet energy (and consequently p_{T})

[a]Both φ_{jet} and Ψ_n are defined in the laboratory frame, see § 3.2 for the definition of the coordinate system.

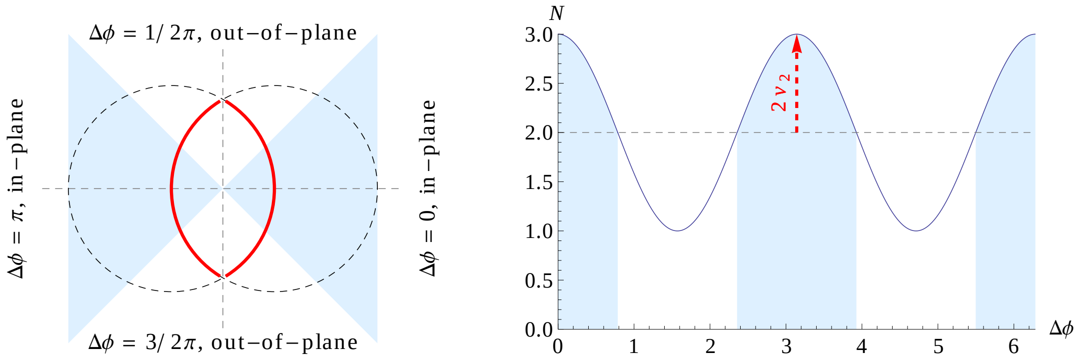

Figure 4.1: Definition of $v_2^{\text{ch jet}}$. Left: overlapping nuclei (dashed circles) form an approximately elliptical overlap region (red) in the plane transverse to the beam axis. The blue shaded areas indicate the in-plane direction. Right: sketch of the expected resulting distribution of jet yield in $\Delta\varphi_2$ (the orientation of the jet azimuthal angle φ_{jet} relative to the symmetry plane angle Ψ_n). The blue shaded areas again indicate the in-plane directions. The amplitude of the modulation in of the jet yield in $\Delta\varphi_2$ has magnitude $2\ v_2^{\text{ch jet}}$.

is not unambiguously defined. Clustering of background tracks affects mostly the jet p_{T} scale, by giving a φ-dependent boost to the jet p_{T}. An additional complication is that the distribution of $\varphi - \Psi_n$ of these uncorrelated tracks also shows a cosine modulation (the earlier explained hydrodynamic flow), which means that even in the *absence* of quenched hard scatterings, non-zero $v_2^{\text{ch jet}}$ is measured when evaluating Eq. 4.2 directly. Lastly, the measurement is limited by instrumental resolution and will suffer from statistical fluctuations.

Because of these experimental limitations, $v_2^{\text{ch jet}}$ cannot be obtained directly from Eq. 4.2. Eq. 4.1 can however be rewritten in terms of quantities that *are* available experimentally: the p_{T}-differential *in-plane* (N_{in}) and *out-of-plane* (N_{out}) jet yields[b] with respect to the *event plane*$\Psi_{\text{EP, 2}}$, an experimental estimate of the orientation of symmetry plane Ψ_2, derived from the density of outgoing particles in the transverse plane.

The jet yields N_{in} and N_{out} can be expressed by integration of Eq. 4.1 over $\Delta\varphi_2$ intervals. Taking into account only the second order harmonic and substituting $\Psi_{\text{EP, 2}}$ for Ψ_n,

$$\begin{aligned}
N_{\text{in}}(p_{\text{T}}) &= \int_{\frac{-\pi}{4}}^{\frac{\pi}{4}} \frac{\mathrm{d}N}{\mathrm{d}(\Delta^{\text{EP}}\varphi_2)}\mathrm{d}(\Delta^{\text{EP}}\varphi_2) + \int_{\frac{3\pi}{4}}^{\frac{5\pi}{4}} \frac{\mathrm{d}N}{\mathrm{d}(\Delta^{\text{EP}}\varphi_2)}\mathrm{d}(\Delta^{\text{EP}}\varphi_2) \\
N_{\text{out}}(p_{\text{T}}) &= \int_{\frac{\pi}{4}}^{\frac{3\pi}{4}} \frac{\mathrm{d}N}{\mathrm{d}(\Delta^{\text{EP}}\varphi_2)}\mathrm{d}(\Delta^{\text{EP}}\varphi_2) + \int_{\frac{5\pi}{4}}^{\frac{7\pi}{4}} \frac{\mathrm{d}N}{\mathrm{d}(\Delta^{\text{EP}}\varphi_2)}\mathrm{d}(\Delta^{\text{EP}}\varphi_2).
\end{aligned} \tag{4.3}$$

where $\Delta^{\text{EP}}\varphi_2 = \varphi_{\text{jet}} - \Psi_{\text{EP, 2}}$, gives

$$\begin{aligned}
N_{\text{in}}(p_{\text{T}}) &= a\left(\pi + 4v_2^{\text{obs}}\right) \\
N_{\text{out}}(p_{\text{T}}) &= a\left(\pi - 4v_2^{\text{obs}}\right)
\end{aligned} \tag{4.4}$$

where a is a normalization constant. The notation v_2^{obs} is introduced in Eq. 4.4 to indicate that the harmonic coefficients in this intermediate step quantify azimuthal anisotropy with respect

[b] *Yield* is used in the general sense as quantity or number; the p_{T}-differential jet yield is therefore simply the number of jets, measured in finite p_{T} intervals.

to the event plane angles $\Psi_{\mathrm{EP},\ 2}$ rather than symmetry plane angles Ψ_2. Introducing a term $\mathcal{R}$ which corrects for the finite precision with which the event plane $\Psi_{\mathrm{EP},\ 2}$ approaches the real symmetry plane Ψ_2 and rewriting Eq. 4.4, an expression for $v_2^{\mathrm{ch\ jet}}$ relative to the symmetry plane Ψ_2 is obtained

$$v_2^{\mathrm{ch\ jet}}(p_{\mathrm{T}}^{\mathrm{jet}}) = \frac{\pi}{4}\frac{1}{\mathcal{R}_2}\frac{N_{\mathrm{in}}(p_{\mathrm{T}}^{\mathrm{jet}}) - N_{\mathrm{out}}(p_{\mathrm{T}}^{\mathrm{jet}})}{N_{\mathrm{in}}(p_{\mathrm{T}}^{\mathrm{jet}}) + N_{\mathrm{out}}(p_{\mathrm{T}}^{\mathrm{jet}})}. \tag{4.5}$$

By rewriting Eq. 4.1, an expression for $v_2^{\mathrm{ch\ jet}}$ in measurable quantities is found. Eq. 4.5 is insensitive to v_4 as a result of the integration limits; the first other harmonic that contributes to the measured v_2^{obs} is v_6^{obs} (under the assumption, confirmed the by observation of $\langle\cos(2[\varphi_{\mathrm{tracks}} - \Psi_3])\rangle = 0$ [91], that the odd harmonic symmetry planes have no correlation with Ψ_2).

The rest of this chapter is dedicated to explaining the steps that need to be taken to arrive at these quantities, from jet reconstruction and background energy subtraction (§ 4.2), to the determination of $\Psi_{\mathrm{EP},\ 2}$ and its resolution (§ 4.3), continuing with the parameterization of the underlying event itself (§ 4.4) and finishing with unfolding (§ 4.5). Any bias that cannot be removed experimentally from the observed $v_2^{\mathrm{ch\ jet}}$ is a systematic uncertainty. These uncertainties, as well as closure tests that validate the analysis, are described in Chapters 5 and 6.

4.2 Jet finding and selection

Jets are theoretically well defined objects, in the sense that they are collimated sprays of particles showered from a single parton. Experimentally however there is no way to connect a track to a specific parton, and a jet needs to be reconstructed from the collection of final state particles in a detector. Jets are reconstructed using a jet finding algorithm, which clusters tracks that are most likely part of the same shower, and recombines these *constituent* tracks into a jet. Experimentally, the jet definition depends on the jet finding algorithm that is used.

4.2.1 Jet finding

The most commonly used jet finding algorithms are sequential recombination algorithms, which iteratively recombine objects according to given recombination criteria. Two specific implementations of such sequential recombination algorithms used for this work are the k_{T} and anti-k_{T} algorithms [152, 153], implemented in the FastJet [154, 155] suite. The (anti)-k_{T} operates as follows:

- As a first step, all tracks within an event are considered as (in this work) massless protojets with distance to the beam

$$d_i = {p_{\mathrm{T}}}_{,i}^{2p}. \tag{4.6}$$

- For each protojet pair i, j within the event, the separation distance $d_{i,j}$ is calculated

$$d_{i,j} = \min\left({p_{\mathrm{T}}}_{,i}^{2p}, {p_{\mathrm{T}}}_{,j}^{2p}\right)\frac{\Delta_{i,j}^2}{R^2} \tag{4.7}$$

  where R is the jet resolution parameter and

$$\Delta_{i,j}^2 = (\eta_i - \eta_j)^2 + (\varphi_i - \varphi_j)^2. \tag{4.8}$$

- In the 'recombination' step, the algorithm searches for the smallest number in the list $\{d_i, d_{i,j}\}$. If this smallest number is a $d_{i,j}$ pair, protojets i and j are merged, following - in this specific analysis - a p_{T} recombination scheme [155], to a new protojet k:

$$\begin{aligned} p_{\mathrm{T},k} &= p_{\mathrm{T},i} + p_{\mathrm{T},j} \\ \varphi_k &= (p_{\mathrm{T},i}\varphi_i + p_{\mathrm{T},j}\varphi_j)/p_{\mathrm{T},k} \\ \eta_k &= (p_{\mathrm{T},i}\eta_i + p_{\mathrm{T},j}\eta_j)/p_{\mathrm{T},k}. \end{aligned} \tag{4.9}$$

  If the smallest number is d_i, protojet i can no longer be merged (if $d_i < d_{i,j}$, all other protojets are at a distance greater than R from i) and i is considered a jet and removed from the list of protojets.
- The preceding steps are repeated until all protojets in the event are considered jets (meaning that *all* tracks in an event, regardless of origin, are clustered into jets).

Parameter p in Eqs 4.6 and 4.7 defines whether the highest or lowest p_{T} track is used as a seed for jet finding. The k_{T} algorithm uses $p = 1$, starting at low momentum 'edge' of a jet, whereas the anti-k_{T} algorithm uses $p = -1$ and starts at a high p_{T} seed.

In § 4.4, the concept of *jet area* - the surface in η–φ that is occupied by a jet's constituent tracks - is used. The jet area is determined by embedding a fixed number of near zero-momentum *ghost particles* per event prior to jet finding; the number of ghost particles in each reconstructed jet then gives a direct measure of the jet area. As explained in the next section, adding near-zero momentum particles does not change the jets that are found by the (anti)-k_{T} algorithm. A 'ghost density' of 200 particles per unit area is used in this work, so that approximately 25 ghost particles are clustered into a jet with a radius of 0.2.

4.2.2 Collinear and infrared safety

Experimental jets are defined by the employed jet finding algorithm. For a meaningful comparison to theory however the experimental definition of a jet must coincide with quantities that can be calculated from pQCD. When a $q\bar{q}$ pair is created, either of the two quarks can emit a gluon. The differential cross section for the process particle $\rightarrow q\bar{q}g$ [c] follows the proportionality

$$\frac{\mathrm{d}\sigma}{\mathrm{d}x_q \mathrm{d}x_{\bar{q}}} \propto \alpha_s \frac{x_q^2 + x_{\bar{q}}^2}{(1-x_q)(1-x_{\bar{q}})} \tag{4.10}$$

with x_i the fractions

$$x_i \equiv \frac{2E_i}{Q} \tag{4.11}$$

where Q is the usual total momentum transfer in $x \rightarrow q\bar{q}g$ and E_i is the energy of parton i. To calculate the total cross section, integration of Eq. 4.10 must be performed over x_i from 0 to 1; the integrand however diverges for $x_i \rightarrow 1$. For a physical interpretation of these divergences, definitions of Eq. 4.11 are substituted into the terms of the denominator of Eq. 4.10,

$$\begin{aligned} 1 - x_q &\simeq \frac{2}{Q^2}\,(p_{\bar{q}} \cdot p_g) \\ &\simeq \frac{2}{Q^2}\,(E_{\bar{q}}E_g\{1-\cos\theta_{\bar{q}g}\}) \end{aligned} \tag{4.12}$$

[c] This discussion follows [2], Ch. 10 and 11.

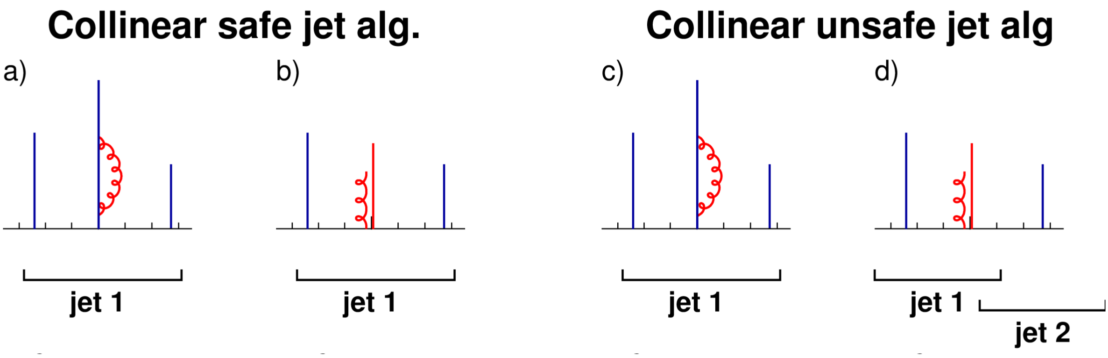

Figure 4.2: Partons are vertical lines, their height is proportional to their transverse momentum, and the horizontal axis indicates rapidity. In the left-hand figure, collinear emission of a soft gluon does not change the experimental definition of the jet. In the right-hand side, the jet definition changes under collinear emission of a gluon. Adapted from [156].

where p_i is the four-momentum of parton i and θ_{ij} is the opening angle between i, j[d]. The integrand diverges either when the gluon that is emitted is very soft ($E_g \to 0$) or when the gluon emission is collinear to the quark trajectory ($\theta_{\overline{q}g} \to 1$). These divergences are called *infrared* and *collinear* divergences, and can only occur in QCD as the gluon are massless.

To calculate an actual cross-section for these processes, the singularities in Eq. 4.10 need to be regularized. This is accomplished by introducing a fictitious gluon mass m_g. Doing so adds several terms to the cross-section which are equal but opposite in sign to the divergent terms, effectively removing singularities. The total cross section is finite and does not depend on the fictitious gluon mass.

To be able to compare theory to experiment, the set of hard jets that is found has to remain unchanged under collinear splitting or emission of a soft gluon, otherwise the renormalization ansatz of cancellation of divergent terms is broken (as illustrated in Fig. 4.2 for collinear emissions). The (anti)-k_{T} algorithm meets these criteria and is *IRC* (infrared and collinear) *safe*.

4.2.3 Background subtraction

The left panel of Fig. 4.3 shows transverse momentum density as function of η and φ in a simulated *pp* event. Jet finding using the anti-k_{T} algorithm has been performed, tracks clustered into a jet have equal colors. Jet finding in *pp* can be verified more or less 'by-eye': the colored clusters found by the jet finder are spatially separated, well defined jets. The right panel of Fig. 4.3 shows the same *pp* event, embedded in a simulated nucleus-nucleus collision without

[d]These relations follow from four-momentum conservation, and hold under the assumption that participating particles are massless ($m \simeq 0, p_i^2 \simeq 0, \mathrm{E}_i \simeq |p_i|$). In a system where virtual particle x splits into two quarks, $\overline{q}$ and q, and radiated gluon g,

$$Q^2 = p_x^2 = (p_q + p_{\overline{q}} + p_g)^2 \simeq 2p_q \cdot p_{\overline{q}} + 2p_q \cdot p_g + 2p_{\overline{q}} \cdot p_g, \tag{4.13}$$

combining this expression with a bit of optimism one gets

$$2p_{\overline{q}} \cdot p_g \simeq p_x^2 - 2p_q \cdot (p_{\overline{q}} + p_g) \simeq p_x^2 - 2p_q \cdot (p_{\overline{q}} + p_g + p_q) \simeq p_x^2 - 2p_q \cdot p_x \simeq Q^2 \left(1 - \frac{2E_q}{Q}\right) \simeq Q^2 (1 - x_q)\,. \tag{4.14}$$

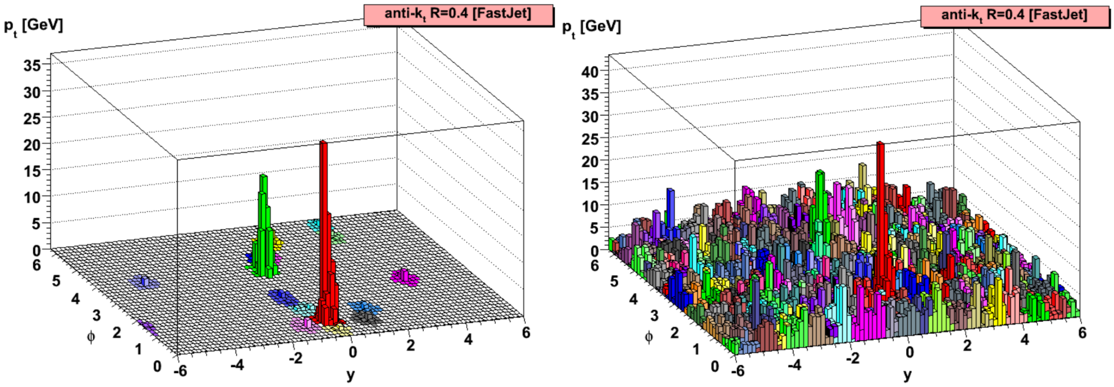

Figure 4.3: Transverse momentum (p_{T}) density as function of η and φ in simulated proton-proton (left) [153] collisions and Pb–Pb collisions (right). Different colors are used to mark reconstructed anti-k_{T} cluster.

hard jets. Jet finding is performed on the combined *pp*, nucleus-nucleus event. The figure directly illustrates the main difficulty in jet analyses in heavy-ion collisions: *all* tracks in an event are clustered into jets, meaning that:

- a significant fraction of jets found by the algorithm are clusters of uncorrelated tracks which meet the merging criteria of Eqs 4.6 and 4.7, called *fake* or *combinatorial* jets;
- clusters that actually contain particles from a parton shower will *also* contain uncorrelated particles that happen to be emitted in the same phase-space.

The collection of tracks unrelated to the initial hard scatterings of interest is called the *underlying event* (UE). The fraction of a measured jet's energy that is generated by the UE rather than the result of a hard scattering needs to be subtracted in order to obtain the true jet energy or $p_{\mathrm{T}}^{\mathrm{jet}}$. The energy density of the underlying event is parametrized by background energy density description which at a given η–φ position in an event has value $\rho_{\mathrm{ch\ local}}$[e]. The corrected transverse momentum $p_{\mathrm{T}}^{\mathrm{jet}}$ of a jet of area A is then calculated from the measured raw jet momentum, $p_{\mathrm{T}}^{\mathrm{raw}}$, as [157]

$$p_{\mathrm{T}}^{\mathrm{jet}} = p_{\mathrm{T}}^{\mathrm{raw}} - \rho_{\mathrm{ch\ local}}\, A. \tag{4.15}$$

4.2.4 Jet selection criteria

Jets of which $v_2^{\mathrm{ch\ jet}}$ is measured are reconstructed with the anti-k_{T} algorithm in the central barrel of ALICE, using information from the ITS and TPC. A fiducial cut of $|\eta_{\mathrm{jet}}| < 0.7$ is applied on the signal jets to ensure that all jets are fully contained within the ITS and TPC acceptances and edge effects are avoided (see Fig. 4.5). The contribution of combinatorial jets to the measured jet spectrum is reduced by requiring that reconstructed jets contain at least one charged particle with $p_{\mathrm{T}} > 3$ GeV/c and have an area of at least $0.56\,\pi R^2$ (see Fig. 4.6). These selection criteria leave the hard part of the jet spectrum unaltered while significantly reducing the number of combinatorial jets which stabilizes the unfolding procedure [108, 120, 158, 159] (see § 4.5).

[e] How $\rho_{\mathrm{ch\ local}}$ is determined is treated in § 4.4. The subscript $_{\mathrm{ch}}$ indicates that only charged particles are taken into consideration.

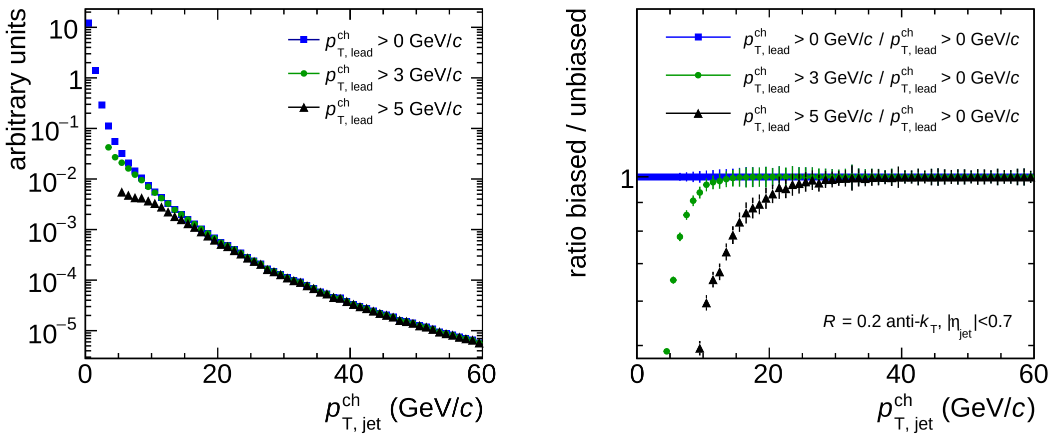

Figure 4.4: Effect of leading hadron minimum p_{T} requirement in PYTHIA. Left: normalized PYTHIA jet yields with three different leading hadron biases: no bias (blue), a $p_{\mathrm{T}} > 3$ GeV/c leading hadron requirement (green) and a $p_{\mathrm{T}} > 5$ GeV/c (black) leading hadron requirement. Right panel: ratio of biased to unbiased yields, using equal color coding.

The bias that is introduced by the requirement that a jet must contain at least one particle with $p_{\mathrm{T}} > 3$ GeV/c is quantified in events generated with PYTHIA, (see Fig. 4.4) by investigating the changes in the p_{T} differential jet yield for various requirements on the minimum p_{T} of the most highly energetic particle in a jet. The jet spectra are unchanged in the $p_{\mathrm{T}}^{\mathrm{jet}}$ ranges in which the final results (Ch. 7) are reported for the $p_{\mathrm{T}} > 3$ GeV/c requirement.

4.3 Event plane angles

The coefficient $v_2^{\mathrm{ch\ jet}}$ is defined relative to the symmetry plane Ψ_2. As the initial distribution of nucleons is not accessible experimentally, the *event plane angles* $\Psi_{\mathrm{EP},\ n}$ are used in place of Ψ_n when evaluating 4.1. The event plane angles $\Psi_{\mathrm{EP},\ 2}$ and $\Psi_{\mathrm{EP},\ 3}$ in this study, corresponding to the two dominant Fourier harmonics v_2 and v_3, are reconstructed using the V0 detectors. In order to determine the event plane angle, flow vectors $\mathbf{Q}$ [160] are constructed

$$\mathbf{Q}_n = \sum_i w_i \exp\left(in\varphi_i\right). \tag{4.16}$$

where the sum is taken over all i V0 channels, and w_i corresponds to the multiplicity incident on the cell. As explained in Ch. 3, the V0 detector consists of two arrays of scintillators (V0A and V0C) and does not give tracking information. Azimuthal angle φ_i is taken from the location of the center of gravity of each scintillator, and evaluated as

$$\varphi_i = \frac{\pi}{4}\left(\frac{1}{2} + i\%8\right) \tag{4.17}$$

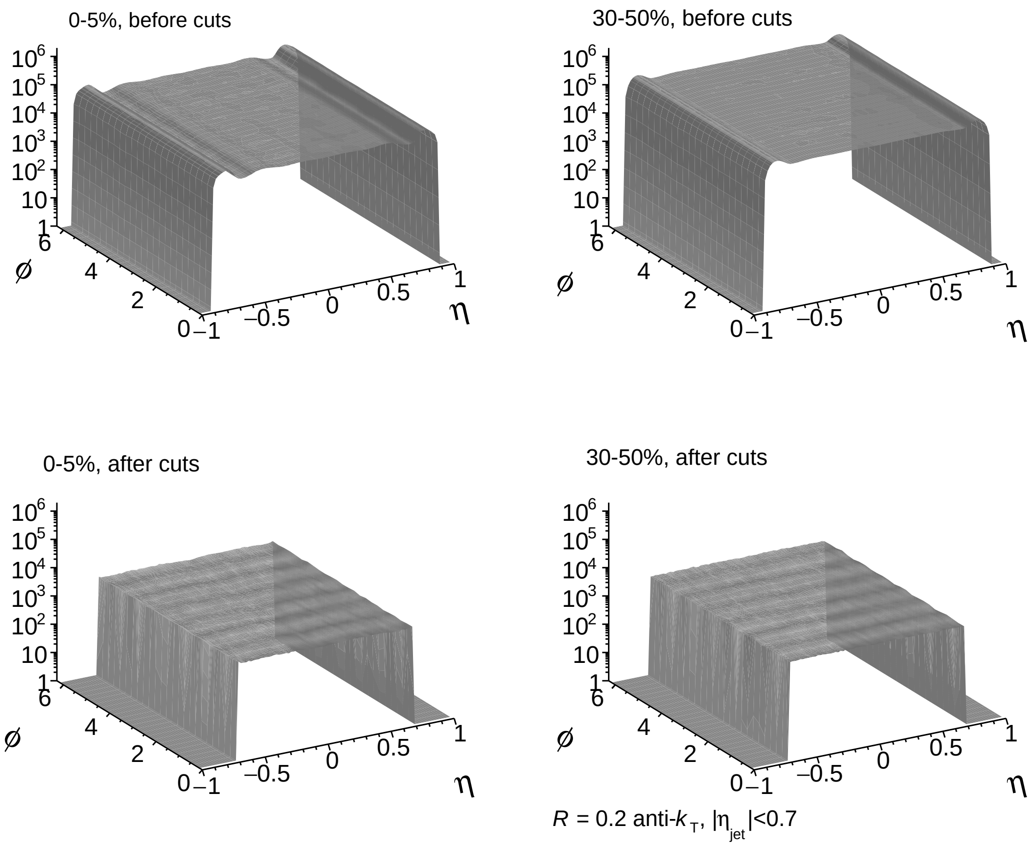

Figure 4.5: Top panels: jet yield in η, φ for 0–5% (left) and 30–50% (right) collision centrality, prior to jet selection. For $|\eta| > 0.7$ a 'ridge' is visible, caused by the limited detector acceptance, which leads to a high number of reconstructed jets with smaller than average area and p_{T}. Lower panels: jet yields *after* jet selection for the same centrality intervals. Jets are distributed homogeneously in η, φ, the 'edge effects' are removed.

with $i = 1$–32 for V0C and $i = 33$–64 for V0A and $i\%8$ is the remainder of Euclidean division of i by 8. The event plane angles are calculated from the real and imaginary parts of $\mathbf{Q}_n$ as

$$\Psi_{\mathrm{EP},\ n} = \arctan\left(\frac{\Im\left[\mathbf{Q}_n\right]}{\Re\left[\mathbf{Q}_n\right]}\right)/n. \tag{4.18}$$

4.3.1 V0 calibration and event plane

Before the V0 signal can be used for the construction of **Q**-vectors, its signals must be calibrated to ensure that an equal incident multiplicity gives an equal response in each of the V0 cells. The calibration is performed in two steps: gain equalization and recentering of the **Q**-vectors.

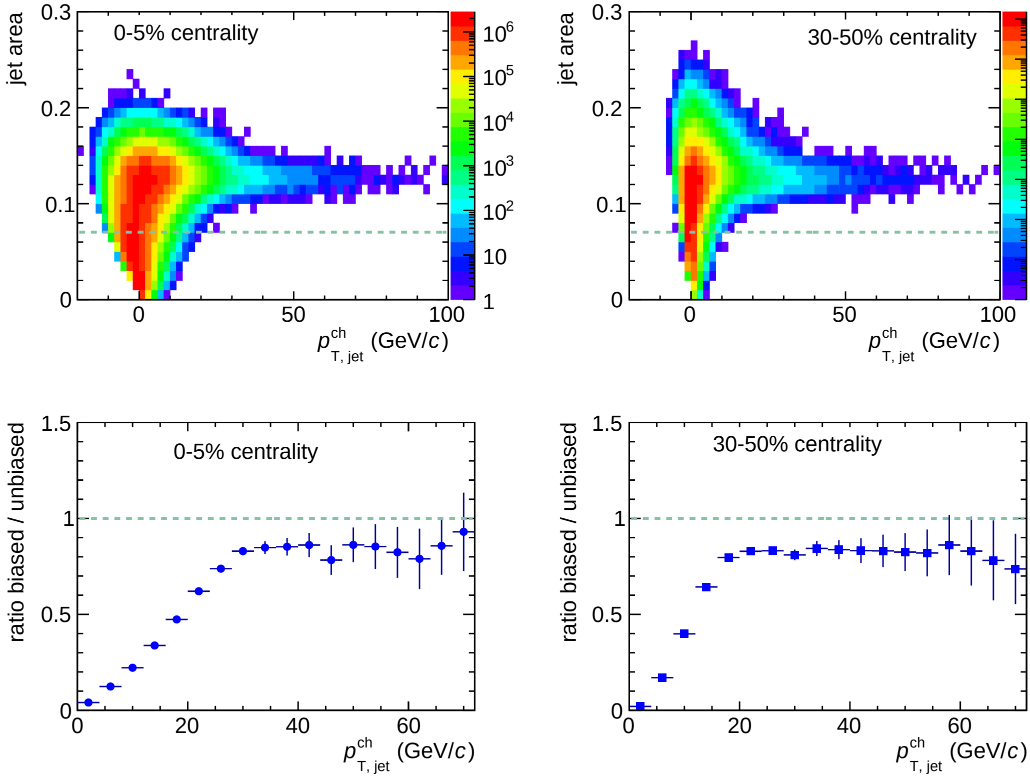

Figure 4.6: Illustration of the effect of the minimum area requirement on the jet yield (top). Jet area distributions as function of $p_{\mathrm{T}}^{\mathrm{jet}}$ are shown for 0–5% (left) and 30–50% (right) centrality. The dashed line is drawn at 0.56 πR^2 (the minimum jet area). In both centrality classes the area requirement does not alter the jet p_{T} distribution for $p_{\mathrm{T}}^{\mathrm{jet}} > 20$ GeV/c. Lower panels: p_{T}-differential ratio of jet yield prior to jet selection (*unbiased*) to the yield after selection (*biased*) for the same centrality classes. The reduction in jet yield is strongest at low transverse momenta, where the selection criteria are aimed at rejecting combinatorial jets.

4.3.1.1 Gain equalization

Gain equalization requires a prior analysis of the data in which the calibration information is gathered. In this first step, the signal of each scintillator is stored (see figure 4.7, left). When calculating **Q**-vectors (in the second pass over the data), cell multiplicities w_i are evaluated as

$$w_i = M_i \frac{\xi}{\langle M_i \rangle} \tag{4.19}$$

where M_i is the multiplicity recorded in channel i in the current event, $\langle M_i \rangle$ the average multiplicity in channel i for a given run[f], and ξ is a correction factor (see Fig. 4.7, top) which

[f]Data are collected in *runs*, with one or several of which comprising a *fill*. A fill starts with stable beams in the LHC and ends when the beams - for whatever reason - are dumped, which generally lasts less than 12 hours. The V0 response is not stable over time, therefore calibration is performed on a run-by-run basis.

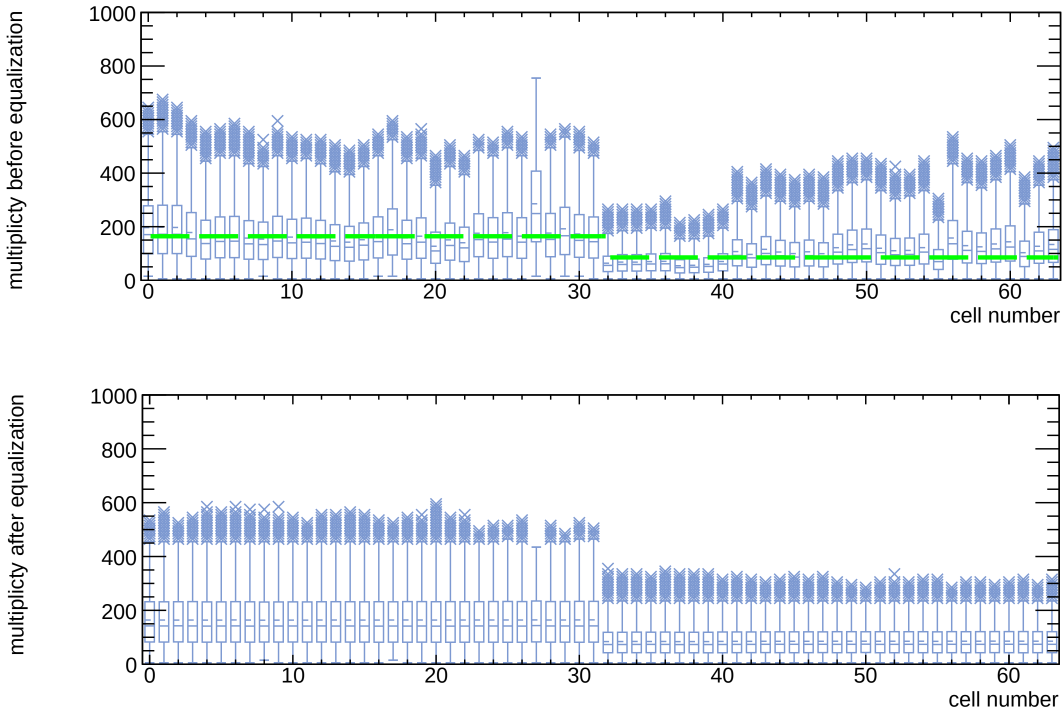

Figure 4.7: V0 multiplicity per cell prior to gain equalization (top) and after (bottom) equalization for one run as boxplots. The boxplots summarize the characteristics of a distribution: 50% - two quartiles - of measured points lies within the box, with is split by a solid line, indicating the median of the distribution, and a dashed line, indicating the mean (which is only visible when it differs from the median). The whiskers span 3 quartiles of the distribution ($\pm \approx 2.698\ \sigma$); data that lie outside of this range are represented by crosses. The green dashed line indicates the value of ξ (Eq. 4.19) in the V0A and V0C detector.

is obtained by fitting a constant $y = \xi$ through the mean multiplicity distribution of *all* cells of either the V0A or V0C, using χ^2 minimization. Earlier studies [93] have shown that a pseudorapidity-dependent fit (i.e. constructing factor ξ for the eight distinct η regions of the V0 system independently) does not alter the outcome of v_2 analyses. The lower panel of Fig. 4.7 shows the distributions of corrected multiplicities w_i obtained via multiplication of M_i with $\frac{\xi}{\langle M_i \rangle}$ for one run.

4.3.1.2 Q-vector recentering

After gain equalization, residual unevenness in the **Q**-vector distribution is removed by **Q**-vector recentering [132, 161]. In recentering, the centroids of the **Q**-vector distributions are shifted to 0 (as in minimum bias data the event plane angle distribution is random and therefore a non-zero centroid is an artifact of non-uniform detector response). Recentering also relies on a prior pass over the data. A database is built of components of gain-equalized **Q**-vectors. This database contains the centrality-dependent distribution of **Q**-vector means $\langle \mathbf{Q}_n \rangle$ and widths $\sigma_{\mathbf{Q}_n}$. The

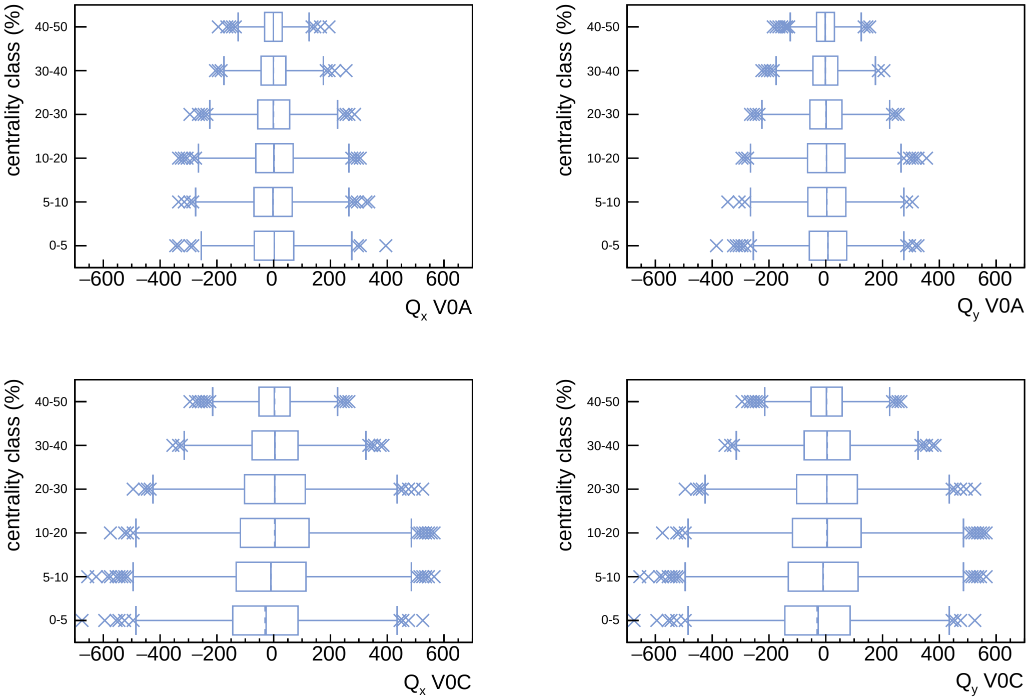

Figure 4.8: Boxplots of the $\mathbf{Q}_{2,x}$ and $\mathbf{Q}_{2,y}$ distributions for the V0 detectors before **Q**-vector recentering for various centrality classes (see caption of Fig. 4.7 for an explanation of the plotting format).

event-by-event **Q**-vector is calculated from the equalized V0 signal, and then recentered according to

$$\mathbf{Q}'_n \rightarrow \frac{\mathbf{Q}_n - \langle \mathbf{Q}_n \rangle}{\sigma_{\mathbf{Q}_n}}. \tag{4.20}$$

Figures 4.8 and 4.9 show boxplots of the $\mathbf{Q}_{2,x}$ and $\mathbf{Q}_{2,y}$ distributions for the V0 detectors before and after **Q**-vector recentering for various centrality classes.

4.3.1.3 Q-vector combination

Q-vectors for the V0A and V0C detector are constructed independently. Prior to determining $\Psi_{\mathrm{EP},\ n}$, the information of the two V0 detectors needs to be combined. The V0A and V0C detectors cover different η regions in which multiplicity N and background flow v_n differs [162–165]. The total V0 **Q**-vector is therefore constructed using weights χ_n [89] that are approximately proportional to the event plane resolution (explained in § 4.3.3) in each detector,

$$\mathbf{Q}_{n,\mathrm{V0}} = \chi^2_{n,\mathrm{V0A}} \mathbf{Q}_{n,\mathrm{V0A}} + \chi^2_{n,\mathrm{V0C}} \mathbf{Q}_{n,\mathrm{V0C}}, \tag{4.21}$$

to achieve the optimal combined event plane resolution[g]

[g] The derivation of weights χ is not straightforward. Details can be found in [87], a short summary is given in App. C.

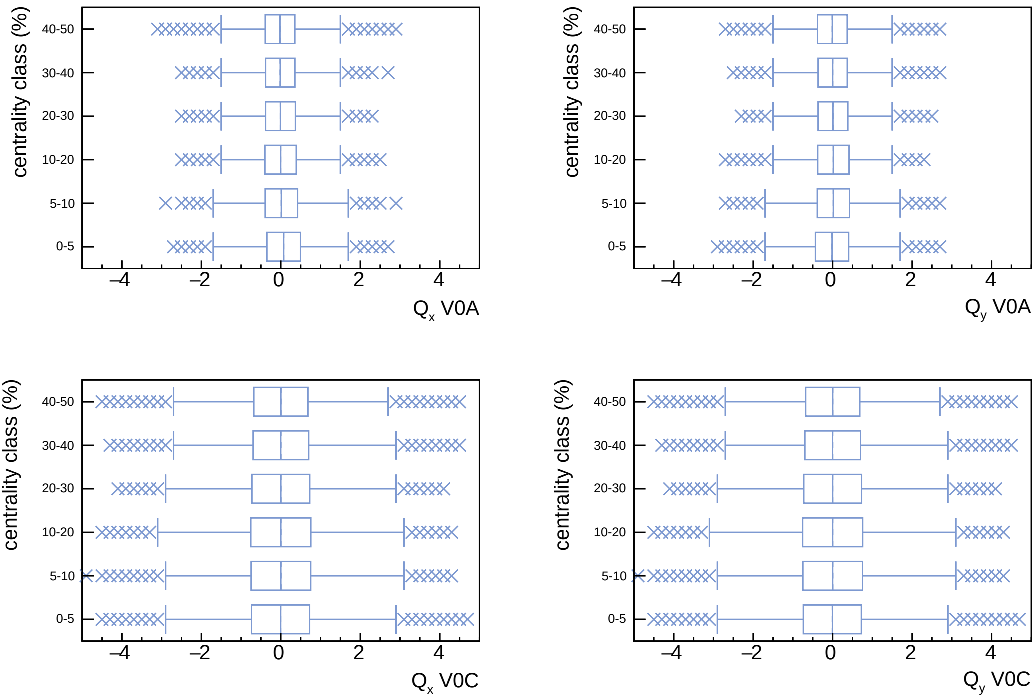

Figure 4.9: Boxplots of the $\mathbf{Q}_{2,x}$ and $\mathbf{Q}_{2,y}$ distributions for the V0 detectors after **Q**-vector recentering for various centrality classes (see caption of Fig. 4.7 for an explanation of the plotting format).

As a systematic check, Eq. 4.21 has been evaluated using either no weights (trivially summing over all 64 V0 cells) or using the squared inverse of the statistical uncertainty ($1/\sigma^2_{\mathcal{R}_2}$) on the event plane resolution as weights (assuming Poisson distribution of the number tracks incident on the V0, this estimate is proportional to the χ weights). No effect on the final $v_2^{\text{ch jet}}$ was found.

4.3.2 Bias of di-jet systems

Using the V0 detectors for the reconstruction of the event plane guarantees that the jet axis and event plane information are separated in pseudorapidity by $|\Delta\eta| > 1$. The orientation of single jets within the ITS, TPC acceptance therefore does not affect the event plane angle orientation. The event plane orientation can however be biased when a correlated signal, such as a *di-jet*, is detected in the ITS, TPC and V0 system simultaneously.

Di-jet systems are $2 \rightarrow 2$ processes in which two partons are produced from a hard scattering. The resulting jets are emitted 'back to back', i.e. $\Delta\varphi = |\varphi_{\text{jet}\,1} - \varphi_{\text{jet}\,2}| = \pi$ in the transverse plane. When a di-jet system is produced within the TPC and V0 acceptance, a trivial bias, not related to the initial overlap region of the colliding nuclei, is generated, as the event plane orientation is partially determined by the azimuthal angle of the jet in the V0[h].

[h] As the V0 detector is not a hodoscope, it is not possible to 'reject' particles from energetic jets from the

The fraction of events in which these di-jet configurations are produced has been studied in PYTHIA, by selecting di-jet events, defined in the simulation as events in which a pair of jets is found for which $\Delta\varphi > \pi - 0.3$, in which the leading (most energetic) jet of a di-jet pair lies within the TPC acceptance, and the sub-leading jet in either of the V0 detectors. The rate of such di-jet configurations was found to be negligible (less than 1 per mil of the total di-jet rate at mid-rapidity) for a leading $p_{\mathrm{T}}^{\mathrm{jet}} > 20$ GeV/c. Possible effects from back-to-back jet pairs with a jet in each of the V0 detectors are even smaller.

4.3.3 Event plane resolution

Coefficient $v_2^{\mathrm{ch\ jet}}$, in Eq. 4.1, quantifies the azimuthal anisotropy of jet production relative to the symmetry planes Ψ_n. The quantity v_2^{obs} in Eq. 4.4 is the azimuthal anisotropy determined from the p_{T} differential jet yield with respect to the experimentally available event plane $\Psi_{\mathrm{EP},\ 2}$. To correct for the finite precision with which the true symmetry plane is approximated by $\Psi_{\mathrm{EP},\ n}$, the measured v_n^{obs} is corrected using an event plane resolution correction $\mathcal{R}_n$, which relates $v_2^{\mathrm{ch\ jet}}$ and v_2^{obs} as[i]

$$\begin{aligned} v_2^{\mathrm{ch\ jet}} = \langle \cos(2[\varphi_{\mathrm{jet}} - \Psi_2]) \rangle &= \frac{\langle \cos(2[\varphi_{\mathrm{jet}} - \Psi_{\mathrm{EP},\ 2}]) \rangle}{\langle \cos(2[\Psi_{\mathrm{EP},\ 2} - \Psi_2]) \rangle} \\ &= \frac{v_2^{\mathrm{obs}}}{\mathcal{R}_2}. \end{aligned} \tag{4.22}$$

The event plane resolution $\mathcal{R}_n = \langle \cos(n[\Psi_{\mathrm{EP},\ n} - \Psi_n]) \rangle$ as expressed in Eq. 4.22 is not directly measurable. It can however be derived from data by combining products of event plane resolutions from *sub-events* [166, 167], which are independent samples of tracks from the event (e.g. tracks taken from different η ranges). The product of the resolutions of sub-events i and j is given by

$$\begin{aligned} \mathcal{R}_n^i \mathcal{R}_n^j &= \langle \cos(n[\Psi_{\mathrm{EP},\ n}^{\mathrm{i}} - \Psi_n]) \rangle \langle \cos(n[\Psi_{\mathrm{EP},\ n}^{\mathrm{j}} - \Psi_n]) \rangle \\ &= \langle \cos(n[\Psi_{\mathrm{EP},\ n}^{\mathrm{i}} - \Psi_{\mathrm{EP},\ n}^{\mathrm{j}}]) \rangle. \end{aligned} \tag{4.23}$$

Combining several equalities of the type of Eq. 4.23, involving event plane angles of different sub-events, event plane resolution in one sub-event i can be expressed as

$$\mathcal{R}_n^i = \sqrt{\frac{\left(\mathcal{R}_n^i \mathcal{R}_n^j\right)\left(\mathcal{R}_n^i \mathcal{R}_n^k\right)}{\left(\mathcal{R}_n^j \mathcal{R}_n^k\right)}} \tag{4.24}$$

Using the negative and positive η regions of the TPC as sub-events, the event plane resolution of the V0 detector in Eq. 4.5 is

$$\mathcal{R}_2^{\mathrm{V0}} = \left(\frac{\left\langle \cos\left[2\left(\Psi_{\mathrm{EP},\ 2}^{\mathrm{V0}} - \Psi_{\mathrm{EP},\ 2}^{\mathrm{TPC},\ \eta > 0}\right)\right]\right\rangle \left\langle \cos\left[2\left(\Psi_{\mathrm{EP},\ 2}^{\mathrm{V0}} - \Psi_{\mathrm{EP},\ 2}^{\mathrm{TPC},\ \eta < 0}\right)\right]\right\rangle}{\left\langle \cos\left[2\left(\Psi_{\mathrm{EP},\ 2}^{\mathrm{TPC},\ \eta > 0} - \Psi_{\mathrm{EP},\ 2}^{\mathrm{TPC},\ \eta < 0}\right)\right]\right\rangle} \right)^{1/2}. \tag{4.25}$$

information of which $\Psi_{\mathrm{EP},\ n}$ is calculated, as will be done in § 4.4 for the TPC v_n determination.

[i] The validity of Eqs 4.22 and 4.23 can be shown explicitly by expression the equalities in complex exponentials, where the sine terms vanish due to reflection symmetry with respect to the reaction plane [89].

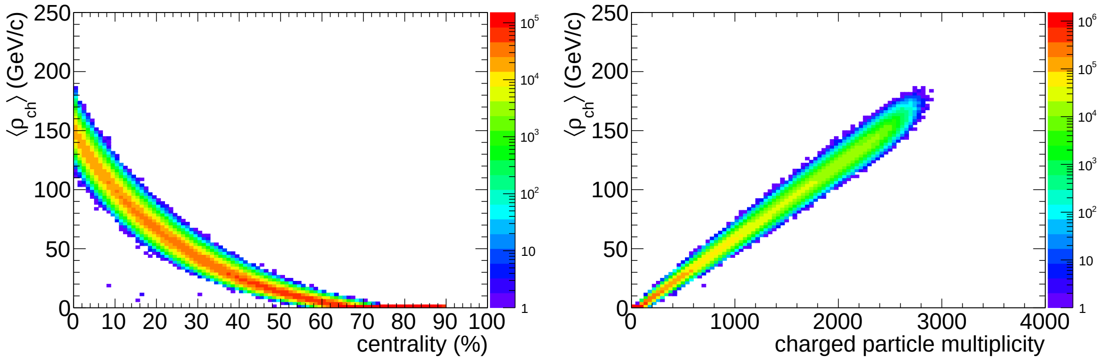

Figure 4.10: Left: $\langle\rho_{\mathrm{ch}}\rangle$ as a function of centrality, right panel: $\langle\rho_{\mathrm{ch}}\rangle$ as function of multiplicity. The charged transverse momentum background density per unit area ($\langle\rho_{\mathrm{ch}}\rangle$) has a linear dependence on the charged particle multiplicity.

The $\Psi_{\mathrm{EP},\,2}$ angles in the TPC are obtained following the procedure of Eq. 4.18 on tracks with $0.15 < p_{\mathrm{T}} < 4$ GeV/c, using unit track weights in the construction of the flow vectors $\mathbf{Q}_2$ (see Eq. 4.16). The event plane resolution $\mathcal{R}_2^{\mathrm{V0}}$ is 0.47 in 0–5% collision centrality and 0.75 in 30–50% collision centrality with negligible uncertainties. This second number is found by measuring $\mathcal{R}_2$ in 30–40 and 40–50% collision centrality, and combining the obtained resolutions, using the p_{T}-integrated jet yields within the same intervals between $20 < p_{\mathrm{T}}^{\mathrm{jet}} < 90$ GeV/c as weights.

The factorization in Eq. 4.23 only holds when the underlying Ψ_n is equal for both sub-events. Recent studies indicate that the angle Ψ_n depends weakly on pseudorapidity; at rapidity intervals used in this analyses however, relative event plane angle fluctuations do not exceed 5% [168].

4.4 The underlying event

As explained in § 4.2 and Eq. 4.15, the measured jet energy in Pb–Pb collisions needs to be corrected for the contribution of energy from the underlying event. The average transverse-momentum density per unit area $\langle\rho_{\mathrm{ch}}\rangle$ is estimated event-by-event as

$$\langle\rho_{\mathrm{ch}}\rangle = \mathrm{median}\left\{\frac{p_{\mathrm{T}}^{\mathrm{raw}}{}_i}{A_i}\right\} \tag{4.26}$$

where $p_{\mathrm{T}}^{\mathrm{raw}}{}_i$ is the uncorrected p_{T} of k_{T} jets and A_i the corresponding area. Subscript '$_{\mathrm{ch}}$' in $\langle\rho_{\mathrm{ch}}\rangle$ indicates that the variable is, in this work, constructed from charged particles only. The k_{T} algorithm is chosen because it produces, in uniform distributions of tracks, jets with a stable area $A \propto \pi R^2$ (contrary to the anti-k_{T} algorithm, which tends to find a small number of hard jets with area $A \propto \pi R^2$, and a large number of very small, low momentum jets). The influence of hard jets on $\langle\rho_{\mathrm{ch}}\rangle$ is reduced by using the median of the distribution rather than the mean, and by excluding the two most highly energetic k_{T} clusters from the jet sample prior to evaluating $\langle\rho_{\mathrm{ch}}\rangle$. Fig. 4.10 shows $\langle\rho_{\mathrm{ch}}\rangle$ as function of centrality and charged particle multiplicity. The charged transverse momentum background density per unit area has, as expected, a linear dependence on the charged particle multiplicity.

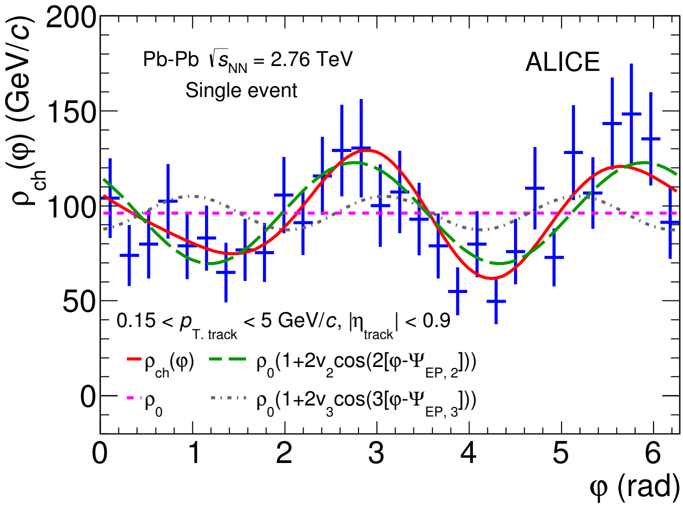

Figure 4.11: Left: Transverse momentum density of charged tracks as a function of azimuthal angle for a single event from the most central 0-5% event class. Data points (blue) are given with statistical uncertainties only. The red curve is the fit of Eq. 4.27 to the distribution, the green and gray curves, obtained from the fit of Eq. 4.27 as well, show the independent contributions of v_2 and v_3 to $\rho_{\text{ch}}(\varphi)$. The dashed magenta line is the normalization constant ρ_0.

4.4.1 Anisotropic flow of the underlying event

In each event, the anisotropy of the underlying event is modeled using the dominant [169] flow harmonics v_2 and v_3,

$$\rho_{\text{ch}}(\varphi) = \rho_0 \left(1 + 2\{v_2 \cos\left[2\left(\varphi - \Psi_{\text{EP},\ 2}\right)\right] + v_3 \cos\left[3\left(\varphi - \Psi_{\text{EP},\ 3}\right)\right]\}\right). \tag{4.27}$$

Here, $\rho_{\text{ch}}(\varphi)$ is the azimuthal distribution of summed track p_{T} for tracks with $0.15 < p_{\text{T}} < 5$ GeV/c and $|\eta_{\text{track}}| < 0.9$. The parameters ρ_0 and v_n are determined event-by-event from a fit of the right side of Eq. 4.27 to data. The event plane angles $\Psi_{\text{EP},\ n}$ in Eq. 4.27 are fixed to the V0 event plane angles. A single event example of this procedure is illustrated in Fig. 4.11, where the data points represent the transverse momentum density distribution in a single event, the red curve represents the full functional description of $\rho_{\text{ch}}(\varphi)$ (Eq. 4.27), the green and gray curves give the contributions of the separate harmonics v_2 and v_3, and the dashed magenta line is the normalization constant ρ_0. To reduce the bias of hard jets in the estimates of v_n in Eq. 4.27 while retaining azimuthal uniformity, the leading jet in each event is removed by rejecting all tracks for which $|\eta_{\text{jet}} - \eta_{\text{track}}| < R$. The η separation between the tracks and the V0 detectors also removes short range correlations between the event planes and tracks.

The number of bins into which the azimuthal range is divided is set on an event-by-event basis to the square root of the number of tracks. The fit maximizes the estimated likelihood [170], which is based on a Poisson distribution for the bin content. Since the bin contents are not pure counts, but weighted by p_{T}, the statistical uncertainties on each bin σ_i are estimated as the sum of the squares of the p_{T} of the individual particles $\sigma_i = \sigma(\sum p_{\text{T}}) = \sqrt{\sum p_{\text{T}}^2}$. A scaled

Poisson distribution $P(x_i/w_i|\mu_i/w_i)$ is used as the probability distribution for the data points in the likelihood calculation, with a scale factor $w_i = \sigma_i^2/y_i$ where y_i is the bin content and μ_i is the expected signal from the fit function. The compatibility of each fit with the data is tested by calculating the χ^2 and evaluating the probability of finding a test statistic at least as large as the observed one in the χ^2 distribution. When this probability is less than 0.01, the average event background density $\langle\rho_{\mathrm{ch}}\rangle$ is used instead of $\rho_{\mathrm{ch}}(\varphi)$; this occurs in 3% (most central) to 7% (semi-central) of events. The acceptance criterion is varied in the systematic studies; the sensitivity to it is small. In the centrality ranges in which the final results are given, minima of $\rho_{\mathrm{ch\ local}}$ are always positive.

Equation 4.15 shows that the corrected transverse momentum $p_{\mathrm{T}}^{\mathrm{jet}}$ of a jet of area A is calculated as $p_{\mathrm{T}}^{\mathrm{jet}} = p_{\mathrm{T}}^{\mathrm{raw}} - \rho_{\mathrm{ch\ local}}\,A$. In this expression, $\rho_{\mathrm{ch\ local}}$ is obtained from integration of $\rho_{\mathrm{ch}}(\varphi)$ around $\varphi_{\mathrm{jet}} \pm R$[j]

$$\rho_{\mathrm{ch\ local}} = \frac{\langle\rho_{\mathrm{ch}}\rangle}{2R\rho_0}\int_{\varphi-R}^{\varphi+R}\rho_{\mathrm{ch}}(\varphi)\mathrm{d}\varphi. \tag{4.28}$$

The pre-factor of the integral, $\frac{\langle\rho_{\mathrm{ch}}\rangle}{2R\rho_0}$, is chosen such that integration over the full azimuth yields the average transverse momentum density $\langle\rho_{\mathrm{ch}}\rangle$.

4.4.2 Subtracted flow harmonics

Figure 4.12 shows the v_n harmonics, corrected using $\mathcal{R}_2$ and $\mathcal{R}_3$, extracted by fitting Eq. 4.27 as function of centrality (square markers) together with v_2 and v_3 measurements from two ($v_n\{2\}$) and four ($v_n\{4\}$) particle correlations (circular markers) [169]. Although a direct quantitative comparison between the two measurements can not be made (as explained below), Fig. 4.12 qualitatively validates the underlying event parametrization.

The flow measurement in Fig. 4.12 is performed using the unweighted two- and four-particle Q-cumulant method [171] ($v_n\{2\}$ and $v_n\{4\}$) at mid-rapidity ($|\eta| < 0.9$). The $v_n\{2\}$ (closed circles) and $v_n\{4\}$ (open circles) coefficients measure 'number flow', i.e. $v_n = \langle\cos(n[\varphi - \Psi_n])\rangle$ where each track that enters the average contributes equally to the amplitude of v_n. Coefficients v_n in Eq. 4.27 are fitted to the angular distribution of summed track p_{T} rather than the modulation in the *number* of tracks only. For a more meaningful comparison, Fig. 4.12 therefore also shows v_n harmonics obtained by fitting Eq. 4.27 to the angular distribution of *number* of tracks $\mathrm{d}N/\mathrm{d}\varphi$ (open squares).

The fitted v_n harmonics from the distribution of $\mathrm{d}N/\mathrm{d}\varphi$ follow the trend of the $v_2\{4\}$ measurement, which is in good agreement with expectations, as the $\mathrm{d}N/\mathrm{d}\varphi$ method has a small sensitivity to *non-flow* effects because the track and event plane information are separated in pseudorapidity by $|\Delta\eta| > 1$. Non-flow effects are angular correlations between particles that are *not* a remnant of collective expansion of the QGP, but rather a result of e.g. resonance decay or a parton shower. Two particle correlations are inherently sensitive to such correlations. More-particle correlations are less affected by non-flow, as e.g. a $x \to yy$ decay does not correlate three or more particles. This sensitivity is visible in Fig. 4.12, as $v_n\{2\}$ is consistently larger than $v_n\{4\}$.

[j] Integration over φ is in this analysis introduced to account for the flow harmonics v_n which modulate the underlying event. In studies where event plane dependence is irrelevant, a subtraction of the form of $p_{\mathrm{T}}^{\mathrm{jet}} = p_{\mathrm{T}}^{\mathrm{raw}} - \rho\,A$ suffices. η dependence of $\rho(\varphi,\eta)$ is treated in § 4.4.

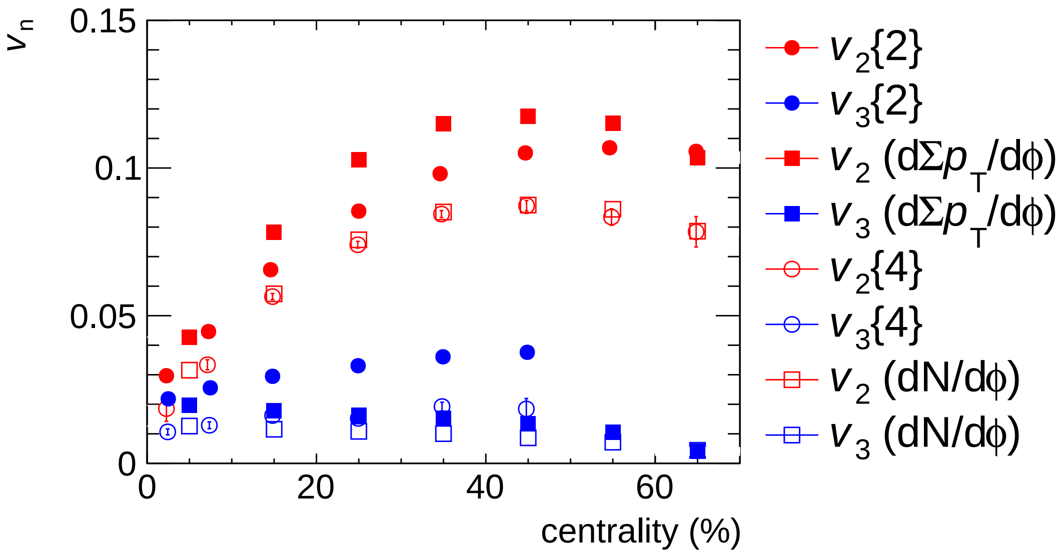

Figure 4.12: All-event average of the v_n coefficients obtained by event-by-event fitting of Eq. 4.27, either to the azimuthal distribution of transverse momentum ($\rho(\varphi)$) or to the azimuthal distribution of number of tracks $\mathrm{d}N/\mathrm{d}\varphi$, compared to anisotropic flow measurements ($v_n\{2\}$ and $v_n\{4\}$) at mid-rapidity from [91, 169]).

Qualitative agreement is also observed for the v_3 measurements, but the data are less compatible than those of the second order harmonic coefficient. The small amplitude of v_3 and low resolution $\mathcal{R}_3$ possibly hinder the fitting procedure and lead to a poorer compatibility.

4.4.3 The δp_T distribution

The validity of Eq. 4.27 as a description of the contribution of background flow to the underlying event energy is tested by placing cones of radius $R = 0.2$ at random positions (excluding the location of the leading jet) in the η–ϕ plane and subtracting the expected summed transverse momentum in a cone from the measured transverse momentum in the cone,

$$\delta p_\mathrm{T} = \sum p_\mathrm{T}^{\mathrm{tracks}} - \rho \pi R^2. \tag{4.29}$$

Here, ρ is the measured background transverse momentum density. This procedure is repeated multiple times per event, until the full phase space is covered, to obtain a distribution of δp_T values. The δp_T distribution as a function of the cone azimuthal angle φ_RC relative to the event plane $\Psi_{\mathrm{EP},\,2}$ is shown in Fig. 4.13. In panel (a) $\langle \rho_\mathrm{ch} \rangle$ has been used to estimate the underlying event summed p_T and in panel (b) $\rho_\mathrm{ch}(\varphi)$. Incorporating azimuthal dependence into the underlying event description leads to a sizable reduction in the cosine modulation of the δp_T distribution.

The effectiveness of the subtraction of background flow is quantified by comparing the expected and measured widths of the δp_T distribution in the *absence* of background flow, $\sigma(\delta p_\mathrm{T}{}^{v_n=0})$, (see Fig. 4.13b) to the expected and measured widths of the δp_T distribution in the

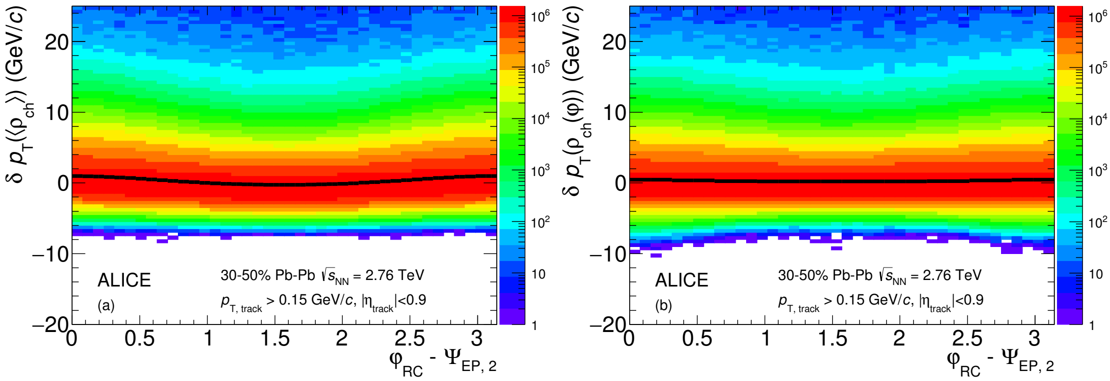

Figure 4.13: The δp_{T} distribution (Eq. 4.29) from the random cone (RC) procedure as function of cone azimuthal angle φ_{RC} relative to the event plane. In panel (a) the azimuthally-averaged background $\langle\rho_{\mathrm{ch}}\rangle$ has been subtracted; in panel (b) the azimuthally dependent $\rho_{\mathrm{ch}}(\varphi)$ from an event-by-event fit of the p_{T}-density with Eq. 4.27. The solid black line represents the mean of the δp_{T} distribution.

presence of background flow, $\sigma(\delta p_{\mathrm{T}}{}^{v_n})$ (Fig. 4.13a). Assuming independent particle emission and Poisson statistics, the expected width of the δp_{T} distribution in the absence of background flow ($v_n = 0$) can be calculated by quadratic summing of the relative uncertainties on expected particle $\langle p_{\mathrm{T}}\rangle$ ($\sigma(p_{\mathrm{T}})$) and multiplicity ($\sigma(N_A)$) within a cone [158]

$$\frac{\sigma(\delta p_{\mathrm{T}}^{v_n=0})}{p_{\mathrm{T}}{}^{\mathrm{RC}}} = \sqrt{\left(\frac{\sigma(N_A)}{\langle p_{\mathrm{T}}\rangle}\right)^2 + \left(\frac{\sigma(p_{\mathrm{T}})}{N_A}\right)^2}. \tag{4.30}$$

Using $\sigma(N_A) = \sqrt{N_A}$ and $p_{\mathrm{T}}{}^{\mathrm{RC}} = N_A\langle p_{\mathrm{T}}\rangle$ an expression for $\sigma(\delta p_{\mathrm{T}}^{v_n=0})$ is found in quantities that are readily available

$$\sigma(\delta p_{\mathrm{T}}^{v_n=0}) = \sqrt{N_A\sigma^2(p_{\mathrm{T}}) + N_A\langle p_{\mathrm{T}}\rangle^2} \tag{4.31}$$

where N_A is the average expected number of tracks within a cone, $\langle p_{\mathrm{T}}\rangle$ the mean p_{T} of a single particle spectrum and $\sigma(p_{\mathrm{T}})$ the standard deviation of this spectrum. This expectation can be extended to include contributions from background flow by introducing non-Poisson density fluctuations (the background flow harmonics v_n) [158], as

$$\sigma(\delta p_{\mathrm{T}}^{v_n}) = \sqrt{N_A\sigma^2(p_{\mathrm{T}}) + (N_A + 2N_A^2(v_2^2 + v_3^2))\langle p_{\mathrm{T}}\rangle^2}. \tag{4.32}$$

The measured widths are obtained from the δp_{T} distributions directly; the distributions are constructed using as the transverse momentum density ρ in Eq. 4.29 either $\langle\rho_{\mathrm{ch}}\rangle$ to obtain $\sigma(\delta p_{\mathrm{T}}^{v_n})$ or $\rho_{\mathrm{ch\ local}}$ for $\sigma(\delta p_{\mathrm{T}}^{v_n=0})$.

Figure 4.14 shows the expected and measured relative change in the width of the δp_{T} distribution,

$$(\sigma(\delta p_{\mathrm{T}}^{v_n}) - \sigma(\delta p_{\mathrm{T}}^{v_n=0}))/\sigma(\delta p_{\mathrm{T}}^{v_n}), \tag{4.33}$$

as function of collision centrality. The blue points give the expected reduction from Eqs 4.31 and 4.32. The red points use the measured widths from δp_{T} distributions. The expected change

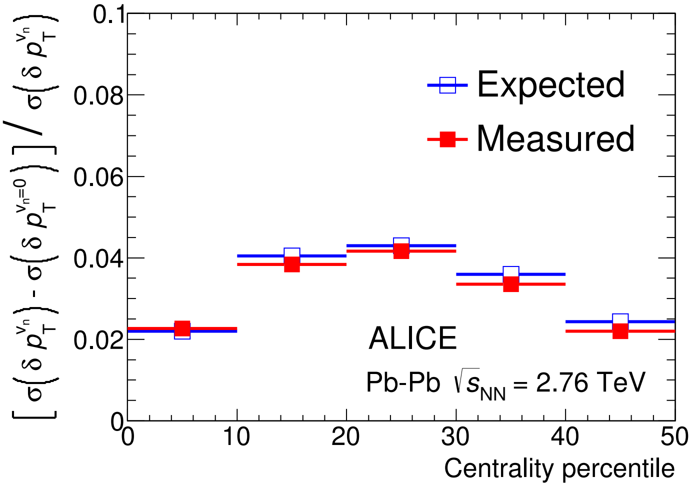

Figure 4.14: Centrality dependence of the measured and expected relative change in the δp_T distribution width from using the azimuthally dependent $\rho_{\mathrm{ch\ local}}$ instead of the median $\langle\rho_{\mathrm{ch}}\rangle$. The blue points give the expected reduction from simple assumptions about the behavior of charged particle spectra and flow harmonics v_n (following Eq. 4.31 and 4.32). The red points use the measured widths from δp_T distributions directly. Statistical uncertainties are smaller than the marker size.

is in good quantitative agreement with the measured change over the entire centrality range, indicating that the width of the δp_T distributions can be understood in terms of a simple independent particle emission model with background flow contributions.

4.4.3.1 η dependence of random cone energy

Random cones are constructed in η–φ, and as such, the δp_T distribution should be evaluated as

$$\delta p_T = \sum_{\mathrm{tracks}} p_T - A_{\mathrm{RC}} \int_{A_{\mathrm{RC}}} \rho(\varphi, \eta) \mathrm{d}\varphi \mathrm{d}\eta \tag{4.34}$$

where integration is performed over circular area A_{RC} in η and φ. Equation 4.34 however has no analytical solution. Approximate numerical solutions, such as using a Riemann sum $\sum \rho(\varphi, \eta)\Delta\varphi\Delta\eta$ instead of integration, can be used to quantify the effect of taking into account the η dependence of Eq. 4.34. The difference in random cone energy between the two integration approaches is shown in Fig. 4.15, which gives the ratio of random cone energy obtained by a numeric solution of Eq. 4.34 to that obtained from integration over dφ only as function of random cone p_T for different centrality classes, and does not exceed 1% for cone radius $R = 0.2$.

Integration in dη and dφ is (depending on the precision of the numerical approach) an order of magnitude slower than integrating over dφ only; as default approach therefore, the δp_T definition of Eq. 4.29 is used in this work. It should also be noted - as will be explicitly shown in Ch. 5 - that the exact definition of the functional form of the background description does

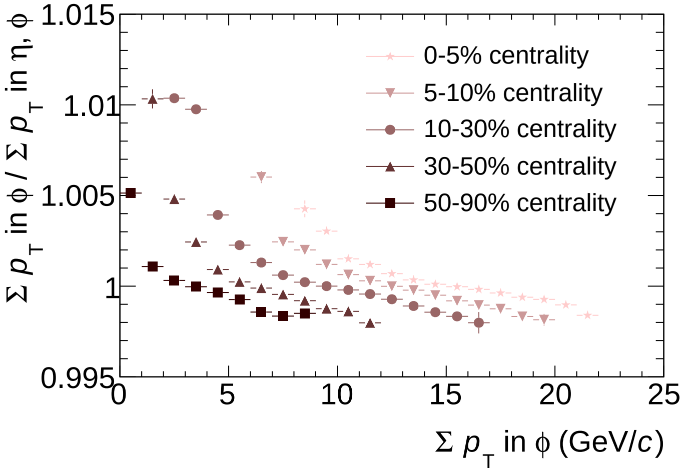

Figure 4.15: Ratio of random cone energy obtained from Riemann sum $\sum \rho(\varphi,\eta)\Delta\varphi\Delta\eta$ to random cone energy integrated in dφ only (Eq. 4.29) as function of random cone energy integrated in dφ for various centrality classes.

not affect the measured $v_2^{\text{ch jet}}$ as long as the jet spectra are unfolded properly (although it does have an effect on the systematic uncertainties of the measurement).

4.5 Unfolding

Unfolding is the general problem of estimating probability distributions from data that are smeared by random fluctuations [172, 173]. The unfolding problem is a *deconvolution* of the convolution that relates the *true* ($f_{\text{true}}(x)$) to the *measured* ($f_{\text{meas}}(y)$) distribution,

$$f_{\text{meas}}(x) = \int R(x|y) f_{\text{true}}(y) dy \tag{4.35}$$

where $R(x|y)$ is a *response function* that gives the conditional probability of the true signal to be smeared to the measured one.

After the subtraction procedure presented in the previous section, the measured jet spectrum has to be unfolded to correct for detector effects and fluctuations in the underlying event transverse momentum density. Eq. 4.35 for unfolding jet spectra is written as

$$M(p_{\text{T,chjet}}^{\text{rec}}) = \int G(p_{\text{T,chjet}}^{\text{rec}}, p_{\text{T,chjet}}^{\text{gen}}) T(p_{\text{T,chjet}}^{\text{gen}}) \epsilon(p_{\text{T,chjet}}^{\text{gen}}) \mathrm{d}p_{\text{T,chjet}}^{\text{gen}} \tag{4.36}$$

for $T(p_{\text{T,chjet}}^{\text{gen}})$, the unfolded true jet spectrum, where $M(p_{\text{T,chjet}}^{\text{rec}})$ is the measured jet spectrum, $G(p_{\text{T,chjet}}^{\text{rec}}, p_{\text{T,chjet}}^{\text{gen}})$ is a functional description (*response function*) of distortions due to background fluctuations and detector response, and $\epsilon(p_{\text{T,chjet}}^{\text{gen}})$ is the jet finding efficiency.

The jet finding efficiency is studied by generating particle-level jets in PYTHIA [144], and transporting these through the detector using GEANT [140]. The particle- and detector-level

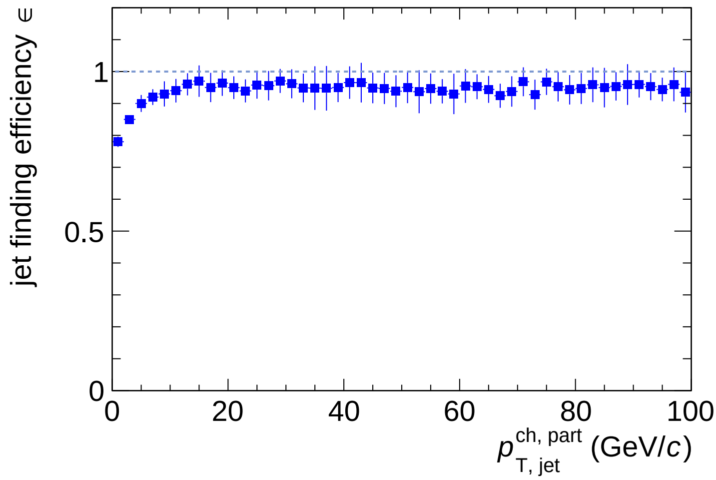

Figure 4.16: Jet finding efficiency ϵ as function of particle level $p_{\mathrm{T,jet}}^{\mathrm{ch,part}}$. Statistical uncertainties only.

jets are matched, using a matching algorithm (see Ch. 5), and the p_{T} differential ratio

$$\epsilon(p_{\mathrm{T,chjet}}^{\mathrm{gen}}) = \frac{N_{\mathrm{matched,\ detector\ level}}(p_{\mathrm{T,chjet}}^{\mathrm{gen}})}{N_{\mathrm{gen\ (particle\ level)}}^{|\eta|<0.5}(p_{\mathrm{T,chjet}}^{\mathrm{gen}})}, \tag{4.37}$$

with $N_{\mathrm{matched,\ detector\ level}}$ and $N_{\mathrm{gen\ (particle\ level)}}$ both taken as function of particle level $p_{\mathrm{T,chjet}}^{\mathrm{gen}}$, defines the jet finding efficiency. The jet finding efficiency ϵ for $R = 0.2$ anti-k_{T} as function of $p_{\mathrm{T}}^{\mathrm{jet}}$ is shown in Fig. 4.16. In the p_{T} range in which $v_2^{\mathrm{ch\ jet}}$ is measured, the efficiency is constant, and will therefore be omitted from hereon as it appears both in the enumerator and denominator of Eq. 4.1.

Since the measured jet spectrum is binned, Eq. 4.36 is discretized by replacing the integral by a matrix multiplication

$$\mathbf{M_m} = \mathbf{G_{m,t}} \cdot \mathbf{T'_t} \tag{4.38}$$

where $\mathbf{T'_t}$ is the solution of the discretized equation (the prime indicates that $\mathbf{T'_t}$ is not corrected for jet-finding efficiency).

The combined response matrix $\mathbf{G_{m,t}}$ is the product of the response matrices from detector effects and transverse momentum density fluctuations, the latter of which are constructed independently for the in-plane and out-of-plane spectra by embedding random cones at specific relative azimuth with respect to the event plane.

4.5.1 The detector response matrix

The detector response matrix is, like the efficiency, obtained by matching jets generated by PYTHIA [144] (particle-level jets) to the *same* jets after transport through the detector (detector-level jets) by GEANT3 [140], where the detector conditions are tuned to those of the

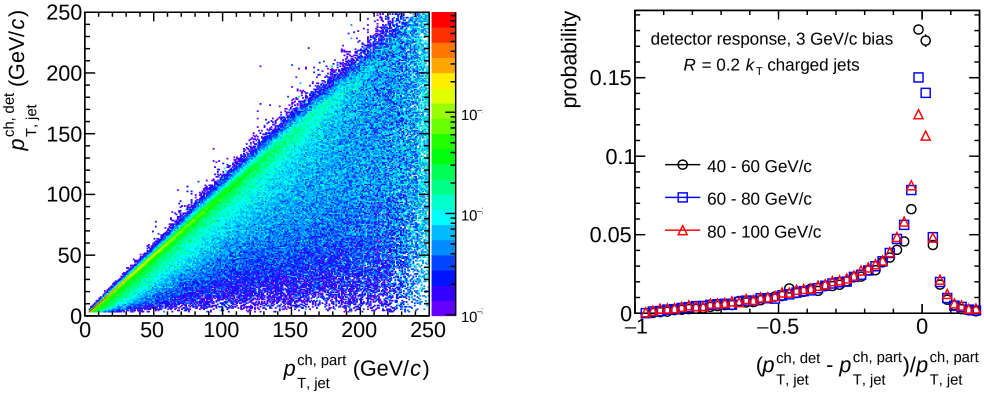

Figure 4.17: Detector response matrix for $R = 0.2$ charged jets with a leading track selection of 3 GeV/c. The x-axis represents the true (particle level) spectrum, the y-axis shows the detector level (measured) spectrum (left). Corresponding probability distribution for several particle level $p_{\mathrm{T}}^{\mathrm{jet}}$ intervals (right).

Pb–Pb data-taking periods. Particle-level jets contain only primary charged particles produced by the event generator, which comprise all prompt charged particles produced in the collision, as well as products of strong and electromagnetic decays, while products of weak decays of strange hadrons are rejected. Matching is based on the shortest distance in the η–φ plane between detector level and particle level jets and is bijective, meaning that there is a one-to-one correspondence between detector and particle level jets.

Figure 4.17 shows the detector response for $R = 0.2$ charged jets containing at least one charged hadron of $p_{\mathrm{T}} > 3$ GeV/c. The sum of each column of the detector response matrix is normalized to one so that it represents the probability distribution of reconstructing a particle-level jet generated with $p_{\mathrm{T,chjet}}^{\mathrm{gen}} = x$ at reconstructed $p_{\mathrm{T,chjet}}^{\mathrm{rec}} = y$. The most probable value in all columns is the diagonal of the matrix, indicating is that the detector-level p_{T} or a reconstructed jet is most likely to be very close to the particle-level p_{T}. Smearing to lower transverse momenta is a result of tracking efficiency and tracking momentum resolution, whereas smearing to higher momenta is attributable to resolution effects only.

4.5.2 Background fluctuations matrix

Even though the local background density (Eq. 4.27) is used for background subtraction for each jet, fluctuations in the energy density of the underlying event still influence the measured jet p_{T} (as can be seen in Fig. 4.13 (right): δp_{T} is still a distribution rather than a single value).

The background fluctuations matrix is constructed from the δp_{T} distribution by converting it to a probability distribution (normalizing its integral to one), and filling the matrix with the probability that a jet with $p_{\mathrm{T,chjet}}^{\mathrm{gen}} = x$ is measured at $p_{\mathrm{T,chjet}}^{\mathrm{rec}} = y$. This is done for the in-plane and out-of-plane orientations independently by projecting the distribution in Fig. 4.13 over the corresponding $\Delta^{\mathrm{EP}}\varphi_2$ intervals, to accommodate residual effects of hydrodynamic flow (which lead to off diagonal elements in the δp_{T} matrix), and to account for the fact that background

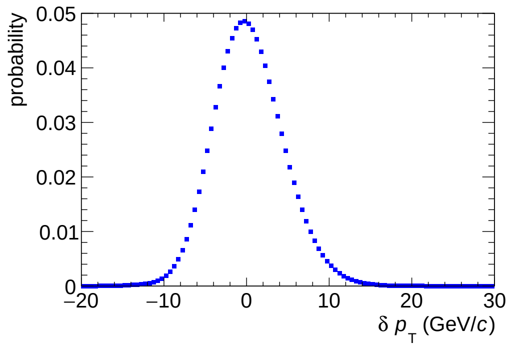

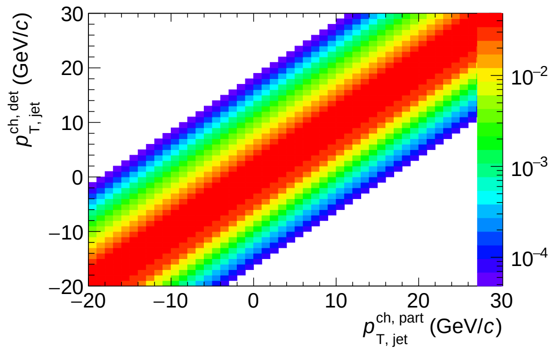

Figure 4.18: δp_T probability distribution for 30–50% collision centrality (left). Background fluctuations response matrix (right) obtained from the δp_T distribution.

fluctuations are larger in the in-plane than in the out-of-plane orientation. Figure 4.18 shows a δp_T probability distribution for 30–50% collision centrality (left panel) and the background fluctuation response matrix (right) that is constructed from this distribution.

Constructing the background fluctuations matrix from the δp_T distribution relies on the underlying assumption that the smearing of the jet spectrum is equal for all jet p_T and that the orientation of the jet axis is not changed by the fluctuations. These assumptions are tested (and validated) in Ch. 5.

4.5.3 Combined response matrix

Unfolding in this work is performed in one step, in which the jet spectra are unfolded using a combined response matrix containing information on both the background fluctuations and the detector response. This combined response matrix is obtained by multiplication of the background fluctuations matrix $\mathbf{G}_{\mathbf{m},\mathbf{d}}$ and the detector response matrix $\mathbf{G}_{\mathbf{d},\mathbf{t}}$

$$
\begin{aligned}
\mathbf{M}_{\mathbf{m}} &= \mathbf{G}_{\mathbf{m},\mathbf{d}} \cdot \mathbf{G}_{\mathbf{d},\mathbf{t}} \cdot \mathbf{T}'_{\mathbf{t}} \\
&= \mathbf{G}_{\mathbf{m},\mathbf{t}} \cdot \mathbf{T}'_{\mathbf{t}}.
\end{aligned} \tag{4.39}
$$

A fine-binned combined response matrix is generally not suitable for unfolding since uncertainties on the measured spectrum are too large to lead to a satisfactory result. Since jet spectra are steeply falling distributions, a weighted re-binning procedure of the response matrix is used, where as bin weights a fit [158] of a Tsallis function [174] to a PYTHIA spectrum is used

$$
f(p_T) = p_T \left(1 + \frac{p_T}{7.2}\right)^{-8} \tag{4.40}
$$

4.5.3.1 p_T ranges of measured and unfolded jet spectra

For the results presented in Ch. 7, the measured jet spectra are taken as input for the unfolding routine in the range $30 < p_T^{\text{jet}} < 105$ GeV/c for 0–5% collision centrality and $15 < p_T^{\text{jet}} < 90$ GeV/c for 30–50% collision centrality. The lower bound corresponds to five times the width of the δp_T distribution, the upper bound is the edge of the last measured bin which contains at least 10 counts. This configuration was found to lead to reliable unfolded solutions in Monte

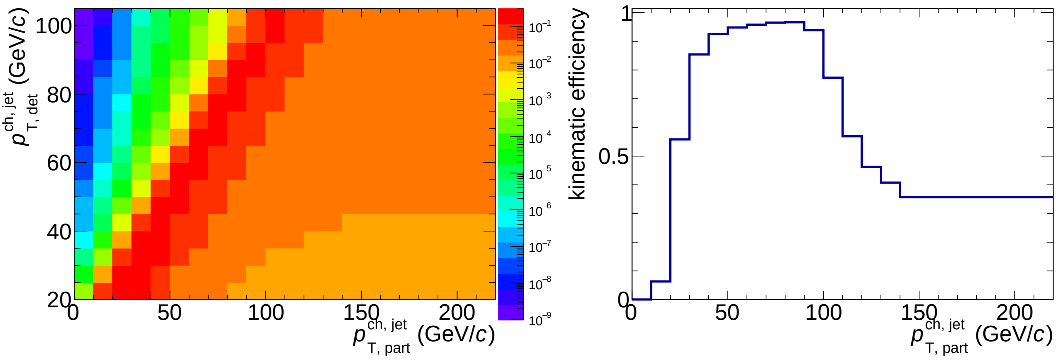

Figure 4.19: Combined response matrix after rebinning (left), from which kinematic efficiency (right) is obtained by projecting the matrix on its x-axis.

Carlo studies [108, 175]. The unfolded jet spectrum starts at 0 GeV/c to allow for feed-in of true jets with low $p_{\mathrm{T}}^{\mathrm{jet}}$. In addition, combinatorial jets which are not rejected by the jet area and leading charged particle requirements are migrated to momenta lower than the minimum measured $p_{\mathrm{T}}^{\mathrm{jet}}$. The unfolded solution ranges up to 200 GeV/c (0–5%) and 170 GeV/c (30–50%) to allow for migration of jets to a $p_{\mathrm{T}}^{\mathrm{jet}}$ higher than the maximum measured momentum. As the data points of the unfolded solution are strongly correlated for $p_{\mathrm{T}}^{\mathrm{jet}}$ outside the experimentally measured interval, $v_2^{\mathrm{ch\ jet}}$ will be reported only within the limits of the measured jet spectra.

Figure 4.19 shows a combined response matrix (left) that has been truncated to correspond to the ranges of measured and unfolded jet spectra. As a result of truncation, part of the true jet yield in the response matrix will not be reconstructed. The *kinematic efficiency* (Fig. 4.19, right) represents the fraction of the jet yield that can be affected by smearing within a $p_{\mathrm{T,chjet}}^{\mathrm{gen}}$ interval and is accounted for in the final results through the unfolding procedure.

4.5.4 Regularized unfolding

Solving Eq. 4.38 by simple inversion of $\mathbf{G_{m,t}}$ generally leads to non-physical results which oscillate wildly due to the statistical fluctuations of the measured jet yield [176, 177]. This type of behavior is shown in the following short example, which starts by discretizing Eq. 4.35

$$\mathbf{x}_i = \mathbf{R}_{ij}\mathbf{y}_j \tag{4.41}$$

with $\mathbf{x}_i$ a histogram with i bins (the measured distribution), $\mathbf{y}_j$ a histogram with j bins (the true distribution) and $\mathbf{R}_{ij}$ the response matrix. $\mathbf{x}_i$ is not what is seen in the detector, rather, $\mathbf{n}_i$ data points, subject e.g. Poisson statistics, are observed. Using the observed distribution in matrix inversion leads to the following relations

$$\mathbf{R}_{ij}^{-1}\mathbf{n}_i \to \mathbf{R}_{ij}^{-1}\mathbf{R}_{ij}\mathbf{y}_j \to \mathbf{y}_j + \sigma_j^{\mathbf{y}_j}. \tag{4.42}$$

In a simple example, where the response matrix represents e.g. efficiency ϵ,

$$\underbrace{\begin{pmatrix}0.8\\1\\0.9\end{pmatrix}}_{\epsilon} \qquad \underbrace{\begin{pmatrix}1\\2\\3\end{pmatrix}}_{\mathbf{n}} = \underbrace{\begin{pmatrix}0.8 & 0 & 0\\0 & 1 & 0\\0 & 0 & 0.9\end{pmatrix}}_{\mathbf{R}} \cdot \underbrace{\begin{pmatrix}?\\?\\?\end{pmatrix}}_{\mathbf{y}} \tag{4.43}$$

inverting $\mathbf{R}$ works and gives (omitting the variance of $\mathbf{y}$)

$$\underbrace{\begin{pmatrix} 1.25 & 0 & 0 \\ 0 & 1 & 0 \\ 0 & 0 & 1.111 \end{pmatrix}}_{\mathbf{R}^{-1}} \cdot \underbrace{\begin{pmatrix} 1 \\ 2 \\ 3 \end{pmatrix}}_{\mathbf{n}} = \underbrace{\begin{pmatrix} 1.25 \\ 2 \\ 3.333 \end{pmatrix}}_{\mathbf{y}}. \tag{4.44}$$

In practice, the bin size of a measurement is small compared to experimental resolution, i.e. the response matrix has off-diagonal terms (such as the response matrix of Fig. 4.19),

$$\underbrace{\begin{pmatrix} 0.8 \\ 1 \\ 0.9 \end{pmatrix}}_{\epsilon} \qquad \underbrace{\begin{pmatrix} 1 \\ 2 \\ 3 \end{pmatrix}}_{\mathbf{n}} = \underbrace{\begin{pmatrix} 0.5 & 0.3 & 0 \\ 0.3 & 0.4 & 0.3 \\ 0 & 0.4 & 0.5 \end{pmatrix}}_{\mathbf{R}} \cdot \underbrace{\begin{pmatrix} ? \\ ? \\ ? \end{pmatrix}}_{\mathbf{y}} \tag{4.45}$$

and which case matrix inversion gives

$$\underbrace{\begin{pmatrix} -16 & 30 & -18 \\ 30 & -50 & 30 \\ -24 & 40 & -22 \end{pmatrix}}_{\mathbf{R}^{-1}} \cdot \underbrace{\begin{pmatrix} 1 \\ 2 \\ 3 \end{pmatrix}}_{\mathbf{n}} = \underbrace{\begin{pmatrix} -10 & \pm & 293 \\ 20 & \pm & 382 \\ -10 & \pm & 338 \end{pmatrix}}_{\mathbf{y} \pm \sigma^{\mathbf{y}}} \tag{4.46}$$

which is in principle a correct (unbiased) estimator of $\mathbf{y}$, but is a wildly oscillating solution with large variances[k].

Unfolding via matrix inversion is generally not possible as a result of the resolution of the measurement. The unfolded solution therefore needs to be regularized, which means that, in order to reduce the variance of the unfolded result, a small systematic bias is introduced. In general this is done by introducing a penalty term (*regularization*) for large local curvatures associated with oscillations.

In this work, two regularized unfolding approaches are used: singular value decomposition (SVD) unfolding (the default approach) and χ^2 minimization (used as a systematic check, and to generate priors for the SVD unfolding). Both will briefly be discussed, starting at χ^2 minimization, as it most intuitively illustrates regularization.

4.5.4.1 χ^2 unfolding

The χ^2 method unfolds the spectrum by minimizing the difference between the measured and *refolded* spectrum, where the refolded spectrum is the convolution of the unfolded spectrum with the combined response matrix. Fluctuating solutions are suppressed by introducing a regularization term to the χ^2

$$\chi^2 = \underbrace{\sum_i \left(\frac{\mathbf{n}_i^{\text{refolded}} - \mathbf{n}_i^{\text{measured}}}{\sigma_i^{\text{measured}}} \right)^2}_{\text{unfolding}} + \beta \underbrace{P(\mathbf{n}_i^{\text{unfolded}})}_{\text{regularization}} \tag{4.47}$$

the relative importance of which is set by regularization *strength* β. $\mathbf{n}_{\text{refolded}}$ in Eq. 4.47 are the refolded data points, $\mathbf{n}_{\text{measured}}, \sigma_{\text{measured}}$ represent the measured points and their statistical

[k] See [177] for the calculation of the variances in Eq. 4.46.

uncertainties. When unfolding jet spectra [159], the regularization term is chosen such that it favors a power law distribution,

$$\chi^2 = \underbrace{\sum_i \left(\frac{\mathbf{n}_i^{\mathrm{refolded}} - \mathbf{n}_i^{\mathrm{measured}}}{\sigma_i^{\mathrm{measured}}} \right)^2}_{\text{unfolding}} + \underbrace{\beta \sum_i \left(\frac{\mathrm{d}^2 \log \mathbf{n}_i^{\mathrm{unfolded}}}{\mathrm{d} \log p_{\mathrm{T}}^2} \right)^2}_{\text{regularization}} \tag{4.48}$$

For unfolded solutions which deviate in shape from a power law, the regularization term in Eq. 4.48 will be large. Sensitivity to the regularization can systematically be studied by varying the magnitude of β.

4.5.4.2 Singular Value Decomposition

Singular value decomposition (SVD) is a general technique for factorizing matrices. In the SVD unfolding method, the unfolding problem is reduced to minimizing a system of linear equations by employing singular value decomposition. SVD unfolding can be performed in many different ways; the approach outlined in this section is taken from [178] and implemented in [179]. For the remainder of this section, boldface capitals are used to indicate matrices whereas boldface non-capitalized letters denote vectors. Italics are used to represent scalar values.

The SVD unfolding ansatz is similar to that of the χ^2 method insofar as the distance between the response matrix $\mathbf{G}$ multiplied by the unfolded result $\mathbf{w}$ (which, in the SVD unfolding method, is defined as the unfolded jet yield divided by a best estimate of the yield called a *prior*), and the measured data $\mathbf{n}$ must be found, whilst imposing some regularization criterion to suppress oscillating solutions. To do so, a term similar to Eq. 4.48 is minimized

$$\underbrace{(\tilde{\mathbf{G}}\mathbf{w} - \tilde{\mathbf{n}})^{\mathbf{T}}(\tilde{\mathbf{G}}\mathbf{w} - \tilde{\mathbf{n}})}_{\text{unfolding}} + \tau \cdot \underbrace{(\mathbf{C}\mathbf{w})^{\mathbf{T}}\,\mathbf{C}\mathbf{w}}_{\text{regularization}} \tag{4.49}$$

in which $^{\mathbf{T}}$ denotes a transpose matrix. Equation 4.49 is a system of linear equations. To give all equations equal weight, the system is *rescaled* by dividing the values in all columns by the uncertainty on the measured jet yield. Rescaled values are denoted by a tilde; rescaling is performed both for the measurement data (e.g. $\tilde{n}_i = n_i/\sigma_{n_i}$) and the response matrix $\tilde{\mathbf{G}}$.

The response matrix is multiplied by a 'best estimate' of the unfolded solution, the prior, before it is rescaled; in this way it contains the actual number of jets that were generated in bin j but measured in bin i, rather than conditional probabilities. In this work, both a PYTHIA jet yield and the unfolded spectrum that is generated by χ^2 minimization are used as priors. Vector $\mathbf{w}$ holds the unfolded result, which must eventually be multiplied by the prior to obtain the actual unfolded jet yield.

The unfolding term of Eq. 4.49 is identical in function to the first term on the right-hand side of Eq. 4.47 and means that χ^2 minimization is used to find a solution in which the difference between the refolded result and the measured spectra is minimal. The regularization term dictates that unfolded solution must not oscillate. When a realistic prior is chosen, $\mathbf{w}$ is a smooth set of points with little bin-to-bin variations, therefore the regularization term in Eq. 4.49 should be large when $\mathbf{w}$ is not smooth. The 'curvature' of $\mathbf{w}$ can be expressed as the sum of the squares of the second derivatives of $\mathbf{w}$, which has the simple form

$$\sum_i \left[(w_{i+1} - w_i) - (w_i - w_{i-1})\right]^2 . \tag{4.50}$$

and enters Eq. 4.49 as a multiplication of $\mathbf{w}$ by the curvature matrix $\mathbf{C}$,

$$\mathbf{C} = \begin{pmatrix} -1 & 1 & 0 & 0 & \cdots & \\ 1 & -2 & 1 & 0 & \cdots & \\ 0 & 1 & -2 & 1 & \cdots & \\ & & \cdots & & \cdots & \\ & & \cdots & 1 & -2 & 1 \\ & & \cdots & & 1 & -1 \end{pmatrix}. \tag{4.51}$$

Now that all components of Eq. 4.49 have been motivated, actual minimization via singular value decomposition can commence. Equation 4.49 can easily be written as a system of linear equations,

$$\begin{bmatrix} \tilde{\mathbf{G}} \\ \sqrt{\tau}\cdot \mathbf{C} \end{bmatrix} \mathbf{w} = \begin{bmatrix} \tilde{\mathbf{n}} \\ \mathbf{0} \end{bmatrix}. \tag{4.52}$$

which in principle is straightforward to solve, but has a solution for each value of τ.

A general (approximate) solution valid for any τ can be found by applying the method of *damped least squares* [180]. This method starts by making the regularization term proportional to the identity matrix $\mathbf{I}$[1], by taking out common factor $\mathbf{C}$

$$\begin{bmatrix} \tilde{\mathbf{G}}\mathbf{C}^{-1} \\ \sqrt{\tau}\cdot \mathbf{I} \end{bmatrix} \mathbf{C}\mathbf{w} = \begin{bmatrix} \tilde{\mathbf{n}} \\ \mathbf{0} \end{bmatrix} \tag{4.53}$$

and solving Eq. 4.52 for the non-regularized case $\tau = 0$. To do so, system 4.53 is rewritten using singular value decomposition (the aforementioned factorization into multiple matrices) of the left-hand side of the equation,

$$\tilde{\mathbf{G}}\mathbf{C}^{-1} = \mathbf{U}\mathbf{S}\mathbf{V}^{\mathbf{T}} \tag{4.54}$$

where $\mathbf{U}$, $\mathbf{V}$ are orthogonal matrices and $\mathbf{S}$ is a diagonal matrix with non-negative values s_i which are called the *singular values*. Defining

$$\mathbf{d} \equiv \mathbf{U}^{\mathbf{T}}\tilde{\mathbf{n}} \qquad \mathbf{z} \equiv \mathbf{V}^{\mathbf{T}}\mathbf{C}\mathbf{w} \tag{4.55}$$

so that the exact solution to $\mathbf{w}$ for $\tau = 0$ can be found through

$$\begin{aligned} \mathbf{G}\mathbf{C}^{-1}\mathbf{C}\mathbf{w} &= \tilde{\mathbf{n}} \\ \mathbf{U}\mathbf{S}\mathbf{V}^{\mathbf{T}}\mathbf{C}\mathbf{w} &= \tilde{\mathbf{n}} \\ \mathbf{U}\mathbf{S}\mathbf{z} &= \tilde{\mathbf{n}} \\ \mathbf{z} &= \mathbf{S}^{-\mathbf{1}}\mathbf{U}^{\mathbf{T}}\tilde{\mathbf{n}}. \end{aligned} \tag{4.56}$$

Because $\mathbf{S}$ is a diagonal matrix,

$$\mathbf{S}^{-\mathbf{1}} = \frac{1}{s_i} \tag{4.57}$$

and

$$z_i^{\tau=0} = \frac{d_i}{s_i}. \tag{4.58}$$

[1] As $\mathbf{C}$ is degenerate (the sum of the values in each row or column is 0), it can only be inverted approximately by adding a small diagonal component $\mathbf{C}_{ii} \rightarrow \mathbf{C}_{ii} + \xi$ where $\xi \approx 10^{-4}$

The unfolded jet yield is found by multiplying $\mathbf{w}$ by the prior, but becomes unstable for small values of s_i at which z_i diverges.

Following the dampened least square formalism, the unfolded solution can be regularized by introducing the regularization parameter τ to $\mathbf{d}$ following

$$d_i^{\tau \neq 0} = d_i \left(\frac{s_i^2}{s_i^2 + \tau} \right), \tag{4.59}$$

so that

$$z_i^{\tau \neq 0} = \frac{d_i s_i}{s_i^2 + \tau}, \tag{4.60}$$

and the regularized solution $\mathbf{w}^{\tau \neq 0}$ is given by

$$\mathbf{w}^{\tau \neq 0} = \mathbf{C}^{-1} \mathbf{V} \mathbf{z}^{\tau \neq 0}. \tag{4.61}$$

When s_i in Eq. 4.60 is very small, τ regularizes singularities by suppressing divergent behavior of z_i.

The optimal regularization strength (i.e. the magnitude of τ) can be determined from the distribution of the variable $\log |d_k|$. Only the first few terms of this distribution are expected to be significant; the rest of the values have zero mean and unit variance (this unit variance is a result of the rescaling of the equations). If the regularization parameter τ is be chosen as

$$\tau = s_k^2, \tag{4.62}$$

which means that it is equal to the square of the k^{th} singular value of the system where k is chosen as the element for which $\log |d_i|$ is no longer significant, divergences in Eq. 4.59 are suppressed. Examples of singular values s_i and $\log |d_i|$ distributions are shown in Ch. 6.

4.6 Summary

The analysis steps described in the previous sections are summarized in Fig. 4.20. The largest experimental challenge in the $v_2^{\text{ch jet}}$ analysis is the separation of the jet signal from the background of mostly low-p_{T} particles from the underlying event and from unrelated scatterings that take place in the collision. The jet energy is corrected on a jet-by-jet basis using an estimate of the background transverse momentum density which takes into account the dominant flow harmonics v_2 and v_3 of the background event-by-event. The coefficient $v_2^{\text{ch jet}}$ is obtained from p_{T}-differential jet yields measured with respect to the experimentally accessible event plane $\Psi_{\text{EP, 2}}$, which is reconstructed at forward rapidities ($2.8 < \eta < 5.1$ and $-3.7 < \eta < -1.7$).

The reported $v_2^{\text{ch jet}}$ has been corrected back to the azimuthal anisotropy with respect to the underlying symmetry plane Ψ_2 by applying an event plane resolution correction. Jets are reconstructed at mid-rapidity ($|\eta_{\text{jet}}| < 0.7$) using charged constituent tracks with momenta $0.15 < p_{\text{T}} < 100$ GeV/c, and are required to contain a charged hadron with $p_{\text{T}} \geq 3$ GeV/c. The in-plane and out-of-plane jet spectra are unfolded independently to take into account detector effects and remaining azimuthally-dependent fluctuations in the underlying event transverse momentum density. The jet spectra are corrected back to particle-level jets consisting of only primary charged particles from the collision.

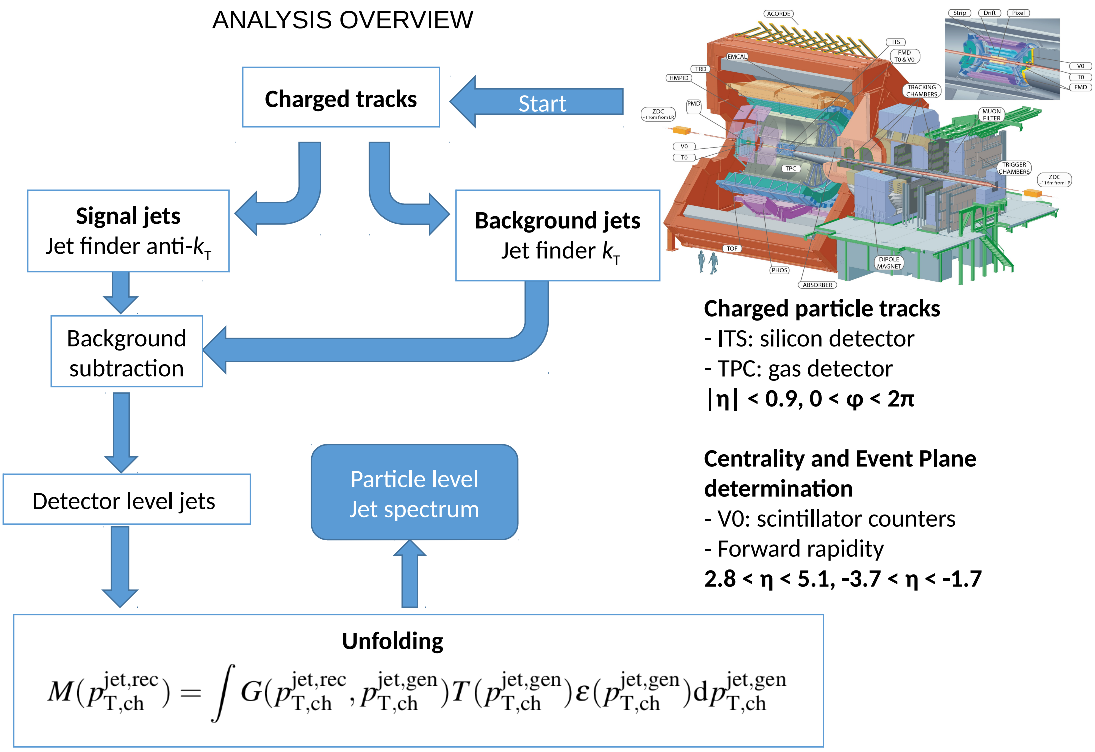

Figure 4.20: Analysis summary. The particle level jet spectra are measured independently in the in-plane and out-of-plane orientation.

5 | Closure tests

In the previous chapters corrections to $v_2^{\text{ch jet}}$ for experimental effects were outlined, such as the finite event plane resolution and detector effects on the jet energy scale as well as the effects of the uncorrelated background and its fluctuations using the corrections outlined in § 4.2, §4.3 and § 4.5. Closure tests are performed to validate the efficaciousness of these corrections. Two types of tests are performed, one based purely on simulated events (§ 5.1) and a (more) data driven approach (§ 5.2). Uncertainties and biases that cannot experimentally be removed are treated as systematic uncertainties in Ch. 6.

5.1 Thermal model studies

To test if possible biases from the underlying event are effectively removed by incorporating hydrodynamic flow in the underlying event description and by unfolding the in-plane and out-of-plane jet spectra independently, Monte Carlo events are generated in which both v_n and $v_2^{\text{ch jet}}$ can be controlled independently.

5.1.1 Event generation

The *thermal model* that is used, following the approach suggested in [175], generates events with both a 'soft' component (to simulate the underlying event) and a 'hard' component (mimicking jet production). The p_{T} distribution of particles of the soft background is modeled as a Boltzmann distribution as function of p_{T} with a mean of $\langle p_{\text{T}} \rangle = 0.67$ GeV/c. The 'jet' distribution follows a power law function $\propto {p_{\text{T}}}^{-5}$, scaled by a factor that represents $T_{\text{AA}}\ \text{d}\sigma/dp_{\text{T}}$, where T_{AA} is the nuclear overlap function and $\text{d}\sigma/\text{d}p_{\text{T}}$ is the charged jet cross-section in pp collisions. Rather than modeling (and reconstructing) parton showers, jets do not undergo fragmentation but are represented by single particles.

Events of fixed multiplicity $M = 2200$, are generated by drawing a random value from a single distribution which comprises both the hard and soft component of the spectrum for M times,

$$P(p_{\text{T}}) = ab^2 p_{\text{T}} \exp\left(-bp_{\text{T}}\right) + \begin{cases} 0 & p_{\text{T}} \leq 1\text{GeV}/c \\ \left(\frac{1}{1+\exp(-[p_{\text{T}}-e]/f)}\right)\left(\frac{1}{c{p_{\text{T}}}^d}\right) & p_{\text{T}} > 1\text{GeV}/c \end{cases} . \tag{5.1}$$

The total particle spectrum, as well as the independent contributions of the soft and hard component, is shown in Fig. 5.1. Parameters a through f are tuned so that the measured jet spectra and width and mean of the δp_{T} distributions as measured in the model agree to those

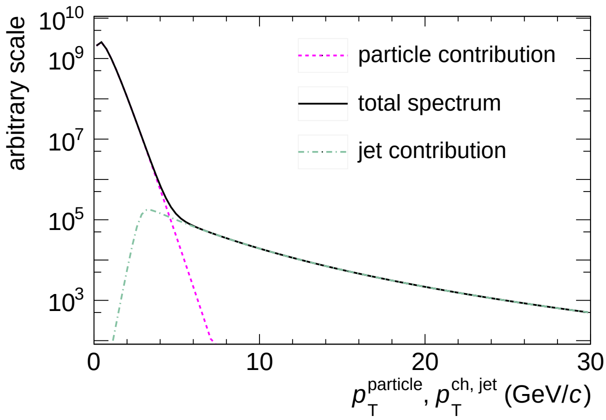

Figure 5.1: Total particle spectrum that is used in the model (solid line) and independent contributions of the soft and hard component (dashed lines). The total spectrum is the sum of the independent contributions.

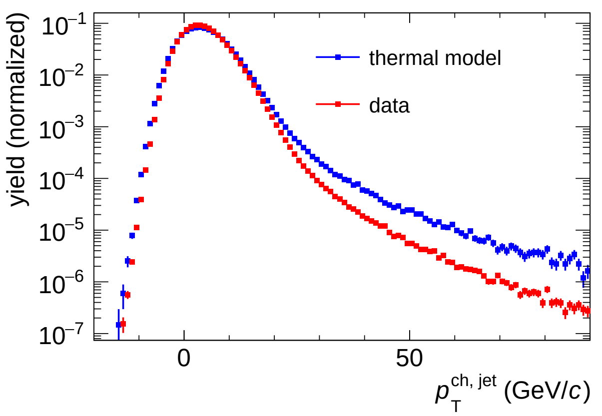

Figure 5.2: Normalized jet yield in data (red) and model (blue). The background distributions are qualitatively similar to those obtained from data. Statistical uncertainties only, yields are not unfolded.

observables in data, as can be seen in Fig. 5.2, where the thermal jet yield is shown in blue and a jet yield in central collisions (prior to unfolding) in red, and by comparing Figs 5.3 to 4.13. For each track, η and φ are chosen randomly from uniform distributions. The multiplicity ($M = 2200$) is chosen to simulate mid-central events, where the contribution of the underlying event to the measured jet energy is expected to be large, as well as the number and energy of purely combinatorial jets.

The initial azimuthal distribution of tracks in the thermal model is uniform. To introduce v_n harmonics to the 'underlying event', or to add non-zero $v_2^{\mathrm{ch\ jet}}$, the azimuthal distribution of the generated tracks is modified following[a]

$$\varphi = \varphi_0 - v_2 \sin\left[2\left(\Delta\varphi_2\right)\right], \tag{5.6}$$

which means that v_2 can be introduced to thermal model events by, for each track in an event with initial azimuthal angle φ_0,

- solving Eq. 5.6 for φ;
- and substituting the track's azimuthal angle $\varphi_0 \to \varphi$.

Fluctuations in the initial geometry of heavy-ion collisions lead to fluctuations of the generated v_n harmonics, as explained in § 2.4.1. These fluctuations are incorporated in the model by sampling v_n not as a static value, but rather following a model [181] of Gaussian fluctuations with probability distribution

$$f(v_n'|v_n, \sigma) = \frac{1}{\sigma\sqrt{2\pi}} \exp\left[-\frac{(v_n' - v_n)^2}{2\sigma^2}\right]. \tag{5.7}$$

which gives the probability to find fluctuation v_n' given the mean v_n and standard deviation of fluctuations σ. In practice, fluctuations are introduced by drawing a random number r between 0 and 1, and using this number to generate a fluctuation from the inverse of the cumulative distribution function,

$$v_n' \to v_n + \sqrt{2}\sigma\mathrm{erf}^{-1}\left(2r - 1\right) \tag{5.8}$$

where erf^{-1} is the inverse error function (which is single valued in the domain -1, 1). In this test, fluctuations of 25% ($v_n/4$) are introduced in the 'soft' part of the spectrum.

The procedure to generate azimuthal modulations (Eq. 5.6) allows for the introducing of p_{T} dependent v_2 harmonics. Since particle production in the thermal model is governed by one single distribution there is no clear separation between jets and underlying event (as the Boltzmann distribution decreases asymptotically to 0 for $p_{\mathrm{T}} \to 0$), v_2 and $v_2^{\mathrm{ch\ jet}}$ can be introduced semi-independently by imposing the requirement that the hydrodynamic flow of the underlying event decreases to 0 at relatively low momenta, while at the same time generating $v_2^{\mathrm{ch\ jet}}$ for only sufficiently energetic particles.

[a] Equation 5.6 is derived as follows. The initial, uniform azimuthal distribution of tracks has the form

$$\frac{\mathrm{d}N}{\mathrm{d}\varphi_0} = \frac{1}{2\pi}. \tag{5.2}$$

To introduce v_2, $\mathrm{d}N/\mathrm{d}\Delta\varphi_2$ is expressed as the familiar Fourier expansion,

$$\frac{\mathrm{d}N}{\mathrm{d}\Delta\varphi_2} = \frac{1}{2\pi}\left(1 + v_2\cos\left[2\left(\Delta\varphi_2\right)\right]\right) \tag{5.3}$$

which can be re-written, using φ_0 from Eq. 5.3, as

$$\frac{\mathrm{d}N}{\mathrm{d}\Delta\varphi_2} = \frac{\mathrm{d}N}{\mathrm{d}\varphi_0}\frac{\mathrm{d}\varphi_0}{\mathrm{d}\Delta\varphi_2} = \frac{1}{2\pi}\frac{\mathrm{d}\varphi_0}{\mathrm{d}\Delta\varphi_2}. \tag{5.4}$$

From Eq. 5.3 and Eq. 5.4 the relation

$$\int\left(1 + 2\cos\left[\Delta\varphi_2\right]\right)\mathrm{d}\Delta\varphi_2 = \int\frac{\mathrm{d}\varphi_0}{\mathrm{d}\Delta\varphi_2}\mathrm{d}\Delta\varphi_2 \tag{5.5}$$

is obtained. Solving the integrals in Eq.5.5 gives the expression of Eq. 5.6.

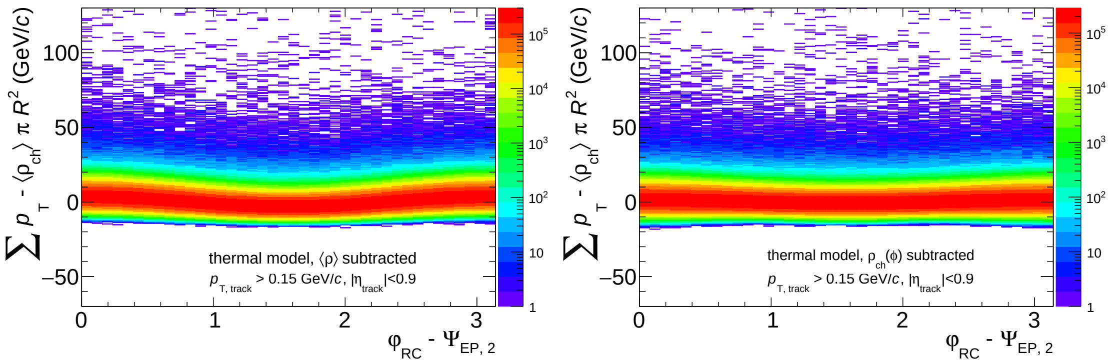

Figure 5.3: The δp_{T} distribution (Eq. 4.29) from the random cone (RC) procedure as function of cone azimuthal angle φ_{RC} relative to the event plane for thermal events. Left: the azimuthally-averaged background $\langle\rho_{\mathrm{ch}}\rangle$ has been subtracted; right: the azimuthally dependent $\rho_{\mathrm{ch}}(\varphi)$ from an event-by-event fit of the p_{T}-density with Eq. 4.27.

5.1.2 Results: $v_2^{\mathrm{ch\ jet}}$ in the presence of hydrodynamic flow

To test if the modulation of the underlying event does not bias the measured $v_2^{\mathrm{ch\ jet}}$, 6×10^6 events are generated in which the underlying event exhibits strong hydrodynamic flow, but jet production itself is isotropic in azimuth. To achieve this, p_{T} differential v_2 is sampled from

$$v_2(p_{\mathrm{T}}) = \begin{cases} 0.07 & p_{\mathrm{T}} < 3\mathrm{GeV}/c \\ 0.07 - (p_{\mathrm{T}} - 3) \times 0.035 & 3 < p_{\mathrm{T}} < 5\mathrm{GeV}/c \\ 0 & \mathrm{else} \end{cases} \tag{5.9}$$

The corresponding δp_{T} distributions, obtained from these events by using either $\langle\rho_{\mathrm{ch}}\rangle$ or $\rho_{\mathrm{ch}}(\varphi)$ to evaluate $\rho_{\mathrm{ch\ local}}$ in Eq. 4.15, are shown as function of $\Delta^{\mathrm{EP}}\varphi_2$ in Fig. 5.3. The left panel shows a strong cosine modulation in the mean of the δp_{T} distribution, similar in magnitude to that observed in data (Fig. 4.13).

Figure 5.4 (right) shows $v_2^{\mathrm{ch\ jet}}$ values that are obtained prior to unfolding the jet spectra in the in-plane and out-of-plane orientation independently. The blue line is obtained by using $\rho_{\mathrm{ch}}(\varphi)$ in the evaluation of $\rho_{\mathrm{ch\ local}}$ in Eq. 4.15, the red line by using $\langle\rho_{\mathrm{ch}}\rangle$. Not taking into account the hydrodynamic flow of the underlying event (i.e. using $\langle\rho_{\mathrm{ch}}\rangle$ as parametrization both in the jet background subtraction and calculation of δp_{T}) leads to a strong non-zero $v_2^{\mathrm{ch\ jet}}$ (weighted arithmetic mean of 0.11 for $p_{\mathrm{T}} > 40$ GeV/c), generated fully by v_2 of combinatorial jets and background v_2, prior to unfolding over the entire p_{T} range in which $v_2^{\mathrm{ch\ jet}}$ is measured. When hydrodynamic flow of the underlying event *is* taken into account, the effect of independent in-plane and out-of-plane unfolding on $v_2^{\mathrm{ch\ jet}}$ is limited (and has a weighted arithmetic mean of 0.02 for $p_{\mathrm{T}} > 40$ GeV/c; a further exploration of the effect of unfolding on the change in $v_2^{\mathrm{ch\ jet}}$ is given in Ch. 6).

$v_2^{\mathrm{ch\ jet}}$, obtained by following the procedure outlined in Ch. 4, is shown in Fig. 5.4 (left; systematic uncertainties (boxes) are treated in Ch. 6). The red dashed line in the same figure represents the p_{T} differential input v_2 of the thermal events. Coefficient $v_2^{\mathrm{ch\ jet}} = 0$ over the full momentum range in which the jet spectrum is unfolded meaning that the initial $v_2^{\mathrm{ch\ jet}}$ is recovered by the analysis procedure.

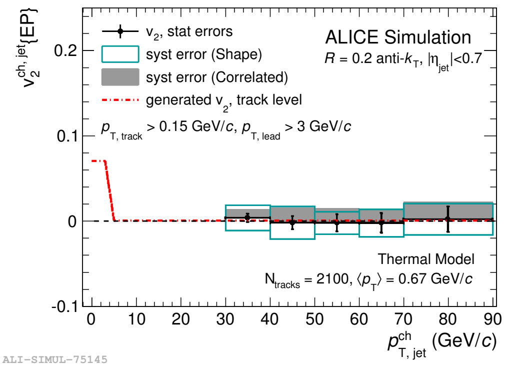

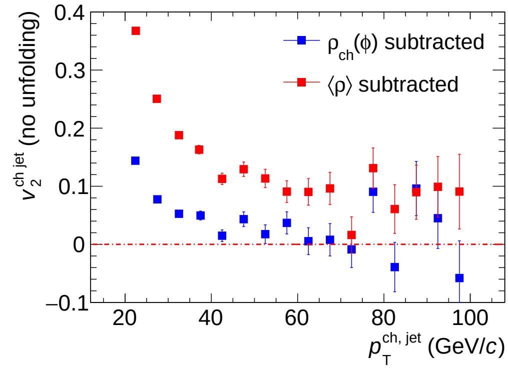

Figure 5.4: Left: $v_2^{\text{ch jet}}$ in thermal model events obtained by following the procedure given in Ch. 4. Systematic uncertainties (boxes) are treated in Ch. 6; the red dashed curve is the v_2, $v_2^{\text{ch jet}}$ used as input for the thermal events. Right: $v_2^{\text{ch jet}}$ values that are obtained *prior* to unfolding the jet spectra in the in-plane and out-of-plane orientation independently. The blue points are obtained by using $\rho_{\text{ch}}(\varphi)$ in the evaluation of $\rho_{\text{ch local}}$ in Eq. 4.15, the red points by using $\langle\rho_{\text{ch}}\rangle$.

5.1.2.1 Using unfolding for subtraction of v_n

In the analysis procedure of § 4.4, hydrodynamic flow is taken into account on an event-by-event basis in the description of the underlying event. As can be seen in Fig. 5.3, hydrodynamic flow contributes strongly to the measured $v_2^{\text{ch jet}}$ prior to unfolding when not taken into account in the underlying event description.

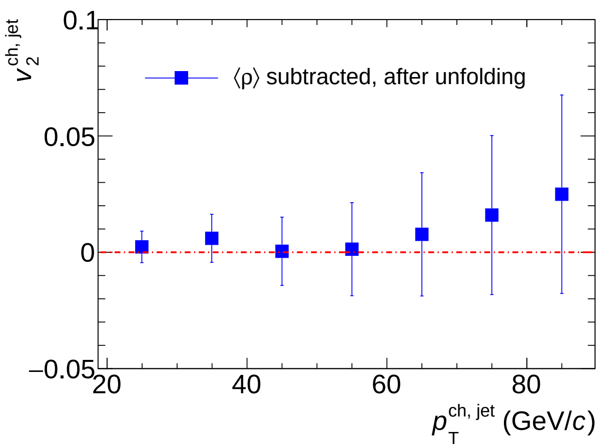

Figure 5.5: $v_2^{\text{ch jet}}$ obtained from unfolding jet spectra that are constructed from jet energies which are corrected using the φ-independent ($\langle\rho_{\text{ch}}\rangle$) underlying event transverse momentum density. Analysis performed on thermal events; as input $v_2^{\text{ch jet}}$, Eq. 5.9 is used (given by the red dashed line). Statistical uncertainties only.

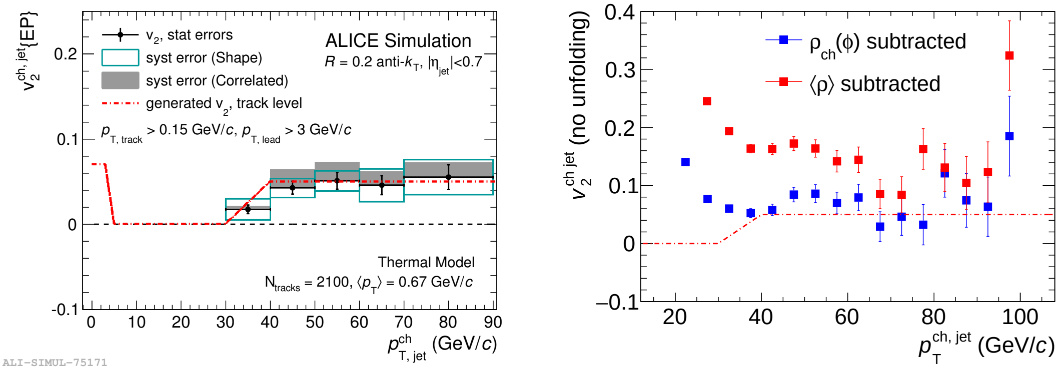

Figure 5.6: Left: $v_2^{\text{ch jet}}$ in thermal model events obtained by following the procedure given in Ch. 4. Systematic uncertainties (boxes) are treated in Ch. 6; the red dashed curve is the v_2, $v_2^{\text{ch jet}}$ used as input for the thermal events. Right: $v_2^{\text{ch jet}}$ values that are obtained prior to unfolding the jet spectra in the in-plane and out-of-plane orientation independently. The blue points are obtained by using $\rho_{\text{ch}}(\varphi)$ in the evaluation of $\rho_{\text{ch local}}$ in Eq. 4.15, the red points by using $\langle \rho_{\text{ch}} \rangle$.

Hydrodynamic flow harmonics v_n *can* also be removed from the measured $v_2^{\text{ch jet}}$ by unfolding alone, as is illustrated in Fig. 5.5. For this figure, the unmodulated underlying event description $\langle \rho_{\text{ch}} \rangle$ is used both in measuring $v_2^{\text{ch jet}}$ and in quantifying the background fluctuations response (Fig. 5.3, left).

Unfolding in this case is difficult, as the background fluctuations response matrices are off-diagonal and wide, but still the original input of zero $v_2^{\text{ch jet}}$ is retrieved - albeit with large statistical uncertainties - indicating that even in an 'extreme' scenario where unfolding has to compensate for the entire contribution of background flow to the modulation in the azimuthal jet distribution, $v_2^{\text{ch jet}}$ is properly recovered.

5.1.2.2 Non-zero $v_2^{\text{ch jet}}$ in the presence of hydrodynamic flow

To test if *non-zero* $v_2^{\text{ch jet}}$ can be resolved in the presence of strong flow of the underlying event, a second set of events is generated, in which also the jet orientation has a preferred direction with respect to the reaction plane. To achieve this, v_2 is sampled from

$$v_2(p_{\text{T}}) = \begin{cases} 0.07 & & p_{\text{T}} & < 3\text{GeV}/c \\ 0.07 - (p_{\text{T}} - 3) \times 0.035 & 3 < & p_{\text{T}} & < 5\text{GeV}/c \\ (p_{\text{T}} - 30) \times 0.005 & 30 < & p_{\text{T}} & < 40\text{GeV}/c \\ 0.05 & & p_{\text{T}} & > 40\text{GeV}/c \\ 0 & & \text{else} & \end{cases}, \tag{5.10}$$

meaning that $v_2^{\text{ch jet}}$ is non-zero for $p_{\text{T}}^{\text{jet}} > 30$ GeV/c. Figure 5.6 shows $v_2^{\text{ch jet}}$ that also in this case, the input $v_2^{\text{ch jet}}$ values are recovered correctly by the analysis.

5.2 Embedding studies

To validate the analysis method in real data, isotropically emitted jets are embedded into Pb–Pb events. As these jets, generated by PYTHIA, have no preferred orientation, $v_2^{\text{ch jet}} = 0$, while the heavy-ion underlying event has non-zero azimuthal modulation, which will generate a difference between the in-plane and out-of-plane jet yield before correcting for the underlying event and its fluctuations, as shown in § 5.1.

5.2.1 Embedding and matching

The embedding ansatz is simple:

- For each (real) Pb–Pb event, a minimum bias PYTHIA event is generated following the $p_{\mathrm{T}}^{\text{hard}}$ weighting procedure outlined in § 3.4;
- Tracks of the PYTHIA event are added to the Pb–Pb event (*embedding*), so that a *combined* event is obtained. Analysis is performed on these combined events;
- Jets in the combined event are matched to jets in the original PYTHIA jets. As the original PYTHIA jets have no preferred azimuthal direction (the emission is isotropic in azimuth, $v_2^{\text{ch jet}} = 0$), the matched jets should, after correction for effects of the underlying event, also have $v_2^{\text{ch jet}} = 0$.

A key aspect of embedding studies is matching the initial PYTHIA jets to jets that are reconstructed in the combined event. Matching is, in a first step, done geometrically, which starts with performing jet finding simultaneously on the PYTHIA and combined event. If jets in PYTHIA and combined events are emitted in the same η, φ interval, they are geometrically matched. This proximity criterion is satisfied when

$$\sqrt{(\eta_{\text{jet, PYTHIA}} - \eta_{\text{jet, combined}})^2 + (\varphi_{\text{jet ,PYTHIA}} - \varphi_{\text{jet, combind}})^2} < R \tag{5.11}$$

where R is the jet resolution parameter. In this first matching step, all PYTHIA and combined event jet pairs are matched. Geometric matching alone however leads to a situation in which one PYTHIA jet can be matched to multiple jets in the combined event, and vice versa. In a second matching step, a bijection from the set of PYTHIA jets to the set of combined jets is made, by preferring pairs in which the distance between the PYTHIA and combined jet is minimal.

The 'purity' of the matched jet sample is controlled by requiring that a matched jet contains at least 60% of the p_{T} of the PYTHIA jet to which it is matched. This criterion ensures that a matched jet truly originates from a PYTHIA jet, rather than being a combinatorial jet which is by chance reconstructed at the same location. Figure 5.7 shows the ratio of the matched jet p_{T} to the PYTHIA jet p_{T} (red) and the fraction of p_{T} of the original jet that is recovered in the matched jet (blue). The jet selection criteria of the matched jets are equal to those in the data analysis (see § 4.2).

5.2.2 Results: $v_2^{\text{ch jet}}$ of embedded jets

Asides from testing the general validity of the analysis method, embedding tests whether or not the orientation of the jet axis (in this exercise of the PYTHIA jets) in reconstruction is altered by the presence of underlying event - something the analysis method cannot correct for since Eq. 4.15 can only change the *magnitude* of the jet p_{T} but not the *orientation* of the jet axis (for that, a component-wise correction in four-momentum would be necessary).

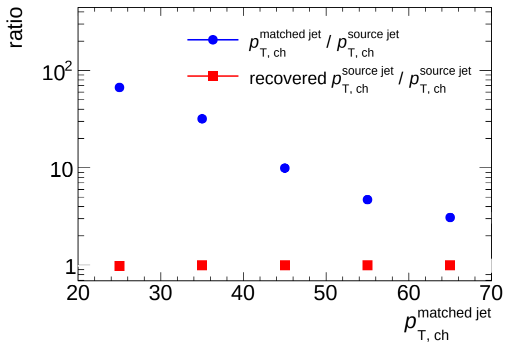

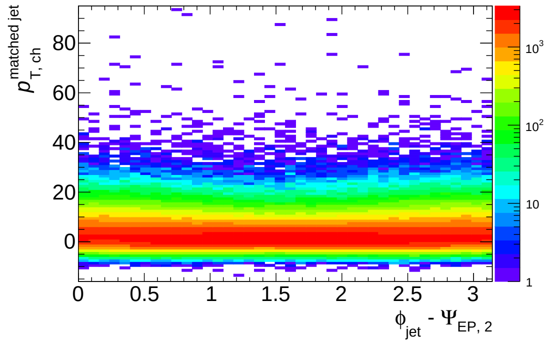

Figure 5.7: Left: p_{T}-differential ratio of the matched jet p_{T} to the PYTHIA jet p_{T} (blue) and the p_{T}-differential fraction of p_{T} of the original PYTHIA jet that is recovered within the matched jet (red). Right: distribution of matched jet p_{T} as function of the relative azimuthal angle $\Delta^{\mathrm{EP}}\varphi_2$ between jet angle φ_{jet} and the combined events after subtraction of flow-modulated underlying event energy.

Figure 5.7 (right) shows the distribution of matched jet p_{T} as function of $\Delta^{\mathrm{EP}}\varphi_2$ in the combined events. It should be noted that the event plane angles of the combined events do not change under embedding as the PYTHIA tracks are generated only within the central barrel acceptance, whereas the event plane angles are evaluated in the V0 system.

Coefficient $v_2^{\mathrm{ch\ jet}}$ of matched jets, prior to unfolding and using the ϕ-independent underlying event description $\langle\rho_{\mathrm{ch}}\rangle$, is shown as the red dashed line in Fig. 5.8 (left). The contribution of the underlying event to the width of the p_{T} distribution of matched jets is striking; the strong non-zero $v_2^{\mathrm{ch\ jet}}$ of the red line is a bias from the azimuthal modulation of the momentum density of the underlying event. The blue line shows $v_2^{\mathrm{ch\ jet}}$ after subtraction of the flow modulated underlying event contribution to the matched jet p_{T}, which is still non-zero due to background fluctuations.

The $v_2^{\mathrm{ch\ jet}}$ of matched jets after unfolding is given in Fig. 5.8 (right) and equals 0 over the entire p_{T} range, meaning that the initial $v_2^{\mathrm{ch\ jet}}$ values are correctly reconstructed.

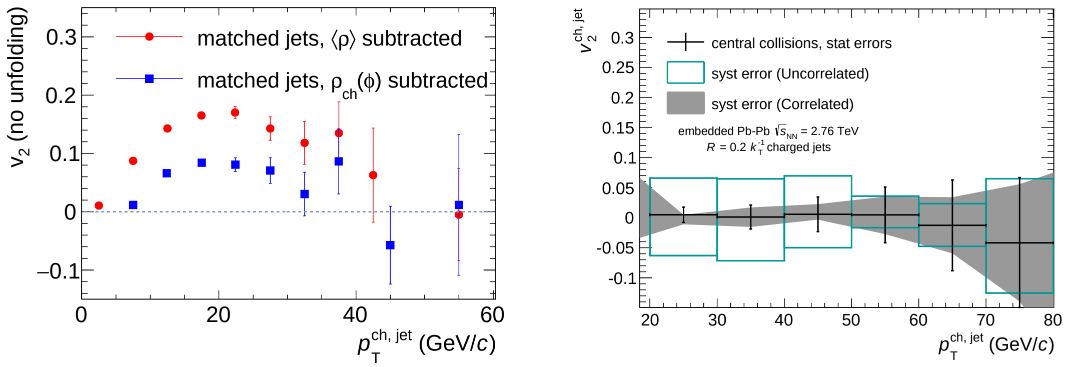

Figure 5.8: Left: $v_2^{\text{ch jet}}$, prior to unfolding, using either a flow-modulated (blue) or φ-independent (red) underlying event description. Right: coefficient $v_2^{\text{ch jet}}$ for matched jets in combined events. Boxes indicate systematic uncertainties; details can be found in Ch. 6.

6 | Systematic uncertainties

Uncertainties in the corrections on $v_2^{\text{ch jet}}$ measurement that are outlined in § 4.2–4.5 are treated as systematic uncertainties. This chapter explains how the nominal measurement is chosen (§ 6.2), what are the sources of systematic uncertainties (§ 6.3) and how systematic uncertainties are assigned and propagated (§ 6.1 and parts of § 6.3).

6.1 Propagation of uncertainties

Coefficient $v_2^{\text{ch jet}}$ is derived from the p_{T} differential jet yields N_{in} and N_{out}, with negligible uncertainty on the event plane resolution $\mathcal{R}_2$. Uncertainties - statistical or systematic - are therefore propagated to $v_2^{\text{ch jet}}$ from the uncertainties on N_{in} and N_{out} (with the exception of the unfolding uncertainty, as treated in § 6.3.3.1, that is estimated directly from $v_2^{\text{ch jet}}$) using partial derivatives of Eq. 4.1.

Any function $f(a, b)$ that is continuous in the neighborhood of a and b, and has continuous derivatives of the first and second order with respect to a and b, has a limiting normal distribution[a] with mean E and variance σ^2 described by the well known expressions

$$\begin{aligned} E_{f(a,b)} &\approx f(a,b)\big|_{a,b} \\ \sigma^2_{f(a,b)} &\approx \left.\frac{\partial f}{\partial a}\right|^2_{a,b} \sigma_a^2 + \left.\frac{\partial f}{\partial b}\right|^2_{a,b} \sigma_b^2 + 2 \left.\frac{\partial f}{\partial a}\frac{\partial f}{\partial b}\right|_{a,b} \sigma_{ab} \end{aligned} \tag{6.1}$$

where $|_{a,b}$ indicates that the function is evaluated at a, b and σ_a^2 and σ_b^2 variances of a, b and $\sigma_{a,b}$ the concomitant covariance. The variance and covariances are related by the Pearson correlation coefficient

$$\rho_{a,b} = \frac{\sigma_{a,b}}{\sigma_a \sigma_b} \tag{6.2}$$

which ranges from 0 (no correlation between variables a and b) to $\pm$ 1 (variations in a and b are fully (anti-)correlated).

Using Eq. 4.1 as $f(a, b)$ with variables N_{in}, N_{out}, and variances $\sigma^2_{N_{\text{in}}}$, $\sigma^2_{N_{\text{out}}}$, the variance of

[a] A proof of this method can be found following §28.4 in [182], approximate equalities ($\approx$) are used in Eq. 6.1 to indicate that these are leading terms of an expansion.

$v_2^{\text{ch jet}}$ can be expressed as[b]

$$\sigma^2_{v_2^{\text{ch jet}}} = \left(\frac{1}{\mathcal{R}_2}\frac{\pi}{4}\right)^2 \left(\frac{4{N_{\text{out}}}^2}{(N_{\text{in}}+N_{\text{out}})^4}\sigma^2_{N_{\text{in}}} + \frac{4{N_{\text{in}}}^2}{(N_{\text{in}}+N_{\text{out}})^4}\sigma^2_{N_{\text{out}}} - \frac{8N_{\text{out}}N_{\text{in}}}{(N_{\text{in}}+N_{\text{out}})^4}\sigma_{N_{\text{in}}}\sigma_{N_{\text{out}}}\rho_{N_{\text{in}},N_{\text{out}}}\right). \tag{6.3}$$

Systematic uncertainties on $v_2^{\text{ch jet}}$ are grouped into two categories, *shape* and *correlated*, based on their point-to-point correlation (as will be detailed in § 6.3). This correlation however should *not* be confused with the correlation coefficient $\rho_{N_{\text{in}},N_{\text{out}}}$ in Eq. 6.3, which governs the strength between correlated changes of N_{in} and N_{out}; both shape uncertainties and correlated uncertainties have contributions which lead to correlated changes in N_{in} and N_{out}.

6.1.1 Resampling and interference from statistical uncertainties

A general approach to finding systematic uncertainties is selecting a measurement which is deemed the most reliable (the nominal measurement) and comparing the results of this measurement to the results of alternative measurement which are obtained by introducing a variation in the analysis setup. If these variations lead to a different analysis outcome (not as a result of *chance* (statistical effects) but rather of inaccuracies in the measurement or assumptions in the analysis which cannot be removed), they reflect inaccuracies in the analysis or corrections which should be covered by the quoted uncertainties.

Finding systematic uncertainties therefore starts by asking the question: is a given parameter, used in the nominal measurement, the *only* valid choice, or is it based on some assumption and is there an alternative measurement which should also give a valid answer? And if so, does this alternate measurement give a *statistically compatible* outcome, or does it *deviate significantly* from the nominal measurement? *Only* if the latter is true, a systematic uncertainty should be assigned.

In tests where a comparison between a nominal measurement m and a *single* variation v is made, the ratio of m to v is used as a measure of deviation. Establishing whether or not a deviation from unity is significant, requires accurate propagation of the (statistical) uncertainties on m and v which is generally not possible as the covariance $\sigma_{m,v}$ is not known. To overcome this, a data driven approach to estimating the statistical uncertainty on the ratio of m to v is suggested, based on *resampling*. The resampling procedure starts by

- Constructing (*resampling*) a new nominal measurement, m', by, for each p_{T} interval in m with N jets and statistical uncertainty σ_{N}, drawing a random number N' from a Gaussian distribution with mean N and width σ_{N}. The resampled measurement m' in each p_{T} interval is then N' with uncertainty $\sqrt{N'}$;
- In a similar way, alternate measurement v is resampled to v';
- Assuming $m(m')$ and $v(v')$ are obtained prior to unfolding, unfolding is performed and Eq. 4.1 is evaluated using m' and v';
- Compare $v_2^{\text{ch jet}}$ obtained from the resampled nominal measurement m' and resampled alternate measurement v' by taking the ratio of $v_2^{\text{ch jet}}|_{m'}$ to $v_2^{\text{ch jet}}|_{v'}$;

[b] For readability, p_{T} dependence is omitted in Eq. 6.3, as well as in other expressions in this chapter. p_{T} dependence is however implied in all *measurable* quantities, i.e. $\sigma^2_{v_2^{\text{ch jet}}}(p_{\text{T}})$, $N_{\text{in}}(p_{\text{T}})$, $\sigma^2_{N_{\text{in}}}(p_{\text{T}})$, etc.

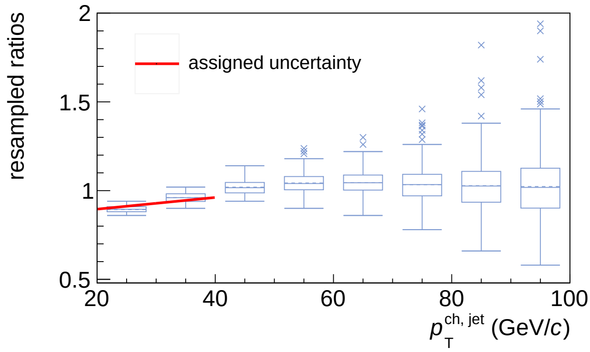

Figure 6.1: Boxplot of p_{T}-dependent distributions of ratio of alternate to nominal measurements. In this particular example, a systematic effect would be derived from evaluating $f(p_{\mathrm{T}})$ (red line) and assigned up to 40 GeV/c (see caption of Fig. 4.7 for an explanation of the plotting format).

- Repeat the preceding steps multiple times in each p_{T} to obtain distributions of $v_2^{\text{ch jet}}|_{m'} / v_2^{\text{ch jet}}|_{v'}$. The width of such a distribution is the true statistical uncertainty on the ratio of m to v obtained without making assumptions on the correlation between m and v; to resolve a systematic uncertainty from the difference between m and v, this statistical uncertainty must be smaller than the deviation of the ratio from unity.

An illustration of the resampling procedure is given in Fig. 6.1, where a boxplot of distributions of the ratio of alternate to nominal measurements is shown. The red line indicates the assigned systematic uncertainty in this example.

The systematic uncertainty is extracted (as will be done in § 6.3) by fitting a function of the form of

$$f(p_{\mathrm{T}}) = (p_{\mathrm{T}} > a) \times (b \times p_{\mathrm{T}} + c) + (p_{\mathrm{T}} <= a) \times d \tag{6.4}$$

to the ratio of alternate to nominal measurement, which means that a linear dependence on p_{T} is allowed up to a given value a, after which the effect is taken to be constant (d), motivated by the fact that for most systematic uncertainties, p_{T} dependence is observed at low transverse momenta, but not at higher p_{T}[c]. Using a fit suppresses the sensitivity to statistical fluctuations which might be present in the ratio. The magnitude of a relative systematic uncertainty is then defined as a (significant) deviation from unity of $f(p_{\mathrm{T}})$ in Eq. 6.4.

In the particular example of Fig. 6.1, a systematic effect would be derived from evaluating $f(p_{\mathrm{T}})$ (red line) and assigned up to $p_{\mathrm{T}} = 40$ GeV/c. This strategy used for all sources of uncertainties in which just *one* (or two) alternate measurement is (are) available; in situations where a distribution of alternate measurements is tested, resampling techniques are not necessary (as will be discussed in the relevant sections).

[c]This behavior is also observed in thermal model studies following the procedure outlined in § 5.1. 1.6×10^8 events were generated and analyzed to study the magnitude and p_{T} dependence of systematic variations without limitations from statistical uncertainties.

6.2 Nominal measurement

Prior to discussing systematic uncertainties resulting from variations in the nominal measurement, the nominal measurement itself must be defined. Motivations for these nominal values can be found in Ch. 4 and Ch. 5, to make this chapter self-contained however, important points are repeated here.

6.2.1 Jet definitions and kinematic ranges

The jet spectra are unfolded according to the best practices that are described in [108, 159], in which unfolding in the presence of a large, fluctuating background, is validated e.g. using extensive Monte Carlo studies following [175]. The measured jet spectrum is binned into p_{T} intervals of 5 GeV/c width and unfolded into 10 GeV/c intervals.

The measurement is carried out in 0–5% and 30–50% collision centrality. Jets are reconstructed in $|\eta_{\mathrm{jet}}| < 0.7$ with the anti-k_{T} algorithm with a resolution parameter or $R = 0.2$, using charged tracks only. The contribution of combinatorial jets to the measured jet spectrum is reduced by requiring that reconstructed jets contain at least one charged particle with $p_{\mathrm{T}} > 3$ GeV/c and have an area of at least 0.56 πR^2.

The measured jet spectrum is taken as input for the unfolding routine between $30 < p_{\mathrm{T}}^{\mathrm{jet}} < 105$ GeV/c for 0–5% collision centrality and $15 < p_{\mathrm{T}}^{\mathrm{jet}} < 90$ GeV/c for 30–50% collision centrality. The lower bound corresponds to five times the width of the δp_{T} distribution, the upper bound is the edge of the last measured bin which contains at least 10 counts. The unfolded jet spectrum starts at 0 GeV/c to allow for feed-in of true jets with low $p_{\mathrm{T}}^{\mathrm{jet}}$; in addition combinatorial jets which are not rejected by the jet area and leading charged particle requirements are migrated to momenta lower than the minimum measured $p_{\mathrm{T}}^{\mathrm{jet}}$. The unfolded solution ranges up to 200 GeV/c (0–5%) and 170 GeV/c (30–50%) to facilitate feed-in of jets with a $p_{\mathrm{T}}^{\mathrm{jet}}$ higher than the maximum measured momentum. As the data points of the unfolded solution are strongly correlated for $p_{\mathrm{T}}^{\mathrm{jet}}$ higher than the maximum measured $p_{\mathrm{T}}^{\mathrm{jet}}$, $v_2^{\mathrm{ch\ jet}}$ will be reported only up to the upper limit of the measured jet spectra.

6.2.2 Unfolding

The SVD algorithm regularizes the unfolding by omitting components of the measured spectrum for which the singular value is small, which amplify statistical noise in the result (see § 4.5). The optimal regularization strength is not known a-priori, but chosen by studying:

- *The distribution of* $\log|d_i|$ (see Eq. 4.59). Only the first terms of the singular value decomposition are expected to be significant, while oscillating solutions lead to values for d_i which are statistically compatible with 0 (since d_i is scaled, the statistical uncertainty on all d is 1). d_i should be significant for small i and fall towards a Gaussian-distributed random value with a mean close to 0 for large i [178]. The critical value, after which d_i is no longer significant, determines the effective rank k of the system of linear equations to be solved and sets the regularization parameter by Eq. 4.62;
- *Correlation between points of the unfolded spectrum.* The (anti-)correlation between bins i and j of the unfolded spectrum is quantified in terms of the correlation coefficients $\rho_{i,j}$ (Eq. 6.2) which are derived from the covariance matrix of the unfolded solution. Unfolded solutions with strong off-diagonal correlations are not accepted as they indicate over- or under-regularization;

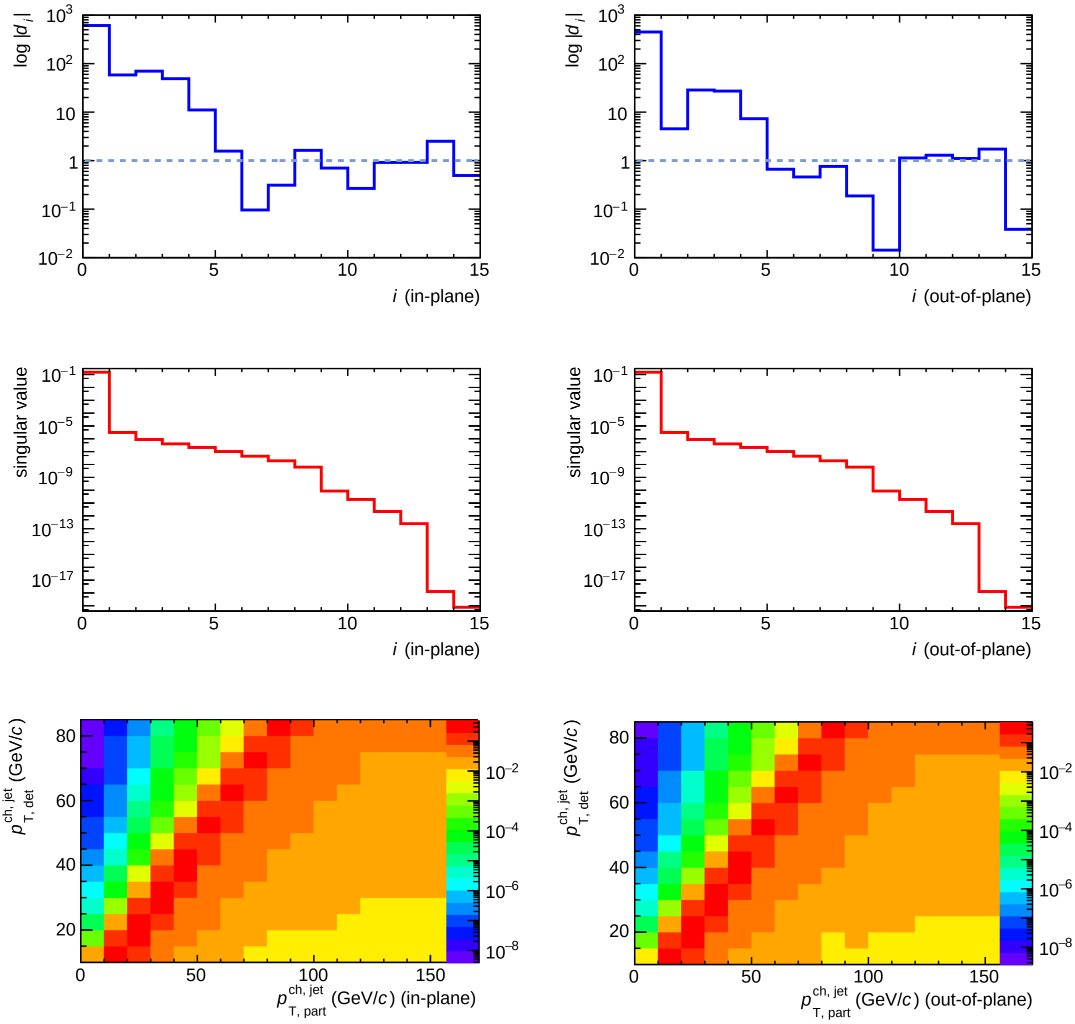

Figure 6.2: From top to bottom: log $|d_i|$ distribution, singular values s, and combined response matrix for in- (left) and out-of-plane (right) jet spectra, 30–50% collision centrality.

- *The ratio of the measured spectrum to the refolded spectrum*, where the refolded spectrum is obtained by multiplication of the unfolded spectrum with the combined response matrix. The ratio should be statistically compatible with 1. If the regularization strength is chosen poorly, the ratio will either oscillate or - in the case of an under-constrained system - be exactly 1.

The values of log $|d_i|$, singular values, and combined response matrices are shown in Fig. 6.2 for the in-plane and out-of-plane jet spectra in 30–50% centrality collisions. Correlation coefficients and ratios of measured to refolded spectra for in-plane and out-of-plane jet spectra are shown in Figs 6.3 for the nominal measurement in the same centrality interval.

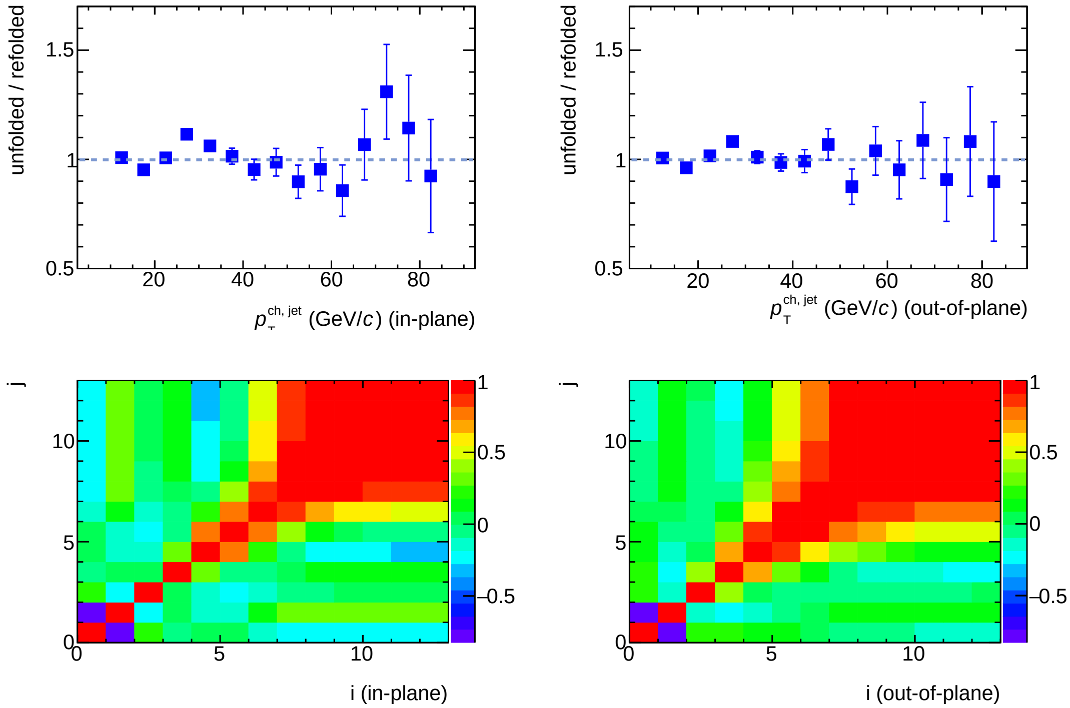

Figure 6.3: 30–50% collision centrality. Ratio of measured over refolded spectrum (top) and $\rho_{i,j}$ (bottom), for the in-plane (left) and out-of-plane (right) jet spectrum.

6.3 Systematic uncertainties

Systematic uncertainties on $v_2^{\mathrm{ch\ jet}}$ are grouped into two categories, *shape* and *correlated*, based on their point-to-point correlation. Shape uncertainties are anti-correlated between parts of the unfolded spectrum: when the yield in part of the spectrum increases, it decreases elsewhere and vice versa. Correlated uncertainties are correlated point-to-point. The difference in behavior is visualized in Fig. 6.4, where shape uncertainties (left) and correlated uncertainties (right) are illustrated by plotting nominal jet spectra (solid line) and variations (dotted lines) and the resulting systematic uncertainties (dashed lines), obtained from taking ratios. The uncertainties cover

- Correlated
  - Tracking efficiency;
  - Variations in the p_{T} range of the unfolded jet spectrum.
- Shape
  - Sensitivity to combinatorial jets;
  - Variations in the underlying event description;
  - Unfolding uncertainties.

Both types of uncertainties have - as mentioned - contributions which lead to correlated changes of N_{in} and N_{out}. The relevance of the distinction between these two types of uncertainties is

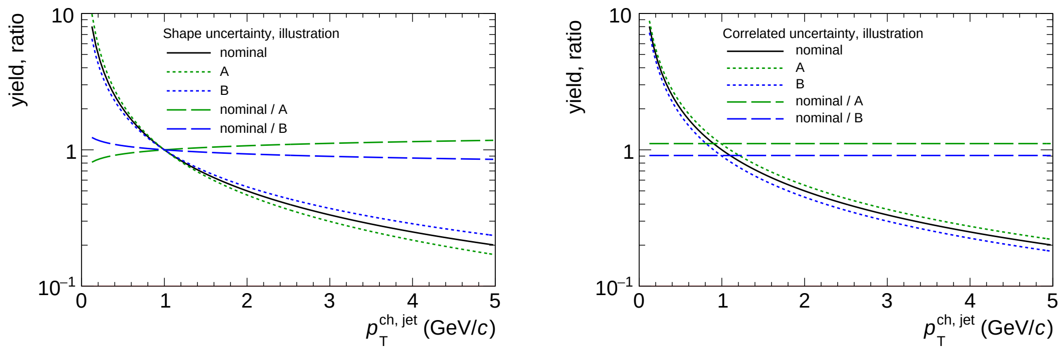

Figure 6.4: Illustration of different behavior of the two types of systematic uncertainties on the unfolded jet spectra. Shape uncertainties are anti-correlated between parts of the unfolded spectrum: when the yield in part of the spectrum increases, it decreases elsewhere and vice versa (left). Correlated uncertainties are correlated point-to-point (right).

will be explicitly shown when estimating the significance of the results using Eq. 7.1 in Ch. 7.

6.3.1 Correlated uncertainties

Correlated uncertainties are estimated for the in-plane and out-of-plane jet spectra independently. Two sources of correlated uncertainties are considered: tracking efficiency and the inclusion of combinatorial jets in the measured jet spectrum.

6.3.1.1 Tracking efficiency

The dominant correlated uncertainty ($\lesssim$ 10%) arises from tracking and is estimated by constructing a detector response matrix with a tracking efficiency reduced by 4% (motivated by studies [108] comparing reconstructed tracks to simulations of HIJING [141] events). The observed difference between the nominal and modified unfolded solution is taken as a symmetric uncertainty to allow for an over- and underestimation of the tracking efficiency. As no p_{T} dependence is expected in this variation, the difference is quantified as parameter a of a fit of a zeroth-order polynomial ($y = a$) to the ratio.

The relative uncertainty obtained from the ratio of nominal measurement to variation is shown in Fig. 6.5 for the in-plane (left) and out-of-plane jet (right) spectra for 30–50% collision centrality to illustrate the clear correlation. The red line represents the assigned constant uncertainty.

6.3.1.2 Inclusion of combinatorial jets

The sensitivity of the unfolded result to the unknown number of combinatorial jets at low p_{T} in the measured jet spectrum is tested by changing the lower range of the unfolded solution from 0 to 5 GeV/c, which leads to an overall (correlated) increase of the unfolded jet yield as the total number of unfolded jets is conserved in the unfolding procedure (i.e. the same amount of measured jets is distributed over a smaller range). The effect on the in-plane and out-of-plane jet spectra (an enhancement of the jet yield at low momenta from conservation of total number of jets) is similar, and leads to an approximately bin-by-bin correlated shift in $v_2^{\mathrm{ch\ jet}}$. The relative

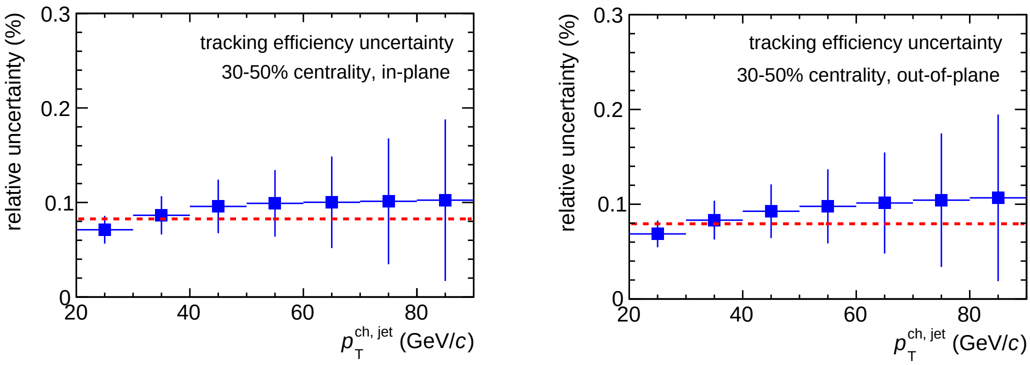

Figure 6.5: Relative systematic uncertainty from variations in the tracking efficiency for the in-plane (left, 8.3% relative uncertainty) and out-of-plane (right, 7.9% relative uncertainty) jet spectra.

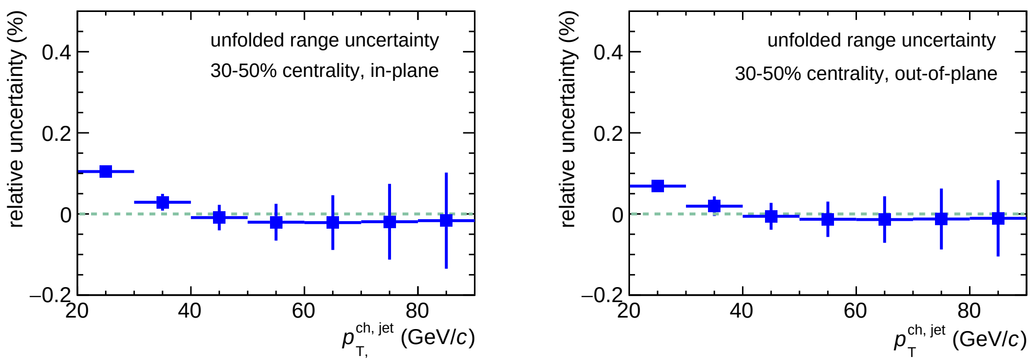

Figure 6.6: Relative systematic uncertainty from variations in the range of the unfolded spectrum for the in-plane (left) and out-of-plane (right) jet spectra. For $p_{\mathrm{T}} > 40$ GeV/c, statistical uncertainties are large and a systematic effect can no longer be resolved.

uncertainty obtained from the ratio of nominal measurement to variation is shown in Fig. 6.6 for the in-plane (left) and out-of-plane jet spectra for 30–50% collision centrality. The in-plane and out-of-plane uncertainties behave similarly; for $p_{\mathrm{T}} > 40$ GeV/c no systematic effects can be resolved.

6.3.2 Total correlated uncertainty

Both correlated uncertainties are added in quadrature and propagated to $v_2^{\mathrm{ch\ jet}}$, following Eq. 6.3, asymmetrically, assuming that variations are strongly correlated between the in-plane and out-of-plane jet spectra, while still allowing for effects from azimuthally-dependent variations in track occupancy and reconstruction efficiency, by setting the sample correlation coefficient $\rho \equiv \sigma_{i,j}/(\sigma_i \sigma_j)$ to 0.75.

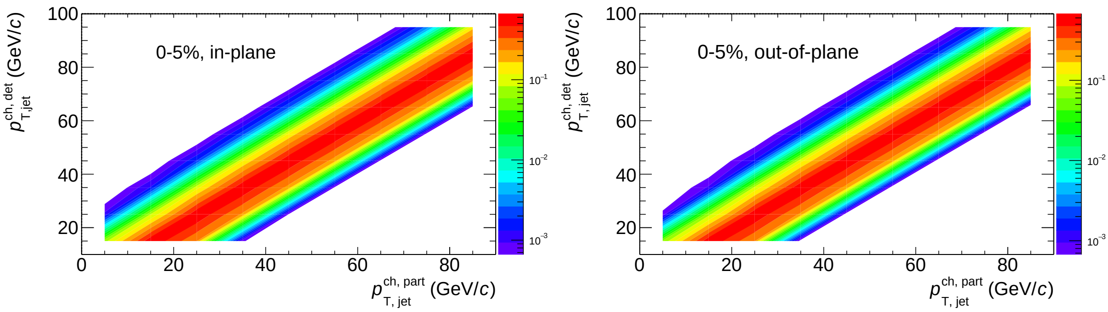

Figure 6.7: Background fluctuation responses for 0–5% collision centrality in the in-plane (left) and out-of-plane orientation (right).

As $\rho = 0.75$, the final correlated uncertainty on $v_2^{\mathrm{ch\ jet}}$ is small, given that the relative uncertainties on the in-plane and out-of-plane jet yields are similar in magnitude. Correlated uncertainties are depicted as open boxes in the results figures of Ch. 7.

6.3.3 Shape uncertainties

Shape uncertainties are anti-correlated between parts of the unfolded spectrum: when the yield in part of the spectrum increases, it decreases elsewhere and vice versa. Shape uncertainties fall into three categories: assumptions in the unfolding procedure, feed-in of combinatorial jets, and the sensitivity of the unfolded solution to the shape of the underlying event energy distribution.

6.3.3.1 Unfolding uncertainty

The dominant contribution to the unfolding uncertainty is related to the regularization of the unfolded solution. The SVD algorithm [178] regularizes the unfolding by omitting components of the measured spectrum for which the singular value is small and which amplify statistical noise in the result. To explore the sensitivity of the result to the regularization strength, the effective rank of the matrix equation that is solved is varied by changing the integer regularization parameter k by $\pm$ 1.

As a default, the unfolded solution from the χ^2 algorithm [183] is used as a prior[d] for the SVD algorithm, a PYTHIA spectrum is used as a variation. The bias from the choice of unfolding algorithm itself is tested by comparing the results of the SVD unfolding and the χ^2 algorithm.

It is assumed that the systematic uncertainty resulting from the unfolding procedure is correlated between the in-plane and out-of-plane jet spectra, as the same nominal unfolding approach is used for both spectra, and the δp_{T} distributions for the in-plane and out-of-plane background fluctuations are similar in shape (the background fluctuation responses for 0–5% collision centrality in the in-plane and out-of-plane orientation are shown in Fig. 6.7).

This assumption is tested by folding (multiplying by the response matrix) a PYTHIA jet spectrum with the in-plane and out-of-plane background fluctuations matrices. The ratio of the folded 'in-plane' to 'out-of-plane' PYTHIA spectra are shown in Fig. 6.8 for 0–5% (left) and 30–50% (right) collision centrality. The differences between the folded spectra are small[e]

[d]See the explanation below Eq. 4.48, and at Eqs 4.51 and 4.50.

[e]It should be noted that this statement only holds when the azimuthal modulation of the underlying event is taken in to account event-by-event.

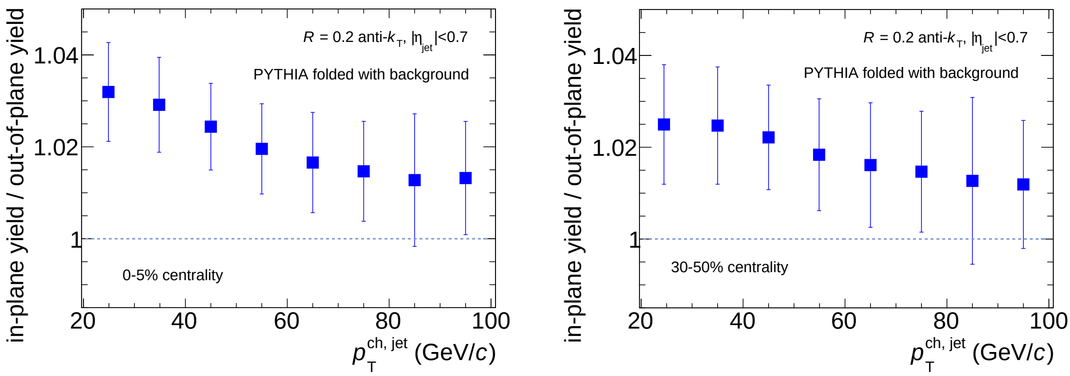

Figure 6.8: Difference in in-plane and out-of-plane spectra for central (0-5% collision centrality, top panels) and peripheral (30-50% collision centrality, lower panels) in terms of the ratio of the spectra (left) and the v_2 value.

($\lesssim$ 3 %), systematic variations in e.g. the unfolding setup are therefore similar in the in-plane and out-of-plane spectrum orientation. The unfolding uncertainty is therefore estimated by introducing the same variations in the in-plane and out-of-plane unfolding setup simultaneously and observing changes in $v_2^{\text{ch jet}}$ directly rather than propagating the variations in N_{in} and N_{out} independently via Eq. 6.3.

The total uncertainty from unfolding is determined by constructing a distribution (as suggested in [184]) of $v_2^{\text{ch jet}}$ in each $p_{\text{T}}^{\text{jet}}$ bin and assigning the width of this distribution as a systematic uncertainty,

$$\sigma_i = \sqrt{\frac{1}{N}\sum_{i=1}^{N}(x_i - \mu)^2}. \tag{6.5}$$

The absolute uncertainty on $v_2^{\text{ch jet}}$ as a result of unfolding is shown in Fig. 6.9 for 0–5% (left) and 30–50% (right) collision centrality. The systematic uncertainty does not depend on p_{T} even though the jet spectra are steeply falling; using Eq. 6.5 effectively removes interference from statistical uncertainties.

6.3.3.2 Sensitivity to combinatorial jets

The other two components of the shape uncertainty are the sensitivity of the unfolded solution to combinatorial jets and uncertainties arising from the description of the underlying event; both are estimated on the in-plane and out-of-plane jet spectra independently and propagated to $v_2^{\text{ch jet}}$ as uncorrelated.

The effect of combinatorial jets is tested by varying the minimum $p_{\text{T}}^{\text{jet}}$ of the measured jet spectrum by $\pm$ 5 GeV/c, effectively increasing or decreasing the possible contribution of combinatorial jet yield at low jet momentum. As varying the range by $\pm$ 5 GeV/c constitutes *two* variations, taking one ratio does not suffice for exploring a systematic effect, neither does two variations give the possibility to take the approach of Eq. 6.5. To quantify a systematic effect, ratios of the nominal measurement to both variations are taken; per p_{T} bin, the variation that leads to the *most extreme* deviation from unity is kept as possible systematic uncertainty

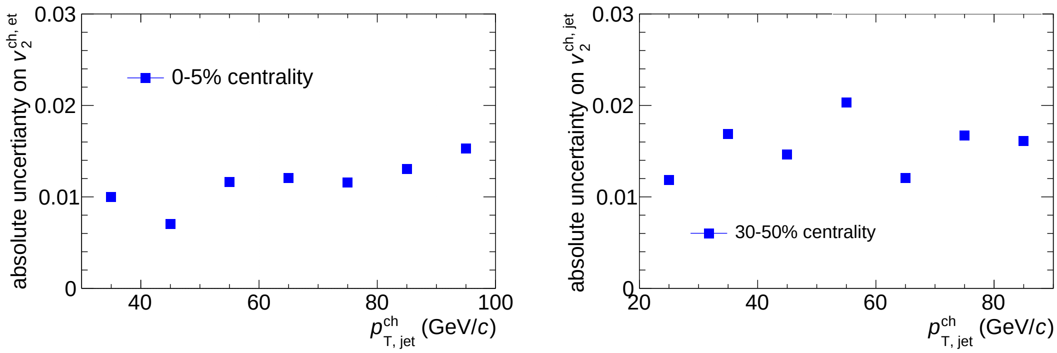

Figure 6.9: Absolute systematic uncertainty on $v_2^{\text{ch jet}}$ from unfolding for 0–5% (left) and 30–50% collision centrality.

(in practice, extending the range towards lower p_{T} leads to the largest deviation). Explicitly, the uncertainty is derived in each p_{T} bin by calculating

$$\frac{N}{N_{+5\ \text{GeV/c}}} = a \qquad \frac{N}{N_{-5\ \text{GeV/c}}} = b. \tag{6.6}$$

Where N denotes the yield in a p_{T} bin. If $|a-1| > |b-1|$, a is chosen as possible systematic variation, for $|b-1| > |a-1|$, b. An uncertainty is assigned only if the effect is deemed significant after resampling.

6.3.3.3 Underlying event description

To test the assumptions made in the fitting of Eq. 4.27, the maximum p_{T} of accepted tracks is lowered to 4 GeV/c, changing the contribution of hydrodynamic flow of the underlying event that is removed by unfolding rather than subtraction from the raw jet energy $p_{\text{T}}^{\text{raw}}$ (Eq. 4.27). Additionally, the minimum p-value that is used as a goodness of fit criterion is changed from 0.01 (the nominal value) to 0.1. Analogous to the approach of § 6.3.3.2, *two* variations are tested with respect to the nominal measurement instead of one, the prescription of Eq. 6.6 is used to assign a systematic effect.

Lastly, the minimum required distance of tracks to the leading jet axis in pseudorapidity (used in the evaluation of Eq. 4.27) is enlarged to 0.3, no effect is found.

6.3.4 Total shape uncertainty

The uncertainties on the in-plane and out-of-plane jet yield resulting from variations in the p_{T} range of the measured jet spectrum and of variations in the determination of the underlying event energy density are added in quadrature; a resulting uncertainty on $v_2^{\text{ch jet}}$ is propagated using Eq. 6.3 assuming that the different sources of uncertainty are uncorrelated. The unfolding uncertainty, obtained from variations in $v_2^{\text{ch jet}}$ directly, is added in quadrature to this uncertainty to obtain the total shape uncertainty.

		uncertainty on $v_2^{\text{ch jet}}$					
	$p_{\text{T}}^{\text{jet}}$ (GeV/c)	30-40	60-70	80-90	30-40	60-70	80-90
	centrality (%)	0-5			30-50		
shape	unfolding	0.017	0.012	0.016	0.016	0.011	0.015
	$p_{\text{T}}^{\text{jet}}$-measured	0.013	$\ll$ stat	$\ll$ stat	0.024	$\ll$ stat	$\ll$ stat
	$\rho_{\text{ch}}(\varphi)$fit	0.015	$\ll$ stat	0.016	$\ll$ stat	$\ll$ stat	$\ll$ stat
total		0.027	0.012	0.023	0.029	0.011	0.015
correlated	tracking	0.009	0.009	0.009	0.0067	0.0067	0.0067
	$p_{\text{T}}^{\text{jet}}$-unfolded	$\ll$ stat	$\ll$ stat	$\ll$ stat	$\ll$ stat	$\ll$ stat	$\ll$ stat
total		0.009	0.009	0.009	0.0067	0.0067	0.0067

Table 6.1: Systematic uncertainties on $v_2^{\text{ch jet}}$ per source for various transverse momenta. Fields with the value '$\ll$ stat' indicate that no systematic effect can be resolved within the statistical limits of the analysis.

6.4 Summary

An overview of the systematic uncertainties as function of p_{T} for all the different sources are given in table 6.1. The contribution of independent sources of uncertainties to the total uncertainty on $v_2^{\text{ch jet}}$ are shown, as well as the total shape and correlated uncertainties. High statistics thermal model tests (see § 5.1) have been used to verify that the uncertainties labeled '$\ll$ stat' are indeed negligible compared to other uncertainties.

Part III

Results, discussion and outlook

7 | Results and discussion

The coefficients $v_2^{\text{ch jet}}$ as function of $p_{\text{T}}^{\text{jet}}$ for 0–5% and 30–50% collision centrality are presented in Fig. 7.1. Significant positive $v_2^{\text{ch jet}}$ is observed in semi-central collisions and no (significant) p_{T} dependence is visible. The observed behavior is indicative of path-length-dependent in-medium parton energy loss.

The observed $v_2^{\text{ch jet}}$ in central collisions is of similar magnitude as that seen in semi-central collisions. The systematic uncertainties on the measurement however are larger than those on the semi-central $v_2^{\text{ch jet}}$ data, in particular at lower $p_{\text{T}}^{\text{jet}}$, as a result of the larger background contribution to the measured jet energy.

7.1 Comparison to high-p_{T} v_2, $v_2^{\text{calo jet}}$

To get a better qualitative understanding of the results, the v_2 of single charged particles v_2^{part} [185, 186] and the ATLAS $v_2^{\text{calo jet}}$ measurement [187] are shown together with the $v_2^{\text{ch jet}}$ measurement in Fig. 7.2. The results are compared to model predictions in Fig. 7.3.

The ATLAS result is for jets with resolution parameter $R = 0.2$ within $|\eta| < 2.1$ comprising both charged and neutral fragments. The event plane angle is measured by the forward calorimeter system at $3.2 < |\eta| < 4.9$. Jets are reconstructed by applying the anti-k_{T} algorithm to calorimeter towers, after which, in an iterative procedure, a flow-modulated underlying event energy is subtracted. Each jet is required to lie within $\sqrt{\Delta\eta^2 + \Delta\varphi^2} < 0.2$ of either a calorimeter cluster of $p_{\text{T}} > 9$ GeV/c or a $p_{\text{T}} > 10$ GeV/c track jet with resolution parameter $R = 0.4$ built from constituent tracks of $p_{\text{T}} > 4$ GeV/c (the full reconstruction procedure can be found in [187, 188]).

It is important to realize that the energy scales of the ATLAS $v_2^{\text{calo jet}}$ and ALICE $v_2^{\text{ch jet}}$ measurements are different (as the ALICE jets do not include neutral fragments) which complicates a direct comparison between the two measurements. The most central ATLAS results are measured in 5–10% collision centrality. The ALICE and ATLAS measurements are in qualitative agreement, both indicating path-length-dependent parton energy loss. Given the uncertainties, the difference in the central values of the measurement is not significant[a].

Figure 7.2 also shows the v_2 of single charged particles v_2^{part} (from [185, 186]), which is expected to be mostly caused by in-medium energy loss at intermediate and high momenta ($p_{\text{T}} \gtrsim 5$ GeV/c, the single charged hadron R_{AA}, shown in Fig. 2.4, is smaller than unity in this range as well). Even though a direct quantitative comparison between $v_2^{\text{ch jet}}$ and v_2^{part} cannot be made as the energy scales for jets and single particles are different, the measurements can

[a]The significance of the results is explored in more detail in § 7.2.

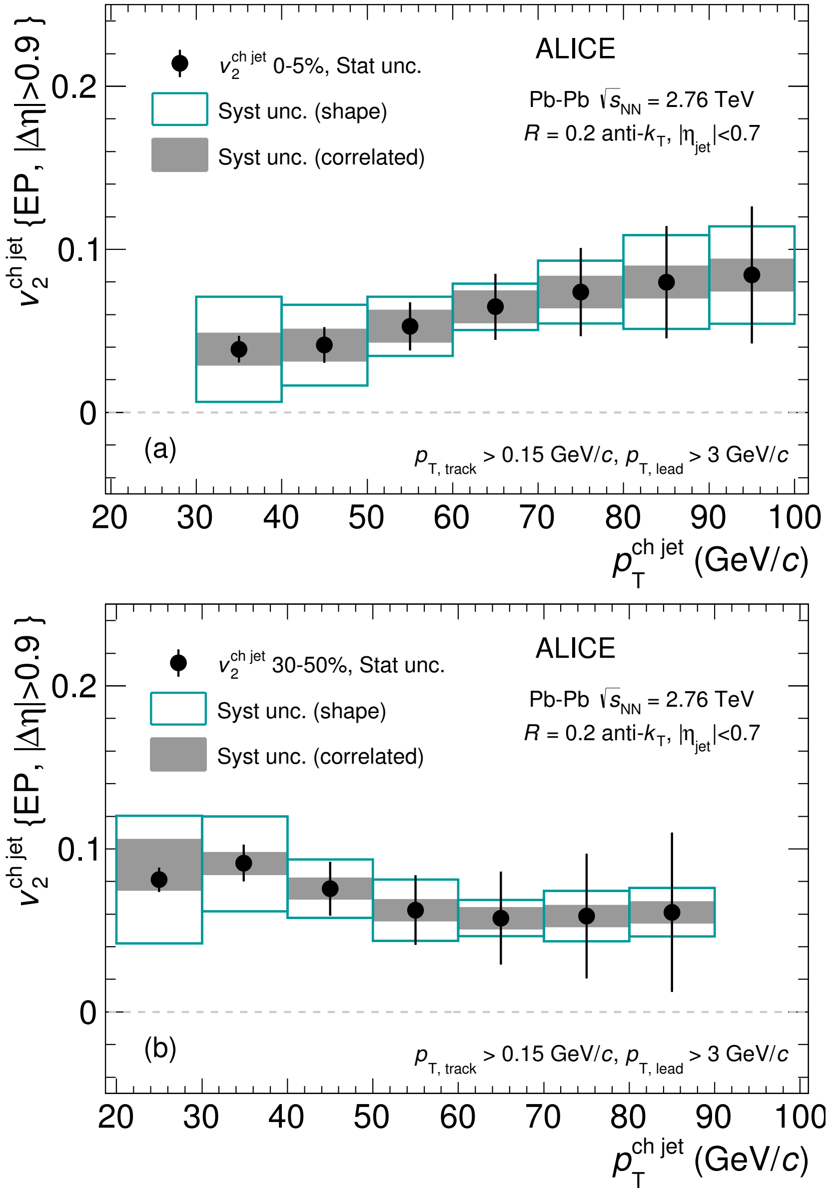

Figure 7.1: Second-order harmonic coefficient $v_2^{\text{ch jet}}$ as function a of p_T^{jet} for 0–5% (a) and 30–50% (b) collision centrality. The error bars on the points represent statistical uncertainties, the open and shaded boxes indicate the shape and correlated uncertainties (as explained in Ch. 6).

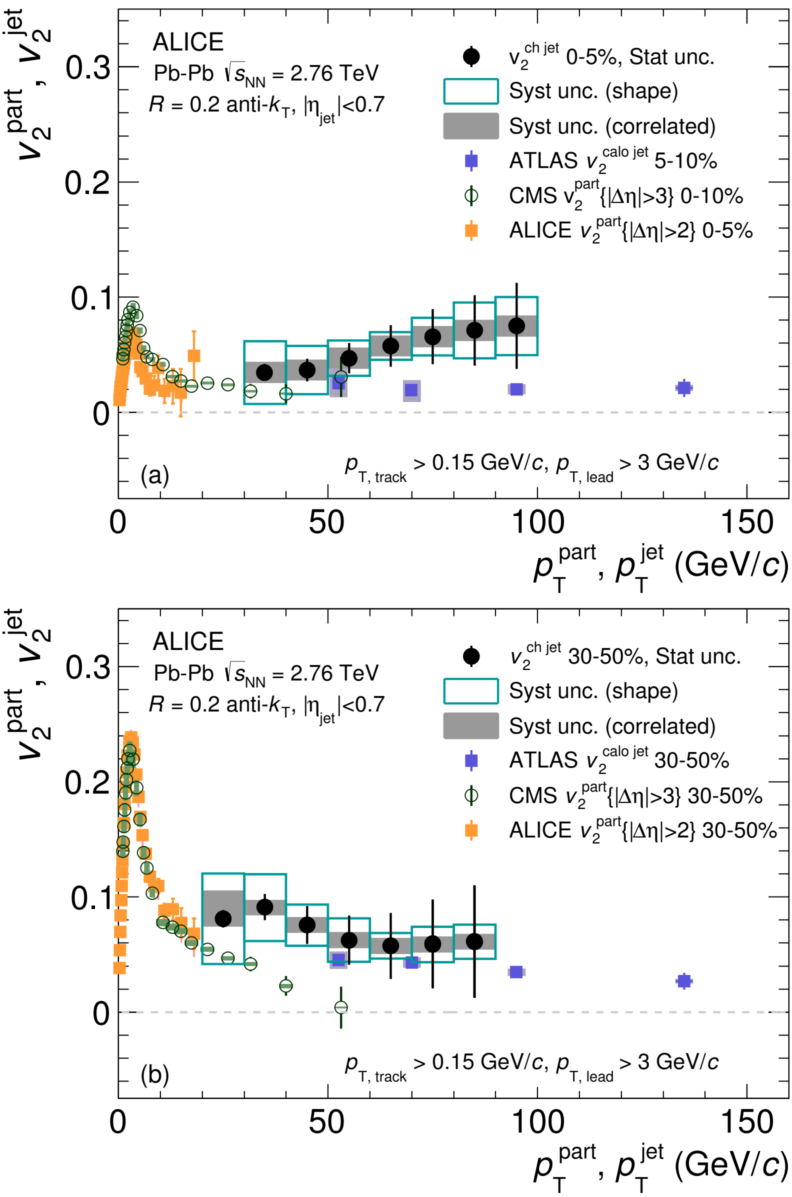

Figure 7.2: Elliptic flow coefficient v_2 of charged particles [185, 186] (red, green) and $R = 0.2$ full jets (comprising both charged and neutral fragments) measured within $|\eta| < 2.1$ [187] (blue) superimposed on the results from the current analysis of $R = 0.2$ charged jets $v_2^{\text{ch jet}}$. In all measurements, statistical errors are represented by bars and systematic uncertainties by shaded or open boxes. Note that the same parton p_{T} corresponds to different single particle, full jet and charged jet p_{T}. ATLAS $v_2^{\text{calo jet}}$ and CMS v_2 from [186, 187] in 30–50 % centrality are the weighted arithmetic means of measurements in 10% centrality intervals using the inverse square of statistical uncertainties as weights.

be compared qualitatively, and it can be seen that for central events, the single particle v_2^{part} and $v_2^{\text{ch jet}}$ are of similar magnitude and only weakly dependent on p_{T} over a large range of p_{T} ($\approx 20-50$ GeV/c). For non-central collisions (30–50%), the measurements of v_2 for single particles and jets are also in qualitative agreement in the p_{T} range where the uncertainties allow for a comparison.

7.2 Some notes on significance

As mentioned in the previous section, the difference between the ATLAS $v_2^{\text{calo jet}}$ and $v_2^{\text{ch jet}}$ results is not significant, even though the central values of the measurements are different. This is an effect of the statistical uncertainties and (correlated) systematic uncertainties, which are large in central collisions and mainly result from the background contribution to the measured jet energy. Since two types of systematic uncertainties, with different point-to-point correlations, are shown in the figures, compatibility between results, or with the null hypothesis, is difficult to estimate visually. The significance of the results is therefore assessed by calculating a p-value for the hypothesis that $v_2^{\text{ch jet}} = 0$ over the presented momentum range. The p-value is evaluated starting from a modified χ^2 calculation that takes into account both statistical and (correlated) systematic uncertainties, as suggested in [189]. The modified χ^2 for the hypothesis $v_2^{\text{ch jet}} = \mu_i$ is calculated by minimizing

$$\tilde{\chi}^2(\epsilon_{\text{corr}}, \epsilon_{\text{shape}}) = \sum_{i=1}^{n} \frac{(v_{2,i} + \epsilon_{\text{corr}}\sigma_{\text{corr,i}} + \epsilon_{\text{shape}} - \mu_i)^2}{\sigma_i^2} + \epsilon_{\text{corr}}^2 + \frac{1}{n}\sum_{i=1}^{n} \frac{\epsilon_{\text{shape}}^2}{\sigma_{\text{shape,i}}^2} \tag{7.1}$$

with respect to the systematic shifts ϵ_{shape}, ϵ_{corr}, where $v_{2,i}$ represent the measured data (n points), σ_i are statistical uncertainties and $\sigma_{\text{shape,i}}$, $\sigma_{\text{corr,i}}$ denote the two specific types of systematic uncertainties.

The parameter ϵ_{corr} is a measure of the fully correlated shifts; a shift of all data points by the correlated uncertainty $\sigma_{\text{corr,i}}$ gives a total contribution to $\tilde{\chi}^2$ of one unit. The systematic shifts for the shape uncertainty are taken to be of equal size for each point, since this gives the best agreement with the $v_2^{\text{ch jet}} = 0$ hypothesis and thus provides a conservative estimate of the significance; the penalty factor is constructed such that an average shift of all data points by σ_{shape} adds one unit to $\tilde{\chi}^2$.

The p-value itself is calculated using the χ^2 distribution with $n-2$ degrees of freedom. For semi-central collisions a p-value of 0.0009 is found, indicating significant positive $v_2^{\text{ch jet}}$. It should be noted that the most significant data points are at $p_{\mathrm{T}}^{\text{jet}} < 60$ GeV/c; the results in the range $60 < p_{\mathrm{T}}^{\text{jet}} < 100$ GeV/c are compatible with $v_2^{\text{ch jet}} = 0$ (p-value 0.02[b]). In central collisions, a p-value with respect to the hypothesis of $v_2^{\text{ch jet}} = 0$ of 0.12 is found which indicates that $v_2^{\text{ch jet}}$ is compatible with 0 within two standard deviations. The same p-value of 0.12 is consistent with an upper limit of $v_2^{\text{ch jet}} = 0.088$.

[b] For more details, see § B.2. It should be noted that Eq. 7.1 does not follow a perfect χ^2 distribution; numbers here should therefore be seen as a guideline.

7.3 Model comparisons

To elucidate the path-length dependence of parton energy loss, theory predictions of $v_2^{\text{ch jet}}$ must be made, which can be compared to the measured data. Figure 7.3 shows the $v_2^{\text{ch jet}}$ of $R = 0.2$ charged jets from the JEWEL Monte Carlo [103, 104] compared to the measured $v_2^{\text{ch jet}}$. JEWEL simulates a parton shower evolution in the presence of a dense QCD medium by generating hard scatterings according to a collision geometry from a Glauber [57] density profile. A 1D Bjorken expansion is used to simulate the time evolution of the medium. After radiative and collisional energy loss, PYTHIA is used to hadronize the fragments to final state particles.

The analysis on the JEWEL events is performed with the same jet definition and acceptance criteria that are used for the $v_2^{\text{ch jet}}$ analysis in data. As symmetry plane $\Psi_{\text{EP, }2}$, the idealized symmetry axis from the optical Glauber geometry is used, with event plane resolution $\mathcal{R}_2 = 1$[c].

The JEWEL Monte Carlo shows finite significant $v_2^{\text{ch jet}}$ in semi-central collisions; in central collisions $v_2^{\text{ch jet}}$ is compatible with zero. The JEWEL result for semi-central 30–50% collisions is compatible with the measured values (p-value 0.4 using Eq. 7.1 with the JEWEL results as hypothesis μ_i and the quadratic sum of the statistical uncertainties of both datasets as σ_i in the denominator of the first sum of Eq. 7.1). In central JEWEL collisions $v_2^{\text{ch jet}}$ is consistent with zero, while the measured values are compatible with the JEWEL $v_2^{\text{ch jet}}$ within two standard deviations.

It should also be noted that JEWEL currently uses an optical Glauber model (see § 2.2.3.1) for the initial state and therefore does not include fluctuations in the participant distribution due to the spatial configuration of nuclei in the nucleus. This simplified treatment of the overlap geometry is expected to underestimate the $v_2^{\text{ch jet}}$ ([190, 191], see also § 2.4.1). This comparison of $v_2^{\text{ch jet}}$ in JEWEL to experimental data complements earlier studies of the path-length dependence of parton energy loss and model predictions for the jet R_{AA} ([120], see Fig. 2.14).

7.4 Conclusion

The azimuthal anisotropy of $R = 0.2$ charged jet production, quantified as $v_2^{\text{ch jet}}$, has been presented in central and semi-central collisions. Significant positive $v_2^{\text{ch jet}}$ is observed in semi-central collisions, which indicates that jet suppression is sensitive to the initial geometry of the overlap region of the collision. This observation can be used to constrain predictions on the path-length dependence of in-medium parton energy loss. In central collisions, the central values of the measurement are positive, but the uncertainties preclude drawing a strong conclusion on the magnitude of $v_2^{\text{ch jet}}$.

The measured $v_2^{\text{ch jet}}$ for charged jets is also compared to single particle v_2 from ALICE and CMS and $v_2^{\text{calo jet}}$ from ATLAS. The measurements cannot be directly compared quantitatively since the energy scales are different, but qualitatively, the results agree and indicate a positive v_2 for both charged particles and jets to high p_{T} in central and semi-central collisions. This observation indicates that parton energy loss is large and that the sensitivity to the collision geometry persists up to high transverse momenta.

[c] Particles that are part of the underlying event are not stored in JEWEL, hence the event plane angles cannot be reconstructed following the procedure of § 4.3 and the symmetry plane angles Ψ_2, which are known exactly in the model, are used directly, using an event plane resolution $\mathcal{R}_2$ of 1.

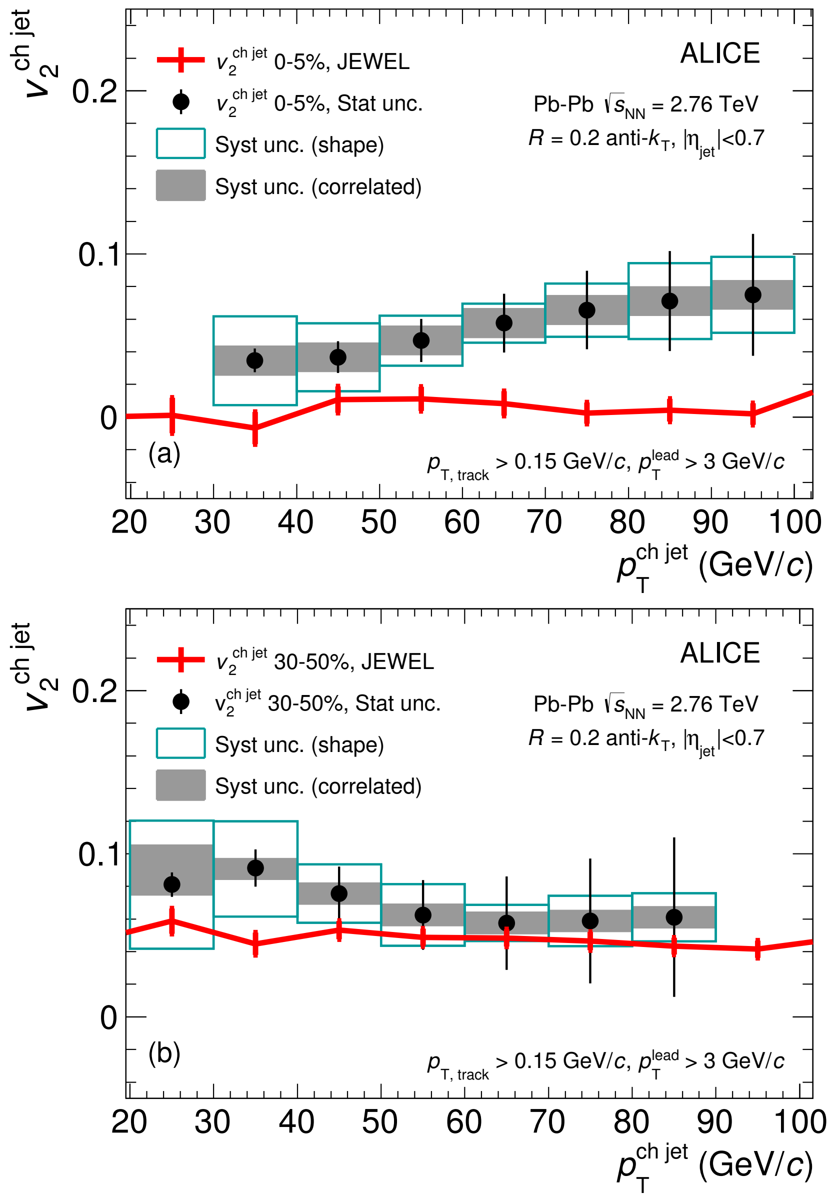

Figure 7.3: $v_2^{\text{ch jet}}$ of $R = 0.2$ charged jets obtained from the JEWEL Monte Carlo (red) for central (a) and semi-central collisions (b) compared to data. JEWEL data points are presented with only statistical uncertainties.

The JEWEL Monte Carlo predicts sizable $v_2^{\text{ch jet}}$ for semi-central collisions and very small to zero $v_2^{\text{ch jet}}$ in central events. These predictions are in good agreement with the semi-central measurement. For central collisions, the JEWEL prediction is below the measurement, but more data would be needed to reduce the uncertainties on the measurement sufficiently to constrain the model.

8 | Outlook and exploratory studies

The results presented in Figs 7.1 and 7.3 suggest that aside from effects from initial geometry, fluctuations in the initial distribution of nucleons play an important role in generating energy loss. A number of studies in Pb–Pb collisions, aimed at further constraining the path-length dependence of jet energy loss and the interactions associated with this, are discussed in the first section (§ 8.1) of this chapter, after which some exploratory measurements are presented in § 8.2.

8.1 Outlook

Partons traversing the QGP medium lose energy via collisional and radiative processes, both of which contribute to the total energy loss of the initial hard partons. Collisional and radiative energy loss have different dependencies on L, the length of the parton's trajectory through the medium (as argued in § 2.2, $\langle \Delta E \rangle \propto L$ for collisional energy loss and $\langle \Delta E \rangle \propto L^2$ - or even L^3 - for radiative processes). The $v_2^{\text{ch jet}}$ measurement is aimed at constraining the relative importance of these two mechanisms.

Strong statements on the L dependence of parton energy loss cannot be made at this point, because the (statistical) uncertainties on the measured $v_2^{\text{ch jet}}$ are large, and because fluctuations in the initial distribution of nucleons within the nuclei contribute to generating a non-zero $v_2^{\text{ch jet}}$; the magnitude of this contribution is unknown. Larger jet samples are necessary to improve the statistical precision of the $v_2^{\text{ch jet}}$ measurement and further constrain theory predictions. Additional information on the initial state of heavy-ion collisions and the medium evolution can be obtained from v_n measurements of particles at low transverse momenta, but also by performing more differential measurements of jet observables are. A number of these jet measurements, which should be pursued, are outlined below.

- *Measurements of v_3^{jet}.* Fluctuations in the initial distribution of nucleons within the overlap region of the colliding nuclei generate higher order asymmetries, which are not correlated to orientation of the impact parameter. v_3^{jet}(the azimuthal modulation of jet production relative to the 3$^{\text{rd}}$-order symmetry plane) can quantify the effect of fluctuations on parton energy loss in the QGP, as the 3$^{\text{rd}}$-order symmetry is generated fully by fluctuations, independent of the orientation of the impact parameter. See also [192];
- *Event-shape engineering and 'ultra-central' collisions.* 'Ultra-central' nuclear collisions are collisions at vanishing impact parameter, with approximately circular overlap regions (the

eccentricity is absent or very small). Measuring v_2^{jet} in these collisions can, just as v_3^{jet}, be used to determine the effect of fluctuations on parton energy loss. In addition, jet energy loss measurements can be carried out as function of eccentricity directly via 'event-shape engineering', an experimental approach in which the eccentricity of the collision system is quantified event-by-event. Measurements can be carried out for R_{AA}, v_n and v_2^{jet}. A large number of events would be required to reduce the statistical uncertainties enough to draw conclusions;

- *Azimuthal-angle dependence of di-jet production.* Di-jet systems originate from $2 \rightarrow 2$ processes, in which two energetic partons are emitted in opposite direction with equal transverse momenta. Di-jet systems are powerful probes of the QGP, as the momentum asymmetry of the end-state observed jets is a result of vacuum-like and medium-induced energy loss. Recent theoretical developments suggest that di-jet imbalance in Pb–Pb collisions is generated largely by energy-loss fluctuations and only to a lesser extent by path-length differences [193, 194]. Measuring the di-jet energy asymmetry as a function of the angle relative to the symmetry plane allows for a direct measure of the effect of medium geometry on the generation of the di-jet imbalance.

As shown in Ch. 7, the limited significance of the $v_2^{\text{ch jet}}$ results precludes drawing strong conclusions on the path-length dependence of parton energy loss. Statistical uncertainties are dominant at high ($p_{\text{T}} > 60$ GeV/c) transverse momenta, where the jet yield is low. Systematic uncertainties dominate at lower transverse momenta ($p_{\text{T}} < 60$ GeV/c), where the contribution of background energy to the jet yield is high.

To successfully carry out the suggested, more differential measurements, larger jet samples than the ones used for the $v_2^{\text{ch jet}}$ study are necessary. Tentative studies on thermal Monte Carlo events (§ 5.1) indicate that the intrinsic systematic uncertainties in the unfolding routine (such as feed-in of combinatorial jets) for the presented p_{T} ranges are reached at jet samples ≈ 10 times larger than the current size for minimum bias events (this conclusion was reached after noting that generating larger data samples (up to 1.5×10^8) did not lead to smaller systematic uncertainties from unfolding). Using *triggered* events (events selected on the presence of large energy deposit in the electromagnetic calorimeter) is expected to increase the statistical precision of the measurements, by simultaneously enhancing the jet yield at high transverse momenta, and suppressing the combinatorial jet yield at low p_{T}.

8.2 Exploratory studies

Jet yields can be enhanced either by studying triggered events, or by enlarging the overall data sample; both of which will be discussed in the following sections.

8.2.1 EMCal: jet triggered events

The EMCal detector (introduced in § 3.2.4) can be used to trigger on highly energetic jets by selecting events in which a certain threshold energy is deposited in a limited detector area. If the area is small and the energy is high, this deposit most likely corresponds to a jet. The jet patch trigger for *central* Pb–Pb events in 2011 has a threshold of 80 GeV/c which must be deposited in 32×32 EMCal patch in η, φ. With a cluster size 0.0145×0.0145, the trigger patch area equals 0.216 ($= 0.0145^2\times 32^2$).

Additionally, the EMCal measures energy of neutral mesons, such as the π^0 and η, via their decay into photons, so that by combining information from the EMCal with information

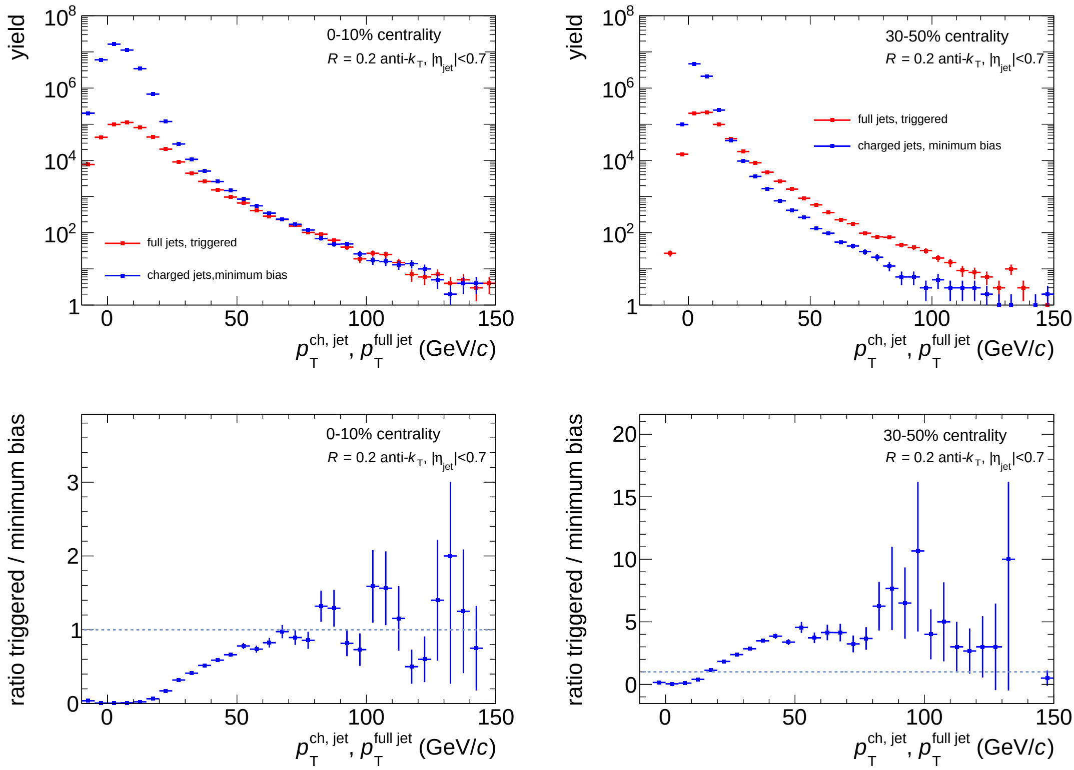

Figure 8.1: Jet spectra (top, not divided into N_{in} and N_{out} but measured over full azimuth) of $R = 0.2$ charged jets, measured in minimum bias events (blue) and $R = 0.2$ full jets in triggered events (red). Ratio of the transverse momentum distributions of triggered full jets (lower panels) to that of minimum bias charged jets, for central (left) and semi-central collisions (right). Statistical uncertainties only.

on charged particles from the central barrel tracking detectors (ITS and TPC), *'full' jets* - comprising both charged and neutral fragments - can be reconstructed[a].

Figure 8.1 shows jet yields as function of p_{T} (upper panels, not divided into N_{in} and N_{out} but measured over full azimuth) of $R = 0.2$ charged jets, measured in minimum bias events (blue) and $R = 0.2$ full jets in triggered events (red). The jet selection criteria are equal to those of § 4.2 for the minimum bias case (although of course the EMCal jets are reconstructed only within EMCal acceptance). In central collisions (0–10%), the jet yield in triggered events is not larger than the yield found in untriggered events. At low momenta however it can be seen that triggering reduces the combinatorial jet yield strongly. In semi-central collisions (30–50%), triggering strongly enhances the jet yield at high (> 20 GeV/c) transverse momenta.

The lower panels of Fig. 8.1 show the ratio of the transverse momentum distributions of triggered full jets to that of minimum bias charged jets for central (left) and semi-central (right)

[a]Combining information from the EMCal and central barrel is not trivial, as it requires correcting the energy deposits in the EMCal for charged particle trajectories, and converting the (partially) contained EMCal showers to a measure of transverse momentum. As this chapter only serves as a 'proof of principle', the readers is referred to e.g. [120] for further information.

collisions[b]. In semi-central events, the jet yield at high p_T is five times larger than the minimum bias charged jet yield.

The gain in jet yield of using triggered events in future data taking periods might differ from that presented in Fig. 8.1, as it depends strongly on the trigger configuration. In minimum bias data taking (and in other data taking schemes as well) not all observed events are recorded. The number of events, of a particular trigger, that is observed in order for one event to be recorded is referred to as the *prescale factor*. In 2011, a centrality-dependent prescale was used for the minimum bias data taking. For the most central collisions, the minimum bias prescale factor was approximately two times smaller than the jet trigger prescale factor, for more peripheral minimum bias collisions, a larger factor was used (which is visible in Fig. 3.8, where the centrality distribution is not uniform). The gain in statistics of using triggered data will therefore depend on the prescale factors that are used, and the event rate delivered by the LHC.

8.2.2 $v_2^{\text{calo jet}}$ in the presence of a trigger bias

As explained in § 3.2.4, the EMCal detector has a limited acceptance ($|\eta| < 0.7$, $1.4 < \varphi < \pi$). Events are triggered in the EMCal when the energy deposited in a limited area exceeds a predefined threshold; no distinction however can be made between energy originating from parton showers and energy resulting from uncorrelated background. As the average energy flow - as well as the magnitude of the fluctuations of the underlying event energy density - is larger along the event plane direction than in the perpendicular direction, triggering leads to an *event plane bias*: events in which the event plane angle points towards the EMCal detector are more likely to meet the triggering criteria. A bias in the event plane distribution in and of itself has no effect on v_n, but since full jets can only be measured within the EMCal acceptance, the formalism of Eq. 4.1 can not directly be applied, which will be illustrated by a simple Monte Carlo exercise in which the EMCal trigger is emulated. The Monte Carlo setup works as follows:

- Thermal events (see § 5.1) are generated, sampling the event plane orientation $\Psi_{\text{EP, 2}}$ randomly from a uniform distribution between $-\frac{\pi}{2}$ and $\frac{\pi}{2}$ from a uniform distribution for each event; p_T-differential v_2 is added (red line in the two lower panels of Fig. 8.2) following the procedure as described in § 5.1;
- To mimic EMCal acceptance, tracks of which v_2 will be calculated, are only stored when they are generated within the EMCal acceptance. The event plane angles will be reconstructed using *all* tracks however, as in data analysis these would be reconstructed by the V0 system;
- Two types of triggers are modeled:
  - A simple *(charged) particle* trigger, which accepts events *only* when a track of $p_T >$ 5GeV/c is found within the EMCal acceptance;
  - A *patch* trigger, which accepts events *only* when the total energy that is deposited in the EMCal acceptance exceeds a threshold. This patch trigger approaches the triggering mechanism of the EMCal more closely, but is less illustrative than the particle trigger;
- Analysis is performed on both event types, using Eq. 4.1 to evaluate v_2.

Generated v_2 (red dashed line) and v_2 measured in single particle triggered (green triangles) and patch triggered (blue squares) events are shown in Fig. 8.2. In both trigger scenarios, at

[b]A similar remark as that made on the comparison between ATLAS v_2^{jet} and ALICE $v_2^{\text{ch jet}}$ in Ch. 7 should be made here: the p_T scales of both jet spectra are different, therefore only a qualitative comparison at high p_T should be made.

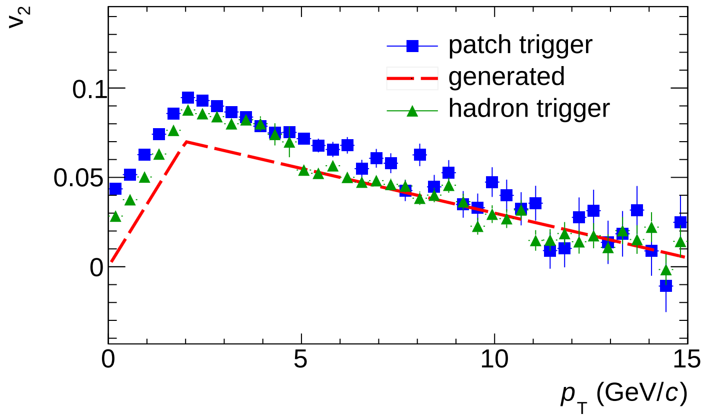

Figure 8.2: Generated v_2 (red dashed line) and v_2 measured in single particle triggered (green triangles) and patch triggered (blue squares) events.

low momenta, the measured v_2 does not correspond to the generated v_2. At high transverse momenta however, v_2 is recovered correctly. This effect can be understood by considering trigger efficiencies ϵ_{in} and ϵ_{out} to Eq. 4.1,

$$v_2 = \frac{1}{\mathcal{R}_2} \frac{\pi}{4} \frac{\epsilon_{\text{in}} N_{\text{in}} - \epsilon_{\text{out}} N_{\text{out}}}{\epsilon_{\text{in}} N_{\text{in}} + \epsilon_{\text{out}} N_{\text{out}}} \tag{8.1}$$

where $\epsilon_{\text{in}}(\epsilon_{\text{out}})$ is the efficiency of measuring the in(out-of)-plane p_{T}-differential jet yield. v_2 will correctly be retrieved when $\epsilon_{\text{in}} = \epsilon_{\text{out}}$. Because the particle spectrum in the in-plane direction has a higher mean p_{T} than the spectrum in the out-of-plane direction (as the energy flow in this direction is larger), this condition is, in events selected using the simulated particle trigger, only met for v_2 measured at 5 GeV/c and upwards. In the case of the jet patch trigger, a similar argumentation can be followed, but the threshold p_{T} at which $\epsilon_{\text{in}} = \epsilon_{\text{out}}$ is not clearly defined as a minimum total energy in a patch does not put constraints on the minimum p_{T} of a track *within* the patch (e.g. 10 tracks of 1 GeV/c lead to a similar trigger signal as 1 track of 10 GeV/c).

In reality, calculating the exact threshold at which $\epsilon_{\text{in}} = \epsilon_{\text{out}}$ from e.g. hardware settings is complicated by the fact that triggering is done on on uncorrected energy within an EMCal patch, rather than on the subtracted jet energy, meaning that fluctuations of the underlying event, and even mis-calibrations of the detector, can lead to triggering. The p_{T} threshold at which the trigger bias disappears from the v_2^{jet} measurement using EMCal jets in EMCal triggered events, can however obtained from data by directly measuring the in-plane and out-of-plane trigger efficiencies.

The p_{T}-dependent trigger efficiency, $\varepsilon_{\text{trigger}}(p_{\text{T}})$, is obtained from data as

$$\varepsilon_{\text{trigger}}(p_T) = \frac{N(p_{\text{T}})|_{\text{minimumbias + trigger}}}{N(p_{\text{T}})|_{\text{minimum bias}}}. \tag{8.2}$$

which is the (p_{T}-differential) ratio of the jet spectrum measured in events which pass the minimum bias *and* trigger criteria ($N(p_{\text{T}})|_{\text{minimumbias + trigger}}$) to the jet spectrum measured in

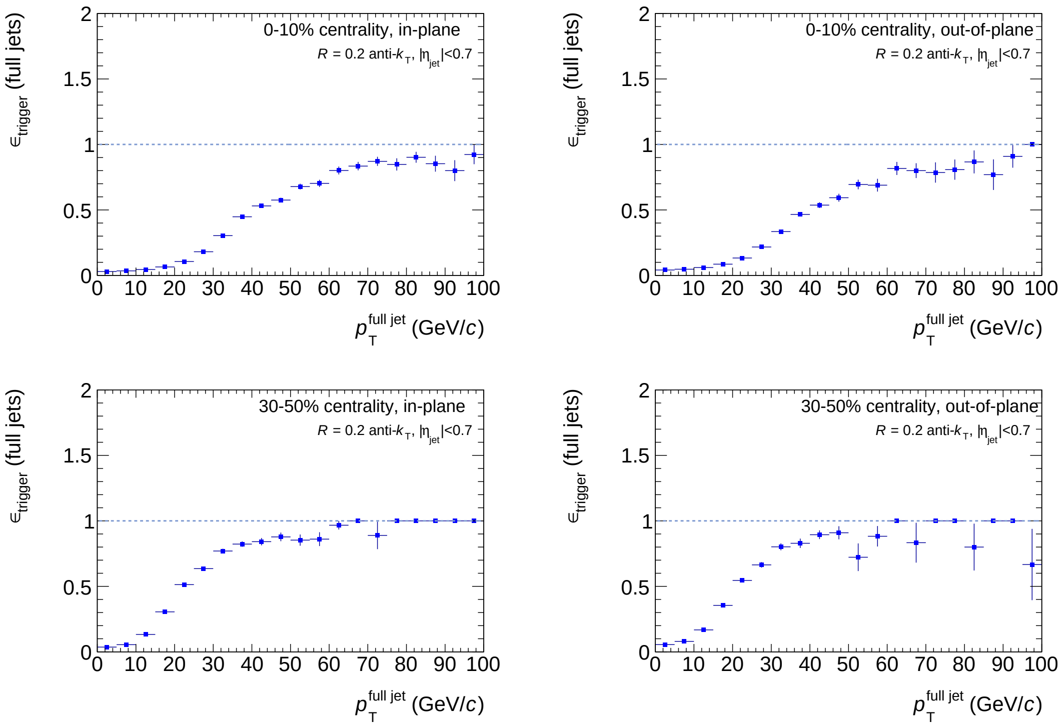

Figure 8.3: Efficiency of the EMCal jet patch trigger as function of $p_{\mathrm{T}}^{\mathrm{jet}}$ for N_{in} (left) and N_{out} (right) for 0–10% (top) and 30–50% collision centrality (bottom). Statistical uncertainties only.

triggered events $(N(p_{\mathrm{T}})|_{\text{minimum bias}})$[c]. These efficiencies are shown in Fig. 8.3 for 0–10% (top) and 30–50% (bottom) collision centrality, with in-plane efficiencies on the left and out-of-plane efficiencies on the right.

The ratios of in-plane and out-of-plane trigger efficiencies are given for 0–10, 10–20, 20–30 and 30–50% collision centrality in Fig. 8.4; for jet $p_{\mathrm{T}} > 40$ GeV/c the ratio is equal to one within statistical uncertainties for all centralities (for 30–50% collision centrality the efficiencies are equal at even lower p_{T}). This means that v_2^{jet} can be measured via the method of Eq. 4.1 if jets of sufficiently high p_{T} ($>$ 40GeV/c) are chosen for analysis only.

8.2.3 Expectations for 2015

So far, only events recorded in 2010 and 2011 have been considered. During the 2015 - 2018 period (*run 2*), the LHC will accelerate lead ions to $\sqrt{s_{\mathrm{NN}}}$= 5.02 TeV. Although this data was not available for analysis at the time of writing, projections of the systematic and statistical uncertainties of future measurements can be made using simple assumptions and taking into account the planned triggering schemes. Fig. 8.5 shows expected *relative* uncertainties on $v_2^{\text{calo jet}}$

[c] By requiring that events pass both the minimum bias *and* trigger criteria in the enumerator of Eq. 8.2, the minimum bias prescale factor is canceled in the division.

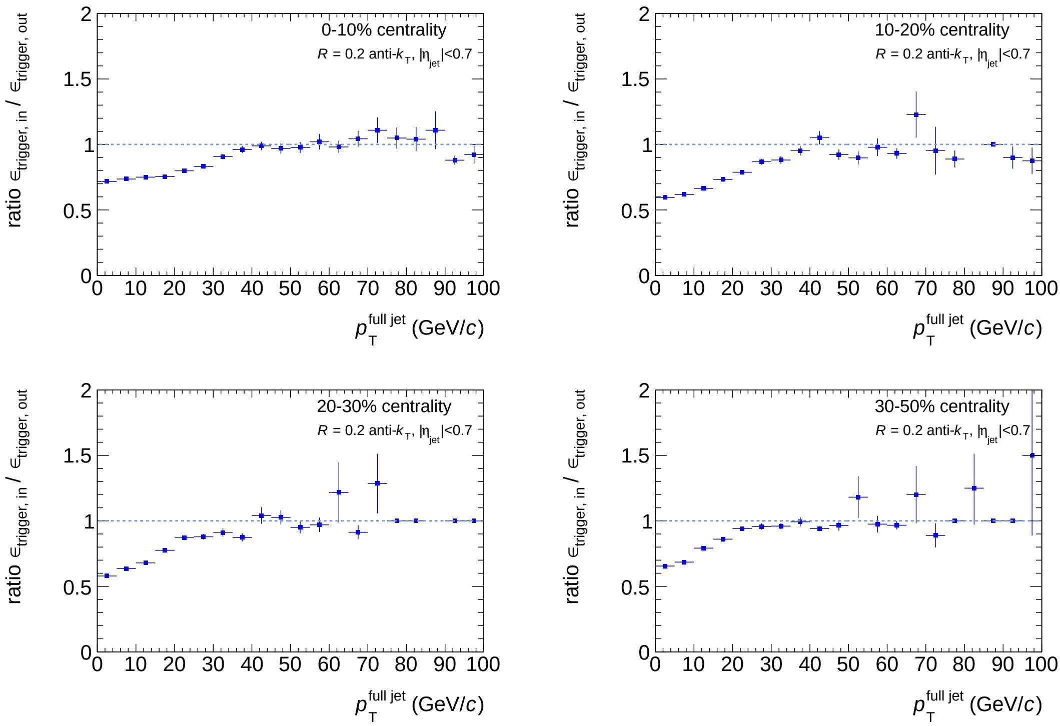

Figure 8.4: The ratios of in-plane and out-of-plane trigger efficiencies, using the EMCal jet patch trigger, for 0–10, 10–20, 20–30 and 30–50% collision centrality. Statistical uncertainties only.

of full jets, measured using the EMCal and DCal[d] detectors together with the central barrel tracking detectors.

To calculate the *relative* uncertainties as shown in Fig. 8.5, an expected value of $v_2^{\text{jet}} = 0.08$ is used, with an absolute shape uncertainty of 0.012 and an absolute correlated uncertainty of 0.009 (corresponding to the values found in the charged jet $v_2^{\text{ch jet}}$ in $60 < p_{\text{T}}^{\text{jet}} < 70$ GeV/c interval, see table 6.1). It is assumed in this study, that the magnitude of the systematic uncertainties does not strongly depend on the jet yield; the reference p_{T} range of $60 < p_{\text{T}}^{\text{jet}} < 70$ GeV/c however is still chosen such as to avoid including any trailing effects from combinatorial jets at low transverse momenta or from limited statistics at high p_{T}. The relative expected shape uncertainties are shown in Fig. 8.5 as green bars, the expected relative correlated uncertainties as dark blue bars.

The statistical uncertainty on $v_2^{\text{calo jet}}$ is evaluated from the statistical uncertainties on $R = 0.2$ PYTHIA jet yields, generated at $\sqrt{s} = 5.02$ TeV. The PYTHIA jet yields are scaled by the expected N_{coll} in 0–10% collision centrality. Energy loss effects are accounted for by multiplying the PYTHIA jets yields by an R_{AA} of 0.5. A total of 150 million minimum bias events is expected in 2015, complemented by $\approx 210\ \mu b^{-1}$ of EMCal triggered events, which are used in

[d]The DCal - not treated in Ch. 3 - is a calorimeter, commissioned in 2015, opposite in azimuth from the EMCal. The combined acceptance - taking into account edge effects - of the EMCal, DCal is 1.6 times larger than the EMCal acceptance. The DCal is visible on the event display in Fig. 3.6.

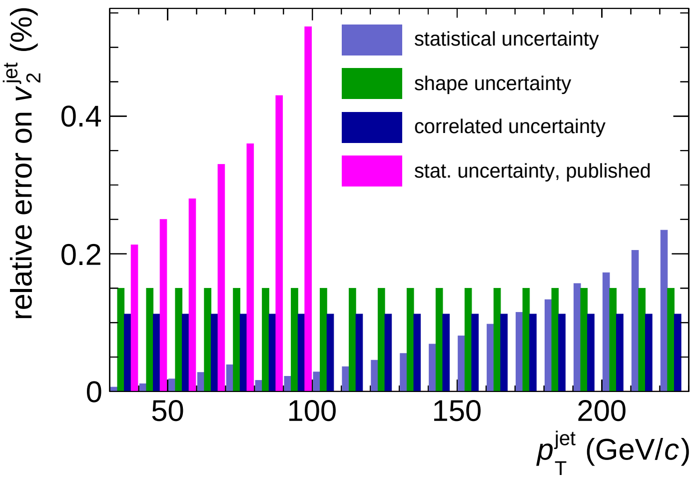

Figure 8.5: Relative uncertainty on $v_2^{\text{ch jet}}$ in 0–5% collision centrality (magenta) and expected relative uncertainties (green, light blue and dark blue) on $v_2^{\text{calo jet}}$ for the 2015 data sample at $\sqrt{s_{\text{NN}}}$= 5.02 TeV, obtained from scaled PYTHIA simulations.

the evaluation of v_2^{jet} only for transverse momenta higher than 80 GeV/c (to avoid the trigger bias as explained in the preceding section). The expected relative uncertainties - also evaluated against a constant $v_2^{\text{jet}} = 0.08$ - are shown in Fig. 8.5 as light blue bars. As a reference, the relative statistical uncertainty on $v_2^{\text{ch jet}}$ in 0–5% collision centrality (from the measurement presented in Ch. 7) is shown as magenta bars.

The projected statistical uncertainties for the 2015 data taking period are smaller than those of the 2010 and 2011 data samples combined, indicating that repetition of the v_2^{jet} measurement on new data could more strongly constrain model predictions. The effect of larger multiplicities at $\sqrt{s_{\text{NN}}} = 5.02$ TeV - which would increase the magnitude of background fluctuations and the combinatorial jet yield - is not taken into account however, but expected to be small, as the expected increase in multiplicity is around 20%.

9 | Summary

This work was aimed at determining properties of the quark-gluon plasma (QGP), a phase of matter created at extreme densities or temperatures, in which quarks and gluons are not confined into hadrons but can move freely over long distances. The QGP can be created in relativistic heavy-ion collisions, and is studied by measuring the production rate of highly energetic partons (quarks or gluons), which are emitted in initial hard scatterings prior to the QGP formation. These highly energetic partons cannot be observed directly, but fragment into collimated showers of particles - *'jets'* - that can be reconstructed in experiment.

The production rate of hard partons can be calculated using quantum-field theory and the known parton distributions in the proton and neutron. When produced in a dense medium, partons will lose energy via gluon radiation and inelastic scatterings. These different types of parton-plasma interactions are expected to give a different dependence of parton energy loss on the length of the parton trajectory L through the QGP. Jet production in the laboratory can therefore be used for QGP 'tomography': the modification of the parton shower, which manifests itself as a modification of the measured jet yield, is used to derive plasma properties.

In this work, the dependence of the energy loss of the parton on path length L is studied directly by looking at jet production relative to the symmetry axis of Pb–Pb collisions. These symmetries are generated because in non-central heavy-ion collisions, the initial overlap region of the colliding nuclei projected into the plane perpendicular to the beam direction has an approximately elliptic shape. The amplitude of the modulation of jet production around the collision's symmetry axis is quantified by coefficient $v_2^{\text{ch jet}}$.

The $v_2^{\text{ch jet}}$ measurement is challenging as the general modulation of the yield of particles that do not belong to the jet needs to be separated from the $v_2^{\text{ch jet}}$ signal. It is unique however in the sense that path-length dependence of parton energy loss is quantified along different paths *within* the same event, testing L dependence at equal global conditions (e.g. temperature and density), contrary to the R_{AA} (Eq. 2.31) or R_{CP} (Eq. 2.39) measurements in which energy loss differences between different systems are compared.

The observed $v_2^{\text{ch jet}}$ in non-central collisions indicates that partons lose energy while traversing the QGP. The indication of non-zero $v_2^{\text{ch jet}}$ in central collisions (where there is a full overlap of the nuclei) indicates that deviations from a homogeneous distribution of nucleons within the overlap region might play an important role in generating energy loss as well, analogous to effects from fluctuations that were established by using higher harmonic v_n studies of particles at lower momentum. Future, high-accuracy measurements, will be necessary however to further elucidate the exact nature of parton energy loss in the QGP, and to more precisely determine power n in the energy loss expectation $\langle \Delta E \rangle \propto L^n$.

Part IV

Appendix

A | Track selection and TPC non-uniformity

The track selection criteria (Ch. 3) are chosen to optimize track *length*, and thereby p_{T}, since p_{T} is determined from the track curvature (Eq. 3.2), which can most accurately be measured when tracks have great length. The complete set of track selection criteria is:

- Maximum DCA in the transverse plane: 2.4 cm;
- Maximum DCA in the longitudinal (z) direction: 3.2 cm;
- Maximum χ^2 between tracks reconstructed in the TPC and TPC tracks which are constrained to the primary interaction vertex is 36;
- Maximum fraction of TPC clusters shared with another track of 0.6;
- Minimum of crossed TPC rows of 70;
- Minimum ratio of crossed rows over geometrically findable clusters in the TPC is 0.8;
- Maximum of the χ^2 between space points in the TPC and the reconstructed track is 4;
- Daughter particles of kink decays are rejected;
- An ITS and TPC *refit* is required, meaning that, as a last tracking pass, a complete fit over all assigned clusters is performed in the TPC and ITS: both refits must be successful;
- Maximum of the χ^2 between space points in the ITS and the track is 36.

As explained in § 3.3.3, two classes of tracks are used. The first class requires at least three hits per track in the ITS, with at least one hit per track in the SPD. The second class contains tracks without hits in the SPD, in which case the primary interaction vertex is used as an additional constraint for the momentum determination. The η, φ distribution of these two classes of tracks is shown in the upper two panels of Fig. A.1 (left: tracks with at least three hits in the ITS, right: the complementary tracks).

In 2011, the efficiency of data taking within certain sectors of the TPC was not constant. This is illustrated in the lower panels of Fig. A.1, where the η, φ distribution of selected tracks is shown, split again into the two classes of tracks. In the lower right panel, at negative η and around $\varphi = 4.6$, a loss of about 50% of all tracks is seen, resulting from the lower TPC efficiency.

Non-uniformity in azimuth invalidates the hypothesis that Eq. 4.27 can be used as description of the underlying event energy density. In addition, the reduced efficiency introduces artefacts in the jet distribution, as illustrated in Fig. A.2 (left), which shows the η, φ distribution of jets measured in these events. A depletion of jet yield is visible in the region of reduced TPC efficiency. In runs that are affected by TPC non-uniformity, track and jet selection is therefore limited to the interval $0 < \varphi < 4$. Limiting the jet and track selection to $0 < \varphi < 4$ for the events with non-uniform TPC acceptance removes any bias from reduced efficiency from both the underlying event description and the $v_2^{\mathrm{ch\ jet}}$ measurement.

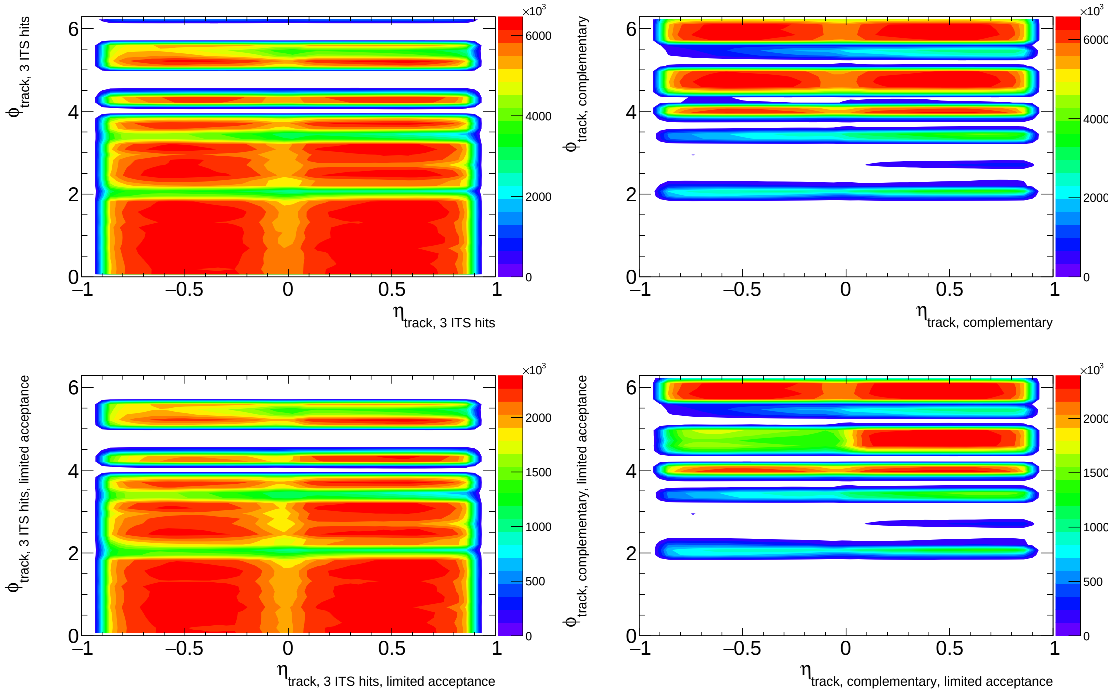

Figure A.1: η, φ distribution of selected tracks is shown, split into the two classes of tracks (left: tracks with at least three hits in the ITS, right: the complementary tracks). The upper panels show distributions obtained in runs in which the TPC efficiency is uniform in η, φ. In the lower right panel, at negative η and around $\varphi = 4.6$, a loss of about 50% of all tracks is seen, resulting from the lower TPC efficiency.

Figure A.2 shows, as validation, v_2 and v_3 coefficients obtained from fitting Eq. 4.27 to data in events in which the TPC is fully efficient (dashed lines) and in the events in which the efficiency is limited (solid lines), and the fit is performed on data gathered between $0 < \varphi < 4$. No difference is found between the extracted v_n values.

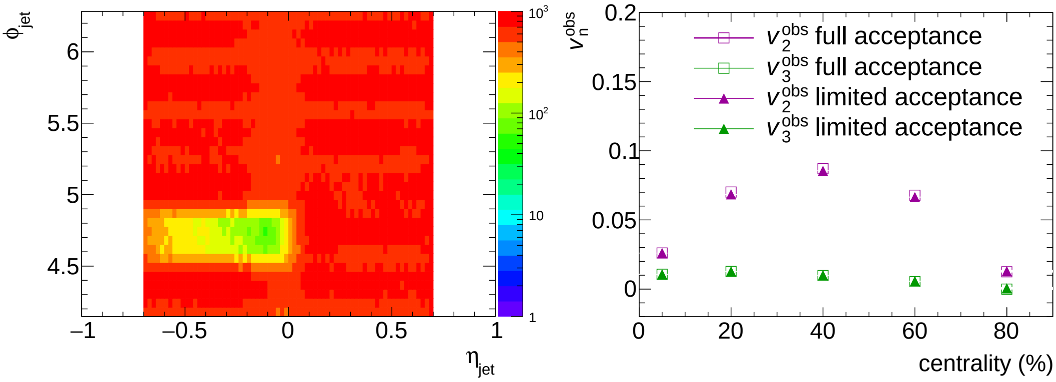

Figure A.2: Left: η, φ distribution of jets measured in events with non-uniform TPC efficiency. A depletion of jet yield is visible in the region of reduced TPC efficiency. Right: v_2 and v_3 coefficients obtained from fitting Eq. 4.27 to data in events in which the TPC is fully efficient (open squares) and in the events in which the efficiency is limited (full circles), and the fit is performed on data gathered between $0 < \varphi < 4$.

B | Some notes on p-values

B.1 Hydrodynamic flow and the underlying event

In § 4.4 it is explained that the fit of Eq. 4.27 to the data is accepted only if its p-value, derived from a χ^2 statistic, is larger than 0.01. The χ^2 statistic of a fit is given by

$$\chi^2 = \sum_{n=0}^{i} \left(\frac{x_i - \mu_i}{\sigma_i} \right)^2, \tag{B.1}$$

where x_i represents the content of bin i, μ_i is the fit value evaluated at the bin center, and σ_i is the statistical uncertainty on the x_i. In a simple scenario, where the number of bins (and consequently the number of degrees of freedom) in a fitted histogram is equal for each event, a goodness of fit criterion could be imposed by selecting directly on χ^2[a]. However, since the binning of the histogram to which Eq. 4.27 is fitted varies from event to event, k also varies to event. The standard deviation of the χ^2 distribution is $\sqrt{2k}$, rendering χ^2 or $\widetilde{\chi}^2$ suboptimal parameters to use directly as a goodness of fit criterion, as the absolute width of the distribution, and thus the absolute criterion for selecting certain confidence intervals, changes event-by-event.

The p-value, which is the probability of finding a statistic (i.e. χ^2) *at least as far away from the hypothesis* as the observed one, is used as a criterion which can be constructed independent of k. Analytically it is obtained from the χ^2 cumulative distribution function (CDF) with the appropriate number of degrees of freedom k, and $x = \chi^2$,

$$p = 1 - \mathrm{CDF}(k, x) = 1 - \left(\frac{1}{\Gamma\left(\frac{k}{2}\right)} \gamma \left[\frac{k}{2}, \frac{x}{2} \right] \right), \tag{B.3}$$

where Γ is the Gamma function and γ the lower incomplete gamma function. The p-value distribution itself is uniform when the null-hypothesis (i.e. Eq. 4.27) perfectly describes the observed data, which is only approximately true in this specific case, for two reasons.

The χ^2 statistic relies on the assumption of normally distributed data. The uncertainties on x_i are not truly normally distributed (as explained in § 4.4); therefore, it is expected that the data will not exactly follow the χ^2 distribution. Furthermore, the hypothesis of Eq. 4.27 is purposefully incomplete: it is known that higher harmonic coefficients (v_4, v_5, etc. are non-zero,

[a] Or on the reduced χ^2,

$$\widetilde{\chi}^2 = \frac{\chi^2}{k}, \tag{B.2}$$

where k denotes the number of degrees of freedom. Since the χ^2 distribution has its mean at k, $\widetilde{\chi}^2$ has a mean of 1.

and in addition to track-to-track correlations from hydrodynamic expansion of the background, non-flow effects (jets, resonance decays, etc. will play a role in generating structures in $\Delta\varphi_n$ as well.

To explore and quantify the effect of these issues, the χ^2 goodness of fit criterion is tested both in data and in a simple 'Monte Carlo' model[b]. This exercise starts by performing a normal analysis pass over the data. For each event, v_2 and v_3 are estimated by fitting of Eq. 4.27; information on the fit (such as p-value and χ^2) is stored. After this, all tracks in the event are assigned 'new' azimuthal angles, drawn this time randomly from the functional description of Eq. 4.27 itself (with v_2, v_3 and event plane angles fixed to the values just found by fitting in the same event). Eq. 4.27 is then fitted *again*, to the 'simulated' azimuthal distribution; information from this ideal fit is also stored. The procedure is repeated for all events in the data sample. Following this simple routine, the effect of higher harmonics, non-flow and non-normal uncertainties on the p-value and χ^2 statistic is quantified.

Figure B.1 shows p-values as function of centrality (top left), the correlation of $\widetilde{\chi}^2$ and p-value (top right), $\widetilde{\chi}^2$ as function of centrality (bottom left) and percentage of accepted fits according to the $p > 0.01$ criterion as function of centrality (lower right) obtained from fitting Eq. 4.27 to *simulated* azimuthal distributions (the 'Monte Carlo' case). As expected, the p-value distributions are uniform and the $\widetilde{\chi}^2$ distributions are centered around 1. 99% of fits is accepted at the most central collisions (which corresponds to the $p > 0.01$ criterion), at higher collision centralities this number decreases a bit, most likely as sparsely filled bins hinder the accuracy of the fitting procedure.

Figure B.2 shows the same distributions, but obtained from fitting Eq. 4.27 to actual, unaltered data. The p-value distribution is no longer flat - an effect which is more pronounced at higher centrality - and the $\widetilde{\chi}^2$ distributions have a slightly displaced mean. The deviations of these statistics from their behavior in Fig. B.1 is expected, as it is known that Eq. 4.27 gives a limited description of the underlying event's structure, and in addition to this, the uncertainties on the data to which Eq. 4.27 are fitted are not strictly normally distributed. The deviations from the expected behavior as small however, and the p-value derived from the χ^2 statistic is considered a just choice.

B.2 Significance: a short addendum

Figure 7.1 shows coefficient $v_2^{\text{ch jet}}$, the compatibility of which is tested against the hypothesis $v_2 = 0$ by calculating a p-value, using Eq. 7.1, over the full p_{T} range of the measurement. The (statistical) uncertainties on the $v_2^{\text{ch jet}}$ measurement increase in magnitude at high p_{T} however. Splitting up the data into independent sub-ranges in p_{T} and assessing the p-value in these ranges allows for quantifying *which* parts of the jet spectra contribute most strongly to the significance of the measurement. Since the χ^2 test of Eq. 7.1 is performed for $n-2$ degrees of freedom (with n the number of measured data points), a minimum of three data points is necessary to evaluate the p-value. Testing is therefore limited to only two p_{T} sub-ranges per centrality interval: 30–60 and 60–100 GeV/c for 0–5% collision centrality, and 20–60 and 60–90 GeV/c for 30–50% collision centrality.

The p-values found in these sub-ranges are given in Tab B.1; the values of nuisance parameters ϵ_{corr} and ϵ_{shape} are shown as well, where ϵ_{corr} is expressed in units of the correlated systematic

[b]'Monte Carlo' is used in quotation marks, as this simple model relies on reshuffling of real data, rather than generating independent events, as done for other Monte Carlo studies in this dissertation.

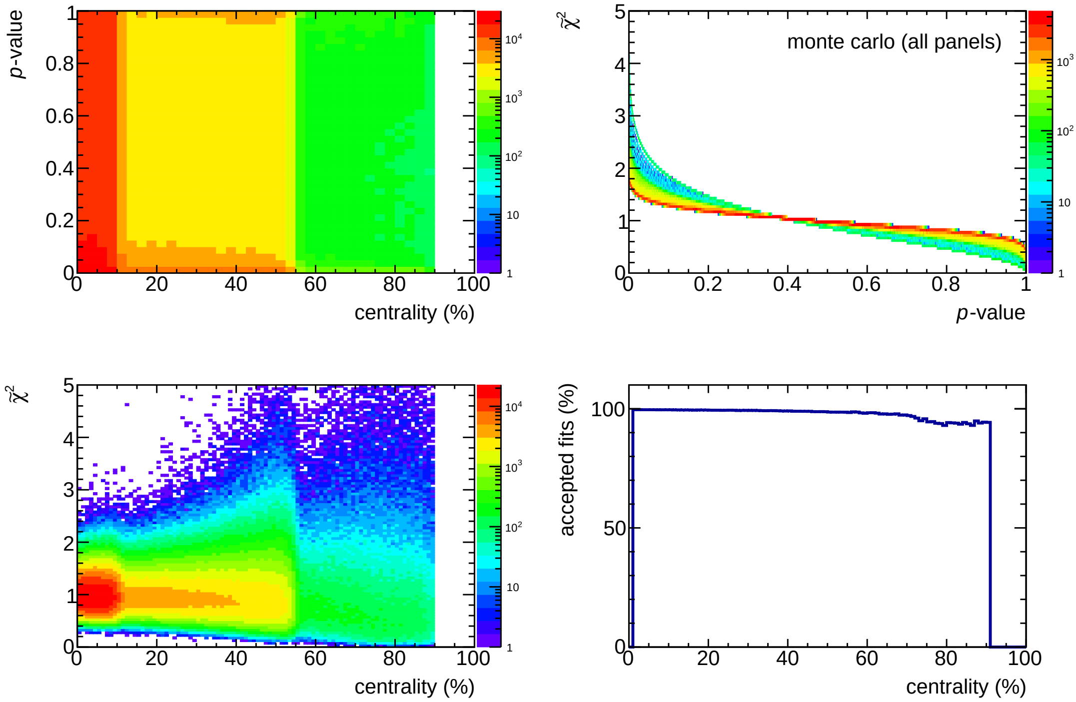

Figure B.1: p-values as function of centrality (top left), the correlation of $\widetilde{\chi}^2$ and p-value (top right), $\widetilde{\chi}^2$ as function of centrality (bottom left) and percentage of accepted fits according to the $p > 0.01$ criterion as function of centrality (lower right) obtained from fitting Eq. 4.27 to *simulated* azimuthal distributions.

centrality (%)	0-5			30-50		
$p_{\mathrm{T}}^{\mathrm{jet}}$ range (GeV/c)	30–100	30–60	60–100	20–90	20–60	60–90
ϵ_{corr}	-0.80	-0.62	-1.03	-1.47	-0.91	-0.61
$\epsilon_{\mathrm{shape}}$	-0.0.36	-0.033	-0.041	-0.064	-0.071	-0.016
p-value	0.12	0.07	0.02	0.000888	0.0015	0.022

Table B.1: p-values and nuisance parameters ϵ_{corr} and $\epsilon_{\mathrm{shape}}$ for sub-ranges in p_{T} and evaluated over the full p_{T} range for 0–5 and 30–50% collision centrality.

error (a value of 1 means a shift up by 1 standard deviation), while $\epsilon_{\mathrm{shape}}$ is presented in terms of absolute $v_2^{\mathrm{ch\ jet}}$ values (a shift by 0.05 changes $v_2^{\mathrm{ch\ jet}}$ by 0.05).

At face value, the p-values for different p_{T} ranges in 0–5% collision centrality are surprising, as the compatibility with 0 is stronger over the whole p_{T} range ($p = 0.12$) than when taken over sub-ranges ($p = 0.07$ and $p = 0.02$). All p-values however still indicate that the results lie within 1.5–2 standard deviations of the $v_2^{\mathrm{ch\ jet}} = 0$ hypothesis; as the number of data points over which Eq 7.1 is evaluated is small, fluctuations may play a large role in generating the differences between the p-values.

As can be seen in Table B.1, the deviation from $v_2^{\mathrm{ch\ jet}} = 0$ is mostly significant at low p_{T}.

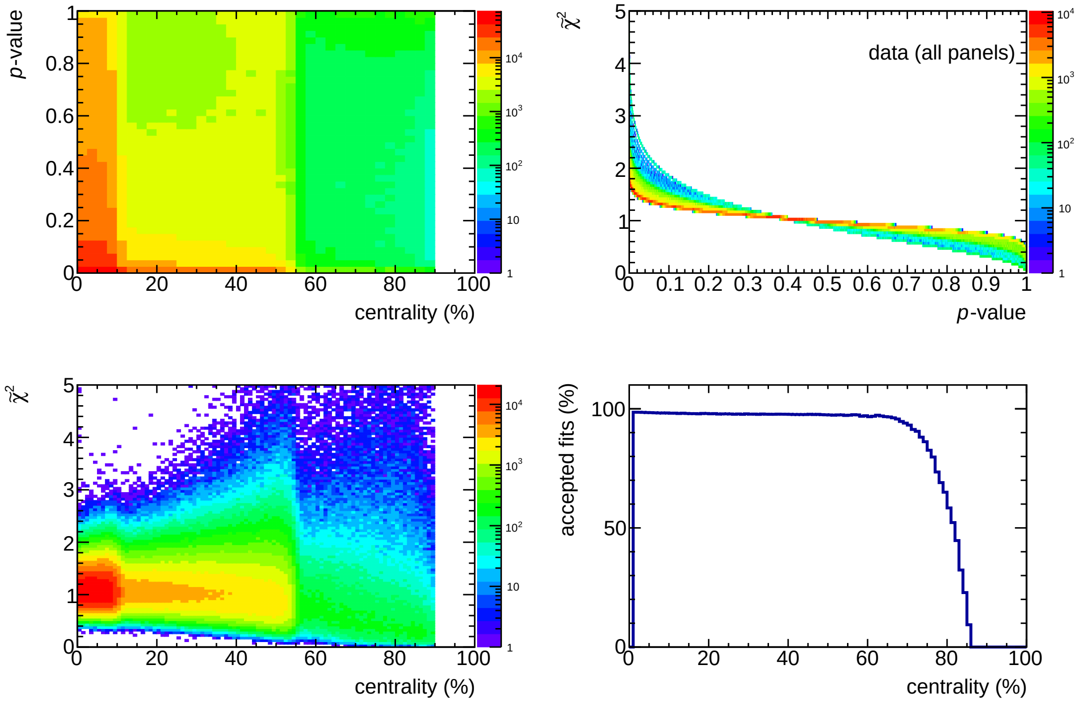

Figure B.2: p-values as function of centrality (top left), the correlation of $\widetilde{\chi}^2$ and p-value (top right), $\widetilde{\chi}^2$ as function of centrality (bottom left) and percentage of accepted fits according to the $p > 0.01$ criterion as function of centrality (lower right) obtained from fitting Eq. 4.27 to unaltered data.

At high transverse momenta, for both central and semi-central collisions, $v_2^{\text{ch jet}}$ is consistent with zero within two standard deviations ($p = 0.02$ and $p = 0.022$ respectively).

The p-value evaluation can also be used to better understand how unfolding changes the jet spectra. The effect that unfolding has on the significance and uncertainties on the data points is explored by looking at $v_2^{\text{ch jet}}$ obtained from evaluating Eq. 4.1 using the *measured* spectra *prior* to unfolding rather than using the unfolded jet spectra. This 'uncorrected' $v_2^{\text{ch jet}}$ is shown in Fig. B.3, for 0–5% (left) and 30–50% (right) collision centrality.

Since jet production follows a steeply falling, asymmetric distribution, the expected net effect of unfolding is that jet counts are moved from low to higher p_{T}[c]. As can be seen in Fig. B.3, the statistical uncertainties at high p_{T} are large on $v_2^{\text{ch jet}}$ obtained from the measured jet spectra; in the final $v_2^{\text{ch jet}}$ results (Fig. 7.1), these uncertainties are smaller. To quantify the reduction of the statistical uncertainties by unfolding, the χ^2 statistic can be evaluated for both the uncorrected and the unfolded $v_2^{\text{ch jet}}$. Since the $v_2^{\text{ch jet}}$ prior to unfolding has no systematic uncertainties,

[c]Unfolding redistributes the jet spectra in p_{T} (i.e. moves jets to lower and higher p_{T}), according to probabilities that are quantified as the combined response matrix. Since the measured jet spectra are steeply falling, it is expected that the unfolding moves more counts from low to high p_{T} than vice versa by the simple reason that there *are* more jets to be moved from low to high p_{T} than the other way around.

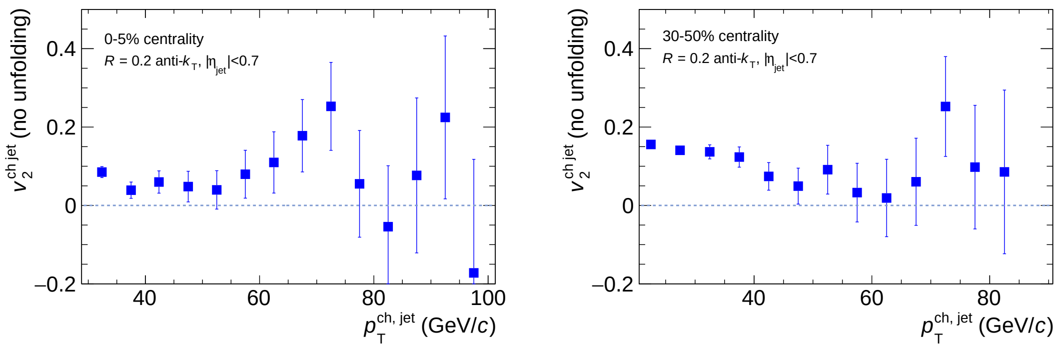

Figure B.3: Coefficient $v_2^{\text{ch jet}}$ prior to unfolding for 0–5% (left) and 30–50% (right) collision centrality, statistical uncertainties only.

centrality (%)	0-5		30-50	
p_T^{jet} range (GeV/c)	60–100	50–100	60–90	50–90
$\chi^2_{\text{uncorrected}}$	13.5	19.2	5.0	7.2
$\chi^2_{\text{unfolded, stat only}}$	27.0		8.0	

Table B.2: χ^2 statistic for $v_2^{\text{ch jet}} = 0$, evaluated over sub-ranges of the measurement, using only statistical uncertainties, for $v_2^{\text{ch jet}}$ evaluated on measured jets (prior to unfolding) and unfolded jets.

Eq. 7.1 must be reduced to the 'standard' χ^2 definition,

$$\chi^2 = \sum_{i=1}^{n} \frac{(v_{2,i} - \mu_i)^2}{\sigma_i^2}. \tag{B.4}$$

Table B.2 gives the χ^2 statistics for compatibility with $v_2 (= \mu_i) = 0$ in the high p_T range (60-100 GeV/c for 0–5% and 60–90 for 30–50% collision centrality). The χ^2 after unfolding is larger than before unfolding, confirming that the statistical uncertainties at high p_T are decreased. The change is (very roughly) compatible to evaluating the χ^2 values over a p_T range that is extended by 10 GeV/c to start at 50 GeV/c (as also given in the table), indicating that unfolding indeed effectively moves jets to higher p_T, thereby reducing the statistical uncertainty on $v_2^{\text{ch jet}}$ for highly energetic jets.

C | Event plane angles from different η intervals

The derivation of weights χ, introduced in § 4.3, is not straightforward, and starts with the entity

$$n(\Psi_{\mathrm{EP},\ n} - \Psi_n), \tag{C.1}$$

which is the difference between the orientation of the event plane angle ($\Psi_{\mathrm{EP},\ n}$) and the symmetry plane angle (Ψ_n) at order n, multiplied by order n (the use of this entity is motivated in § 4.3.3). The distribution of this difference can be written as [87]

$$\frac{\mathrm{d}P}{\mathrm{d}n(\Psi_{\mathrm{EP},\ n} - \Psi_n)} = \int \frac{v_n' \mathrm{d}v_n'}{2\pi\sigma^2} \times \left(- \frac{v_n^2 + v_n'^2 - 2 v_n v_n' \cos[n(\Psi_{\mathrm{EP},\ n} - \Psi_n)]}{2\sigma^2} \right) \tag{C.2}$$

with

$$\sigma^2 = \frac{1}{2N} \frac{\langle w^2 \rangle}{\langle w \rangle^2} \tag{C.3}$$

in which v_n are the harmonic flow coefficients (determined from the same track sample as used in determining $\Psi_{\mathrm{EP},\ n}$, introduced in § 2.4.1), v_n' are flow coefficients 'measured' directly with respect to the impact parameter, N is the number of particles that is used to determine $\Psi_{\mathrm{EP},\ n}$ and w weights as used in the construction of the **Q**-vectors (see e.g. Eq. 4.16). Weights χ are defined as

$$\chi = \frac{v_n}{\sigma} \simeq v_n \sqrt{2N} \tag{C.4}$$

where the last equality holds when v_n is defined as anisotropy in the *number* of particles that is produced rather than anisotropy of total 'energy' flow (i.e. the number of particles weighted with their transverse momentum). The integral in Eq. C.2 can be solved analytically [86, 87], giving an expression for the average value for $\langle \cos(n[\Psi_{\mathrm{EP},\ n} - \Psi_n]) \rangle$ (which, will be shown in § 4.3.3, corresponds to the event plane resolution $\mathcal{R}$)

$$\langle \cos(n[\Psi_{\mathrm{EP},\ n} - \Psi_n]) \rangle = \frac{\sqrt{\pi}}{2\sqrt{2}} \chi_n \exp\left(\frac{-\chi_n^2}{4} \right) \times I_{(k-1)/2}\left(\chi_n^2/4\right) + I_{(k+1)/2}\left(\chi_n^2/4\right) \tag{C.5}$$

in which I_k is the k^{th} order modified Bessel function. At any given event plane resolution, χ can be solved numerically from Eq. C.5 by iterative techniques.

Part V

Miscellany

Samenvatting in het Nederlands

Jets - gecollimeerde bundels van deeltjes afkomstig van de fragmentatie van een parton - kunnen gebruikt worden om het quark-gluon plasma (QGP), dat in botsingen van zware ionen gecreëerd wordt, te onderzoeken, aangezien door het medium geïnduceerd energieverlies van partonen door verstrooiing en straling leidt tot een modificatie van het gemeten jet spectrum.

De afhankelijkheid van energieverlies op de afstand die een parton in het medium aflegt, verschaft inzicht in deze energieverliesmechanismen en kan bestudeerd worden door de productie van jets, relatief aan de orientatie van het tweede-orde symmetrievlak Ψ_2, te meten. De anisotropie van de jetproductie wordt gekwantificeerd als $v_2^{\text{ch jet}}$, de tweede coëfficient van de Fourierexpansie van de azimuthale verdeling van jets ten opzichte van Ψ_2,

$$\frac{\mathrm{d}N}{\mathrm{d}\left(\varphi_{\text{jet}} - \Psi_n\right)} \propto 1 + \sum_{n=1}^{\infty} 2v_n^{\text{jet}} \cos\left[n\left(\varphi_{\text{jet}} - \Psi_n\right)\right], \tag{C.6}$$

waar φ_{jet} de azimuthale hoek van de jet is en Ψ_n de richting van de vlakken van symmetrie van de initiële distributie van botsende nucleonen.

Dit proefschrift beschrijft de nieuwe resultaten van de ALICE $v_2^{\text{ch jet}}$ metingen in centrale en semi-centrale Pb–Pb botsingen en toont modelvoorspellingen en vergelijkingen met andere metingen welke gevoelig zijn voor energieverlies van partonen in het QGP.

De gebruikte data is verzameld in 2010 en 2011 en omvat 6.8×10^6 centrale (0–5%) botsingen en 8.6×10^6 semi-centrale (30–50%) botsingen waarvan de interactievertex binnen 10 cm van het noniname botsingenpunt ligt. Geladen-deeltjessporen worden gereconstrueerd door het Inner Tracking System en de Time Projection Chamber tussen $|\eta| < 0.9$; selectiecriteria zijn gericht op het optimaliseren van impulsresolutie en het behouden van volledige detectoracceptantie. Centralitietsbepaling en reconstructie van de symmetryvlakken $\Psi_{\text{EP},\,n}$ (de experimentele schatting van de initiële symmetrievlakken Ψ_n) wordt gedaan met behulp van de V0 detectoren, welke zich bevinden tussen $2.8 < \eta < 5.1$ en $-3.7 < \eta < -1.7$.

Jets worden gereconstrueerd middels het k_{T} en anti-k_{T} algoritme, geïmplementeerd in Fastjet. Anti-k_{T} jets worden gebruikt voor de bepaling van $v_2^{\text{ch jet}}$. De mediaan van de verdeling van de oppervlaktedichtheid van transversale impuls van k_{T} jets wordt per botsing bepaald en gebruikt als schatting van de gemiddelde energiedichtheid. De dominante stromingscoëfficienten v_2 en v_3 zijn gemodelleerd volgens

$$\rho_{\text{ch}}(\varphi) = \rho_0 \left(1 + 2\{v_2 \cos\left[2\left(\varphi - \Psi_{\text{EP},\,2}\right)\right] + v_3 \cos\left[3\left(\varphi - \Psi_{\text{EP},\,3}\right)\right]\}\right). \tag{C.7}$$

Parameters ρ_0 en v_n worden per botsing bepaald door Vgl. C.7 aan de data te fitten (zie Fig. C.1); $\rho_{\text{ch}}(\varphi)$ is de azimuthale distributie van de som van p_{T} voor deeltjes met $0.15 < p_{\text{T}} < 5$ GeV/c en $|\eta| < 0.9$. Het meten van $\Psi_{\text{EP},\,n}$ in het V0 systeem ondervangt correlaties tussen $\Psi_{\text{EP},\,n}$ en deeltjes, welke slechts op korte afstand bestaan. De gecorrigeerde jet impuls $p_{\text{T}}^{\text{jet}}$ wordt verkregen door de lokale achtergrondenergie $\rho_{\text{ch local}}$, bepaald middels integratie van $\rho_{\text{ch}}(\varphi)$ rond $\varphi_{\text{jet}} \pm R$,

$$\rho_{\text{ch local}} = \frac{\langle \rho_{\text{ch}} \rangle}{2R\rho_0} \int_{\varphi-R}^{\varphi+R} \rho_{\text{ch}}(\varphi)\mathrm{d}\varphi, \tag{C.8}$$

te vermenigvuldigen met het jet oppervlak A, en dit van de jet impuls af te trekken: $p_{\text{T}}^{\text{jet}} = p_{\text{T}}^{\text{raw}}$ - $\rho_{\text{ch local}}\ A$.

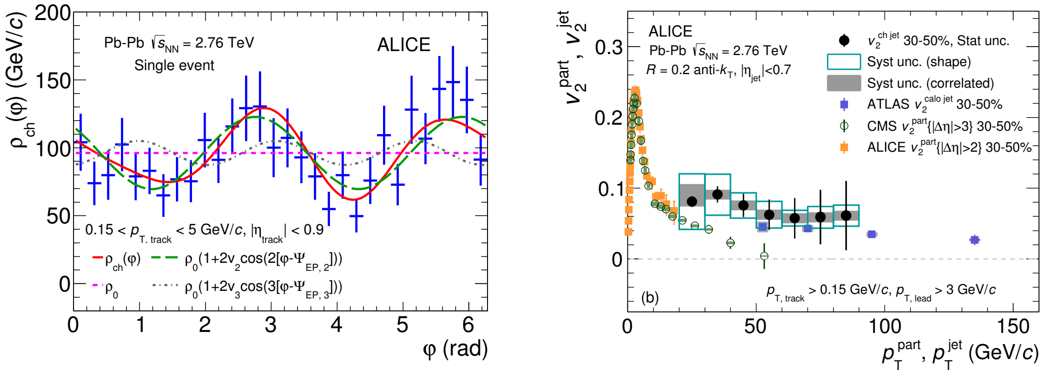

Figure C.1: Links: fit van Vgl C.7 aan de transversale energieverdeling van een botsing. Rechts: $v_2^{\rm ch\ jet}$ in semi-centrale botsingen, samen met $v_2^{\rm part}$ en $v_2^{\rm calo\ jet}$.

Coëfficient $v_2^{\rm ch\ jet}$ wordt bepaald uit het verschil tussen de gedeconvolueerde $p_{\rm T}$-differentiële jet spectra, gemeten langs de korte as van de botsingsellips ($N_{\rm in}$) en langs de lange as van de de botsingsellips ($N_{\rm out}$),

$$v_2^{\rm ch\ jet}(p_{\rm T}^{\rm jet}) = \frac{\pi}{4}\frac{1}{\mathcal{R}_2}\frac{N_{\rm in}(p_{\rm T}^{\rm jet}) - N_{\rm out}(p_{\rm T}^{\rm jet})}{N_{\rm in}(p_{\rm T}^{\rm jet}) + N_{\rm out}(p_{\rm T}^{\rm jet})}. \tag{C.9}$$

Vergelijking C.9 is afgeleid van Vgl. C.6 voor $n = 2$, door integratie over $\left[-\frac{\pi}{4}, \frac{\pi}{4}\right]$ en $\left[\frac{3\pi}{4}, \frac{5\pi}{4}\right]$ voor $N_{\rm in}$ en $\left[\frac{\pi}{4}, \frac{3\pi}{4}\right]$ en $\left[\frac{5\pi}{4}, \frac{7\pi}{4}\right]$ voor $N_{\rm out}$, met substitutie van $\Psi_{\rm EP,\ 2}$ door Ψ_2. De factor $\mathcal{R}_2 \equiv \langle\cos\left[2\left(\Psi_{\rm EP,\ 2} - \Psi_2\right)\right]\rangle$ corrigeert $v_2^{\rm ch\ jet}$ voor de eindige precisie waarmee $\Psi_{\rm EP,\ 2}$ Ψ_2 benadert. Om de jet spectra te corrigeren voor instrumentale resolutie en fluctuaties van de achtergrondenergie, wordt een hoekafhankelijke deconvolutie uitgevoerd van $N_{\rm in}$ en $N_{\rm out}$.

Systematische onzekerheden op $v_2^{\rm ch\ jet}$ zijn in twee categorieën onderverdeeld, afhankelijk van de punt-tot-punt correlatie. Vormonzekerheden, voornamelijk afkomstig uit de deconvolutie, leiden tot een tegengestelde veranderingen voor hoge en lage $p_{\rm T}^{\rm jet}$. Gecorreleerde onzekerheden, gedomineerd door onzekerheden in de deeltjesspoorreconstructie, zijn punt-tot-punt gecorreleerd. Correlaties tussen $N_{\rm in}$ en $N_{\rm out}$ zijn voor alle onzekerheden in acht genomen.

$v_2^{\rm ch\ jet}$ is significant en positief in semi-centrale botsingen (Fig. C.1), wat duidt op energieverlies van partonen in het botingsmedium. In centrale botsingen leiden de achtergrondfluctuaties tot grote onzekerheden. De compatibiliteit van de meting met de hypothese $v_2^{\rm ch\ jet} = 0$ is getest middels een gemodificeerde χ^2 minimalisatie, en ligt tussen 1-2 standaarddeviaties voor centrale- en 3-4 standaarddeviatie voor semi-central botsingen. $v_2^{\rm part}$ van geladen deeltjes en de ATLAS meting van $v_2^{\rm calo\ jet}$ van $R = 0.2$ jets bestaande uit zowel geladen als neutrale deeltjes laten eveneens zien dat partonen energie verliezen in het botsingesmedium; de resultaten zijn kwalitatief vergelijkbaar voor zover de onzekerheden een vergelijking toelaten.

De $v_2^{\rm ch\ jet}$ meting is daarnaast vergeleken met voorspellingen van het JEWEL model, wat energieverlies van partonen door straling en verstrooiing in een QCD medium simuleert. In semi-centrale botsingen komt de voorspelling van JEWEL goed overeen met de metingen. JEWEL geeft echter geen beschrijving van fluctuaties in de distributie van nucleonen binnen de nuclei, hetwelk tot een onderschatting van de grootte van $v_2^{\rm ch\ jet}$ leidt in centrale botsingen.

Bibliography

[1] I. J. R. Aitchison and A. J. G. Hey, *Gauge theories in particle physics: a practical introduction; 4th ed.* CRC Press, Boca Raton, FL, 2013. https://cds.cern.ch/record/1507184.

[2] F. Halzen and A. Martin, *Quarks and leptons: an introductory course in modern particle physics*. Wiley, 1984.

[3] **CMS** Collaboration, S. Chatrchyan *et al.*, "Observation of a new boson at a mass of 125 GeV with the CMS experiment at the LHC," *Phys. Lett.* **B716** (2012) 30–61, arXiv:1207.7235 [hep-ex].

[4] **ATLAS** Collaboration, G. Aad *et al.*, "Observation of a new particle in the search for the Standard Model Higgs boson with the ATLAS detector at the LHC," *Phys. Lett.* **B716** (2012) 1–29, arXiv:1207.7214 [hep-ex].

[5] D. J. Gross and F. Wilczek, "Asymptotically free gauge theories. i," *Phys. Rev. D* **8** (Nov, 1973) 3633–3652. http://link.aps.org/doi/10.1103/PhysRevD.8.3633.

[6] G. Martinez, "Advances in Quark Gluon Plasma," 2013. arXiv:1304.1452 [nucl-ex].

[7] **LHCb** Collaboration, R. Aaij *et al.*, "Observation of J/Ψp Resonances Consistent with Pentaquark States in $\lambda_b^0 \to J/\Psi K^- p$ Decays," *Phys. Rev. Lett.* **115** (2015) 072001, arXiv:1507.03414 [hep-ex].

[8] **Particle Data Group** Collaboration, K. A. Olive *et al.*, "Review of Particle Physics," *Chin. Phys.* **C38** (2014) 090001.

[9] D. J. E. Callaway and A. Rahman, "Lattice gauge theory in the microcanonical ensemble," *Phys. Rev. D* **28** (Sep, 1983) 1506–1514. http://link.aps.org/doi/10.1103/PhysRevD.28.1506.

[10] S. Borsanyi, "Thermodynamics of the QCD transition from lattice," *Nucl. Phys.* **A904-905** (2013) 270c–277c, arXiv:1210.6901 [hep-lat].

[11] T. Boeckel and J. Schaffner-Bielich, "Little inflation at the cosmological QCD phase transition," **85** no. 10, (May, 2012) 103506, arXiv:1105.0832 [astro-ph.CO].

[12] M. J. Fromerth and J. Rafelski, "Hadronization of the quark Universe," arXiv:astro-ph/0211346 [astro-ph].

[13] A. M. Poskanzer, "A history of central collisions at the BEVALAC," in *NATO ASI: International Advanced Courses on The Nuclear Equation of State Peniscola, Spain, May 21-June 3, 1989*. 1989. http://www.osti.gov/energycitations/product.biblio.jsp?osti_id=5939286.

[14] U. W. Heinz and M. Jacob, "Evidence for a new state of matter: An Assessment of the results from the CERN lead beam program," arXiv:nucl-th/0002042 [nucl-th].

[15] RHIC, "Hunting the quark gluon plasma, results from the first three years at rhic,". BNL Report BNL-73847-2005, 18 April 2005.

[16] **ALICE** Collaboration, R. A. Bertens, "Azimuthal anisotropy of charged jet production in $\sqrt{s_{\mathrm{NN}}} = 2.76$ TeV Pb–Pb collisions," in *25th International Conference on Ultra-Relativistic Nucleus-Nucleus Collisions (Quark Matter 2015) Kobe, Japan, September 27-October 3, 2015*. 2015. arXiv:1511.05352 [nucl-ex]. http://inspirehep.net/record/1405136/files/arXiv:1511.05352.pdf.

[17] **ALICE** Collaboration, J. Adam *et al.*, "Azimuthal anisotropy of charged jet production in $\sqrt{s_{\mathrm{NN}}} = 2.76$ TeV Pb-Pb collisions," *Phys. Lett.* **B753** (2016) 511–525, arXiv:1509.07334 [nucl-ex].

[18] **ALICE** Collaboration, R. A. Bertens, "Parton energy loss and particle production at high momenta from ALICE," in *Proceedings, 50th Rencontres de Moriond, QCD and high energy interactions*, pp. 263–266. 2015. arXiv:1505.02915 [hep-ex]. http://inspirehep.net/record/1369334/files/arXiv:1505.02915.pdf.

[19] U. Heinz and R. Snellings, "Collective flow and viscosity in relativistic heavy-ion collisions," *Ann. Rev. Nucl. Part. Sci.* **63** (2013) 123–151, arXiv:1301.2826 [nucl-th].

[20] H. Niemi, "Collective dynamics in relativistic nuclear collisions," *Nuclear Physics A* **931** (2014) 227 – 237. http://www.sciencedirect.com/science/article/pii/S0375947414004825.

[21] J. M. Butterworth, G. Dissertori, and G. P. Salam, "Hard Processes in Proton-Proton Collisions at the Large Hadron Collider," *Ann. Rev. Nucl. Part. Sci.* **62** (2012) 387–405, arXiv:1202.0583 [hep-ex].

[22] G. P. Salam, "QCD in hadron collisions," *Frascati Phys. Ser.* **57** (2013) 155–166, arXiv:1207.0462 [hep-ph]. [Nuovo Cim.C035,no.06,155(2012)].

[23] K. J. Eskola and H. Honkanen, "A Perturbative QCD analysis of charged particle distributions in hadronic and nuclear collisions," *Nucl. Phys.* **A713** (2003) 167–187, arXiv:hep-ph/0205048 [hep-ph].

[24] F. Borzumati and G. Kramer, "Inclusive particle production in $p\bar{p}$ collisions," *Z. Phys.* **C67** (1995) 137–142, arXiv:hep-ph/9502280 [hep-ph].

[25] **UA1** Collaboration, "A study of the general characteristics of proton-antiproton collisions at $\sqrt{s} = 0.2$ to 0.9 tev," *Nuclear Physics B* **335** no. 2, (1990) 261 – 287. http://www.sciencedirect.com/science/article/pii/055032139090493W.

[26] G. Bocquet *et al.*, "Transverse momentum spectra of charged particles in $p\bar{p}$ collisions at $\sqrt{s} = 630$-GeV," *Phys. Lett.* **B366** (1996) 434–440.

[27] **CDF** Collaboration, "Transverse-momentum distributions of charged particles produced in $p \;\; p$ interactions at $\sqrt{\;} \; s$ =630 and 1800 gev," *Phys. Rev. Lett.* **61** (Oct, 1988) 1819–1822. http://link.aps.org/doi/10.1103/PhysRevLett.61.1819.

[28] V. N. Gribov and L. N. Lipatov, "Deep inelastic e p scattering in perturbation theory," *Sov. J. Nucl. Phys.* **15** (1972) 438–450. [Yad. Fiz.15,781(1972)].

[29] Y. L. Dokshitzer, "Calculation of the Structure Functions for Deep Inelastic Scattering and e+ e- Annihilation by Perturbation Theory in Quantum Chromodynamics.," *Sov. Phys. JETP* **46** (1977) 641–653. [Zh. Eksp. Teor. Fiz.73,1216(1977)].

[30] G. Altarelli and G. Parisi, "Asymptotic Freedom in Parton Language," *Nucl. Phys.* **B126** (1977) 298.

[31] V. Sudakov, "Vertex parts at very high energies in quantum electrodynamics," *Sov. Phys. J.E.T.P.* (1956) 65.

[32] T. Plehn, "Lectures on LHC Physics," *Lect. Notes Phys.* **844** (2012) 1–193, arXiv:0910.4182 [hep-ph].

[33] B. Andersson, G. Gustafson, G. Ingelman, and T. Sjöstrand, "Parton fragmentation and string dynamics," *Physics Reports* **97** no. 2-3, (1983) 31 – 145. http://www.sciencedirect.com/science/article/pii/0370157383900807.

[34] X. Artru, "Classical string phenomenology. how strings work," *Physics Reports* **97** no. 2-3, (1983) 147 – 171. http://www.sciencedirect.com/science/article/pii/0370157383900819.

[35] J. G. Milhano, "Theoretical overview of jet quenching," *Nucl. Phys.* **A904-905** (2013) 122c–129c, arXiv:1211.2657 [hep-ph].

[36] J. D. Bjorken, *Energy Loss of Energetic Partons in Quark - Gluon Plasma: Possible Extinction of High p(t) Jets in Hadron - Hadron Collisions*. 1982.

[37] M. Gyulassy and M. Plumer, "Jet Quenching in Dense Matter," *Phys.Lett.* **B243** (1990) 432–438.

[38] R. Baier, D. Schiff, and B. G. Zakharov, "Energy loss in perturbative QCD," *Ann. Rev. Nucl. Part. Sci.* **50** (2000) 37–69, arXiv:hep-ph/0002198 [hep-ph].

[39] M. H. Thoma, "Applications of high temperature field theory to heavy ion collisions," arXiv:hep-ph/9503400 [hep-ph].

[40] E. Braaten and R. D. Pisarski, "Resummation and gauge invariance of the gluon damping rate in hot qcd," *Phys. Rev. Lett.* **64** (Mar, 1990) 1338–1341. http://link.aps.org/doi/10.1103/PhysRevLett.64.1338.

[41] M. Gyulassy and M. Plumer, "Jet Quenching in Dense Matter," *Phys.Lett.* **B243** (1990) 432–438.

[42] R. Baier, Y. Dokshitzer, S. Peigné, and D. Schiff, "Induced gluon radiation in a QCD medium," *Physics Letters B* **345** no. 3, (1995) 277 – 286. http://www.sciencedirect.com/science/article/pii/037026939401617L.

[43] R. Baier, "Jet quenching," *Nucl. Phys.* **A715** (2003) 209–218, arXiv:hep-ph/0209038 [hep-ph].

[44] K. Zapp, G. Ingelman, J. Rathsman, J. Stachel, and U. A. Wiedemann, "A Monte Carlo Model for 'Jet Quenching'," *Eur. Phys. J.* **C60** (2009) 617–632, arXiv:0804.3568 [hep-ph].

[45] K. C. Zapp, J. Stachel, and U. A. Wiedemann, "LPM-Effect in Monte Carlo Models of Radiative Energy Loss," *Nucl. Phys.* **A830** (2009) 171C–174C, arXiv:0907.4304 [hep-ph].

[46] R. Baier, Y. L. Dokshitzer, A. H. Mueller, S. Peigné, and D. Schiff, "Radiative energy loss and p(T) broadening of high-energy partons in nuclei," *Nucl. Phys.* **B484** (1997) 265–282, arXiv:hep-ph/9608322 [hep-ph].

[47] R. Baier, Y. L. Dokshitzer, A. H. Mueller, S. Peigné, and D. Schiff, "Radiative energy loss of high-energy quarks and gluons in a finite volume quark - gluon plasma," *Nucl. Phys.* **B483** (1997) 291–320, arXiv:hep-ph/9607355 [hep-ph].

[48] S. Klein, "Suppression of bremsstrahlung and pair production due to environmental factors," *Rev. Mod. Phys.* **71** (Oct, 1999) 1501–1538. http://link.aps.org/doi/10.1103/RevModPhys.71.1501.

[49] L. Landua and I. Pomeranchuk *Dokl. Akad. Nauk SSSR* **92** (1953) 535,735.

[50] A. Migdal *Phys. Rev.* **103** (1956) 1811.

[51] R. Baier, Y. L. Dokshitzer, A. H. Mueller, S. Peigne, and D. Schiff, "The Landau-Pomeranchuk-Migdal effect in QED," *Nucl. Phys.* **B478** (1996) 577–597, arXiv:hep-ph/9604327 [hep-ph].

[52] F. Dominguez, C. Marquet, A. H. Mueller, B. Wu, and B.-W. Xiao, "Comparing energy loss and $p_\perp$ - broadening in perturbative QCD with strong coupling N = 4 SYM theory," *Nucl. Phys.* **A811** (2008) 197–222, arXiv:0803.3234 [nucl-th].

[53] C. Marquet and T. Renk, "Jet quenching in the strongly-interacting quark-gluon plasma," *Phys. Lett.* **B685** (2010) 270–276, arXiv:0908.0880 [hep-ph].

[54] E. Fermi, "High energy nuclear events," *Progress of theoretical physics* **5** no. 4, (1950) 570–583.

[55] J.-Y. Ollitrault, "Relativistic hydrodynamics for heavy-ion collisions," *Eur. J. Phys.* **29** (2008) 275–302, arXiv:0708.2433 [nucl-th].

[56] T. Hirano, N. van der Kolk, and A. Bilandzic, "Hydrodynamics and Flow," *Lect. Notes Phys.* **785** (2010) 139–178, arXiv:0808.2684 [nucl-th].

[57] M. L. Miller, K. Reygers, S. J. Sanders, and P. Steinberg, "Glauber modeling in high energy nuclear collisions," *Ann.Rev.Nucl.Part.Sci.* **57** (2007) 205–243, arXiv:nucl-ex/0701025 [nucl-ex].

[58] Y. Koychegov, *Quantum Chromodynamics at High Energy*. Cambridge University Press, 2012.

[59] H.-J. Drescher and Y. Nara, "Effects of fluctuations on the initial eccentricity from the color glass condensate in heavy ion collisions," *Phys. Rev. C* **75** (Mar, 2007) 034905. http://link.aps.org/doi/10.1103/PhysRevC.75.034905.

[60] **BCMOR** Collaboration, A. L. S. Angelis *et al.*, "Large Transverse Momentum π^0 Production in $\alpha\alpha dd$ and pp Collisions at the CERN ISR," *Phys. Lett.* **B185** (1987) 213.

[61] **WA98** Collaboration, M. M. Aggarwal *et al.*, "Transverse mass distributions of neutral pions from Pb-208 induced reactions at 158-A-GeV," *Eur. Phys. J.* **C23** (2002) 225–236, arXiv:nucl-ex/0108006 [nucl-ex].

[62] R. Glauber and G. Matthiae, "High-energy scattering of protons by nuclei," *Nuclear Physics B* **21** no. 2, (1970) 135 – 157. http://www.sciencedirect.com/science/article/pii/0550321370905110.

[63] D. G. d'Enterria, "Hard scattering cross-sections at LHC in the Glauber approach: From pp to pA and AA collisions," arXiv:nucl-ex/0302016 [nucl-ex].

[64] **ALICE** Collaboration, B. Abelev *et al.*, "Centrality Dependence of Charged Particle Production at Large Transverse Momentum in Pb–Pb Collisions at $\sqrt{s_{\rm NN}} = 2.76$ TeV," *Phys. Lett.* **B720** (2013) 52–62, arXiv:1208.2711 [hep-ex].

[65] **CMS** Collaboration, S. Chatrchyan *et al.*, "Measurement of isolated photon production in *pp* and PbPb collisions at $\sqrt{s_{NN}} = 2.76$ TeV," *Phys. Lett.* **B710** (2012) 256–277, arXiv:1201.3093 [nucl-ex].

[66] **ATLAS Collaboration** Collaboration, G. e. a. Aad, "Measurement of z boson production in pb-pb collisions at $\sqrt{s_{NN}}$=2.76 TeV with the atlas detector," *Phys. Rev. Lett.* **110** (Jan, 2013) 022301. http://link.aps.org/doi/10.1103/PhysRevLett.110.022301.

[67] **ALICE** Collaboration, J. Adam *et al.*, "Centrality dependence of particle production in p-Pb collisions at $\sqrt{s_{\rm NN}}$= 5.02 TeV," *Phys. Rev.* **C91** no. 6, (2015) 064905, arXiv:1412.6828 [nucl-ex].

[68] **ALICE** Collaboration, B. B. Abelev *et al.*, "Multiparticle azimuthal correlations in p -Pb and Pb-Pb collisions at the CERN Large Hadron Collider," *Phys. Rev.* **C90** no. 5, (2014) 054901, arXiv:1406.2474 [nucl-ex].

[69] **ALICE** Collaboration, B. B. Abelev *et al.*, "Long-range angular correlations of π, K and p in p-Pb collisions at $\sqrt{s_{\rm NN}}$ = 5.02 TeV," *Phys. Lett.* **B726** (2013) 164–177, arXiv:1307.3237 [nucl-ex].

[70] **ALICE** Collaboration, B. Abelev *et al.*, "Long-range angular correlations on the near and away side in p-Pb collisions at $\sqrt{s_{NN}} = 5.02$ TeV," *Phys. Lett.* **B719** (2013) 29–41, arXiv:1212.2001 [nucl-ex].

[71] **CMS** Collaboration, S. Chatrchyan *et al.*, "Multiplicity and transverse momentum dependence of two- and four-particle correlations in pPb and PbPb collisions," *Phys. Lett.* **B724** (2013) 213–240, arXiv:1305.0609 [nucl-ex].

[72] **ATLAS** Collaboration, G. Aad *et al.*, "Measurement of long-range pseudorapidity correlations and azimuthal harmonics in $\sqrt{s_{NN}} = 5.02$ TeV proton-lead collisions with the ATLAS detector," *Phys. Rev.* **C90** no. 4, (2014) 044906, arXiv:1409.1792 [hep-ex].

[73] G. Roland, K. Safarik, and P. Steinberg, "Heavy-ion collisions at the LHC," *Progress in Particle and Nuclear Physics* **77** (2014) 70 – 127. http://www.sciencedirect.com/science/article/pii/S0146641014000349.

[74] A. Majumder, "Elastic energy loss and longitudinal straggling of a hard jet," *Phys. Rev.* **C80** (2009) 031902, arXiv:0810.4967 [nucl-th].

[75] Y. L. Dokshitzer, V. A. Khoze, and S. I. Troian, "Particle spectra in light and heavy quark jets," *J. Phys.* **G17** (1991) 1481–1492.

[76] Y. L. Dokshitzer and D. E. Kharzeev, "Heavy quark colorimetry of QCD matter," *Phys. Lett.* **B519** (2001) 199–206, arXiv:hep-ph/0106202 [hep-ph].

[77] X.-N. Wang, M. Gyulassy, and M. Plümer, "Landau-pomeranchuk-migdal effect in qcd and radiative energy loss in a quark-gluon plasma," *Physical Review D* **51** no. 7, (1995) 3436.

[78] **JET Collaboration** Collaboration, K. M. Burke, A. Buzzatti, N. Chang, C. Gale, M. Gyulassy, U. Heinz, S. Jeon, A. Majumder, B. Müller, G.-Y. Qin, B. Schenke, C. Shen, X.-N. Wang, J. Xu, C. Young, and H. Zhang, "Extracting the jet transport coefficient from jet quenching in high-energy heavy-ion collisions," *Phys. Rev. C* **90** (Jul, 2014) 014909.

http://link.aps.org/doi/10.1103/PhysRevC.90.014909.

[79] B. Schenke, C. Gale, and S. Jeon, "MARTINI: An Event generator for relativistic heavy-ion collisions," *Phys. Rev.* **C80** (2009) 054913, arXiv:0909.2037 [hep-ph].

[80] X.-F. Chen, T. Hirano, E. Wang, X.-N. Wang, and H. Zhang, "Suppression of high p_T hadrons in $Pb+Pb$ Collisions at LHC," *Phys. Rev.* **C84** (2011) 034902, arXiv:1102.5614 [nucl-th].

[81] A. Majumder and C. Shen, "Suppression of the High p_T Charged Hadron R_{AA} at the LHC," *Phys. Rev. Lett.* **109** (2012) 202301, arXiv:1103.0809 [hep-ph].

[82] X.-F. Chen, C. Greiner, E. Wang, X.-N. Wang, and Z. Xu, "Bulk matter evolution and extraction of jet transport parameter in heavy-ion collisions at RHIC," *Phys. Rev.* **C81** (2010) 064908, arXiv:1002.1165 [nucl-th].

[83] G.-Y. Qin, J. Ruppert, C. Gale, S. Jeon, G. D. Moore, and M. G. Mustafa, "Radiative and collisional jet energy loss in the quark-gluon plasma at RHIC," *Phys. Rev. Lett.* **100** (2008) 072301, arXiv:0710.0605 [hep-ph].

[84] T. Renk, H. Holopainen, U. Heinz, and C. Shen, "A Systematic comparison of jet quenching in different fluid-dynamical models," *Phys. Rev.* **C83** (2011) 014910, arXiv:1010.1635 [hep-ph].

[85] C. A. Salgado and U. A. Wiedemann, "Calculating quenching weights," *Phys. Rev. D* **68** (Jul, 2003) 014008. http://link.aps.org/doi/10.1103/PhysRevD.68.014008.

[86] J.-Y. Ollitrault, "Anisotropy as a signature of transverse collective flow," *Phys. Rev. D* **46** (1992) 229–245. http://link.aps.org/doi/10.1103/PhysRevD.46.229.

[87] S. Voloshin and Y. Zhang, "Flow study in relativistic nuclear collisions by Fourier expansion of azimuthal particle distributions," *Zeitschrift für Physik C Particles and Fields* **70** no. 4, (1996) 665–671. http://dx.doi.org/10.1007/s002880050141.

[88] **E877 Collaboration** Collaboration, "Observation of anisotropic event shapes and transverse flow in ultrarelativistic au + au collisions," *Phys. Rev. Lett.* **73** (Nov, 1994) 2532–2535. http://link.aps.org/doi/10.1103/PhysRevLett.73.2532.

[89] A. M. Poskanzer and S. A. Voloshin, "Methods for analyzing anisotropic flow in relativistic nuclear collisions," *Phys. Rev. C* **58** (1998) 1671–1678. http://link.aps.org/doi/10.1103/PhysRevC.58.1671.

[90] A. Bilandzic, *Anisotropic flow measurements in ALICE at the Large Hadron Collider*. PhD thesis, Utrecht University, 2012.

[91] **ALICE** Collaboration, K. Aamodt *et al.*, "Higher harmonic anisotropic flow measurements of charged particles in Pb-Pb collisions at $\sqrt{s_{NN}}$=2.76 TeV," *Phys. Rev. Lett.* **107** (2011) 032301, arXiv:1105.3865 [nucl-ex].

[92] B. H. Alver, C. Gombeaud, M. Luzum, and J.-Y. Ollitrault, "Triangular flow in hydrodynamics and transport theory," *Phys. Rev. C* **82** (Sep, 2010) 034913. http://link.aps.org/doi/10.1103/PhysRevC.82.034913.

[93] **ALICE** Collaboration, B. B. Abelev *et al.*, "Elliptic flow of identified hadrons in Pb-Pb collisions at $\sqrt{s_{\rm NN}} = 2.76$ TeV," *JHEP* **06** (2015) 190, arXiv:1405.4632 [nucl-ex].

[94] H. Song and U. W. Heinz, "Suppression of elliptic flow in a minimally viscous quark-gluon plasma," *Phys. Lett.* **B658** (2008) 279–283, arXiv:0709.0742 [nucl-th].

[95] H. Song and U. W. Heinz, "Causal viscous hydrodynamics in 2+1 dimensions for relativistic heavy-ion collisions," *Phys. Rev.* **C77** (2008) 064901, arXiv:0712.3715 [nucl-th].

[96] H. Song and U. W. Heinz, "Multiplicity scaling in ideal and viscous hydrodynamics," *Phys. Rev.* **C78** (2008) 024902, arXiv:0805.1756 [nucl-th].

[97] H. Song, S. A. Bass, and U. Heinz, "Elliptic flow in $\sqrt{s} = 200$ gev au+au collisions and $\sqrt{s} = 2.76$ tev pb+pb collisions: Insights from viscous hydrodynamics+hadron cascade hybrid model," *Phys. Rev. C* **83** (May, 2011) 054912. http://link.aps.org/doi/10.1103/PhysRevC.83.054912.

[98] H. Song, S. A. Bass, and U. Heinz, "Erratum: Elliptic flow in $\sqrt{s} = 200$ gev au+au collisions and $\sqrt{s} = 2.76$ tev pb+pb collisions: Insights from viscous hydrodynamics+hadron cascade hybrid model [phys. rev. c **83** , 054912 (2011)]," *Phys. Rev. C* **87** (Jan, 2013) 019902. http://link.aps.org/doi/10.1103/PhysRevC.87.019902.

[99] S. de Groot, W. van Leeuwen, and C. van Weert, *Relativistic kinetic theory : principles and applications*. Elsevier North-Holland, 1980.

[100] A. Majumder, B. Müller, and X.-N. Wang, "Small shear viscosity of a quark-gluon plasma implies strong jet quenching," *Phys. Rev. Lett.* **99** (Nov, 2007) 192301. http://link.aps.org/doi/10.1103/PhysRevLett.99.192301.

[101] **CMS** Collaboration, S. Chatrchyan *et al.*, "Modification of jet shapes in PbPb collisions at $\sqrt{s_{NN}} = 2.76$ TeV," *Phys. Lett.* **B730** (2014) 243–263, arXiv:1310.0878 [nucl-ex].

[102] **CMS** Collaboration, C. Collaboration, "Decomposing energy balance contributions for quenched jets in PbPb versus pp collisions at $\sqrt{s_{NN}} = 2.76$ TeV,".

[103] K. C. Zapp, F. Krauss, and U. A. Wiedemann, "A perturbative framework for jet quenching," *JHEP* **1303** (2013) 080, arXiv:1212.1599 [hep-ph].

[104] K. C. Zapp, "Geometrical aspects of jet quenching in JEWEL," *Phys. Lett.* **B735** (2014) 157–163, arXiv:1312.5536 [hep-ph].

[105] T. Renk, "Parton shower evolution in a 3-d hydrodynamical medium," *Phys. Rev.* **C78** (2008) 034908, arXiv:0806.0305 [hep-ph].

[106] T. Renk, "Comparison study of medium-modified qcd shower evolution scenarios," *Phys. Rev. C* **79** (May, 2009) 054906. http://link.aps.org/doi/10.1103/PhysRevC.79.054906.

[107] T. Renk, "Using hard dihadron correlations to constrain elastic energy loss," *Phys. Rev. C* **84** (Dec, 2011) 067902. http://link.aps.org/doi/10.1103/PhysRevC.84.067902.

[108] **ALICE** Collaboration, B. Abelev *et al.*, "Measurement of charged jet suppression in Pb-Pb collisions at $\sqrt{s_{\rm NN}} = 2.76$ TeV," *JHEP* **1403** (2014) 013, arXiv:1311.0633 [nucl-ex].

[109] **STAR** Collaboration, J. Adams *et al.*, "Experimental and theoretical challenges in the search for the quark gluon plasma: The STAR Collaboration's critical assessment of the evidence from RHIC collisions," *Nucl.Phys.* **A757** (2005) 102–183, arXiv:nucl-ex/0501009 [nucl-ex].

[110] **PHENIX** Collaboration, K. Adcox *et al.*, "Formation of dense partonic matter in relativistic nucleus-nucleus collisions at RHIC: Experimental evaluation by the PHENIX collaboration," *Nucl.Phys.* **A757** (2005) 184–283, arXiv:nucl-ex/0410003 [nucl-ex].

[111] **BRAHMS** Collaboration, I. Arsene *et al.*, "Transverse momentum spectra in Au+Au and d+Au collisions at $\sqrt{s_{\mathrm{NN}}} =$ 200 GeV and the pseudorapidity dependence of high p_{T} suppression," *Phys.Rev.Lett.* **91** (2003) 072305, arXiv:nucl-ex/0307003 [nucl-ex].

[112] **PHOBOS** Collaboration, B. Back *et al.*, "Charged hadron transverse momentum distributions in Au + Au collisions at $\sqrt{s_{\mathrm{NN}}} =$ 200 GeV," *Phys.Lett.* **B578** (2004) 297–303, arXiv:nucl-ex/0302015 [nucl-ex].

[113] **ALICE** Collaboration, K. Aamodt *et al.*, "Suppression of Charged Particle Production at Large Transverse Momentum in Central Pb–Pb Collisions at $\sqrt{s_{\mathrm{NN}}} = 2.76$ TeV," *Phys. Lett.* **B696** (2011) 30–39, arXiv:1012.1004 [nucl-ex].

[114] **ALICE** Collaboration, K. Aamodt *et al.*, "Particle-yield modification in jet-like azimuthal di-hadron correlations in Pb-Pb collisions at $\sqrt{s_{\mathrm{NN}}} = 2.76$ TeV," *Phys.Rev.Lett.* **108** (2012) 092301, arXiv:1110.0121 [nucl-ex].

[115] **ATLAS** Collaboration, G. Aad *et al.*, "Measurement of charged-particle spectra in Pb+Pb collisions at $\sqrt{s_{\mathrm{NN}}} =$ 2.76 TeV with the ATLAS detector at the LHC," arXiv:1504.04337 [hep-ex].

[116] **CMS** Collaboration, S. Chatrchyan *et al.*, "Study of high p_{T} charged particle suppression in Pb–Pb compared to *pp* collisions at $\sqrt{s_{\mathrm{NN}}} = 2.76$ TeV," *Eur.Phys.J.* **C72** (2012) 1945, arXiv:1202.2554 [nucl-ex].

[117] **ATLAS** Collaboration, G. Aad *et al.*, "Observation of a Centrality-Dependent Dijet Asymmetry in Lead-Lead Collisions at $\sqrt{s_{\mathrm{NN}}}= 2.76$ TeV with the ATLAS Detector at the LHC," *Phys. Rev. Lett.* **105** (2010) 252303, arXiv:1011.6182 [hep-ex].

[118] **CMS** Collaboration, S. Chatrchyan *et al.*, "Jet momentum dependence of jet quenching in Pb–Pb collisions at $\sqrt{s_{\mathrm{NN}}} = 2.76$ TeV," *Phys.Lett.* **B712** (2012) 176–197, arXiv:1202.5022 [nucl-ex].

[119] **ATLAS** Collaboration, G. Aad *et al.*, "Measurement of the jet radius and transverse momentum dependence of inclusive jet suppression in lead-lead collisions at $\sqrt{s_{\mathrm{NN}}} = 2.76$ TeV with the ATLAS detector," *Phys.Lett.* **B719** (2013) 220–241, arXiv:1208.1967 [hep-ex].

[120] **ALICE** Collaboration, J. Adam *et al.*, "Measurement of jet suppression in central Pb–Pb collisions at $\sqrt{s_{\mathrm{NN}}} = 2.76$ TeV," *Phys. Lett.* **B746** (2015) 1–14, arXiv:1502.01689 [nucl-ex].

[121] L. Evans and P. Bryant, "LHC machine," *Journal of Instrumentation* **3** no. 08, (2008) S08001. http://stacks.iop.org/1748-0221/3/i=08/a=S08001.

[122] **ATLAS** Collaboration, G. Aad *et al.*, "The ATLAS Experiment at the CERN Large Hadron Collider," *JINST* **3** (2008) S08003.

[123] **CMS** Collaboration, S. Chatrchyan *et al.*, "The CMS experiment at the CERN LHC," *JINST* **3** (2008) S08004.

[124] **LHCb** Collaboration, A. A. Alves, Jr. *et al.*, "The LHCb Detector at the LHC," *JINST* **3** (2008) S08005.

[125] **ALICE** Collaboration, K. Aamodt *et al.*, "The ALICE experiment at the CERN LHC," *JINST* **3** (2008) S08002.

[126] **ALICE** Collaboration, F. C. et al, "Alice: Physics performance report, volume i," *Journal of Physics G: Nuclear and Particle Physics* **30** no. 11, (2004) 1517. http://stacks.iop.org/0954-3899/30/i=11/a=001.

[127] **ALICE** Collaboration, B. A. et al, "Alice: Physics performance report, volume ii," *Journal of Physics G: Nuclear and Particle Physics* **32** no. 10, (2006) 1295. http://stacks.iop.org/0954-3899/32/i=10/a=001.

[128] **ALICE** Collaboration, B. Abelev *et al.*, "Performance of the ALICE Experiment at the CERN LHC," *Int. J. Mod. Phys.* **A29** (2014) 1430044, arXiv:1402.4476 [nucl-ex].

[129] P. Steinberg, "First results from the lhc heavy ion program," *New J. of Phys.* **14** no. 3, (2012) 035006. http://stacks.iop.org/1367-2630/14/i=3/a=035006.

[130] **ALICE** Collaboration, K. Aamodt *et al.*, "Alignment of the ALICE Inner Tracking System with cosmic-ray tracks," *JINST* **5** (2010) P03003, arXiv:1001.0502 [physics.ins-det].

[131] **ALICE** Collaboration, J. A. et al, "The ALICE TPC, a large 3-dimensional tracking device with fast readout for ultra-high multiplicity events," *Nuclear Instruments and Methods in Physics Research Section A: Accelerators, Spectrometers, Detectors and Associated Equipment* **622** no. 1, (2010) 316 – 367. http://www.sciencedirect.com/science/article/pii/S0168900210008910.

[132] **ALICE** Collaboration, E. Abbas *et al.*, "Performance of the ALICE VZERO system," *JINST* **8** (2013) P10016, arXiv:1306.3130 [nucl-ex].

[133] **ALICE** Collaboration, P. e. a. Cortese, "ALICE Electromagnetic Calorimeter Technical Design Report," Tech. Rep. CERN-LHCC-2008-014. ALICE-TDR-14, CERN, Geneva, Aug, 2008. https://cds.cern.ch/record/1121574.

[134] **ALICE** Collaboration, B. B. Abelev *et al.*, "Elliptic flow of identified hadrons in Pb-Pb collisions at $\sqrt{s_{\mathrm{NN}}} = 2.76$ TeV," arXiv:1405.4632 [nucl-ex].

[135] **ALICE** Collaboration, B. Abelev *et al.*, "Centrality determination of Pb-Pb collisions at $\sqrt{s_{\mathrm{NN}}} = 2.76$ TeV with ALICE," *Phys.Rev.* **C88** no. 4, (2013) 044909, arXiv:1301.4361 [nucl-ex].

[136] J. F. Grosse-Oetringhaus and K. Reygers, "Charged-Particle Multiplicity in Proton-Proton Collisions," *J. Phys.* **G37** (2010) 083001, arXiv:0912.0023 [hep-ex].

[137] **ALICE** Collaboration, K. Aamodt *et al.*, "First proton-proton collisions at the LHC as observed with the ALICE detector: Measurement of the charged particle pseudorapidity density at s**(1/2) = 900-GeV," *Eur. Phys. J.* **C65** (2010) 111–125, arXiv:0911.5430 [hep-ex].

[138] **ALICE** Collaboration, K. Aamodt *et al.*, "Charged-particle multiplicity measurement in proton-proton collisions at $\sqrt{s} = 0.9$ and 2.36 TeV with ALICE at LHC," *Eur. Phys. J.* **C68** (2010) 89–108, arXiv:1004.3034 [hep-ex].

[139] R. Fruhwirth, "Application of Kalman filtering to track and vertex fitting," *Nucl.Instrum.Meth.* **A262** (1987) 444–450.

[140] R. Brun, F. Carminati, and S. Giani, "GEANT Detector Description and Simulation Tool,".

[141] X.-N. Wang and M. Gyulassy, "HIJING: A Monte Carlo model for multiple jet production in p p, p A and A A collisions," *Phys. Rev.* **D44** (1991) 3501–3516.

[142] B. Andersson, G. Gustafson, and B. Nilsson-Almqvist, "A model for low-pt hadronic reactions with generalizations to hadron-nucleus and nucleus-nucleus collisions," *Nuclear Physics B* **281** no. 1, (1987) 289 – 309. http://www.sciencedirect.com/science/article/pi/0550321387902574.

[143] J. Ranft, "Hadron production in hadron-nucleus and nucleus-nucleus collisions in the dual monte carlo multichain fragmentation model," *Phys. Rev. D* **37** (Apr, 1988) 1842–1850. http://link.aps.org/doi/10.1103/PhysRevD.37.1842.

[144] T. Sjostrand, S. Mrenna, and P. Z. Skands, "PYTHIA 6.4 Physics and Manual," *JHEP* **05** (2006) 026, arXiv:hep-ph/0603175 [hep-ph].

[145] P. Z. Skands, "Tuning Monte Carlo Generators: The Perugia Tunes," *Phys. Rev.* **D82** (2010) 074018, arXiv:1005.3457 [hep-ph].

[146] "AliPhysics." http://git.cern.ch/pubweb/AliPhysics.git. Accessed between: 08.2012-02.2016.

[147] "AliRoot." http://git.cern.ch/pubweb/AliRoot.git. Accessed between: 08.2012-02.2016.

[148] "Analysis in ALICE." http://alice-analysis.web.cern.ch. Accessed between: 08.2012-02.2016.

[149] "ROOT, a data analysis framework." https://root.cern.ch. Accessed between: 08.2012-02.2016.

[150] "Alien - alice environment grid framework." http://alien.web.cern.ch/. Accessed: 02.2016.

[151] "Alice grid." http://pcalimonitor.cern.ch/map.jsp. Accessed: 02.2016.

[152] S. D. Ellis and D. E. Soper, "Successive combination jet algorithm for hadron collisions," *Phys. Rev.* **D48** (1993) 3160–3166, arXiv:hep-ph/9305266 [hep-ph].

[153] M. Cacciari, G. P. Salam, and G. Soyez, "The Anti-k(t) jet clustering algorithm," *JHEP* **04** (2008) 063, arXiv:0802.1189 [hep-ph].

[154] M. Cacciari and G. P. Salam, "Dispelling the N^3 myth for the k_T jet-finder," *Phys.Lett.* **B641** (2006) 57–61, arXiv:hep-ph/0512210 [hep-ph].

[155] M. Cacciari, G. P. Salam, and G. Soyez, "FastJet User Manual," *Eur.Phys.J.* **C72** (2012) 1896, arXiv:1111.6097 [hep-ph].

[156] G. P. Salam, "Towards Jetography," *Eur. Phys. J.* **C67** (2010) 637–686, arXiv:0906.1833 [hep-ph].

[157] M. Cacciari and G. P. Salam, "Pileup subtraction using jet areas," *Phys. Lett.* **B659** (2008) 119–126, arXiv:0707.1378 [hep-ph].

[158] **ALICE** Collaboration, B. Abelev *et al.*, "Measurement of Event Background Fluctuations for Charged Particle Jet Reconstruction in Pb-Pb collisions at $\sqrt{s_{\mathrm{NN}}} = 2.76$ TeV," *JHEP* **1203** (2012) 053, arXiv:1201.2423 [hep-ex].

[159] M. Verweij, R. J. M. Snellings, and R. Kamermans, *Modelling and measurement of jet quenching in relativistic heavy-ion collisions at the LHC*. PhD thesis, Utrecht University, 2013. presented 7 Oct 2013.

[160] P. Danielewicz and G. Odyniec, "Transverse momentum analysis of collective motion in relativistic nuclear collisions," *Physics Letters B* **157** no. 2, (1985) 146 – 150. http://www.sciencedirect.com/science/article/pii/0370269385915357.

[161] I. Selyuzhenkov and S. Voloshin, "Effects of nonuniform acceptance in anisotropic flow measurements," *Phys. Rev. C* **77** (2008) 034904. http://link.aps.org/doi/10.1103/PhysRevC.77.034904.

[162] **CMS** Collaboration, S. Chatrchyan *et al.*, "Measurement of the elliptic anisotropy of charged particles produced in PbPb collisions at $\sqrt{s}_{NN}$=2.76 TeV," *Phys. Rev.* **C87** no. 1, (2013) 014902, arXiv:1204.1409 [nucl-ex].

[163] **PHOBOS** Collaboration, B. B. Back *et al.*, "Centrality and pseudorapidity dependence of elliptic flow for charged hadrons in Au+Au collisions at s(NN)**(1/2) = 200-GeV," *Phys. Rev.* **C72** (2005) 051901, arXiv:nucl-ex/0407012 [nucl-ex].

[164] **ATLAS** Collaboration, G. Aad *et al.*, "Measurement of the centrality and pseudorapidity dependence of the integrated elliptic flow in lead-lead collisions at $\sqrt{s_{\rm NN}}$ = 2.76 TeV with the ATLAS detector," *Eur. Phys. J.* **C74** no. 8, (2014) 2982, arXiv:1405.3936 [hep-ex].

[165] **PHOBOS** Collaboration, B. B. Back *et al.*, "Energy dependence of elliptic flow over a large pseudorapidity range in Au+Au collisions at RHIC," *Phys. Rev. Lett.* **94** (2005) 122303, arXiv:nucl-ex/0406021 [nucl-ex].

[166] **E877** Collaboration, Barrette, J. *et al*, "Energy and charged particle flow in 10.8A GeV/c Au+Au collisions," *Phys. Rev. C* **55** (1997) 1420–1430. http://link.aps.org/doi/10.1103/PhysRevC.55.1420.

[167] **E877** Collaboration, Barrette, J. *et al*, "Erratum: Energy and charged particle flow in 10.8A GeV/c Au+Au collisions [Phys. Rev. C **55**, 1420 (1997)]," *Phys. Rev. C* **56** (Oct, 1997) 2336–2336. http://link.aps.org/doi/10.1103/PhysRevC.56.2336.

[168] **CMS** Collaboration, V. Khachatryan *et al.*, "Evidence for transverse momentum and pseudorapidity dependent event plane fluctuations in PbPb and pPb collisions," *Phys. Rev.* **C92** no. 3, (2015) 034911, arXiv:1503.01692 [nucl-ex].

[169] **ALICE** Collaboration, K. Aamodt *et al.*, "Elliptic flow of charged particles in Pb–Pb collisions at $\sqrt{s_{\rm NN}}$ = 2.76 TeV," *Phys. Rev. Lett.* **105** (2010) 252302, arXiv:1011.3914 [nucl-ex].

[170] S. Baker and R. D. Cousins, "Clarification of the Use of Chi Square and Likelihood Functions in Fits to Histograms," *Nucl.Instrum.Meth.* **221** (1984) 437–442.

[171] A. Bilandzic, R. Snellings, and S. Voloshin, "Flow analysis with cumulants: Direct calculations," *Phys.Rev.* **C83** (2011) 044913, arXiv:1010.0233 [nucl-ex].

[172] V. Blobel, "An Unfolding method for high-energy physics experiments," in *Advanced statistical techniques in particle physics. Proceedings, Conference, Durham, UK, March 18-22, 2002*, pp. 258–267. 2002.

arXiv:hep-ex/0208022 [hep-ex]. http://www.ippp.dur.ac.uk/Workshops/02/statistics/proceedings//blobel2.pdf.

[173] M. Schmelling, "The Method of reduced cross entropy: A General approach to unfold probability distributions," *Nucl. Instrum. Meth.* **A340** (1994) 400–412.

[174] C. Tsallis, "Possible generalization of boltzmann-gibbs statistics," *Journal of Statistical Physics* **52** no. 1, 479–487. http://dx.doi.org/10.1007/BF01016429.

[175] G. de Barros, B. Fenton-Olsen, P. Jacobs, and M. Płoskon, "Data-driven analysis methods for the measurement of reconstructed jets in heavy ion collisions at RHIC and LHC," *Nucl.Phys.* **A910-911** (2013) 314–318, arXiv:1208.1518 [hep-ex].

[176] G. Cowan, *Statistical Data Analysis*. Oxford science publications. Clarendon Press, 1998.

[177] G. Cowan, "A survey of unfolding methods for particle physics," *Conf. Proc.* **C0203181** (2002) 248–257. [,248(2002)].

[178] A. Hocker and V. Kartvelishvili, "SVD approach to data unfolding," *Nucl. Instrum. Meth.* **A372** (1996) 469–481, arXiv:hep-ph/9509307 [hep-ph].

[179] T. Adye, "Unfolding algorithms and tests using roounfold,". http://arxiv.org/abs/1105.1160. arxiv:1105.1160.

[180] C. Lawson and R. Hanson, *Solving Least Squares Problems*. Classics in Applied Mathematics. Society for Industrial and Applied Mathematics, 1995.

[181] S. A. Voloshin, A. M. Poskanzer, A. Tang, and G. Wang, "Elliptic flow in the Gaussian model of eccentricity fluctuations," *Phys. Lett.* **B659** (2008) 537–541, arXiv:0708.0800 [nucl-th].

[182] H. Cramer, *Mathematical methods of statistics*. Princeton Univeristy Press, 1946.

[183] V. Blobel, "Unfolding methods in high-energy physics experiments," No. DESY-84-118, p. 40 p. 1984. http://cds.cern.ch/record/157405.

[184] L. Lyons, "On estimating systematic errors from repeated measurements," *Journal of Physics A: Mathematical and General* **25** no. 7, (1992) 1967. http://stacks.iop.org/0305-4470/25/i=7/a=035.

[185] **ALICE** Collaboration, B. Abelev *et al.*, "Anisotropic flow of charged hadrons, pions and (anti-)protons measured at high transverse momentum in Pb-Pb collisions at $\sqrt{s_{\rm NN}}$=2.76 TeV," *Phys.Lett.* **B719** (2013) 18–28, arXiv:1205.5761 [nucl-ex].

[186] **CMS** Collaboration, S. Chatrchyan *et al.*, "Azimuthal anisotropy of charged particles at high transverse momenta in Pb–Pb collisions at $\sqrt{s_{\rm NN}} = 2.76$ TeV," *Phys.Rev.Lett.* **109** (2012) 022301, arXiv:1204.1850 [nucl-ex].

[187] **ATLAS** Collaboration, G. Aad *et al.*, "Measurement of the Azimuthal Angle Dependence of Inclusive Jet Yields in Pb+Pb Collisions at $\sqrt{s_{\rm NN}} = 2.76$ TeV with the ATLAS detector," *Phys.Rev.Lett.* **111** no. 15, (2013) 152301, arXiv:1306.6469 [hep-ex].

[188] **ATLAS** Collaboration, G. Aad *et al.*, "Measurement of the jet radius and transverse momentum dependence of inclusive jet suppression in lead–lead collisions at $\sqrt{s_{\rm NN}} = 2.76$ TeV with the ATLAS detector," *Phys. Lett.* **B719** (2013) 220–241, arXiv:1208.1967 [hep-ex].

[189] **PHENIX** Collaboration, A. Adare *et al.*, "Quantitative constraints on the transport properties of hot partonic matter from semi-inclusive single high transverse momentum pion suppression in Au+Au collisions at $\sqrt{s_{\mathrm{NN}}} = 200$ GeV," *Phys. Rev. C* **77** (2008) 064907. http://link.aps.org/doi/10.1103/PhysRevC.77.064907.

[190] J.-Y. Ollitrault, "Anisotropy as a signature of transverse collective flow," *Phys. Rev.* **D46** (1992) 229–245.

[191] **PHOBOS** Collaboration, B. Alver *et al.*, "System size, energy, pseudorapidity, and centrality dependence of elliptic flow," *Phys. Rev. Lett.* **98** (2007) 242302, arXiv:nucl-ex/0610037 [nucl-ex].

[192] C. Loizides and J. Putschke, "Remarks on the possible importance of jet v_3 and multiple jet production for the interpretation of recent jet quenching measurements at the LHC," *Phys. Rev.* **C85** (2012) 044916, arXiv:1111.4472 [nucl-ex].

[193] J. G. Milhano and K. C. Zapp, "Origins of the di-jet asymmetry in heavy ion collisions," arXiv:1512.08107 [hep-ph].

[194] F. Senzel, O. Fochler, J. Uphoff, Z. Xu, and C. Greiner, "Influence of multiple in-medium scattering processes on the momentum imbalance of reconstructed di-jets," *J. Phys.* **G42** no. 11, (2015) 115104, arXiv:1309.1657 [hep-ph].

Index and Glossary

Acknowledgements

> *. . . On an exceptionally hot evening early in July a young man came out of the garret in which he lodged in S. Place and walked slowly, as though in hesitation, towards K. bridge.*
>
> – F. M. Dostoyevsky, *Crime and Punishment (1866)*

Thanks to Raimond and Marco.

```
    . . . . o o o o o
          _____      o       _______
 ____====  ]00|_n_n__][.     | all |
[________]_|__|________)<    |done!|
oo    oo  'oo 0000-| oo  _   ~~~|~~~
```

Redmer Alexander Bertens

Curriculum Vitæ

address: Utrecht, Netherlands – Gex, France
phone: (+31) 6 2855 1302
mail: rbertens@cern.ch, linkedin.com/in/rbertens

Profile

Work experience as physicist and data scientist at the ALICE experiment at the Large Hadron Collider (LHC) at CERN, the largest particle physics laboratory in the world. Currently I'm working on understanding the properties of the Quark-Gluon Plasma by studying the petabytes of data that are recorded during the CERN heavy-ion collision program.

Work experience

current **Postdoctoral Research Associate**, CERN, University Of Tennessee, Knoxville, USA

2016.8 **PhD in Particle Physics**, Utrecht University, Utrecht, Netherlands
2012.8 *'Path length dependence of jet quenching measured with ALICE at the LHC'* - Developing software for statistical data analysis of measurements of the ALICE detector at CERN (Geneva), as part of a larger framework. Working with large data sets ($\simeq$ petabyte), using a distributed grid (80.000 CPU cores). Maintaining source code (c/c++, 10.000 lines) using SVN and GIT, responsible for larger framework development and maintenance (100.000 lines) and algorithm design. Responsible for detector operation at CERN during shifts.

Skills

Broad experience with object-oriented programming (c++), scripting (bash, PYTHON) solving numerical and statistical problems (data processing and mining of large data volumes) collaborating internationally on software projects (5.000.000+ lines of code) using version control systems (SVN, GIT), and coaching students (bachelor and master's level) on research processes.

Education

2012.8 **Master of Science**, Utrecht University, Netherlands
2010.8 Experimental physics, specialization in computation and particle physics, GPA 4.0

2010.8 **Bachelor of Science**, Utrecht University, Netherlands
2007.8 Physics and astronomy

Languages

- Dutch (native proficiency)
- English (full professional proficiency)
- German (elementary proficiency)
- French (elementary proficiency)

Publications

As ALICE member

The following are ALICE publications of which I am one of the primary authors:

- A. Adam et al. [ALICE Collaboration], *'Azimuthal anisotropy of charged jet production in $\sqrt{s_{\rm NN}}$= 2.76 TeV Pb-Pb collisions'* , Phys.Lett. B753 (2016) 511-525
- B. Abelev et al. [ALICE Collaboration], *'Elliptic flow of identified hadrons in Pb–Pb collisions at $\sqrt{s_{\rm NN}}$ = 2.76 TeV'*, JHEP 1506 (2015) 190

Conference proceedings

- *'Azimuthal anisotropy of charged jet production in $\sqrt{s_{\rm NN}}$= 2.76 TeV Pb-Pb collisions'* , 25th International Conference on Ultra-Relativistic Nucleus-Nucleus Collisions (Quark Matter 2015) Kobe, Japan, September 27-October 3, 2015
- *'Parton energy loss and particle production at high momenta from ALICE'*, Proceedings, 50th Rencontres de Moriond, QCD and high energy interactions, 2015, 263-266

Other publications

- *Energy loss in the quark-gluon plasma - $v_2^{\rm ch\ jet}$ measurements with ALICE* (with M. van Leeuwen), CERN Courier Volume 56, Number 2, March 2016

Invited talks

2016

- *'Hard probes of the hot plasma'*, **Kernphysikalisches Kolloquium**, Frankfurt am Main, Germany

Conference talks

2016

'Jets with ALICE', **Jet vetoes and multiplicity observables**, Durham, United Kingdom

2015

- *'Azimuthal anisotropy of charged jet production in Pb–Pb collisions at 2.76 TeV with the ALICE detector'*, **NIKHEF annual meeting**, Amsterdam, the Netherlands
- *'Azimuthal anisotropy of charged jet production in Pb–Pb collisions at 2.76 TeV with the ALICE detector'*, **Quark Matter 2015**, Kobe, Japan
- *'Nuclear modification factor in Pb–Pb and p–Pb collisions with ALICE'*, **50$^{\rm th}$ rencontres de Moriond**, La Thuile, Italy

2014

- *'Azimuthal anisotropy of charged jet production in Pb–Pb collisions at 2.76 TeV with the ALICE detector'*, **Najaarsvergadering Nederlandse Natuurkundige Vereniging**, Lunteren, the Netherlands

2013

- *'Anisotropic flow of identified particles in Pb–Pb collisions at 2.76 TeV with the ALICE detector'*, **Najaarsvergadering Nederlandse Natuurkundige Vereniging**, Lunteren, the Netherlands

2012

- *'Anisotropic flow of the ϕ-meson in Pb–Pb collisions at 2.76 TeV with the ALICE detector'*, **WPCF 2012**, Frankfurt am Main, Germany

Poster presentations

2014

- *'Azimuthal anisotropy of charged jet production in Pb–Pb collisions at 2.76 TeV with the ALICE detector'*, **Quark Matter 2014**, Darmstadt, Germany